# A numerical study of spiral galaxies and dynamical effects of spiral arms

---

Robert John James Grand

Thesis submitted for the degree of

**Doctorate of Philosophy (PhD)**

**of**

**University College London**

Mullard Space Science Laboratory

Department of Space and Climate Physics

University College London

I, Robert John James Grand, confirm that the work presented in this thesis is my own. Where information has been derived from other sources, I confirm that this has been indicated in the thesis.

_____

_____

# Acknowledgements

It is a pleasure to thank my supervisors Dr. Daisuke Kawata and Prof. Mark Cropper, to whom I am deeply indebted for their inexhaustible help and support throughout my PhD studies. It is beyond doubt that this thesis would not exist in its present form without their generous teaching, expertise and guidance, from which I have benefited enormously. It has been an absolute pleasure to work with them.

I thank the examiners of this PhD thesis, Dr. Witold Maciejewski and Dr. Ignacio Ferreras, for their attention to detail and a challenging but enjoyable Viva. Their helpful comments and suggestions have improved the quality of this thesis.

I would like to thank the other members of the Astrophysics group at MSSL for contributing to the exciting and stimulating scientific environment in which I have been lucky enough to work. In particular, I would like to thank Prof. Kinwah Wu for many insightful and fascinating discussions on a number of diverse topics. I am grateful to Dr. Stefano Pasetto, Dr Dave Vande Putte and Dr Curtis Saxton for their help and contributions to stimulating discussions. I extend my gratitude to all my other friends here at MSSL for making my time here that much more enjoyable.

Finally, I say a huge thank you to my girlfriend (Salud) and parents (Rob and Joan) for their endless love, support and encouragement. An extra thanks go to Salud for her patience and putting up with many a frustrated mood and astrophysics-induced stupor of mine, particularly those evenings and weekend days when my preoccupation made me less than good company. To my parents Rob and Joan, I am forever grateful for everything they have done for me: from teaching me the importance of hard work and perseverance to their over-generous financial support over the years.

# Abstract

We use high-resolution numerical simulations of disc galaxies to study spiral arms and their dynamical influence on nearby stars. We find that in the numerical simulations the spiral arms are winding, transient features whose pattern speeds decrease with radius in such a way that the pattern speed is almost equal to the rotation curve of the galaxy. We validate this for normal and barred-spirals, and demonstrate that there is no significant offset of different star-forming tracers across the spiral arm. We show from the dynamics of nearby star particles that star particles are drawn towards and join the spiral arm from behind (in front of) the arm and migrate towards the outer (inner) regions of the disc until the arm disappears. The resulting gain (loss) of angular momentum of star particles behind (in front of) the spiral arm is termed radial migration, and occurs over the entire radial range analyzed. A direct consequence of ubiquitous co-rotation radii is that the guiding centre radii of particles are changed while their degree of random motion is unchanged. We show that there are several types of migrator particles, as well as particles that do not migrate, that each have a different orbital evolution. We show that the orbital type depends on position in configuration and phase space, and show how the orbits can make up moving group features in velocity space. We investigate the correlation between the galactic shear rate and the pitch angle of both individual density waves and the apparent co-rotating spiral arms. We find that, in both cases, higher galactic shear rates produce more tightly wound spiral arms, in agreement with observation. We find also that winding spiral arms can naturally explain the scatter in the pitch angle-shear rate relation seen from observations.

# Contents

# List of Figures

# List of Tables

# Chapter 1

# Introduction

## 1.1 Spiral galaxies

Spiral arms are beautiful structures that have fascinated generations since Lord Rosse discovered the nearby spiral galaxy Messier 51, or "Whirlpool" galaxy in 1845. They are features of disc-shaped galaxies, which account for as many as $\sim$ 70% of bright galaxies in the local volume (e.g. Sparke & Gallagher, 2007). Spirals are global enhancements in surface brightness caused by high concentrations of cold gas and young, bright stars (e.g. Fujimoto, 1968; Roberts, 1969). In addition to young stars, multi-wavelength observations have revealed that older stellar populations trace out the spiral arms (e.g. Rix & Zaritsky, 1995). These old, dim stars make up a significant fraction of the disc mass, which means that spiral arm features carry a significant underlying gravitational potential.

There are typically five structural components associated with spiral galaxies: a disc, a bulge, a bar, a stellar halo and a dark matter halo. The most massive component is the dark matter halo. A major piece of evidence for the existence of the invisible matter known as "dark matter" came from circular speed measurements from radio observations of neutral hydrogen, which extends to radii beyond the stellar disc. Outside of the visible extent of the galaxy, the stellar mass distribution may be approximated as a point mass located at the centre of the galaxy. In such a system, the circular velocity decreases as $v_c(r) = (GM/r)^{1/2}$, where $M$ is the stellar mass within a radius $r$, and becomes constant at large radii. However, the radial profiles of circular speed observed in disc galaxies are typically flat, which indicates that there should be a large amount of matter in and

around galaxies that we cannot see (e.g. Carignan & Freeman, 1985; van Albada *et al.*, 1985). Typically the required mass amounts to about $90-95\%$ of the total galaxy mass, and interacts only through gravity (not electromagnetically). Currently, the most widely accepted theory for dark matter is the $\Lambda$ cold dark matter ($\Lambda$CDM) cosmology. $N$-body simulations based on a range of CDM cosmologies suggest that individual galaxy dark matter haloes follow a universal density profile, the so-called "Navarro-Frenk-White" profile (Navarro *et al.*, 1997).

Spiral structure is associated with the rotationally supported disc of stars and gas whose radial profile of surface brightness is well described by an exponential profile (e.g. Freeman, 1970; de Jong *et al.*, 2004), the radial scale lengths of which range from 1 - 10 kpc. The stellar thin disc of the Milky Way, for example, has a radial scale length of about $\sim$ 2.5 - 3.0 kpc (e.g. McMillan, 2011). The vertical density distribution of stellar thin discs is well described also by an exponential profile (e.g. Gilmore & Reid, 1983). The gas disc is composed of multi-phased media with complex structure (McKee & Ostriker, 1977); a hot ionised medium of low density and high volume and temperature, warm ionised and neutral media of lower temperature and higher density (Cox, 2005), and a very dense, thin disc of cold neutral medium in which most star formation sites are situated (see Kennicutt & Evans, 2012, and references therein).

The bulge, located in the centre of spiral galaxies, is a spheroidal stellar system that is centrally concentrated and smooth in appearance. They fall into two categories: classical bulges and pseudo-bulges. Classical bulges contain predominantly older stars than the disc, and are thought to have formed by rapid star forming events at early times. Pseudo-bulges are thought to build up more gradually from internal secular processes (e.g. Kormendy & Kennicutt, 2004) such as angular momentum transport caused by the bar; angular momentum is transported outwards and material falls into the central regions.

Both the disc and the bulge components are defining morphological features of spiral galaxies, on which Hubble (1926) based his scheme for galaxy classification. This scheme was laid out in his "Tuning Fork" diagram shown in Fig. 1.1, which splits galaxies into ellipticals and spiral classes. Spiral galaxies are subclassified into "normal" and "barred" classes. Normal spiral galaxies are further sub-divided into three types: Sa, Sb and Sc. Along the sequence Sa $\rightarrow$ Sc, i) the bulge size (or luminosity) decreases ii) the gas mass fraction increases

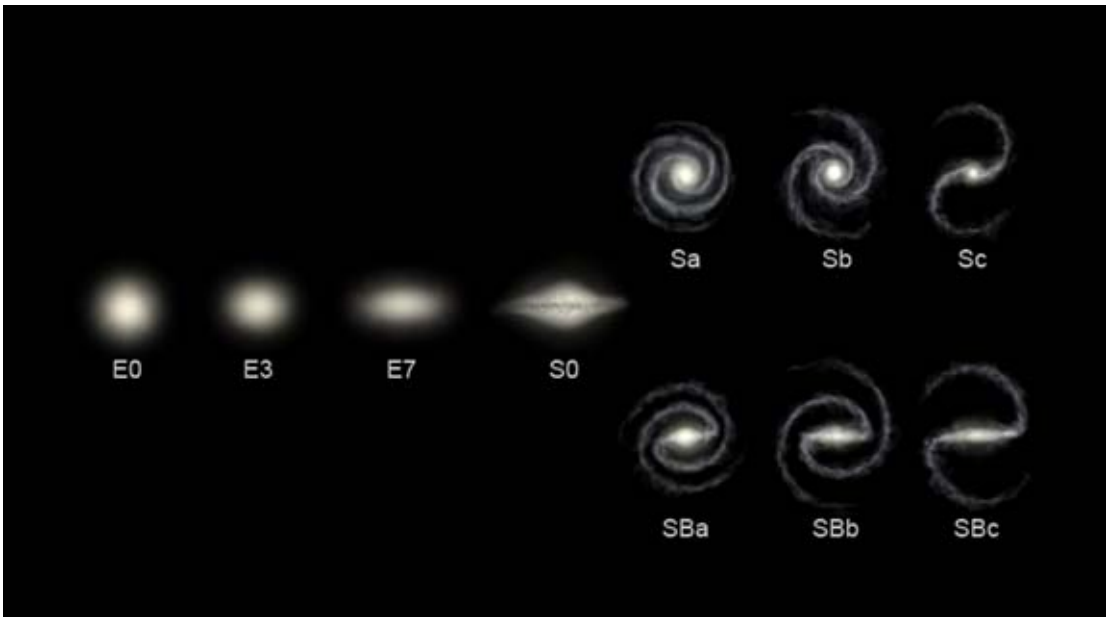


Figure 1.1: Illustration of the Hubble Sequence, i.e., the Tuning fork diagram. The left-hand side groups together elliptical galaxies ranging from E0 to E7, where the higher numbers represent a higher degree of ellipticity. The right-hand side shows the spiral (upper) and barred-spiral (lower) galaxy types (see text for description of sub-types). The central S0 type represents a smooth disc galaxy with no spiral or bar structure: a morphology intermediate to spirals and ellipticals. Credit: Ville Koistinen.

iii) the spirals become less tightly wound and iv) the spiral arms become more clumpy. Barred spiral galaxies have at their centre an elongated, rotating stellar system called a bar. The Hubble types of barred spiral galaxies are designated: SBa, SBb and SBc, and are categorised according to the same criteria as the normal spirals. There is some statistical evidence, gathered from observations (Kormendy & Norman, 1979; Elmegreen *et al.*, 1990), that two-armed grand-design galaxies and bars are more often found with companion galaxies, compared to more flocculent, open spiral galaxies that tend to be more isolated. Elmegreen & Elmegreen (2014) show that under such a correlation, the ratio of barred/grand design galaxies to normal, open spiral galaxies increases with redshift, because mergers and galaxy encounters are thought to be more frequent at earlier epochs of cosmic evolution.

The precise origin and evolution of spiral structure is still unknown despite decades of study. In what follows, we describe the most widely reported theories of spiral structure, their observational predictions, and their implications for spiral arm evolution and impact on stellar dynamics. We describe some methods used to test these predictions from observations and summarise the current findings. We outline how the power and versatility of numerical simulations can bridge the gap between theory and observation in the setting of galactic dynamics, which we use throughout the studies presented in this thesis.

## 1.2 Theories of spiral structure

### 1.2.1 Spiral density wave theory

Lindblad (1960) first postulated that the prominent, quasi-symmetric spiral arms of grand design galaxies are wave-like in nature. This concept was advanced by Lin & Shu (1964); Lin *et al.* (1969); Bertin *et al.* (1989a,b), who developed what is the most widely accepted theory of the spiral arm for 50 years: spiral density wave theory. The theory considers stellar spiral arms to be the crests of a stationary density wave. In this description, spiral arms rotate at a constant angular velocity (pattern speed) over the entire radial range: spiral arms rotate rigidly around the galaxy and preserve their shape, thus avoiding the winding dilemma. Spiral arms are therefore described as long-lived features, which is a major prediction of the theory.

The considerations that lead to spiral density wave theory begin with the overall dynamical interaction of stars through their gravitational forces. In the idealised model of Lin & Shu (1964), the mass of the rotationally supported disc is concentrated in the plane, which reduces the disc to a two dimensional configuration. For a stable planar disc, the four fundamental equations of galactic dynamics: the continuity equation, the radial and azimuthal Euler equations and Poisson's equation, may be linearly perturbed, and to first order are

$$\frac{\partial \Sigma'}{\partial t} + \frac{1}{r}\frac{\partial}{\partial r}(r\Sigma_0 u') + \frac{\Sigma_0}{r}\frac{\partial v'}{\partial \theta} + \frac{v_0}{r}\frac{\partial \Sigma'}{\partial \theta} = 0 \tag{1.1a}$$

$$\frac{\partial u'}{\partial t} + \frac{v_0}{r}\frac{\partial u'}{\partial \theta} - 2\frac{v_0}{r}v' = \frac{\partial \phi'}{\partial r} \tag{1.1b}$$

$$\frac{\partial v'}{\partial t} + \Omega\frac{\partial v'}{\partial \theta} + \frac{\kappa^2}{2\Omega}u' = \frac{1}{r}\frac{\partial \phi'}{\partial \theta} \tag{1.1c}$$

$$\frac{\partial^2 \phi'}{\partial r^2} + \frac{1}{r}\frac{\partial \phi'}{\partial r} + \frac{1}{r^2}\frac{\partial^2 \phi'}{\partial \theta^2} + \frac{\partial^2 \phi'}{\partial z^2} = -4\pi G\Sigma'\delta(z), \tag{1.1d}$$

in cylindrical coordinates, where $r, \theta$ and $z$ are the radial, azimuthal and height above the disc plane coordinates. The surface mass density, rotation velocity, radial velocity and potential are given by $\Sigma, v, u$ and $\phi$ respectively, and unperturbed and perturbed quantities are denoted by the subscript 0 and prime respectively. Equations (1.1) model the dynamical response of stars to a first order perturbation in surface mass density.

The next step that Lin & Shu (1964) took was to integrate equation (1.1d) by an asymptotic method in order to find solutions of the form

$$\Sigma' = Re\{S(r)\exp^{i(\omega t - m\theta + f(r))}\} \tag{1.2a}$$

$$\phi' = Re\{A(r,z)\exp^{i(\omega t - m\theta + \Phi(r,z))}\}, \tag{1.2b}$$

where $\omega$ is rotational frequency, $m \geq 0$ is a natural number that denotes an $m$-fold symmetric pattern, and $f(r)$ and $\Phi(r,z)$ are phase factors (or functions that describe the spiral shape) of the perturbed surface density and potential respectively. These quantities are required to vary quickly with respect to the amplitude functions $S(r)$ and $A(r,z)$ in order for the perturbation to leave a spiral impression. Moreover, the rapid variation of phase factors, $f(r)$ and $\Phi(r,z)$

produces tightly wound spirals, for which the spiral density disturbance can be approximated as a plane wave in the radial direction. In this approximation, the contributions of distant peaks in surface density to the disturbance potential are approximately cancelled out owing to the near-symmetry of the density peaks. Therefore, the potential is well described by the local surface density distribution. This is known as the tight winding approximation (WKB[1]), which is necessary to make in order to equate $f(r)$ and $\Phi(r,z)$ (i.e., the potential and density are in phase) and extract analytic solutions for the density and potential of a density wave mode. Analytic solutions for wave modes outside of the WKB approximation are difficult to derive; the only analytic solution known is for the Kalnajs disc (see Kalnajs, 1972).

The solutions to the two-dimensional Poisson equation (1.1d) must satisfy the boundary condition

$$\left[\frac{\partial\phi'}{\partial z}\right] = \frac{\partial\phi'(r,\theta,0+)}{\partial z} - \frac{\partial\phi'(r,\theta,0-)}{\partial z} = -4\pi G\Sigma', \tag{1.3}$$

in the disc plane, i.e. $z = 0$, where the $0\pm$ coordinates represent infinitesimal departures from the disc plane both above $(+)$ and below $(-)$, because all the mass is contained within an infinitely thin disc.

Lin & Shu (1964) used an asymptotic method (see Appendix A) to solve equations (1.1) with boundary condition (1.3), and showed that the wave solutions obey the dispersion relation:

$$|k| = (\kappa^2 - (\omega - m\Omega)^2)/2\pi G\Sigma_0, \tag{1.4}$$

where $\kappa$ is the epicycle frequency, $\Sigma_0$ is the unperturbed surface density, $|f'(r + iz)| = |k|$, is the radial wavenumber, and $\omega = \omega_r + i\omega_i$ is the complex rotational frequency of the density wave. Because the left hand side of equation (1.4) is always positive regardless of whether the wave is trailing or leading, a density wave may only be supported if the real part of the right hand side of equation (1.4) is positive, i.e., if

$$\kappa^2 + \omega_i^2 - (\omega_r - m\Omega)^2 > 0. \tag{1.5}$$

The spiral shape of the density distribution given in equations (1.2) at $t = 0$

[1]Named after Wentzel-Kramers-Brillouin.

follows $m\theta = \Phi(r)$. For trailing spiral arms, $\Phi'(r) < 0$, and because $\Phi'(r) = k$, the shape of the spiral arm is given by

$$m(\theta_1 - \theta_0) = -\int_{r_0}^{r_1} \frac{[\kappa^2 + \omega_i^2 - (\omega_r - m\Omega)^2]}{2\pi G\Sigma_0} dr. \tag{1.6}$$

Lin & Shu (1964) assumed that if there is a comparatively large concentration of mass in the centre, the surface density, $\Sigma_0$, of the outer disc is lower. Under this assumption, equation (1.6) predicts that galaxies with large bulges have more tightly wound spirals than galaxies that have smaller bulges, which is qualitatively consistent with Hubble classes Sa, Sb and Sc.

### Resonances

Stars that orbit in the disc plane of a spiral galaxy are in resonance with a $m$-symmetric density wave mode of pattern speed, $\Omega_p = \omega/m$, when

$$\Omega_p = \Omega + l\frac{\kappa}{m}, \tag{1.7}$$

where $l$ is a signed integer and denotes harmonic resonances of an $m$-armed pattern, the most important of which occur for $|l| = 0, 1$. For $l = 0$, equation (1.7) defines a resonance at which stars rotate at the same speed as the spiral wave, which is termed a co-rotation resonance. For $l = \pm 1$, the frequency at which stars encounter the density wave, $m(\Omega - \Omega_p)$, is equal to the radial oscillation (epicycle) frequency, $\kappa$. These resonances are termed Lindblad resonances, and mark the inner and outer boundaries of spiral structure, because a stationary density wave is not supported by stars outside this radial range (Sellwood, 2014). Between the outer Lindblad resonance ($l = +1$) and co-rotation, stars move slower than the wave, and fall behind it during rotation. Conversely, between the inner Lindblad resonance ($l = -1$) and co-rotation, stars rotate faster than the spiral wave and overtake it.

Given the expression for the phase factor in equation (1.4) and its appearance in the equation for the potential in equation (A.18), it is evident that the value for the potential (and the velocities, $v'$ and $u'$) diverges for the case $|k| = 0$, i.e., $\kappa = \pm(\omega - m\Omega)$. Therefore, the linear analysis breaks down near resonances for long-lived spiral density waves. The prediction of resonances has important consequences for the orbital motion of stars, which will be described in §1.3.

### 1.2.2 Swing Amplified Travelling Waves

The dispersion relation of equation (1.4) applies to a flat disc of stars with zero velocity dispersion, and relates the rotational frequency, $\omega$, of a density wave to its radial wavenumber, $k$, or wavelength, $\lambda = 2\pi/k$, which is related to the pitch angle of the disturbance. In the absence of random motion, it follows that for *axisymmetric* disturbances ($m = 0$), the disc is stabilised for wavelengths

$$\lambda > \lambda_{crit} \equiv \frac{2\pi}{k_{crit}} = \frac{4\pi^2 G\Sigma}{\kappa^2}. \tag{1.8}$$

Large scale disturbances of wavelength $\lambda > \lambda_{crit}$ are stabilised by the rotation of the disc[1] (Toomre, 1964). On smaller scales, i.e., $\lambda < \lambda_{crit}$, a non-zero velocity dispersion is required for stabilisation; in the absence of random motion, there is no pressure on any scale smaller than the critical wavelength, $\lambda < \lambda_{crit}$, to resist gravitational instability. However, Toomre (1964) showed that a disc may be stable on scales smaller than the critical wavelength if the velocity dispersion, $\sigma_r$, is greater than a critical velocity dispersion, $\sigma_{r,crit}$, yielding a criterion for local axisymmetric stability

$$Q \equiv \frac{\sigma_r}{\sigma_{r,crit}} = \frac{\sigma_r \kappa}{3.36 G\Sigma} > 1. \tag{1.9}$$

Although this expression was derived by Toomre (1964) from the local approximation, numerical experiments (e.g. Hohl, 1971) suggest that equation (1.9) is in fact a good approximation to global axisymmetric stability. Equations (1.8) and (1.9) refer strictly to local axisymmetric stability, and stellar discs that satisfy these criteria for stability may still develop non-axisymmetric structure. However, they serve as important indicators of the dynamical responsiveness of the disc, which is important for all perturbations.

Regarding non-axisymmetric disturbances, Toomre (1969) showed that waves described by the dispersion relation of the kind in equation (1.4) ought to propagate radially at the group velocity, $c_g = \partial\omega(k, r, m)/\partial k$, between co-rotation and

[1]Here, the rotational support is characterised by the epicycle frequency squared, $\kappa^2 = \left(2r\Omega\frac{d\Omega}{dr} + 4\Omega^2\right)$. Rotational support against a collapsing element of mass is provided by a gravity opposing *local* centrifugal force; a star that is pulled radially towards the mass element changes it's rotational velocity in order to conserve angular momentum. The resulting change in relative velocity between the star and the mass element induces a local centrifugal force that depends on the angular rotation and its radial profile (i.e., $\kappa^2$), and acts to stabilise gravitational collapse about the mass element on scales exceeding that described in equation (1.8).

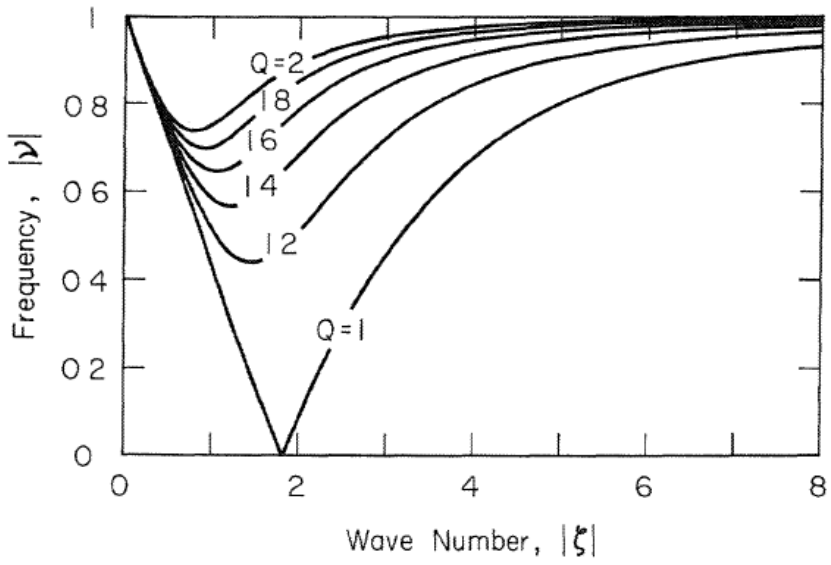


Figure 1.2: The dispersion relation for density waves for different values of the $Q$ parameter: dimensionless frequency ratio, $\nu = (\omega - m\Omega)/\kappa$ as a function of dimensionless wavelength, $\zeta = k/k_{crit}$. Credit: Toomre (1969).

the Lindblad resonances. Such *travelling* waves were shown by Toomre (1969) to change wavelength, $\lambda$, and frequency, $\omega$, as they propagate. Fig. 1.2 shows the dispersion relation plotted with dimensionless frequency ratio $\nu = (\omega - m\Omega)/\kappa$ as a function of dimensionless wavelength, $\zeta = k/k_{crit}$, where $k = 2\pi/\lambda$ is the radial wavenumber ($k < 0$ corresponds to leading spiral arms, whereas $k > 0$ corresponds to trailing spiral arms). Because $\nu = 0$ corresponds to co-rotation, and $\nu = \pm 1$ corresponds to the Inner and Outer Lindblad resonances, the ordinate corresponds to the radial range between the Lindblad and co-rotation resonances. The abscissa corresponds to the wavelength of the wave. The curves and their slopes show the evolution of wavenumber and group velocity respectively for an initially tightly wound wave propagating from the Lindblad resonances toward co-rotation (from right to left in Fig. 1.2). As the wave propagates towards co-rotation, it begins to unwind ($\zeta$ becomes lower). When it reaches co-rotation, the group velocity changes sign and the wave packet is reflected back towards the Lindblad resonances, still unwinding. The wave changes from a loosely wound leading to a loosely wound trailing wave as it is reflected off the Lindblad resonances, and winds further as it travels towards co-rotation (from left to right in Fig. 1.2). As the wave packet is reflected away from co-rotation a final time,

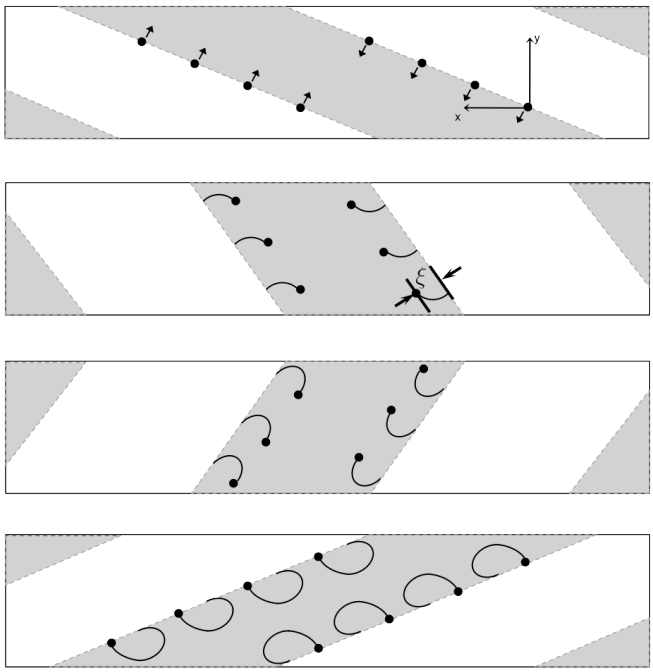


Figure 1.3: Schematic drawing of a shearing disturbance (grey regions) in a small region of the galactic disc. From top to bottom shows a time sequence, in which the direction of rotation, $x$, is from right to left, and $y$ points radially outward. The initially tightly wound leading spiral (top panel) unwinds to a loose leading spiral (second panel). Stars become trapped in the over-dense patch as it swings from leading to trailing (third panel), until they begin to escape when the spiral is tightly wound (bottom panel). Credit: Toomre (1981).

the wave becomes ever more tightly wound as it asymptotically approaches the Lindblad resonances once more. However, this time it is unable to reflect back, and is instead damped away at the Lindblad resonances (Mark, 1974). In this scenario, the wave is not a long-lived feature.

The local stability of non-axisymmetry was extensively studied by Goldreich & Lynden-Bell (1965); Julian & Toomre (1966), who discovered the process of swing amplification. Julian & Toomre (1966) calculated the response density of a shearing sheet to a large mass perturber, and found that wakes formed in the vicinity of the perturber and grew into wavelets that resembled spiral patterns. They found that the wavelets grew to a maximum amplitude for a spiral pitch angle that depends on the shear rate of the sheet i.e. larger shear rates lead to more tightly wound spiral shapes. They found also that for a flat rotation curve, the amplification is most significant for a length ratio

$$X = \frac{\lambda_t}{\lambda_{crit}} = \frac{2\pi r}{m}\frac{\kappa^2}{4\pi^2 G\Sigma} \sim 1-3, \tag{1.10}$$

where $\lambda_t$ is the circumferential wavelength at a radius, $r$. Equation (1.10) indicates that amplification is strong for high $m$-values for relatively light discs, i.e., $\Sigma$ is low, whereas $m$ is comparatively low in heavier discs.

The results of Julian & Toomre (1966) were corroborated by Toomre (1981), who described how shear rate, epicycle motion and self-gravity conspire together to amplify an initially leading spiral that unwinds into a trailing spiral (see Fig. 1.3). A key property of the shearing spiral is that the rate of change of pitch angle is slower for $|k| \gg 0$, i.e. tightly wound spirals, than it is for low values of $|k|$, i.e. more open spirals. The shear rate of the over-dense patch of material reaches a maximum at $k = 0$, i.e. when it "swings" from leading to trailing, which is comparable to the epicycle motion of stars (see also Binney & Tremaine, 2008). The overall effect is that rotational support is compromised at large scales ($\lambda \gg 0$); the epicycle motion that acts to pull stars away from over-dense patch is negated by the shearing of the disturbance during the swing period, effectively trapping the star inside the perturbation for a short period of time. During this time, the self-gravity of the trapped stars draws more stars into the over-density, which results in serious amplification of the non-axisymmetric disturbance. As the enhanced spiral becomes a more tightly wound, trailing shape, the rate of change of pitch angle slows such that the coupling between shear and epicycle

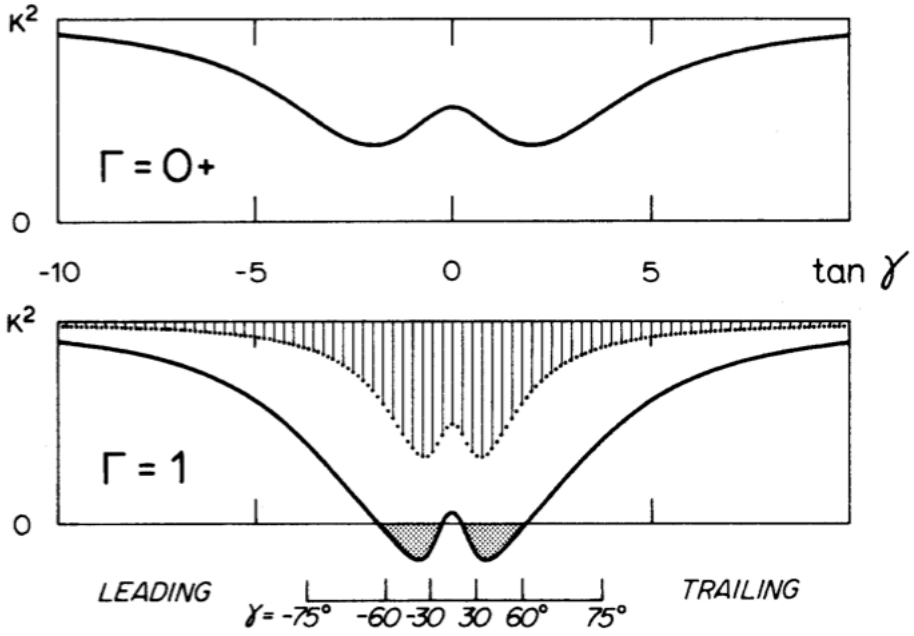


Figure 1.4: *Top panel*: The evolution of the effective spring rate with self-gravity and no shear. *Bottom panel*: The evolution with shear corresponding to a flat rotation curve without (dotted) and with (solid) self-gravity. The ordinate shows the evolution of the effective spring rate, $\tilde{\kappa}^2$, expressed in equation (1.13). Credit: Toomre (1981)

motion vanishes, and the spiral begins to fade.

The strength of the amplification of the disturbance is parameterised in Toomre (1981) as a measure of normal displacement, $\xi$, of an (epicyclic) oscillating star with respect to the edge of the over-dense patch,

$$\xi = x \sin\gamma + y \cos\gamma, \tag{1.11}$$

where $\gamma$ is the pitch angle of the spiral shape[1]. The evolution of the displacement parameter, $\xi$, follows that of a harmonic oscillator:

$$\ddot{\xi} + \tilde{\kappa}^2 \xi = 0. \tag{1.12}$$

The restoring force is provided by the effective spring rate, $\tilde{\kappa}$, which Toomre

[1]Here, $\gamma = 0$ corresponds to the boundary between leading and trailing spirals, and $\gamma \to \pm 90$ degrees corresponds to the most tightly wound leading ($-$) and trailing ($+$) spiral shapes respectively.

(1981) showed to be

$$\tilde{\kappa}^2 = \underbrace{\kappa^2}_{\text{epicycle frequency}} \underbrace{- 4\Omega_0^2\Gamma\cos^2\gamma + 3\Omega_0^2\Gamma\cos^4\gamma}_{\text{shear}} \underbrace{- 2\pi G\Sigma k\mathcal{F}}_{\text{self-gravity}}, \tag{1.13}$$

where $\kappa$ is the epicycle frequency and $\Gamma$ is the galactic shear rate. Exponential growth of the displacement parameter occurs when the effective spring rate becomes negative. The top panel of Fig. 1.4 shows the evolution of the effective spring rate as a function of pitch angle for the case of no shear term in equation (1.13), whereas the bottom panel of Fig. 1.4 shows the evolution for the cases of $\Gamma = 1$ with (solid line) and without (dashed line) the self-gravity term in equation (1.13). The combination of shear and self-gravity can effectively reduce the spring rate to the required negative values that causes rapid growth over a short period during the swing from leading to trailing at large wavelengths.

The parameter $\mathcal{F}$ in equation (1.13), which takes values between 0 and 1, models the effective reduction of self-gravity caused by a non-zero velocity dispersion (it is equal to 1 for zero dispersion). Therefore stellar discs of lower $Q$ values lead to greater amplifications of the spiral over-density.

The swing amplification mechanism represents a significant departure from the stationary density waves postulated by Lin & Shu (1964), namely because it describes the growth and decay of transient, "swinging" perturbations, as opposed to long-lived rigidly rotating spiral structure. Swing amplification is not captured in density wave theory because the WKB approximation is unable to accurately follow the evolution of spirals of large radial wavelengths. It does not, however, exclude the stationary wave mode solutions of equations (1.1a-1.1d), and the connection between the two theories is still under scrutiny. For example, Sellwood & Carlberg (2014) argues that successive swing amplifications of many travelling waves may seed global instabilities such as density wave modes, as long as they are not damped out completely by the Inner Lindblad resonance.

### 1.2.3 Other theories

Over the years, since the Lin-Shu density wave theory and swing amplification theory were proposed, researchers have put forward several theories of the origin of the instability that leads to spiral structure.

Sellwood & Kahn (1991) presented a spiral instability mechanism known as

the "groove" mode, which was reported to develop from under-dense narrow ring features in the surface density[1], around which global wave modes grow. These modes were shown to be transient, owing to their instability leading to the eventual erasure of the wave mode. This recurrent instability cycle was supported by the earlier work of Sellwood & Lin (1989), who found that instabilities of this nature can propagate in radius. However, Sellwood (2012) found that the mechanism could not be replicated in heavy discs with flat rotation curves.

Bertin & Lin (1996) proposed a density wave model for global, long-lived spiral modes that formed stationary structures closely associated to the original density wave theory of Lin & Shu (1964). However, Sellwood (2011) showed that the global modes presented by Bertin & Lin (1996) cannot be sustained owing to heating effects in the outer disc.

Athanassoula *et al.* (2009) proposed that spiral arms can be created by the migration of stars along unstable Lyapunov tube manifolds that originate from the Lagrange points located at the end of a bar. The manifolds were shown to map out spiral and ring-like shapes, which Athanassoula *et al.* (2009) argued naturally accounts for spiral arms growing out from the ends of bars. The presence of these manifolds seems to require the simultaneous existence of a bar, rings and spiral arms, which all rotate at the same pattern speed.

While there is no widely accepted theory of spiral structure, there is a general consensus that spirals are gravitationally driven instabilities that lead to variations in surface density and brightness (e.g. Rix & Zaritsky, 1995; Grosbøl *et al.*, 2004). It is possible that there exist different mechanisms responsible for spiral arm formation that are a function of galaxy environment and morphology. In discs that have satellites or nearby companion galaxies, the spiral structure may be tidally driven (Kormendy & Norman, 1979; Dobbs *et al.*, 2010; Purcell *et al.*, 2011; Kendall *et al.*, 2011), while other galaxies may display bar-driven spirals (Salo *et al.*, 2010). It is clear that gas plays an important role in the development of spiral arms; observations tell us that spiral galaxies are predominantly late-type and gas rich (see §1.1). This is because spiral structure acts to dynamically heat the disc by increasing the random motions of stars, which leads to higher $Q$ parameter values (see §1.2.2) and a less dynamically responsive disc. Gas becomes an important component of the spiral disc because it has a cooling,

[1]A similar instability was found to occur for over-dense "ridges" in angular momentum space (see Sellwood & Kahn, 1991).

dissipative effect, which helps to keep the disc dynamically cool. This is vitally important in the sustention of spiral structure for Gyr-long periods - supported by simulations (e.g. Sellwood & Carlberg, 1984), which is discussed in more detail in §1.5 - that provides an explanation for the presence of gas-rich spirals and featureless S0 galaxies that have very little gas (Oort, 1962).

## 1.3 Radial Migration

A star orbiting in an axisymmetric potential maintains a constant angular momentum that corresponds to a "guiding centre" around which the star radially oscillates at the epicycle frequency, $\kappa$. However, non-axismmetric potentials such as spiral arms can cause changes in the angular momentum (and therefore guiding centre radius) of individual stars. This process is termed "radial migration".

Lynden-Bell & Kalnajs (1972) first discussed angular momentum transport of stars by a steady, rigidly rotating spiral arm potential that grows very slowly (in comparison to orbital periods), and found that the average change in angular momentum for a group of stars is zero everywhere except at resonances (see also Carlberg & Sellwood, 1985).

In a steady potential that rotates in the frame of reference equal to the pattern speed, $\Omega_p$, of a density wave, there is a conserved quantity known as Jacobi's integral, defined as (Binney & Tremaine, 2008, equation 3-88)

$$E_J = E_{tot} - \Omega_p L_z, \tag{1.14}$$

where $L_z$ is the $z$-component of angular momentum, and the total energy is

$$E_{tot} = \phi(r) + \frac{L_z^2}{2r^2} + \kappa J_r. \tag{1.15}$$

Here, $J_r$ is a constant of motion known as the radial action, which is associated with the radial oscillation of a star (Lynden-Bell & Kalnajs, 1972). Therefore changes in the total orbital energy and angular momentum must be related by:

$$\Delta E_{tot} = \Omega_p \Delta L_z. \tag{1.16}$$

Fig. 1.5 illustrates the changes described by equation (1.16) in angular momentum-energy ($E$-$L$) space. The solid curve represents the circular orbit in $E$-$L$ space,

which is the orbit that has zero radial and vertical kinetic energies and a tangential velocity that produces a centripetal force exactly equal to the radial gravitational force acting on the star. This is the minimum energy orbit for a star of a given angular momentum that is bound to the system. Therefore no star can possess a lower energy than the circular orbit at a given angular momentum or, vice versa, no star can possess an angular momentum higher than the circular orbit at a given orbital energy if they are bound. This "inaccessible region" is marked in Fig. 1.5 as the shaded area underneath the circular orbit curve. The dashed line represents the slope along which stars are radially transported. At co-rotation, the slope is tangential to the circular orbit curve, therefore stars that gain/lose angular momentum at the co-rotation resonance experience no change in their degree of random motion. Angular momentum changes at co-rotation can be of either sign. At the Lindlbad resonances however, the slope given by $\Omega_p$ is not tangential to the circular orbit line, and angular momentum exchanges with stars is accompanied by an increase in random motion. On average, stars at the Inner Lindblad resonance lose angular momentum, because angular momentum increase is restricted, particularly for near-circular orbits, by the inaccessible region enclosed by the circular orbit curve. A similar argument supports the net gain of angular momentum of a group of stars at the Outer Lindblad resonance.

An increase in non-circular motion can be described by an increase in radial action. (Sellwood & Binney, 2002) quantified the change in radial action of a star orbit as a function of angular momentum change at resonances by re-expressing the change in total energy as a function of radial action and angular momentum:

$$\Delta E_{tot} = \frac{\partial E_{tot}}{\partial J_r}\Delta J_r + \frac{\partial E_{tot}}{\partial L_z}\Delta L_z. \tag{1.17}$$

Eliminating $\Delta E_{tot}$ from equations (1.16) and (1.17) gives the relation

$$\Delta J_r = \frac{\Omega_p - \Omega(r)}{\kappa}\Delta L_z, \tag{1.18}$$

which shows that $\Delta J_r = 0$ at co-rotation, and $\Delta J_r = |\Delta L_z|/m$ at the Lindblad resonances.

Sellwood & Binney (2002) showed that angular momentum changes at co-rotation are generally much larger than those at the Lindblad resonances, and those predicted by Lynden-Bell & Kalnajs (1972) at co-rotation. Stars that gain

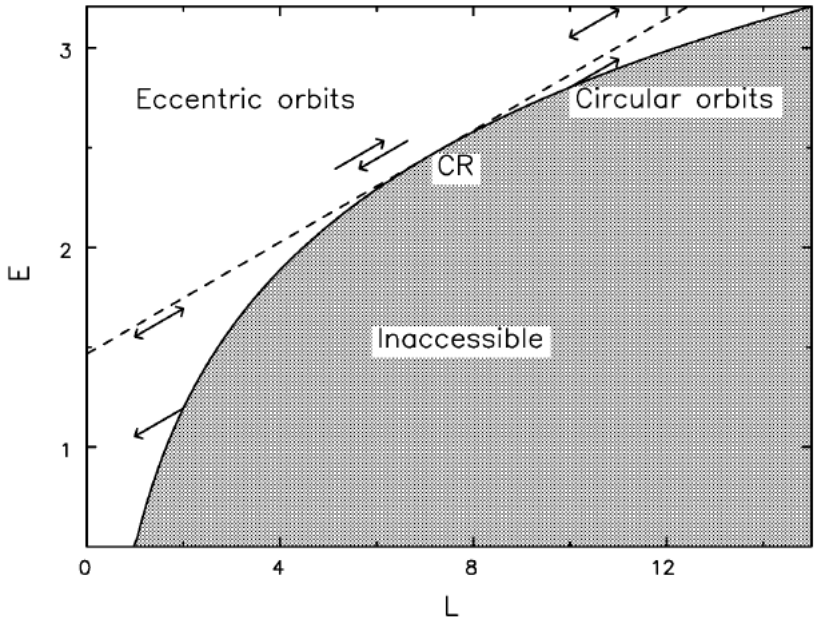


Figure 1.5: Classical Lindblad diagram. The solid curve represents the lowest energy orbits for given angular momenta (circular orbits). Physical orbits exist on or above the curve, where the further from the curve they lie, the more eccentric their orbit. The dashed line is the slope along which radially migrated particles move, as indicated by the movement near principal resonances shown by the solid arrows. Credit: Sellwood & Binney (2002).

angular momentum just inside of co-rotation on the trailing side of the spiral increase their orbital radius, which in turn decreases their orbital frequency. The star then rotates backward with respect to the spiral arm in the co-rotating frame, and approaches the next spiral arm from its leading side. The star can then lose the angular momentum that it gained from the previous spiral arm, subsequently increasing its orbital frequency, which in turn leads to the star rotating faster than the spiral upon crossing co-rotation. These orbits are called "Horseshoe Orbits", named after the shape of orbit in the co-rotating frame. Sellwood & Binney (2002) inserted by hand a spiral wave mode into two-dimensional simulations of a Mestel disc density profile, and found that the growth of the spiral structure was limited by growing radial migration of stars away from the co-rotation resonance, which leads to "transient" spiral waves. This means that for a two-armed spiral structure, the once-migrated particle mentioned above no longer encounters the second spiral arm, therefore the angular momentum changes the first time around are not cancelled out. Sellwood & Binney (2002); Roškar *et al.* (2012b) argued further that the long lasting effect of this radial migration on the disc evolution will be enhanced if successive transient spiral wave modes develop, each of different co-rotation radii. The effect of radial migration has been argued to be even further pronounced if resonances of different modes overlap, for example two spiral modes (Minchev & Quillen, 2006; Minchev *et al.*, 2011, 2012b) or a spiral and bar mode (Minchev & Famaey, 2010; Quillen *et al.*, 2011). Radial migration is thought to play a significant role in galaxy evolution, not only from spirals but from bars as well (e.g. Solway *et al.*, 2012).

There have been many studies on the effect of radial migration on the distribution of chemical abundances of disk stars (Sellwood & Binney, 2002; Lépine *et al.*, 2003; Roškar *et al.*, 2008a,b; Haywood, 2008; Schönrich & Binney, 2009; Sánchez-Blázquez *et al.*, 2009a; Loebman *et al.*, 2011; Minchev *et al.*, 2011; Brook *et al.*, 2012; Minchev *et al.*, 2013; Di Matteo *et al.*, 2013; Haywood *et al.*, 2013). In the plane of the Milky Way, the Geneva Copenhagen Survey (Nordström *et al.*, 2004; Holmberg *et al.*, 2009) revealed that the dispersion in stellar metallicity in the solar neighbourhood is much broader than that of the gas in the solar neighbourhood, and is therefore too broad to be explained by local star formation (Haywood, 2008; Schönrich & Binney, 2009; Casagrande *et al.*, 2011). Sellwood & Binney (2002) reported the presence of such stars in the solar neighbourhood

to be a consequence of radial migration caused by transient spirals. Metal-rich stars that formed in enriched gas in the inner regions of the Milky Way can migrate to the outer regions, and conversely, metal-poor stars from the outer regions can migrate to the inner regions (Haywood, 2008). Therefore, radial migration broadens the metallicity distribution (see also Schönrich & Binney, 2009).

Radial migration has been reported also to be the cause of breaks in the exponential surface brightness profiles of disc galaxies (Pohlen & Trujillo, 2006; Roškar *et al.*, 2008b; Yoachim *et al.*, 2010, 2012). However, the origin of surface brightness breaks is a complicated issue that includes factors such as gas accretion and star formation. For example, Sánchez-Blázquez *et al.* (2009a) argue that a star formation rate threshold in the low density disc outskirts plays an important role in forming the breaks.

Radial migration has been argued to also thicken galactic discs. In particular, Roškar *et al.* (2012a) inferred from a numerical simulation that outward migrating star particles can thicken the disc because they conserve their vertical energy, and therefore the amplitude of their vertical oscillations about the disc plane increases in the outer regions owing to the reduced vertical restoring force of gravity. However, Minchev *et al.* (2012a) found from simulations that the vertical action of the stars is the conserved quantity - and not the vertical energy - which leads to minimal disc thickening (see also Solway *et al.*, 2012).

The large number of recent studies on radial migration have highlighted its importance in spiral galaxy evolution. Because this phenomenon occurs at the co-rotation radius, the position and number of such resonances, which depend on the pattern speed, play important roles in the secular evolution of galaxies. Therefore the extent to which radial migration occurs depends heavily on the radial profile of the pattern speed and the nature of the spiral arm itself. In the next section, I describe some observational techniques that have been used to determine spiral arm patterns speeds, and summarise the current findings.

## 1.4 Observational tests of rigidly rotating spiral structure

The typical timescale for one galactic rotation of a disc galaxy similar in size to the Milky Way is $\sim 10^8$ years, and as such observations of disc galaxies are limited

to effectively provide a snapshot of a single instance in time. Therefore we cannot directly observe the dynamical evolution of large scale galaxy structures such as spiral arms. However, it is possible to test spiral arm theories if the theory can be used to develop observable predictions, such as the constant pattern speed predicted by density wave theory. In this section, I outline two well-used techniques that test density wave theory, by inferring the form of the spiral arm pattern speed: the *tracer offset* method and the *Radial Tremaine-Weinberg* method.

### 1.4.1 The tracer offset method

Multi-wavelength images of spiral galaxies reveal that the luminosity of star forming tracers is enhanced in the spiral arms compared to the inter-arm regions, implying that the highest star formation rate densities in galaxies are in spiral arms. Fujimoto (1968) and Roberts (1969) proposed that enhanced star formation in spirals could be caused by shocks that form along the spiral arm, owing to non-zero relative speeds between gas clouds and the spiral density wave that become supersonic at radii far from co-rotation. The subsequent rapid cooling of the gas coupled with the gravitational potential of the spiral triggers an increase in molecular cloud formation[1]. Star formation then proceeds in the molecular clouds, beginning with dust-enshrouded newborn stars, which evolve into unobscured young stars. The time difference between these stellar evolutionary stages leads to a trail of star formation across the spiral arms, in which each stage is spatially offset from one another. The size of the angular offset corresponds to the relative speed between the star forming material and the spiral arm (pattern), which becomes larger at radial distances farther from co-rotation.

The stages of star formation, including those of gas cloud evolution prior to star formation, can be mapped observationally because each stage emits a characteristic tracer. Atomic and molecular gas can be detected via HI and CO emission lines respectively. Very early star formation can be traced by 24$\mu$m

[1]This model suggests that the star formation efficiency (star formation rate per unit gas mass), is higher in spiral arms. It should be noted, however, that Foyle *et al.* (2010) find an almost equal fraction of molecular gas in the spiral arms and inter-arm regions of three galaxies, and a star formation efficiency that is constant over the disc. This suggests that the star formation rate density in spiral arms is high because the underlying spiral arm potential simply draws molecular gas together into higher concentrations, and not because the star formation efficiency increases (see also Dobbs *et al.*, 2013). However, this is still debated. More observational and theoretical studies are required to answer how the spiral arm affects star formation.

and/or H$\alpha$ emission, and young unobscured stars can be detected in the UV regime. Therefore, multi-wavelength observations can provide an observational test of the pattern speed of the spiral arms because spatial offsets of star forming tracers can be measured directly.

Early observational efforts found evidence for offsets between dust lanes and optical images of spiral arms of the nearby galaxies M51 (e.g. Mathewson *et al.*, 1972) and M81 (e.g. Rots, 1975). When molecular gas (CO) images began to improve in resolution, more quantitative studies comparing the distribution of CO and H$\alpha$ emission reported non-zero angular offsets for M51 (e.g. Vogel *et al.*, 1988; Garcia-Burillo *et al.*, 1993) and M100 (e.g. Rand, 1995). In recent years, other nearby spiral galaxies in addition to M51, M81 and M100 have been studied with ever increasing image tracer resolution (Tamburro *et al.*, 2008; Egusa *et al.*, 2009; Foyle *et al.*, 2011; Ferreras *et al.*, 2012). Tamburro *et al.* (2008) was the first to use the statistical cross correlation method to calculate angular offsets between two star forming tracers, in contrast to the by-eye offset determinations of previous studies (see Foyle *et al.*, 2011). In this method, the disc is divided into concentric radial annuli, and the azimuthal flux profiles of two different star forming tracers, $x$ and $y$, are measured. The azimuthal flux profile of one tracer, $f_k^x$, is fixed, while that of another tracer, $f_{k-l}^y$, is iteratively rotated in azimuth by an offset angle, denoted by $l$, where $k$ represents the original measured azimuth coordinate of the data. Then, the cross-correlation coefficient given by

$$\mathrm{cc}_{xy}(l) = \frac{\Sigma_k[(f_k^x - \bar{f}^x)(f_{k-l}^y - \bar{f}^y)]}{\sqrt{\Sigma_k(f_k^x - \bar{f}^x)^2 \Sigma_k(f_k^y - \bar{f}^y)^2}}, \tag{1.19}$$

where $\bar{f}$ is the azimuthally averaged flux in a radial annulus, is calculated at each radius for different offset angles. The best match between the azimuthal flux profile of both tracers is found for a given $l$ when the correlation coefficient is maximised. The best match offset angle is related to the pattern speed by

$$\Delta\theta(r) = (\Omega(r) - \Omega_p)t_{x\to y}, \tag{1.20}$$

where $t_{x\to y}$ is the time between evolutionary stages that display tracers $x$ and $y$. Tamburro *et al.* (2008) found that the spiral galaxies in their sample show evidence of offsets, which is supported by the later observational work of Egusa

*et al.* (2009) who examined a sample of twelve nearby galaxies[1]. Hirota *et al.* (2014) use high resolution wide field CO images of M83 and find a non-zero offset between the molecular material and H$\alpha$ emission regions.

Most of the studies mentioned above measure the angular offsets between the molecular CO tracer and H$\alpha$ or 24 $\mu m$ as a tracer of early star formation. These tracers probe a few Myr (Egusa *et al.*, 2009) of stellar evolution, which in some cases may lead very small offsets depending on the radial distance away from co-rotation. From this point of view, the recent studies of Foyle *et al.* (2011) and Ferreras *et al.* (2012) may provide tighter constraints because they use also UV light as a tracer of unobscured star formation, which enables the first few hundred Myr of star formation to be tracked.

Foyle *et al.* (2011) adopt the method of Tamburro *et al.* (2008) to analyse high resolution images of CO, H$\alpha$ and NUV of star forming regions. They find no offset in any of the twelve nearby spiral galaxies that they analyse, and show that the angular offsets calculated by Tamburro *et al.* (2008) all lie below the resolution limit of the data, thus casting doubt upon the validity of their offset detections. The result constitutes major evidence against classic density wave theory, which is further supported by the study of Ferreras *et al.* (2012) who found no evidence for angular offsets between different stellar populations from H$\alpha$ and high resolution ultra-violet images of M100.

The ongoing research into the detection of star forming tracer offsets continues to provide a mixture of evidence both for and against density wave theory. This highlights the complexity of the problem at hand, and the need for more studies that cover a wide range of star forming tracers and large samples of galaxies in various environments and morphologies. As telescope resolution and sensitivity increases, this method will continue to provide great insight into the nature of spiral arms.

### 1.4.2 The Tremaine-Weinberg equations

The Tremaine-Weinberg method is an observational method first developed by Tremaine & Weinberg (1984) to determine the pattern speed of non-axisymmetric structure, i.e. bars and spiral arms. It has been used with observations of external

[1]Although only three galaxies were found to display offsets, while most were found to have a complicated structure.

galaxies for which the disc plane can be seen at some inclination angle, $i$, such that the surface density, or surface brightness, $\Sigma$, can be measured at every point on the disc. The method carries a set of assumptions: 1) the spiral arms/bar possess a rigidly rotating pattern speed, $\mathbf{\Omega}_p = \Omega_p \hat{\mathbf{e}}_z$; 2) the kinematic tracer is conserved and orbits in a single plane; 3) the spiral arms/bar is a stationary structure.

Subsequently, the method has been developed to take into account radial variation of a pattern speed (Merrifield *et al.*, 2006), which removes the first assumption listed above. Like the Tremaine & Weinberg (1984) form, the method stems from the 2-dimensional continuity equation

$$\frac{\partial \Sigma}{\partial t} + \frac{\partial (\Sigma v_x)}{\partial x} + \frac{\partial (\Sigma v_y)}{\partial y} = 0, \tag{1.21}$$

where $\Sigma(x, y, t)$ is the surface brightness of the observed tracer in a cartesian coordinate system. In the inertial frame, the change in surface brightness is described by the rotation of the azimuthal density profile characterised by a pattern speed

$$\frac{\partial \Sigma}{\partial t} = -\Omega_p(r) \frac{\partial \Sigma}{\partial \theta}, \tag{1.22}$$

where $\theta$ is the azimuth angle. If this system is chosen such that the $x$-axis is aligned with the *line of nodes* (describing the intersection of the orbital disc plane of the galaxy and the plane on the sky), then the $x$-coordinate contains no observable kinematic information. Therefore, the continuity equation can be integrated over $x$ and expressed as

$$\int_{-\infty}^{\infty} \Omega_p(r) \frac{\partial \Sigma}{\partial \theta} dx - \int_{-\infty}^{\infty} \frac{\partial}{\partial x} \Sigma v_x dx - \int_{-\infty}^{\infty} \frac{\partial}{\partial y} \Sigma v_y dx = 0, \tag{1.23}$$

where the second term disappears because the surface density is assumed to drop to zero at infinite $x$ coordinates. Further integrating over $y$ gives

$$\int_{y'=y}^{\infty} \int_{-\infty}^{\infty} \Omega_p(r) \frac{\partial \Sigma}{\partial \theta} dx dy' + \int_{-\infty}^{\infty} (\Sigma v_y) dx = 0. \tag{1.24}$$

The double integral in Cartesian coordinates can be expressed in polar coordinates

by a change of variables to give

$$\int_{r=y}^{\infty}\int_{\theta=\arcsin(y/r)}^{\pi-\arcsin(y/r)}\Omega_p(r)\frac{\partial\Sigma}{\partial\theta}rd\theta dr+\int_{-\infty}^{\infty}\Sigma v_y dx=0. \tag{1.25}$$

The integration limits in the $\theta$ integral mean that for a given $y$ value that intersects a circle of radius, $r$, the coordinates of the surface brightness measurement in the first term are located at $(x', y)$ and $(-x', y)$, where $x'=\sqrt{r^2-y^2}$. The result is expressed as

$$\int_{r=y}^{\infty}[(\Sigma(x',y)-\Sigma(-x',y))r]\Omega_p(r)dr+\int_{-\infty}^{\infty}\Sigma v_y dx=0. \tag{1.26}$$

The quantity in square brackets and the second term are both observable because the coordinates $x$, $y$ and $v_y$ can be related to the observational coordinates: $x=x_{obs}$, and $y=y_{obs}/\cos i$, and $v_y=v_{obs}/\sin i$, where $i$ is the disc inclination angle and $v_{obs}$ is the line of sight velocity. The first integration in equation (1.26) is reduced to a discrete summation for different values of $r=r_i$ and $y=y_j$, therefore equation (1.26) can be turned into a matrix equation of the form (Merrifield *et al.*, 2006)

$$\sum_{r_i>y_j}K(r_i,y_j)\Omega_p(r_i)=-\int_{-\infty}^{\infty}\Sigma(x,y_j)v_y(x,y_j)dx. \tag{1.27}$$

The $K$ term represents the square brackets term in equation (1.27), whose components are found from the subtraction of the $\Sigma$ values at the two points at which each $y$-slice and radial annulus intersect. This yields a $r_i$-$y_j$ grid of values that make up the matrix coefficients of $K_{ij}=K(r_i,y_j)$. The summation can be carried from $r_i$ to a maximum radius where the surface density drops off sufficiently such that the surface density tends to zero. The known values of $K_{ij}$ and the right hand side of equation (1.27) mean that equation (1.27) can be numerically solved for the pattern speed, $\Omega_p(r_i)$.

The original Tremaine-Weinberg equations have been used to determine the pattern speed of bars (e.g. Merrifield & Kuijken, 1995; Gerssen *et al.*, 1999; Debattista *et al.*, 2002; Aguerri *et al.*, 2003; Maciejewski, 2006; Treuthardt *et al.*, 2009; Gabbasov *et al.*, 2009; Banerjee *et al.*, 2013) and some spiral pattern speeds (e.g. Zimmer *et al.*, 2004; Rand & Wallin, 2004; Emsellem *et al.*, 2006; Speights & Westpfahl, 2011, 2012). A recent application of this method is given in Speights &

Westpfahl (2011), who parameterised the pattern speed as two different forms of power law: $\Omega_p \propto r^{\alpha}$ and $\Omega_p \propto r^{-\alpha}$. With these forms, they solved the Tremaine-Weinberg equations for different integer values of $\alpha$ (including 0) using a least squares method to fit the data of a spiral galaxy. They found that the best fitting model was $\alpha = -1$, which is consistent with a pattern speed that decreases with radius at a similar rate to that of the material speed.

The Radial Tremaine-Weinberg method, developed by Merrifield *et al.* (2006), is an adaptation of the original method that does not assume the form of the radial profile of the pattern speed. This is advantageous for the application to spiral arms, and has been used in several studies in which the spiral pattern speed has been found to decrease with radius (e.g. Merrifield *et al.*, 2006; Meidt *et al.*, 2008a,b, 2009). Although the radial Tremaine-Weinberg method is a significant improvement upon the original method proposed by Tremaine & Weinberg (1984), there are still complications in that it is assumed that the surface brightness (and density) of the spiral structure is constant with time i.e. spirals maintain a constant density. However, we will show in this thesis that the results from recent $N$-body simulations (e.g. Wada *et al.*, 2011; Grand *et al.*, 2012a,b; Baba *et al.*, 2013) contradict this assumption; spiral arms are shown to grow and decay in density with time. Therefore, the suitability of the radial Tremaine-Weinberg method for transient spiral arms is unclear (although see Nelson *et al.*, 2012, for a successful application of the radial Tremaine-Weinberg method to transient, winding spiral arms in an $N$-body simulation).

## 1.5 Spiral galaxy simulations

Simulations have become an extremely powerful tool in the study of galactic physics because they enable one to examine galaxy formation and evolution in detail over cosmic times. They are probes beyond the limitations of analytically derived theories, such as those described in §1.2, which carry several assumptions and are restricted to linear approximations. Simulations therefore serve as useful tests of theory, and can create new predictions that may be tested with observations. However, simulations should be interpreted with caution because many of the physical processes associated with galaxy formation and evolution are simplified in order to make simulations computationally feasible. They are not perfect

representations of real galaxies. Therefore, it is important to understand the limitations of simulations, and interpret the results within these limitations.

The first $N$-body simulations date back to the first light bulb experiments (Holmberg, 1941). The first collisionless $N$-body computer simulations were performed using a total of $N = 16$ by von Hoerner (1960) and $N = 100$ by Aarseth (1963), and since then the particle number has continued to rise year by year (see Dehnen & Read, 2011, and references therein).

In the 1980s, simulators reached up to $N \sim 10^4$ particles (e.g. Efstathiou & Eastwood, 1981; Sellwood & Carlberg, 1984). Sellwood & Carlberg (1984) presented the evolution of an isolated spiral galaxy simulation, and found that the spiral morphology disappeared within a few galactic rotations. They showed that the spiral structure could be maintained for cosmic timescales if cold gas accretion and the formation of kinematically cold young stars are considered, which they mimicked by continually adding new particles on circular orbits to the disc (see also Donner & Thomasson, 1994). However, it was later pointed out by Fujii *et al.* (2011) that the high shot noise that arises from using a low number of particles (such as $N = 2 \times 10^4$ used by Sellwood & Carlberg 1984) can cause rapid growth of strong spiral arms, which go on to heat the disc very quickly. This causes the $Q$ parameter to rise quickly, which then results in the fading of spiral structure. Fujii *et al.* (2011) found that stellar discs of increasing numbers of particles show slower growth of spiral structure and a slower heating rate, until rising above $N > 3 \times 10^6$ particles when simulations converge and the heating rate is so low as to allow spiral structure to exist for 10 Gyr.

Nowadays, owing to recent advancements in numerical algorithms (see §B.1) and computational power, simulations regularly employ $N > 10^6$ star particles (e.g. Wada *et al.*, 2011; Grand *et al.*, 2012a; Baba *et al.*, 2013; Sellwood & Carlberg, 2014), which comfortably avoid such rapid heating described above. In some cases up to as many as $N = 10^9$ particles have been used to model galactic discs (e.g. D'Onghia *et al.*, 2013). Important baryonic processes such as hydrodynamics, star formation and feedback are now modelled with $N > 10^6$ particles (e.g. Roškar *et al.*, 2008b; Grand *et al.*, 2012b; Hopkins *et al.*, 2012; Hopkins, 2013; Bird *et al.*, 2013) with methods such as smoothed particle hydrodynamics (see §B.2) and adaptive mesh codes (e.g. Tasker & Tan, 2009; Renaud *et al.*, 2013).

Despite the progress of numerical simulations, those of spiral galaxies have

never been able to reproduce the long-lived stationary spiral structure predicted by density waves (Thomasson *et al.*, 1990; Sellwood & Kahn, 1991; Sellwood, 2011). While the spiral structure is found to last for as long as a Hubble time (Fujii *et al.*, 2011), individual spiral arms are always found to be recurrent and transient features (e.g. Sellwood & Carlberg, 1984; Carlberg & Freedman, 1985; Bottema, 2003; Baba *et al.*, 2009; Quillen *et al.*, 2011; Sellwood, 2010, 2011; Fujii *et al.*, 2011; Wada *et al.*, 2011). The fact that simulations are presently no closer to reproducing density wave spiral arms than they have ever been suggests that the inconsistency does not have numerical origins. Coupled with observations that report non-constant pattern speeds with radius, it seems that a new theory is needed to explain the spiral structure seen in galaxies. The problem is well posed to be investigated through scrutiny of high resolution simulations, which may provide insight into the underlying nature of spiral arms.

## 1.6 Studies in this thesis

The studies presented in this thesis build upon previous numerical efforts to simulate and understand spiral structure and its role in galaxy evolution. The evolution of the spiral arm is coupled to that of the disc stars: the dynamical evolution of spiral arms is strongly affected by the dynamics of nearby disc stars, which in turn are influenced by the presence of the spiral arm. Therefore, the study of the mutual evolution of spiral arms and disc stars can provide clues to the nature of spiral arms. To this end, we present a series of studies of simulated spiral galaxies in an isolated setting, in order to focus on the internal dynamical evolution alone.

In §2, we present our study on a Milky Way-sized galaxy with a live stellar disc and static dark matter halo. We trace the rotation of the spiral arms and find that they rotate with an angular speed almost equal to the rotation of the stellar disc (the spiral arms co-rotate with the stars). The evolution of nearby star particles is traced, and reveals that stars behind the spiral arm are continuously accelerated by the spiral arm and radially migrate outwards at all radii until the spiral arm disrupts. The opposite occurs for stars on the leading side of the spiral arm. We find that their orbital energy changes such that the orbits of the migrating particles experience no change in the degree of random motion.

In §3, we present an analysis of a barred-spiral galaxy simulation with both a live stellar and gas disc component, and a static dark matter halo. We improve our technique for tracing the spiral arms, and find again that the spiral arms co-rotate with the stars, at two different epochs of bar strength: an early epoch when the bar is strong and a later epoch when the bar is weaker. The conclusions regarding star particle motion and energy evolution found in §2 are confirmed to hold in the barred-spiral simulation. We also analyse the distribution of stars in different age populations, and find that the result is consistent with co-rotating spiral arms.

In §4, we present a suite of $N$-body simulations exploring the relation between galactic shear rate and spiral arm pitch angle. The study explores the effect of various parameters on spiral arm pitch angle, including the shear rate, disc-halo mass ratio, bulge mass, particle number and softening length. We conclude that the spiral arm pitch angle is driven by the shear rate, i.e., the larger the shear rate, the lower the pitch angle. This trend, and the scatter in pitch angle for a given shear rate is consistent with observations, and suggests that the spiral arms of real galaxies may be winding structures.

In §5, we present a detailed orbital analysis of star particles that migrate (migrators) and contrast them with star particles that do not migrate (non-migrators), in order to elucidate the mechanism of radial migration. We find that there are several types of migrator and non-migrator particles, the latter being newly discovered orbits. We find that the epicycle phase and tangential distance to the spiral arm are important parameters that separate migration and non-migration. The migrator particles behind (in front of) the spiral arm tend to be near their apocentre (pericentre) phase of orbit when they are close to the spiral arm, and produce a systematic streaming motion along the spiral arm in the outward (inward) radial direction. We show that although many individual star particles undergo large changes of angular momentum, the cumulative angular momentum distribution profile remains unchanged. The radial metallicity distribution is shown to maintain its radial gradient, however the dispersion in the metallicity distribution increases at all radii, thanks to the co-rotating spiral arms.

Finally, we summarise our conclusions in §6, and suggest some ideas for future work.

# Chapter 2

# The dynamics of stars around Spiral arms in an N-body simulation

*This chapter is based on Grand* et al. *(2012a).*

## 2.1 Introduction

As discussed in §1.2, classic spiral density wave theory (Lin & Shu, 1964) predicts that spiral arms rotate around the galaxy with a constant pattern speed. The constant pattern speed leads to the prediction of a co-rotation resonance at which the stars and spiral arm rotate at the same speed. Early theoretical studies such as Lynden-Bell & Kalnajs (1972), and later Sellwood & Binney (2002), showed that stars close to the co-rotation resonance can be radially transported through angular momentum exchanges between the spiral arm and the stars. This phenomenon, termed radial migration (see §1.3), is limited to occur only at co-rotation, which is found at a single radius in density wave theory.

However, results from both observations and numerical simulations do not corroborate the classic density wave theory: observations find evidence of a radially decreasing pattern speed (see §1.4) and simulations cannot reproduce long-lived spiral arms (see §1.5). Recently, Wada *et al.* (2011) performed simulations of an isolated spiral galaxy, and found a pattern speed that traces very well the rota-

tion curve, which indicates that there is co-rotation of the spiral pattern with the stars at all radii. The lack of consensus on the nature of spiral arms provides our motivation to scrutinise numerical simulations further.

In this study, we analyse the pattern speed of the spiral arm feature and the dynamics of particles around the arm using our N-body simulations of a pure stellar disc. We determine the nature of the spiral arm pattern speed, and monitor how stellar motion is affected by the arm. In agreement with Wada *et al.* (2011), we find that the spiral arms in the simulations are transient and that the pattern speed is always similar to the mean rotational velocity. We offer a qualitative insight into how phenomena such as radial migration might occur with the transient co-rotating spiral arms, and how the co-rotating spiral arm may evolve.

In §2.2 we explain how we set up the model and the initial parameters that we choose. In §2.3 we present the results of our analysis, compare them with previous studies and discuss their implications. In §2.4 we summarise the significance of the results and give concluding remarks.

## 2.2 Method and Model Setup

Our simulations are performed with a Tree $N$-body code, GCD+ (see Appendix B). We set up a disc galaxy that consists of a dark matter halo and a pure stellar disc with no bulge, and which is similar (slightly smaller) in size to the Milky Way. We describe the stellar disc component as a collisionless N-body system of particles, and adopt a static dark matter halo potential.

The dark matter halo density profile follows that of Navarro *et al.* (1997):

$$\rho_{\rm dm} = \frac{3H_0^2}{8\pi G}\frac{\Omega_0 - \Omega_b}{\Omega_0}\frac{\rho_{\rm c}}{cx(1+cx)^2}, \tag{2.1}$$

where $\rho_{\rm c}$ is the characteristic density described by Navarro *et al.* (1997), the concentration parameter, $c = \frac{\rm r_{200}}{\rm r_s}$, and $x = \frac{r}{r_{200}}$. The scale length is $r_{\rm s}$, and $r_{200}$ is the radius inside which the mean density of the Dark Matter sphere is equal to $200\rho_{\rm crit}$:

$$r_{200} = 1.63 \times 10^{-2} \left(\frac{M_{200}}{h^{-1}M_\odot}\right)^{\frac{1}{3}} h^{-1}{\rm kpc}. \tag{2.2}$$

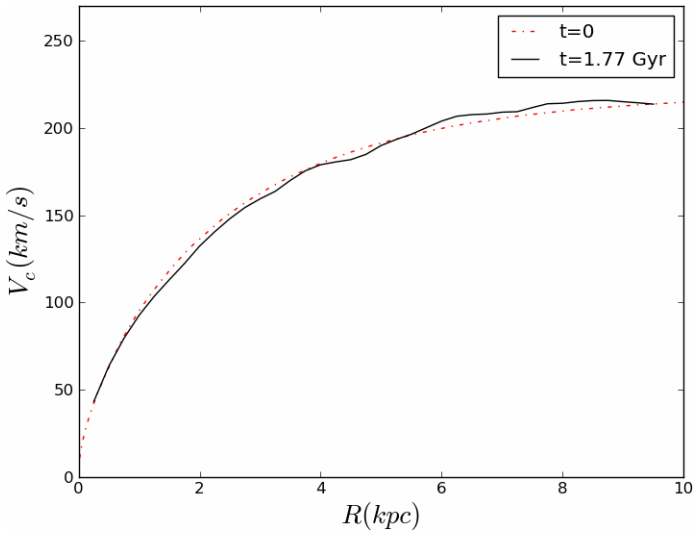


Figure 2.1: The initial circular velocity (dot-dashed red line) and the circular velocity at t= 1.77 Gyr (solid black line).

We assume $M_{200} = 1.7 \times 10^{12}$ M$_\odot$, $c = 15$, $\Omega_0 = 0.266$, $\Omega_b = 0.044$ and $H_0 = 71$ km s$^{-1}$ Mpc$^{-1}$. We do not apply adiabatic contraction for the dark matter halo, for simplicity.

The stellar disc is assumed to follow an exponential surface density profile:

$$\rho_{\rm d} = \frac{M_{\rm d}}{4\pi z_d R_{\rm d}^2} {\rm sech}^2\left(\frac{z}{z_d}\right) \exp\left(-\frac{R}{R_{\rm d}}\right). \tag{2.3}$$

We apply the mass of the disc, $M_d = 3 \times 10^{10}$ M$_\odot$, the scale length, $R_{\rm d} = 3.0$ kpc and the scale height $z_d = 0.35$ kpc, which is constant over the disc. These parameters lead to a stellar surface density of $\Sigma = 37$ M$_\odot$ pc$^{-2}$ at 8 kpc, which is similar to $\Sigma = 35.5$ M$_\odot$ pc$^{-2}$ obtained for disc stars in the solar neighbourhood (Flynn *et al.*, 2006).

The initial circular velocity curve is calculated from the gravitational potential of all particles and the dark matter halo, and is shown in Fig. 2.1. The rotation speed at 8 kpc is 210 km s$^{-1}$, which is slightly lower than the generally accepted value of 220 km s$^{-1}$ or even higher (e.g. McMillan, 2011) for the Milky Way. Although we constructed a galaxy similar in size to the Milky Way, it is not the intention of this study to reproduce the spiral arms of the Milky Way. This set of parameter values also ensures that the disc does not develop an obvious bar structure, which allows us to focus more on the pure effect of spiral arm develop-

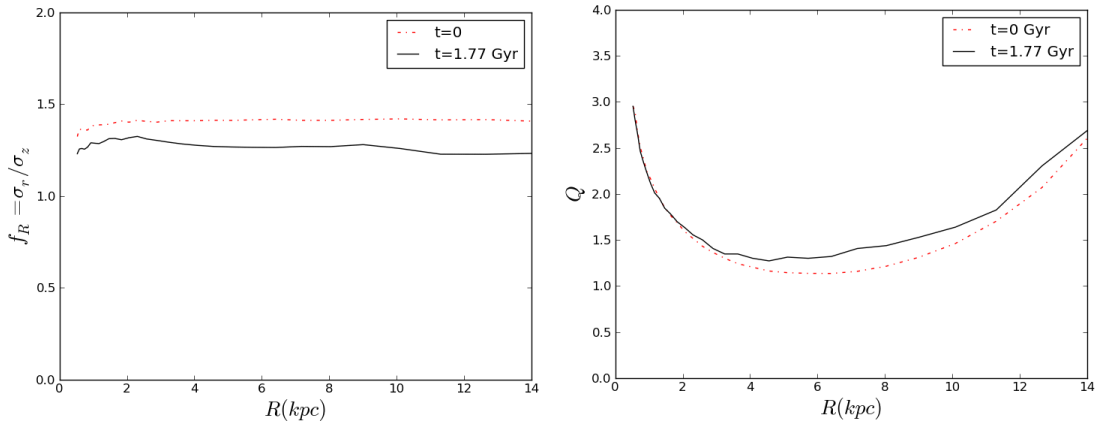


Figure 2.2: The radial profile of the ratio of velocity dispersions in the radial and $z$ direction, $f_R = \sigma_R/\sigma_z$ (left), and Toomre's instability parameter (right), at t=0 (dot-dashed red line) and t = 1.77 Gyr (solid black line).

ment and avoid the added complexity of the bar potential. This is achieved by choosing a concentration parameter high enough to ensure that there is sufficient dark matter mass in the central region to stabilise the stars against bar formation (Ostriker & Peebles, 1973). We use $3 \times 10^6$ particles for the disc component, therefore the mass of each particle is $10^4$ $M_\odot$. We adopt a fixed softening length of 340 pc, with the spline softening suggested by Price & Monaghan (2007).

The velocity dispersion for each three dimensional position of the disc is computed following Springel *et al.* (2005) to construct the almost equilibrium condition. The vertical velocity dispersion is determined from the 1D Jeans equation, and related to the radial velocity dispersion through the free parameter, $f_R = \sigma_R/\sigma_z$. The azimuthal mean velocity and velocity dispersion are set according to the asymmetric drift calculated from $\sigma_R$. The velocity distribution therefore follows a 3-component gaussian, centred on the mean velocities $\bar{\mathbf{v}}_\theta$ and $\bar{\mathbf{v}}_R = \bar{\mathbf{v}}_z = 0$. We choose $f_R = \sqrt{2}$ in the simulation shown in order to set up a disc that is initially kinematically cool enough to form clear spiral structure. This is slightly lower than $f_R \sim 2$ that is the observed ratio for the Milky Way (e.g. Holmberg *et al.*, 2009; Binney, 2010). However, as mentioned above, we do not aim to create a Milky Way-like galaxy. We denote this simulated galaxy S1, to distinguish it from the other simulations presented in this thesis.

## 2.3 Results and Discussion

The simulation set up in §2.2 is evolved for 2 Gyr. In agreement with the previous studies described in §1.5, we find that the disc develops transient and recurrent spiral arms. In this paper, we focus on one arm identified around $t = 1.77$ Gyr. The circular velocity at $t = 1.77$ Gyr is shown in Fig. 2.1, which is not significantly different from the initial circular velocity. The left panel of Fig. 2.2 shows $f_R$ as a function of radius at t = 0 and t = 1.77 Gyr. The value drops slightly with time as the disc heats up slightly during evolution. This is quantified in the right panel of Fig. 2.2, which shows a slight growth of Toomre's instability parameter, Q, at the same time-step. However, this is a very small amount of heating, which does not erase spiral structure (Fujii *et al.*, 2011).

Although we mainly discuss the analysis around $t = 1.77$ Gyr in this paper, we also applied similar analyses to other spiral arms that developed at different times in this simulation as well as spiral arms in other simulations with different initial configurations of the disc and dark matter halo. We find that all the spiral arms we analysed show very similar results to those shown in this section. We also find similar results in several (barred and non-barred) simulations that take gas and star formation into account. These will be described in §3.

First, we present the analysis and results of the pattern speeds of the chosen spiral arm. Then we examine the motion of selected particles around the arm, and present and discuss an analysis of their angular momentum and energy evolution.

### 2.3.1 Pattern Speed and Radial Migration

The middle row of panels in Fig. 2.3 shows three consecutive snapshots of the model galaxy, where the white lines depict the peak density of the chosen spiral arm at each radius. This is calculated by first creating a smoothed normalised density distribution in the $R$-$\theta$ plane, as in the left and middle columns of Fig. 2.7. At each radial bin, we locate the azimuth of maximum density. In this way, we traced the arm in the radial range between 4.5 and 8.5 kpc, and so we focus our analysis on this radial range. The pattern speed, $\Omega_p$, is then easily found from the azimuthal offset of the peak densities between the time-steps.

The angular pattern speed measured from the snapshots in Fig. 2.3 (middle row) is plotted in Fig. 2.4 along with the mean angular rotational velocity of

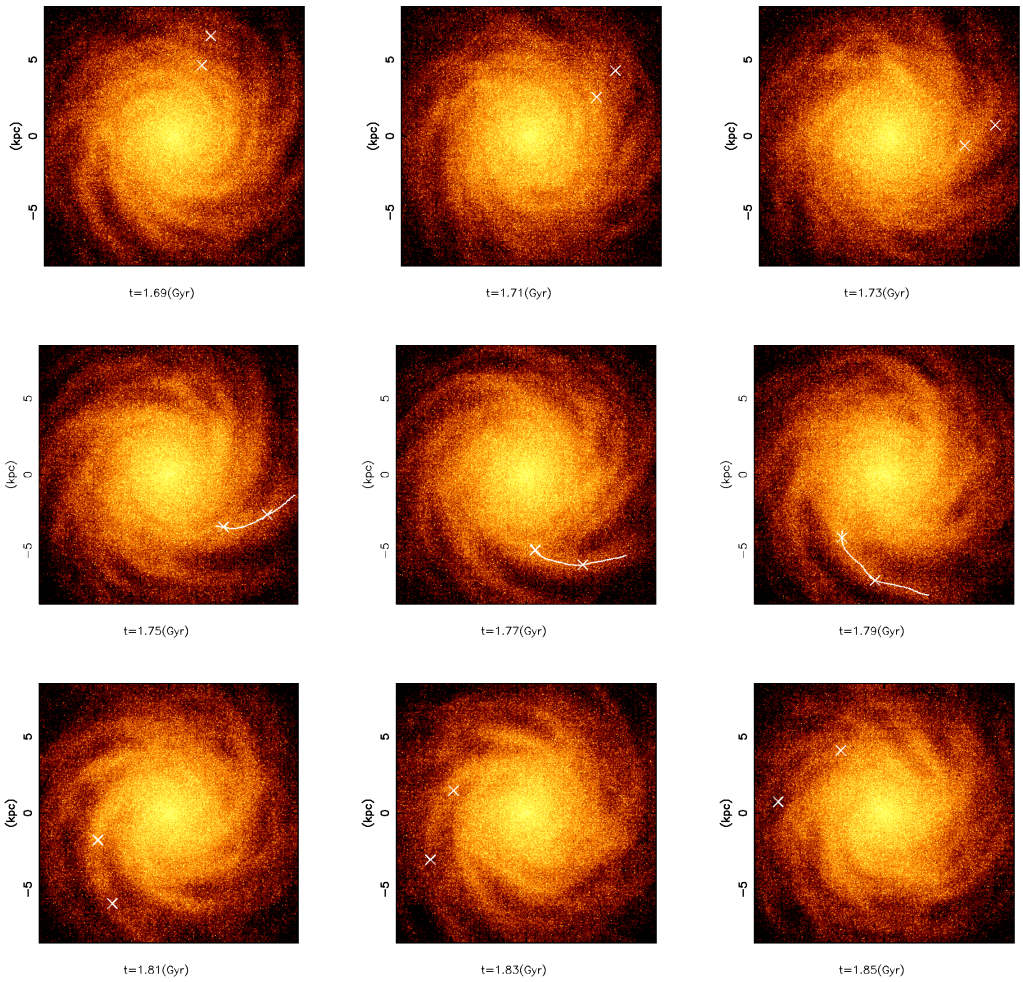


Figure 2.3: Snapshots of the disc from face on view. The white line marks the position of the peak density of the fully formed spiral arm at the time indicated (see text for how this is determined). In the middle row, the white crosses at 5 kpc and 7 kpc radius indicate position of the peak density line at those radii. In the top and bottom rows, the crosses have been rotated from their positions in the middle panel (t= 1.77 Gyr) by an angle derived from the angular rotation speed in Fig. 2.4 for those radii. The purpose of the crosses is to guide the eye to the spiral arm from formation around t= 1.73 Gyr, to its apparent destruction around t= 1.85 Gyr. This indicates that the lifetime of the spiral arm is very short ($\sim$ 120 Myr).

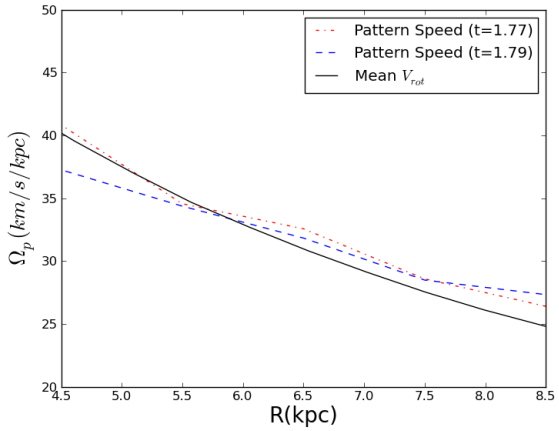


Figure 2.4: The pattern speed calculated between t= 1.75 and 1.77 Gyr (dot-dashed red) and between t= 1.77 and 1.79 Gyr (blue dashed). The mean angular rotation velocity at t= 1.77 Gyr is also plotted (black solid). The pattern speeds agree well with each other, and exhibit a decreasing trend that traces the mean angular rotation velocity very closely over the radial range shown. Similar trends are found at other time-steps with different arms.

the stars, which is calculated (throughout this thesis) by averaging the tangential velocity of all stars in each concentric radial annulus (mean rotational velocity), then dividing these values by radius. The pattern speed is seen to decrease with radius, such that it almost equals the mean angular rotation velocity of stars in the disc at all radii. This indicates that this spiral arm feature is co-rotating, and is therefore unlikely to be long-lived. This is confirmed from the snapshots of our simulation shown in the top and bottom rows of Fig. 2.3, which show that the arm starts developing around t=1.73 Gyr and is winding and disrupted around t=1.85 Gyr. Hence the lifetime of the arm is about 120 Myr and the arm is indeed transient. Bifurcations and breaks in the spiral arm features are seen regularly, which occur as the arms wind up. Wada *et al.* (2011) also find that the spiral arm features in their simulations are co-rotating, winding and short-lived.

As an additional test, and to assist intercomparison with previous studies, we compute spectrograms for $m = 2, 3$ and 4 modes, following Quillen *et al.* (2011). At each time-step, which spans a time period of 1.28 Gyr centred on $t \sim 1.77$ Gyr, and each radial bin, we calculate

$$W_c(r, t, m) = \sum_i \cos\left(m\theta_i(r, t)\right), \tag{2.4}$$

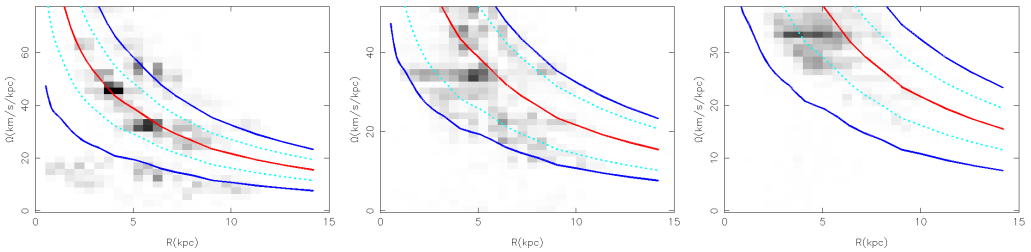


Figure 2.5: Spectrograms of the $m = 2, 3$ and 4 Fourier components in a time window spanning 1.28 Gyr centred on $t \sim 1.77$ Gyr. The plots show the power in frequencies ranging from 0 to the Nyquist frequency as a function of radius. *Left*: The spectrogram of the $m = 2$ component. Also marked is the mean angular rotational velocity line (solid red), the inner and outer Lindblad resonances (solid blue) and the 4:1 resonances (dotted cyan). *Middle*: The same as left panel but for $m = 3$ Fourier component, and 3:1 resonances shown (dashed cyan). *Right*: The same as left panel but for $m = 4$ Fourier component.

$$W_s(r, t, m) = \sum_i \sin\left(m\theta_i(r, t)\right), \tag{2.5}$$

where $\theta_i$ is the angle at the position of the particles within the radial bin. We calculate the amplitude of each mode as a function of radius and find that all modes show similar strength at $t = 1.77$ Gyr, hence there is no one mode that dominates over the others. We then compute the Fourier transform in the above period,

$$\tilde{W}(\omega, r, m) = \int_{T_1}^{T_2} [W_c(r, t, m) + iW_s(r, t, m)]e^{i\omega t}h(t)dt \tag{2.6}$$

where $h(t)$ is the Hanning function, which minimises spectral leakage. This is because the Hanning function is narrowly peaked around the centre of the time window and tapers off smoothly to zero as it approaches the time window edges. Therefore its convolution with the Fourier transformed data concentrates the power near the true frequency (Press *et al.*, 1992, page 547). We compute the power, defined as $P = |\tilde{W}|^2$, at each frequency ranging from zero to the Nyquist frequency, which is shown in Fig. 2.5. The spectrogram analysis shows us the significance of the pattern speeds of the wave modes (which we call *mode pattern speed*), which can be different from what is shown in Fig. 2.4 (i.e. the pattern speed of the spiral arm feature), if multiple wave modes interfere with each other. All three modes, especially the $m = 2$ mode, show that there is some power in the

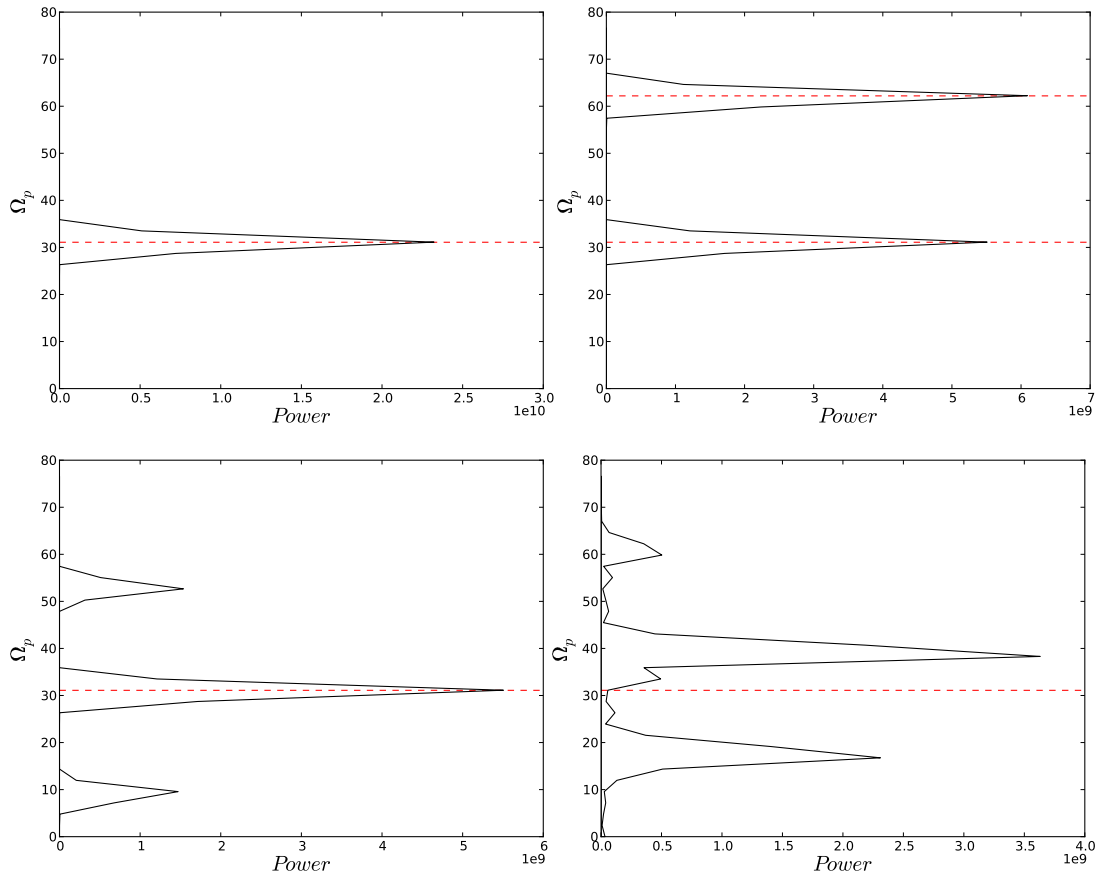


Figure 2.6: Input pattern speeds of the $m = 2$ wave modes (dashed red line) and the power recovered from the spectrogram analysis (solid black line). *Top left*: Single $\Omega_p = 31$ km s$^{-1}$ kpc$^{-1}$ is input and correctly extracted. *Top right*: Two wave modes of $\Omega_p = 31$ and 62 km s$^{-1}$ kpc$^{-1}$ are input. *Bottom left*: Same as top left, but the amplitude of the wave mode is varied. *Bottom right*: Same as bottom left, but random offsets of phase angle are implemented. See text for details.

mode pattern speed that overlaps the rotation velocity at many radii. There are also several horizontal features which could mean that there are a number of wave modes with constant, but different pattern speeds (Sellwood, 2011, and references therein), that span different radii, and may be constructively and destructively interfering with each other. For example, the $m = 2$ mode could be interpreted as having two pattern speeds ($\sim$ 30 and 45 km s$^{-1}$ kpc$^{-1}$), with a faster inner pattern and a slower outer pattern, as suggested by Quillen *et al.* (2011); Sellwood & Lin (1989); Masset & Tagger (1997). This contrasts heavily with the single global wave mode of constant pattern speed predicted by classic spiral density wave theory (Lin & Shu, 1964). Fig. 2.5 also indicates the 1:2, 1:3 and 1:4 Lindblad resonances, i.e. $\Omega_p = \Omega \pm \kappa/m$, for $m = 2, 3$ and 4 respectively.

We note however some caution with regard to the spectrogram analysis method when applied to transient, variable amplitude wave modes. We construct a toy model in which we set a base density of stars and distribute them randomly in a ring. We then add a small fraction (2.5%) of those in the ring at $\theta = 0, \pi$ to mimic the $m = 2$ modes. We impose a single, constant angular rotational frequency on the particles, and perform the same spectrogram analysis as above. Fig. 2.6 (top left panel) shows the case assuming 31 km s$^{-1}$ kpc$^{-1}$ rotation, for which this frequency is correctly extracted. The top right panel shows the case for two overlapping wave modes of 31 and 62 km s$^{-1}$ kpc$^{-1}$ rotation speeds, and both are shown to be extracted.

However, the amplitude of the wave mode can evolve and/or disappear as demonstrated in Sellwood (2011). To demonstrate the effect of variable amplitude, we return to a single pattern speed of 31 km s$^{-1}$ kpc$^{-1}$, and repeatedly increase and decrease the number of $m = 2$ mode particles using a sinusoidal curve from 0 to $\pi$, that spans over 120 Myr, which is roughly consistent with the lifetime of the arm feature in Fig. 2.4. The effect is shown (Fig. 2.6 bottom left panel) to create three peaks, with one at the input frequency, and two others: one either side of the real one.

The appearance of the new mode can shift the azimuthal position, which we model as randomly shifting the azimuthal position of the mode particles within 0 to $\pi$, every 120 Myr. This effect plus the variable amplitude is shown in the bottom right panel. This produces several peaks, none of which corresponds to the real input frequency. Although this is a simple exercise, and our aim is not to

explore many possible cases of transient wave modes, this demonstrates that, for transient wave modes of similar lifetimes to that of the spiral arm feature, there is a possible danger that the spectrogram may not show the real pattern speed of the wave modes. Moreover, any systematic variability could be responsible for the horizontal features seen in the spectrogram.

In any case, if there are indeed several wave modes present, it is evident that they must conspire in a specific way in order to produce a spiral arm feature that is "apparently co-rotating" as is clearly shown in Fig. 2.4. Associating the multiple wave modes to the apparent spiral arm features is beyond the scope of this paper. We rather focus on how this apparently co-rotating spiral arm feature affects the stellar motion. Therefore, the remainder of this chapter is discussed in terms of what is shown in Fig. 2.4. We term this "apparent pattern speed" and "apparent co-rotation".

A direct implication of a decreasing apparent pattern speed is that there are co-rotation radii all over the disc, and therefore the radial migration (Sellwood & Binney, 2002) described in §1.3 is expected to occur at a wide range of radii around the spiral arm. In addition, stars that radially migrate at co-rotation are predicted to maintain their degree of random motion (not to heat them kinematically).

In order to see how stellar motions are affected by this spiral arm whose apparent pattern speed decreases with radius, we trace the motions of individual particles in our simulation, as in Fig. 2.7. First, we select a sample of particles around our chosen arm of interest at 5.5 kpc radius at $t = 1.75$ Gyr when the arm is most prominent. The sample is selected to be near the plane of the disc ($|z| < 200$pc), and has a radial thickness of 0.25 kpc and azimuthal width of $\sim$1 radian centred on highest density point of the arm (left-middle panel of Fig. 2.7). We follow their motion with respect to the spiral arm around which they were selected in Fig. 2.7. The middle row shows the snapshot and smoothed normalised density plots at the time they were selected. The preceding and succeeding rows show that of 60 Myr before and after respectively, and we move in a non-inertial frame of 40 $\mathrm{kms^{-1}kpc^{-1}}$ from the middle step, hence only the middle row shows explicitly the actual co-ordinates in the smoothed plots.

It is seen that as the spiral arm grows stronger, particles from both sides of the arm begin to join the arm, which indicates the apparent co-rotation with

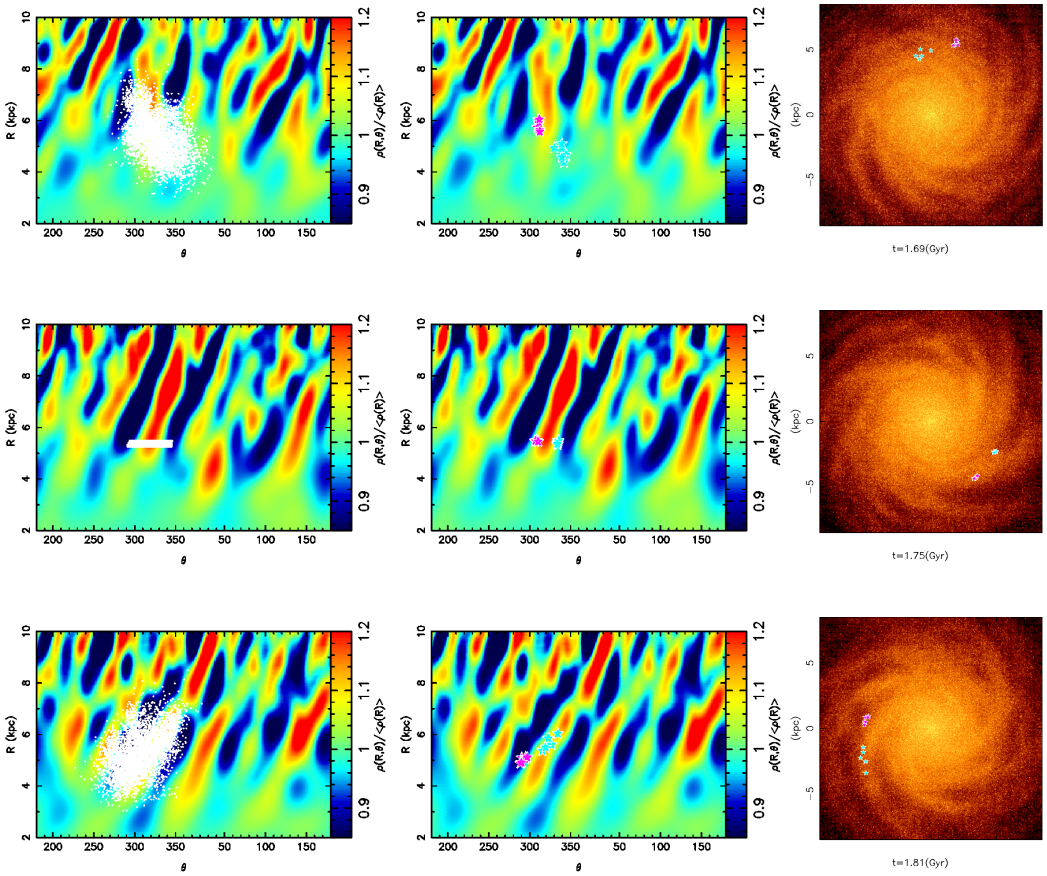


Figure 2.7: Left and Middle columns: the smoothed normalised density distribution (colour map) in the azimuthal angle - radius plane. Right column: the corresponding snapshots of the disc (the time referring to each row is indicated under each panel). In the left column, the particles (white dots) selected at 5.5 kpc at t= 1.75 Gyr are highlighted. In the middle and right columns the extreme migrators (see text) in the sample are highlighted by cyan (particles that migrate toward the outer radii) and pink (particles that move toward the inner radii) stars. Note that the coordinate of the angle in the left and middle panels at the top and bottom rows are shifted by the amount corresponding with $\Omega = 40$ kms$^{-1}$kpc$^{-1}$, to keep the highlighted particles around the central region of each panel.

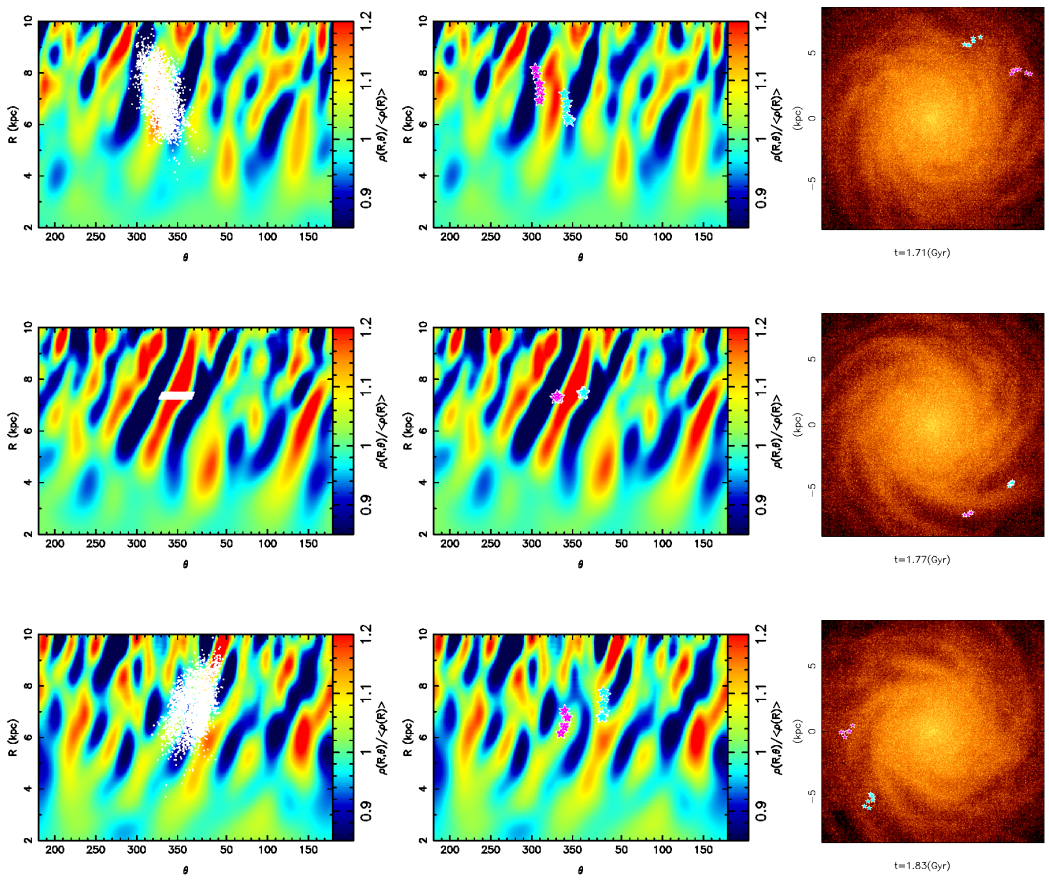


Figure 2.8: The same as Figure 2.7, but for a sample around 7.5 kpc radius. The particles were selected at 1.77 Gyr; one time-step after the 5.5 kpc sample, in order we see the strongest, most clear radial migration. This is because the arm at smaller radii shows more prominence at earlier times than at larger radii.

the star particles. We find that the spiral arm develops in a way akin to swing amplification (Goldreich & Lynden-Bell, 1965; Julian & Toomre, 1966; Toomre, 1981). In swing amplification theory, a leading arm can grow in density as it shears into a trailing arm. The star's epicycle phase and shearing motion of the arm conspire in a way that the stars in the spiral arm remain in the over-dense region for longer. This means that as the leading arm turns into a trailing arm owing to the shear motion, self-gravity becomes stronger and accumulates more stars to the arm, and the amplitude of the arm begins to grow non-linearly.

The left column in Fig. 2.7 indicates that the chosen particles look like a leading feature at $t = 1.69$ Gyr, which become part of a trailing arm at $t = 1.75$ Gyr as it wound up. The selected particles around the arm at 5.5 kpc (white dots) join the arm from the outer (inner) radii at the leading (trailing) side of the spiral arm while at the same time the spiral arm appears to grow in density. We therefore witness swing amplification in action. Note however that this process is different from the classic swing amplification mechanism in which the starting point is a leading spiral arm feature and the co-rotation radius is assumed to be one specific radius, because we do not see a leading spiral arm feature and the spiral arm co-rotates at all radii. What we have found may be described as amplification occurring over a wide range of radii. This is accompanied by strong radial migration, which we describe below.

From the selected sample of particles, we compute the angular momentum change, $\Delta L$, over a period of 80 Myrs and choose those that exhibit the largest values of $\Delta L$. As a fraction of their initial angular momentum, $L$, these have typical values $\Delta L/L \simeq 10 - 20\%$. We term these particles extreme migrators. The middle column of Fig. 2.7 shows the evolution of the extreme positive (cyan) and negative (pink) migrators. The "positive" migrators are the particles that migrate towards the outer radii on the trailing side of the spiral arm. They are trapped by the potential of the spiral arm, which accelerates them. The co-rotating nature of the spiral arm feature ensures that during migration to outer radii, instead of passing through the spiral arm they remain on the trailing side (middle and right hand panels of Fig. 2.7). Therefore, they continue to accelerate until the spiral arm is disrupted. The "negative" migrators are particles that migrate towards the inner radii on the leading side of the spiral arm. They are decelerated as they become caught in the potential of the spiral arm, and because

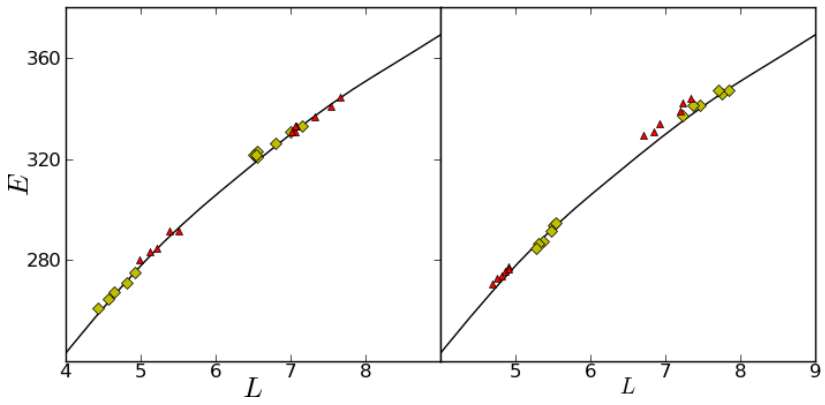


Figure 2.9: The energy, $E$, and angular momentum, $L$, distribution of the extreme migrators in Figs. 2.7 and 2.8 at 40 Myr before (yellow diamonds) and 40 Myr after (red triangles) the time-step at which they were selected. The right (left) panel shows the results of the migrators that moved toward the inner (outer) radii. The solid black line indicates the circular orbit. Units are arbitrary.

of the apparent co-rotation, they continue to decelerate on the leading side of the spiral arm until the spiral arm is disrupted. This illustrates the different motion that occurs on each side of the spiral arm.

To demonstrate that these stellar motions and strong migration occur over a wide range of radii, Fig. 2.8 shows the same dynamical evolution as Fig. 2.7 for a sample selected at the radius of 7.5 kpc. This 7.5 kpc sample and the extreme migrators were selected using the same criteria as the 5.5 kpc sample, however at $t = 1.77$ Gyr, since we find that the spiral arm at the outer radii grows later. It is clearly demonstrated here that exactly the same type of motion expected at the co-rotation radius happens at 7.5 kpc. This motion is at least consistent with the apparent co-rotation found in Fig. 2.4, because the particles continue to join the arm from both sides at a large range of radii as they migrate, instead of passing or being passed by the spiral arm, which is expected if the pattern speed is constant as predicted by density waves. This strengthens our conclusion of apparent co-rotation of the spiral arm feature made from Fig. 2.4.

### 2.3.2 Energy and Angular Momentum Evolution

When discussing the changes in angular momentum associated with radial migration, it is important to look at how the orbital energy of a star is affected. The relevant question becomes: "Is the star scattered during the migration by

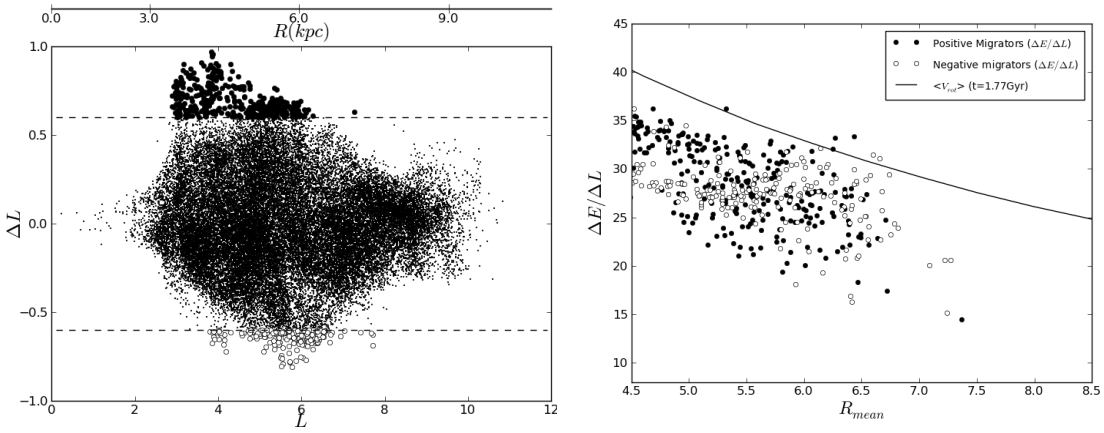


Figure 2.10: *Left*: The angular momentum change over 80Myr for particles in a radial range of 4.0 to 9.0 kpc around the spiral arm at $t = 1.77$ Gyr, as a function of their initial angular momentum at $t = 1.73$ Gyr. We define the extreme migrators to have $|\Delta L| > 0.6$. The radius expected from circular motion with corresponding angular momentum is also shown. *Right*: $\Delta E/\Delta L$ for the extreme migrators selected in the left panel (open and filled circles) as a function of their mean radius between $t = 1.73$ to $t = 1.81$ Gyr. The filled circles are those with positive migration, and the empty are those with negative migration. The solid black line is the mean angular rotational velocity. The units of y-axis or adjusted to match with that of Fig. 2.4.

gaining significant energy of random motion?". To shed light on such a question, we calculate the energy, $E$, and angular momentum, $L$, of the extreme migrators in Figs. 2.7 and 2.8 at 40 Myr before and after the time-step at which they were selected, and show this in Fig. 2.9. We call these two time-steps the "initial" and "final" time-steps respectively. The solid black line indicates the $L$ and $E$ expected for a pure circular orbit at each radius. This represents the minimum energy which a star particle can have at a given angular momentum. In Fig. 2.9 we show the position of the extreme migrators at the initial (yellow diamonds) and final (red triangles) time-steps. We can see that the negative migrators (right panel) and positive migrators (left panel) move along the circular velocity curve in opposite directions to each other. Because they keep close to the circular velocity curve after migration, their orbits must retain a very similar eccentricity, and so they gain little random energy and are not scattered into higher energy orbits (Sellwood & Binney, 2002).

However there is *some* movement away from the circular velocity curve, and this corresponds to heating effects. We therefore test the degree of orbital heating

of migrators with a larger sample of stars at different radii.

We select the most extreme migrators from a sample of particles around the spiral arm in a radial range of 4-9 kpc at $t = 1.77$ Gyr. We plot in the left panel of Fig. 2.10 their change in angular momentum between initial and final time-steps spanning a period of 80 Myr as a function of their angular momentum at the initial time-step of $t = 1.73$ Gyr. We selected the particles with $|\Delta L| > 0.6$, and calculate $\Delta E/\Delta L$ for each particle, which we show plotted against the mean radius of each particle over the 80 Myr period in the right panel of Fig. 2.10. The filled (empty) circles represent the positive (negative) migrators. A clear decreasing trend with radius is seen for both sets of migrators. This trend qualitatively matches what is expected for $dE/dL$ along the curve of circular orbit, $(dE/dL)_c$, in Fig. 2.9 (solid line in the right panel of Fig. 2.10), but the overall position of the particles is slightly lower. For $dE/dL = (dE/dL)_c$, the migrator particles move tangent to the circular orbit curve in Fig. 2.9. For example, a positive migrator, $dL > 0$, must undergo a change in orbital energy equal to $dL(dE/dL)_c$ in order to maintain the degree of random motion. However, the offset in the right panel of Fig. 2.10 means that $dE$ is too low, and as a result there is a slight *heating* of the negative migrators and slight *cooling* for the positive migrators.

However, the overall decreasing trend in parallel with the mean angular rotational velocity line indicates that similar and only small heating losses occur over a range of radii. This demonstrates that radial migration can occur everywhere in the disc, and stars can slide along the spiral arms to different radii all over the disc with little contribution to disc heating.

## 2.4 Conclusions

In this chapter, we have performed $N$-body simulations of a pure stellar disc, and then performed a dynamical analysis of the spiral arms and particles around the spiral arms and traced their evolution. We come to the following conclusions:

(i) We find in our simulations that spiral arms are transient recurring features: we observe the continuous disappearance of spiral arms and the reappearance of new ones. This transient nature has always been found in numerical simulations, and is not consistent with spiral density wave theory.

(ii) We performed two analyses on the pattern speed of the spiral arms: the stellar density trace method; and spectrogram analysis. The latter shows a possible configuration of two or three wave modes that could mean that wave modes interfere constructively and destructively with each other.

Regardless of whether this is the case, the stellar density trace method gave us clear evidence of an apparent spiral arm pattern speed that co-rotates with the stars at a large range of radii, which is reflected in points iii), iv) and v) below. This is consistent with what is found in Wada *et al.* (2011), and contrary to classic spiral density wave theory, which allows a constant pattern speed as a function of radius, and hence there is *only one* co-rotation radius. We cannot reject, however, the idea that the co-rotating spiral arm is a manifestation of a superposition of wave modes (Sellwood, 2014).

(iii) Particles are shown to join the spiral arm from both sides at all radii. This is further evidence for the co-rotating nature of the spiral arm feature, because the arm must move at a similar speed to the particles in order for them to join the arm from both sides at all radii.

(iv) Particles migrate radially along the spiral arm at all radii. Stars behind the arm are accelerated by the arm and slide along the arm to larger radii. Stars in front of the arm are dragged back by the potential, and slide down the arm to smaller radii.

(v) Migrating particles do not actually cross the spiral arm. The co-rotating nature means that the particles stay on their respective sides of the spiral arm, so they are accelerated (decelerated) until the spiral arm is disrupted. This means that radial migration is more efficient than that discussed by Sellwood & Binney (2002), with little contribution to disc heating.

Conclusions (i) and (ii) are already known from previous studies, and we include them to show the consistency of this study. Conclusions (iii), (iv) and (v) are new results which to our knowledge have not been reported before.

# Chapter 3

# Stellar dynamics and star forming tracers in an SPH simulated galaxy

*This chapter is based on Grand* et al. *(2012b).*

## 3.1 Introduction

In §2 we demonstrated a new type of systematic motion of star particles close to the spiral arm in their simulation, that leads to extended radial migration of star particles all along the arm as opposed to the currently considered case of a single co-rotation radius (Lynden-Bell & Kalnajs, 1972; Sellwood & Binney, 2002). The star particles were shown to join the arm from both sides. Star particles behind (in front of) the arm were accelerated (decelerated) continually because the similar rotation speeds of the star particles and spiral arm allowed the migrating star particles to stay very close to the density enhancement of the spiral arm. This mechanism is responsible for the steady gain/loss of angular momentum of the migrating star particles, whereby the star particle is allowed to find a new equilibrium in a higher/lower energy circular orbit, without scattering kinematically. The star particles never crossed the arm as they migrated, and stopped migrating when the high amplitude of the density enhancement disappeared owing to the transient nature of the arms. Because this simulation was

an $N$-body simulation of a pure stellar disc with no bar or bulge, the only factor that could be responsible for the observed motion was the spiral arm features.

In this study, our aim is to build upon our previous study presented in §2 that focused on $N$-body dynamics in a pure stellar disc, and extend this research on the spiral arm pattern speed and star particle dynamics in high resolution $N$-body/SPH simulations of a barred spiral galaxy. This will enable us to study the spiral arm and its effects in a more realistic context, and to determine whether or not the presence of gas, star formation and a bar produces any significant effect on particle motion that may be distinguished from those seen in the pure $N$-body simulation. In comparison to §2, we present a more robust method for determining the apparent pattern speed of the spiral arm, and attention is given to the energy evolution of particles that undergo radial migration at many radii.

Because the simulation includes star formation, it is possible to mimic the tracer offset method applied to observational data (e.g. Foyle *et al.*, 2011; Ferreras *et al.*, 2012). As discussed in §1.4, spiral density wave theory predicts the presence of clear spatial offsets between different star forming tracers across spiral arms, owing to the relative speed between star forming gas clouds and the spiral arm at radii away from co-rotation. In this study, we mimic this test of density wave theory by analysing the distribution of young star particles of different ages around spiral arms. Although the analysis could be extended to the bar region, this chapter focuses on the spiral arm. Hence we leave the analysis of the structure and evolution of bars to future studies.

In §3.2 a description of the simulation set up and initial parameters is given. In §3.3 we present the results of our analysis, compare them with previous studies and discuss their implications. In §3.4 we summarise the significance of the results and remark upon the value of the simulations.

## 3.2 Method and Model Setup

### 3.2.1 GCD+ code

In the simulation presented in this study, we use the galactic chemo-dynamical evolution code, GCD+. The code is a three-dimensional tree $N$-body/SPH code (Gingold & Monaghan, 1977; Lucy, 1977; Barnes & Hut, 1986; Hernquist & Katz, 1989; Katz *et al.*, 1996; Kawata & Gibson, 2003; Kawata *et al.*, 2013b) that incor-

porates self-gravity, hydrodynamics, radiative cooling, star formation, supernova type II and Ia feedback and metal enrichment and diffusion Greif *et al.* (2009). It is fully described in Appendix B.

The main parameters that govern star formation and supernova feedback are set as follows: the star formation density threshold, $n_{th} = 1.0$ cm$^{-3}$ ; star formation efficiency, $C_* = 0.1$ ; supernova energy input, $E_{\rm SN} = 10^{50}$ erg per supernova; and stellar wind energy input, $L_{\rm SW} = 10^{36}$ erg s$^{-1}$. Each particle in the simulation is assigned a unique ID number. This makes it easy to trace any particle during the evolution of the simulation.

### 3.2.2 Simulation Setup

Our simulated galaxy consists of a spherical static dark matter halo and two live discs: a stellar disc and a gas disc. The dark matter halo density profile follows that of Navarro *et al.* (1997) with the addition of an exponential truncation term (Rodionov & Athanassoula, 2011):

$$\rho_{\rm dm} = \frac{3H_0^2}{8\pi G}\frac{\Omega_0 - \Omega_b}{\Omega_0}\frac{\rho_{\rm c}}{cx(1+cx)^2}\exp(-x^2), \tag{3.1}$$

where $\rho_{\rm c}$ is the characteristic density described by Navarro *et al.* (1997), the concentration parameter, $c = r_{200}/r_{\rm s}$, and $x = r/r_{200}$. The truncation term, $\exp(-x^2)$, is introduced in our initial condition generator for a live halo simulation. Although we use a static dark matter halo in this paper, we retain the profile of equation (3.1) because this term does not change the dark matter density profile in the inner region, which is the focus of this paper. The scale length is $r_{\rm s}$, and $r_{200}$ is the radius inside which the mean density of the dark matter sphere is equal to $200\rho_{\rm crit}$ (where $\rho_{crit} = 3H_0^2/8\pi G$; the critical density for closure):

$$r_{200} = 1.63 \times 10^{-2}\left(\frac{M_{200}}{h^{-1}M_\odot}\right)^{\frac{1}{3}} h^{-1}{\rm kpc}. \tag{3.2}$$

We assume $M_{200} = 1.5 \times 10^{12}$ M$_\odot$, $c = 10$, $\Omega_0 = 0.266$, $\Omega_b = 0.044$ and $H_0 = 71$ km s$^{-1}$ Mpc$^{-1}$. We ran several simulations of different parameters and found that a lower value of $c$ than that of §2 was required to form a prominent bar.

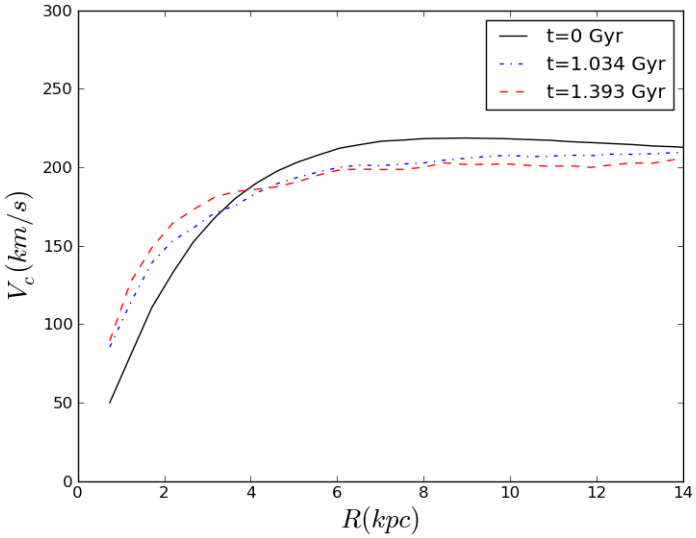


Figure 3.1: The circular velocity at $t = 0$ (solid black line), at t= 1.034 Gyr (dot-dashed blue line) and $t = 1.393$ Gyr (dashed red line).

The stellar disc is assumed to follow an exponential surface density profile:

$$\rho_{\mathrm{d},*} = \frac{M_{\mathrm{d},*}}{4\pi z_{\mathrm{d},*} R_{\mathrm{d},*}^2} \mathrm{sech}^2\left(\frac{z}{z_{\mathrm{d},*}}\right) \exp\left(-\frac{R}{R_{\mathrm{d},*}}\right), \tag{3.3}$$

where the disc mass, $M_{\mathrm{d},*} = 5 \times 10^{10}$ M$_\odot$, the scale length, $R_{\mathrm{d},*} = 2.5$ kpc and the scale height $z_{\mathrm{d},*} = 0.35$ kpc, which is constant over the disc. The velocity dispersion for each three dimensional position of the disc is computed following Springel *et al.* (2005) to construct the almost equilibrium initial condition. One free parameter in this method is the ratio of the radial velocity dispersion to the vertical velocity dispersion, $f_R$, which relates as $f_R = \sigma_R/\sigma_z$. We choose $f_R = 2$ in the simulation shown. The initial circular velocity curve is shown in Fig. 3.1 (solid line). It is calculated in the same way as in §2.2 with the additional step of averaging the value at each radius over the entire azimuthal range. The initial circular speed at 8 kpc is $\sim 220$ km s$^{-1}$.

The gas disc is set up following the method described in Springel *et al.* (2005). The radial surface density profile is assumed to follow an exponential law like the stellar disc. The initial vertical distribution of the gas is iteratively calculated to be in hydrostatic equilibrium assuming the equation of state calculated from our assumed cooling and heating function. For the gas disc, we set the disc

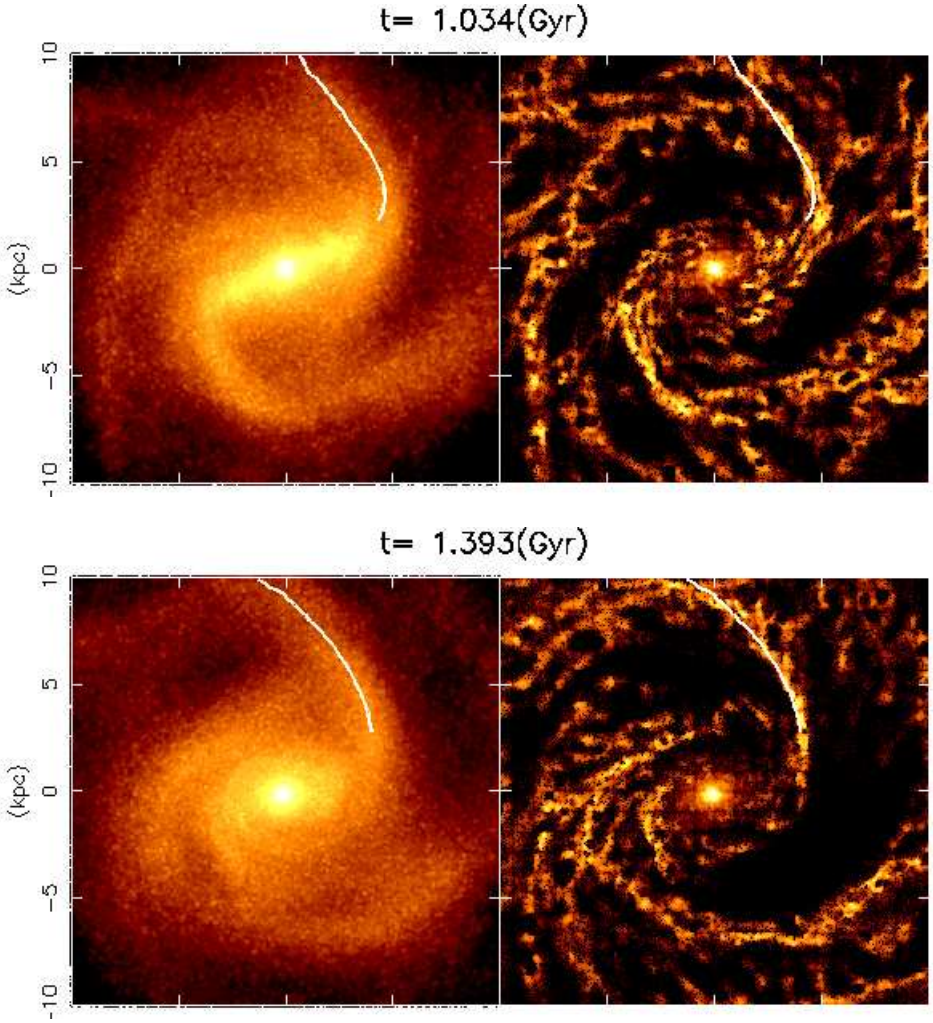


Figure 3.2: Snapshots of the face-on view of the simulated galaxy at $t = 1.034$ Gyr (top) and $t = 1.393$ Gyr (bottom). The left images show the stellar density map, and the right images show the gas density map. The bar is strong at the earlier time, and becomes smaller at the later time.

mass, $M_{\rm d,g} = 1 \times 10^{10}$ M$_\odot$, the scale length, $R_{\rm d,g} = 4.0$ kpc. All the parameters described above are chosen to be similar to those of the Milky Way (McMillan, 2011).

We use $N_{\rm d,*} = 2 \times 10^6$ and $N_{\rm d,g} = 4 \times 10^5$ particles for stars and gas respectively, and therefore the mass of each particle is $2.5 \times 10^4$ M$_\odot$. Fujii *et al.* (2011) show that if more than one million particles are used to describe the disc component, artificial heating that suppresses the spiral arm formation is not significant. Our simulation uses a total of $2.4 \times 10^6$ particles and therefore is expected to be less affected by artificial heating. We adopt a softening length equal to the smoothing length but set the minimum softening length to 340 pc for gas particles and apply a fixed softening length of 340 pc for star particles, with the spline softening suggested by Price & Monaghan (2007). These parameters of the stellar component are similar to that of the non-barred spiral galaxy simulated in §2, but with a higher disc to halo mass ratio. To induce spontaneous bar formation (e.g. Ostriker & Peebles, 1973), we have applied a lower concentration parameter, $c = 10$, in equation (3.1). We denote this simulated galaxy SBg, to distinguish it from the other simulations presented in this thesis.

## 3.3 Results and Discussion

The simulation set up in §3.2 was evolved for about 2 Gyr. The stellar and gas component is shown at two different times in Fig. 3.2, and we see a prominent bar spiral structure in both components. As discussed in §1, gas can enhance the strength of non-axisymmetric structures by helping to keep the disc kinematically cool. We note that the gas, in combination with the structural parameters given in §3.2, likely contributes to the formation of a strong bar and spirals seen in Fig. 3.2. The extent to which the gas affects disc stability is a complicated issue that requires a dedicated and detailed analysis, which is beyond the scope of this study.

The strong bar develops around $t = 1.034$ Gyr, and settles to a smaller bar before $t = 1.393$ Gyr. Similar to previous studies described in §2, we also find that the disc develops transient and recurrent spiral arms. In this paper, we focus our analysis on spiral arms at an early and late epoch in the evolution of the simulated galaxy, highlighted in Fig. 3.2. These times are referred to as the

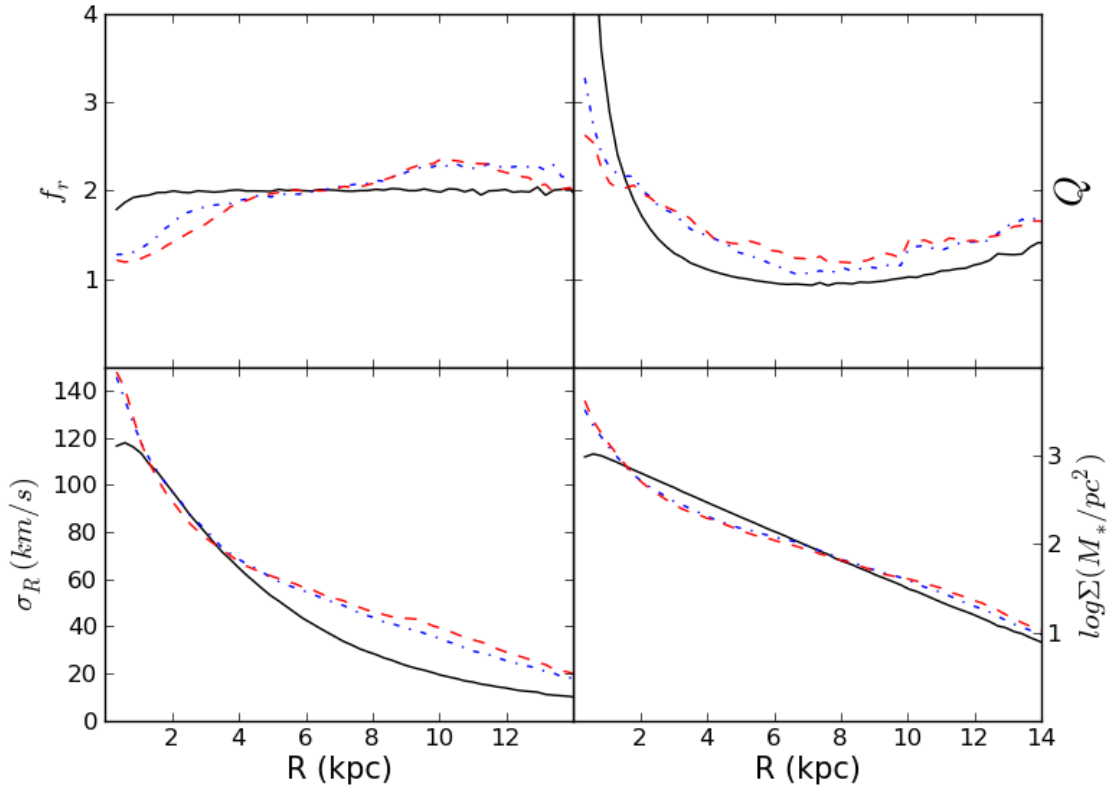


Figure 3.3: The radial profile of the ratio of velocity dispersions in the radial and $z$ direction (top-left), Toomre's stability parameter (top-right), logarithmic surface density (bottom-left) and radial velocity dispersion (bottom-right), at $t = 0$ (solid black line), t= 1.034 Gyr (dot-dashed blue line) and $t = 1.393$ Gyr (dashed red line).

centre of each epoch throughout the paper. Particular attention is paid to these spiral arms because they are prominent arms, which facilitate our analysis and we are able to extract and more clearly demonstrate the key features that we want to identify, namely the pattern speed and the particle motion around the spiral arm.

The circular velocity at $t = 0$ and $t = 1.034$ Gyr (early epoch) and $t = 1.393$ Gyr (late epoch) is shown in Fig. 3.1. The circular velocity in the inner region after $t = 0$ is significantly different from the initial circular velocity, owing to the strong gravitational field created by the developed bulge. The top-left panel of Fig. 3.3 shows $f_R$ as a function of radius at the same time-steps. The value drops with time in the inner radii (bar region). Outside $R \sim 5$ kpc, $f_R$ increases slightly as the disc is heated by strong spiral structure, which increases the velocity dispersion, $\sigma_R$, shown explicitly in the bottom-left panel of Fig. 3.3. The effect on spiral structure is quantified in the top-right panel of Fig. 3.3, which shows an increase of Toomre's instability parameter, $Q = \sigma_R \kappa / 3.36 G \Sigma_*$, in the spiral region, where $\kappa$ is the epicycle frequency and $\Sigma_*$ is the surface density of the stellar component. This is contrary to the bar region where $Q$ is lowered owing to the large surface density excess in the central region shown in the bottom-right panel of Fig. 3.3. A bulge that creates this excess of central density are likely formed through secular evolution caused by the bar (e.g. Pfenniger & Norman, 1990; Kormendy & Kennicutt, 2004, and references therein). The developed bulge is apparent in Fig. 3.2.

We present analysis and discussion of two spiral arms at an early ($t \sim 1.034$ Gyr) and a later ($t \sim 1.393$ Gyr) epoch of the galaxy's evolution. This is because the bar is strong at the early epoch, in contrast with the later epoch when the bar is comparatively weak. To quantify the bar strength, we use a gravitational force field method (e.g. Buta & Block, 2001; Buta *et al.*, 2005). We first define a circular grid that covers an azimuth range of 0 to $2\pi$ and a radial range of 1 kpc to 5 kpc. At the centre of each grid point, the radial and tangential forces are calculated, which are then used to calculate the ratio:

$$Q_T(R,\theta) = \frac{|F_T(R,\theta)|}{\bar{F}_R(R,\theta)}, \tag{3.4}$$

where $F_T(R,\theta)$ is the tangential force at a given grid point of coordinates $(R,\theta)$, and $\bar{F}_R(R,\theta)$ is the mean radial force averaged over each azimuth at a given radius

(Combes & Sanders, 1981). A maximum, $Q_{b,i}$, is found in each quadrant, where quadrants $i = 1, 2, 3$ and 4 are defined by setting the major and minor axes of the bar to the $x-$ and $y-$axes respectively. The bar strength is then defined as the average of these four values: $Q_b = \sum_{i=1}^{4} Q_{b,i}/4$. At the early epoch, $Q_b = 0.27$, and at the late epoch, $Q_b = 0.11$. According to the classification scheme outlined in Buta & Block (2001), these values correspond to a class 3 and class 1 bar at the early and late epochs respectively.

First we present the analysis and results of the pattern speeds of the chosen spiral arms. Then we examine the motion of selected particles around the arm, and present and discuss an analysis of their angular momentum and energy evolution. We compute the angular momentum evolution around both spiral arms, and make a comparison between each case. We also examine the position of star particles of different ages in and around the spiral arm, which would be an observational test for pattern speeds of spiral arms (Tamburro *et al.*, 2008; Egusa *et al.*, 2009; Foyle *et al.*, 2011; Ferreras *et al.*, 2012). If the spiral arms rotate with a constant pattern speed, systematic offsets in azimuth between age populations and the spiral arm as a function of radii are expected.

It should be noted however, that we also applied similar analyses to other spiral arms that developed at different times in this simulation as well as spiral arms in other barred spiral simulations with different initial configurations of the disc and dark matter halo. We find that all the spiral arms we analysed show very similar results to those shown in this chapter (see also Kawata *et al.*, 2012).

### 3.3.1 Pattern Speed

Here we present a method for calculating the rate at which the stellar density enhancement rotates as a function of radius i.e. the pattern speed. The pattern speeds are often measured by spectrogram analysis (e.g. Quillen *et al.*, 2011). However, we focus on the angular pattern speed of the apparent spiral feature, and in this thesis we refer to this as the pattern speed. The location of the stellar density peak is found at a range of radii for a series of snapshots. This is done by weighting the positional information of particles close to the arm by their density. First, an azimuth coordinate is chosen close to the peak as an initial guess at a given radius. Then, a suitable azimuthal range centred on the initial guess is applied to select the particles covering the whole spiral arm or bar. From the

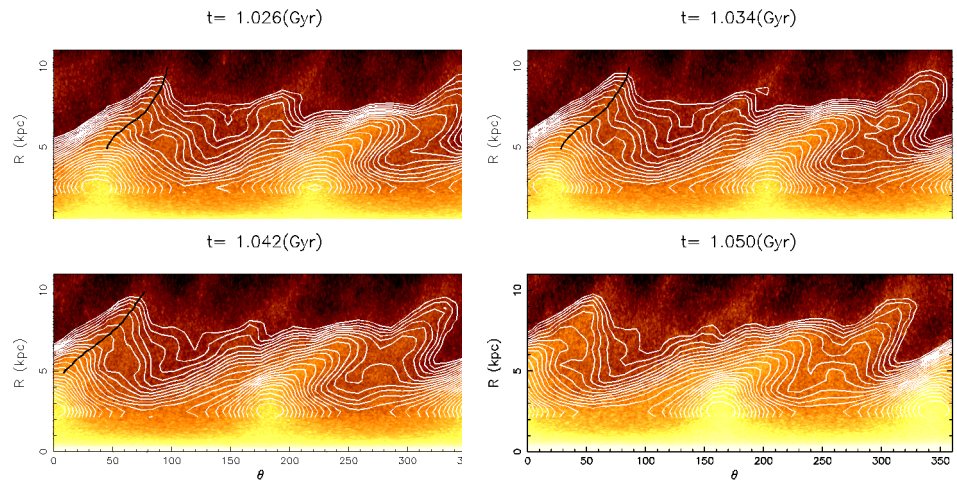


Figure 3.4: The density distribution plotted in polar coordinates. Density contours are overplotted in white to identify the highest density regions. The black line that indicates the position of the spiral arm of interest is omitted in the bottom right panel because the double peak at $R \sim 6.5$ kpc presents ambiguity for the density weighting method at this radius.

selected particles at a given radius, we calculate:

$$\overline{\theta}_{sp}(r) = \frac{\sum_i^N \rho_i \theta_i(r)}{\sum_i^N \rho_i(r)}. \tag{3.5}$$

Here, $\theta_i$ and $\rho_i$ are the azimuth angle and stellar density at the position of the $i$-th star particle. We iteratively find $\overline{\theta}_{sp}(r)$, and narrow the sampling range of $\theta$ progressively. In order to check the reliability of this method and the suitability of spiral arms, we show the density contours plotted over the density map in Fig. 3.4 and Fig. 3.6 at the early and late epoch respectively. The contours show that at some time-steps such as $t = 1.026$ Gyr and $t = 1.385$ Gyr, the spiral arm of interest $(R(\text{kpc}), \theta(\text{deg})) \sim (5, 50)$ in both Fig. 3.4 and 3.6) has a well-defined single peak, which is more suitable for tracing unambiguously. However, at time $t = 1.050$ Gyr ($t = 1.409$ Gyr) in Fig. 3.4 (Fig. 3.6), the arm develops two peaks at a radius around 6.5 kpc as it begins to break. Therefore, to remain robust, the peak tracing method is restricted to those snapshots where the azimuthal density distribution around the spiral arm is made of a single peak at each radius. The bar is unaffected by this caveat, and is traced at many snapshots.

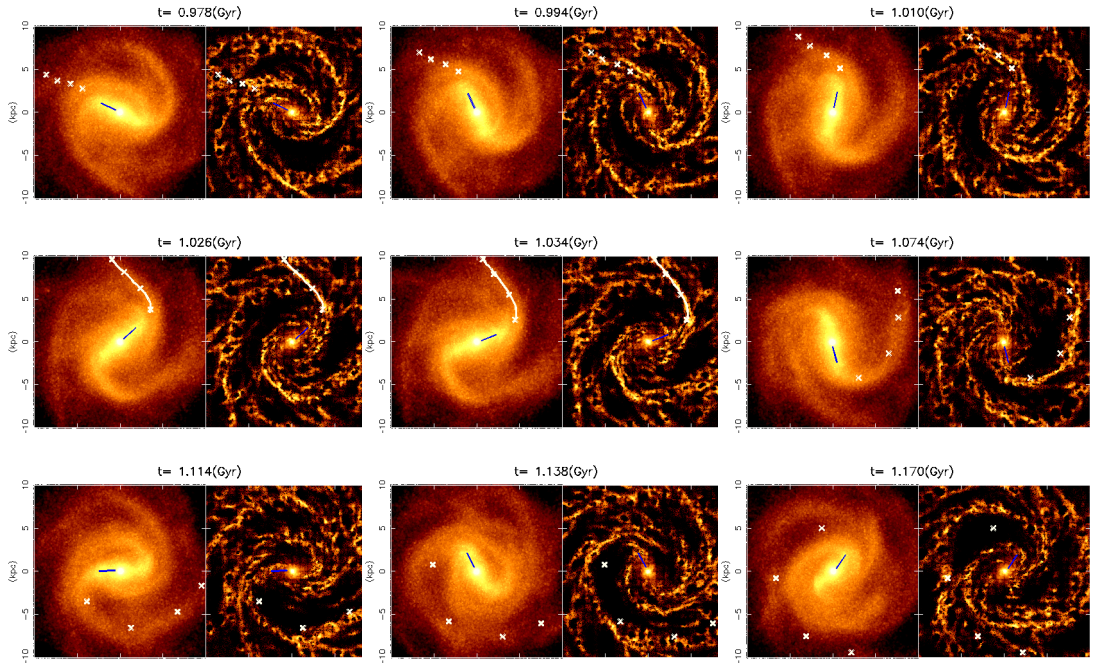


Figure 3.5: Snapshots of the stellar and gas disc from $t = 0.978$ to $t = 1.170$ Gyr. The blue lines mark out the bar and extend from $1 - 3$ kpc. The white lines mark out the position of highest density over the spiral arm found from the method described in the text, and extend from $5 - 10$ kpc. The spiral arm lines are shown at the centre and middle-left panels only, because the spiral arm in all other snapshots shown here has either not fully formed or displays double peak structures, and could not be fitted well by our method. Anchors are plotted over the spiral arm, and are rotated from the centre snapshot with the rotational velocity.

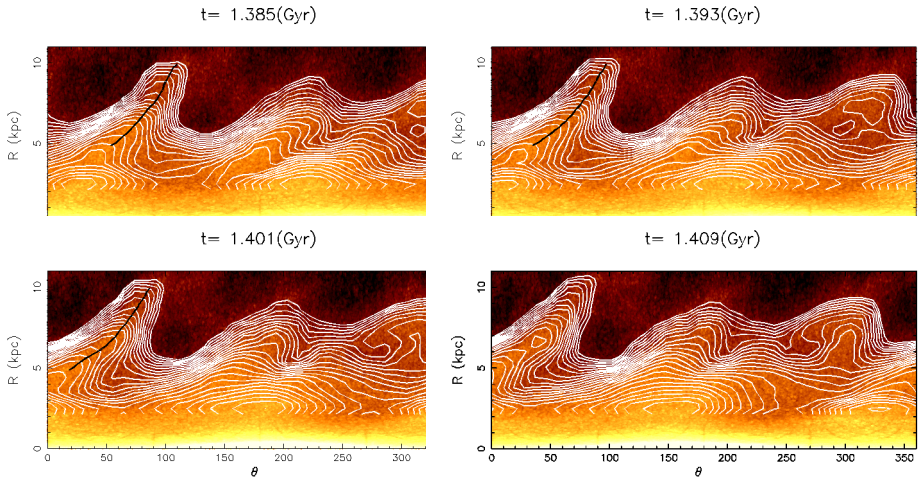


Figure 3.6: Same as Fig. 3.4, but for the late epoch (weak bar case). The black line that highlights the locus of the spiral arm is omitted in the bottom right panel owing to the double peak structure at $R \sim 6.5$ kpc.

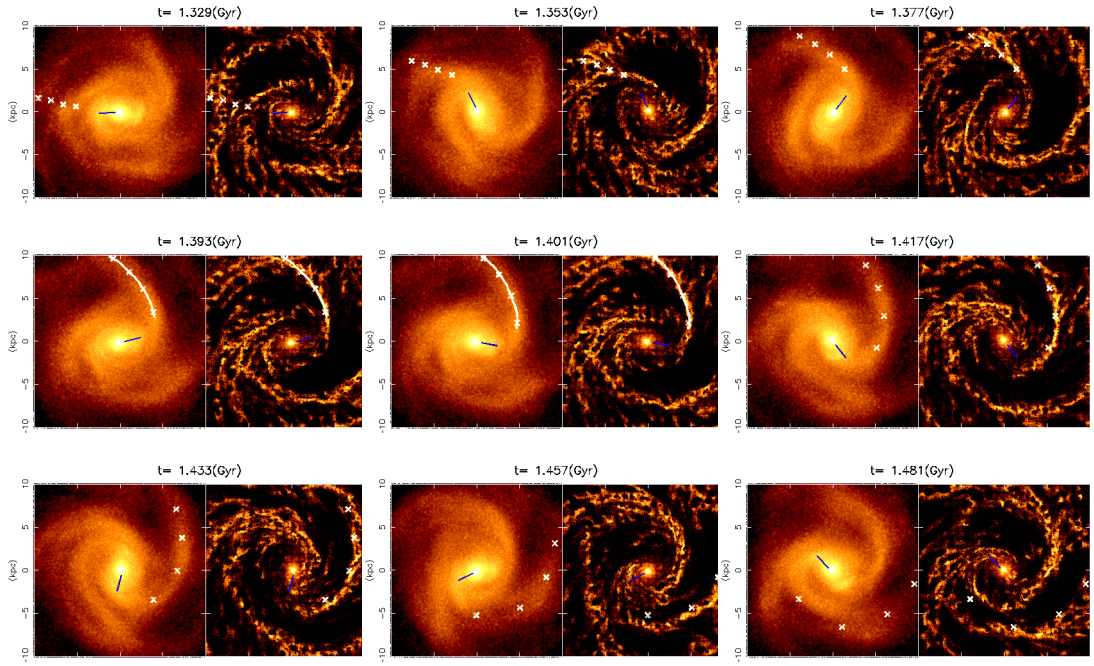


Figure 3.7: Same as Fig. 3.5, but for the late epoch (weak bar case).

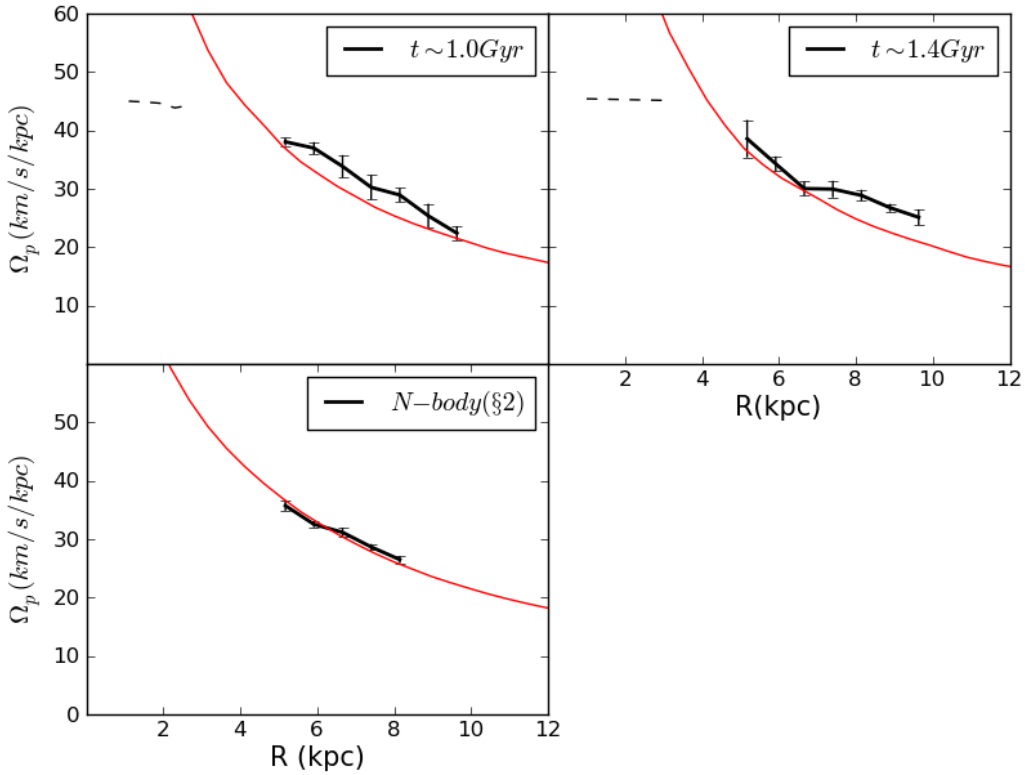


Figure 3.8: *Top row*: The bar and spiral arm pattern speed calculated for the snapshots shown in Fig. 3.5 and Fig. 3.7 respectively. In each case, the spiral arm pattern speed (solid black line) is averaged over several pattern speeds calculated at different snapshots over the course of the spiral arm's evolution. The mean angular rotational velocity is also plotted (solid red line). The bar pattern speed (dashed black line) is found to be $\sim$ 45 km s$^{-1}$ kpc$^{-1}$. The spiral pattern speed exhibits a decreasing trend with radius that is similar to but slightly faster than the mean angular rotational velocity. *Bottom-left panel*: The spiral arm pattern speed (black line) of the simulated galaxy presented in §2 and the mean angular rotational velocity at the corresponding time (red line). This galaxy has no bar.

The peak density of the spiral arm ($5 < R < 10$ kpc) and the bar ($1 < R < 3$ kpc) is shown in Fig. 3.5 and Fig. 3.7 for the early and late epoch respectively. For clarity, anchors (marked by crosses) are placed at four radii spread over the above radial range of the spiral arm. Their positions are initially selected at $t = 1.034$ Gyr and $t = 1.393$ Gyr (early and late epoch respectively) according to the spiral arm peak line traced at that time-step. Their positions at other time-steps are calculated by rotating the anchors with mean rotational velocity at the radius at which the anchors are located. The gas maps (right panels of Figs. 3.5 and 3.7) give some indication to how the spiral arm evolves during the formation stage. For example, in Fig. 3.7, at $t = 1.353$ Gyr, there appear to be two gas arms in the outer radii, one of which is marked by the anchor points. This arm seems to originate from a previously wound up arm that merges with another arm to form the spiral arm for which we trace the peak density at $t = 1.393$ Gyr. The anchors plotted on the star and gas maps clearly show that the apparent spiral arm follows a shearing pattern speed close to the mean rotation of star particles, and helps to define the time of formation, $t_f \sim 0.994$ Gyr and destruction, $t_d \sim 1.170$ Gyr for the early epoch. This gives a lifetime of $\tau \sim 180$ Myr. For the late epoch, the formation time, $t_f \sim 1.353$ Gyr and destruction time, $t_d \sim 1.481$ Gyr, give a lifetime of $\tau \sim 130$ Myr. Both of these spiral arm lifetimes are shorter than the orbital period at the 7.5 kpc radius ($t_{7.5} \sim 250$ Myr).

We calculate the pattern speed and mean rotational velocity at the early epoch, when the bar is relatively strong. The error bars for the pattern speed are calculated from a bootstrap technique: a random 50% of the total number of particles are chosen for the spiral arm peak trace, which is done several times at each time-step. Several pattern speed values are then calculated at each radial point, and the error is taken to be the standard deviation of these values. The top-left panel of Fig. 3.8 shows that the pattern speed decreases with radius, and appears to be systematically faster than the mean angular rotational velocity. For comparison with the relatively weak bar case, we calculate the pattern speed and mean rotational velocity at the late epoch, which is shown in the top-right panel of Fig. 3.8. The pattern speed appears to be similar to the mean angular rotation of star particles in the inner regions ($5 < R < 7$ kpc), and is faster in the outer regions ($7 < R < 10$ kpc). Aside from the kink at $R \sim 6.5 - 7$ kpc, the pattern speed again appears to decrease with the radius. The flattening at

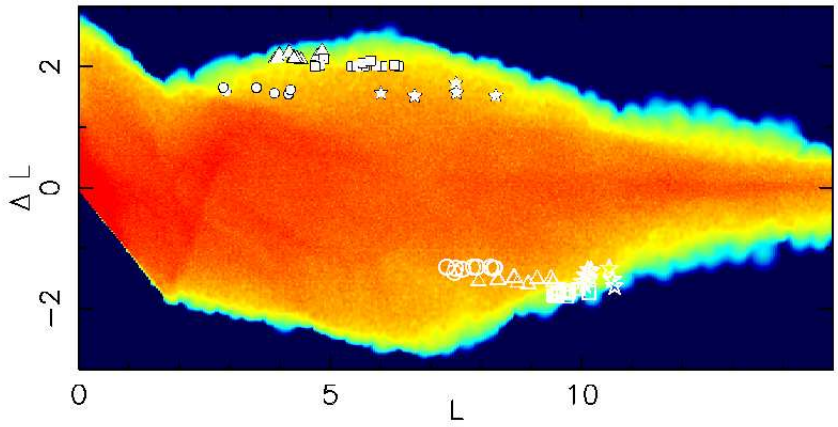


Figure 3.9: The angular momentum, $L$, at the beginning of the late epoch time period (40 Myr before $t = 1.393$ Gyr) plotted against the change in angular momentum, $\Delta L$, 80 Myr later. The smoothed colour map from low number density (dark blue) to high number density (red) incorporates all disc star particles, and shows a broad angular momentum range for migration. Selected positive (filled symbols) and negative (open symbols) extreme migrators (see text) are highlighted by circle (chosen at a radius of $\sim 6$ kpc), triangle ($\sim 7$ kpc), square ($\sim 8$ kpc) and star ($\sim 9$ kpc) symbols. Units are arbitrary.

$R \sim 6.5 - 7$ kpc is approximately the same radius at which a break is observed in the density contours over plotted in Fig. 3.6. The pattern speed of this late epoch is slower than the pattern speed of the earlier epoch when the bar is stronger. This indicates that the bar may boost the pattern speed somewhat, and cause it to become slightly faster than angular rotational velocity. Nevertheless, the anchors in Fig. 3.5 show that the spiral arm rotates in a similar way to the star particles at both epochs.

Further comparison is made with the galaxy presented in §2, which has no bar or gas component. We apply the same peak tracing technique in equation (3.5), and find the pattern speed of arms that have suitable single peaks. This is plotted in the bottom-left panel of Fig. 3.8. The calculated pattern speed follows the same trend as shown in §2, i.e. is the same as the angular rotational velocity at all radii, and therefore the spiral arm co-rotates with the star particles. Therefore, our simulation shows that the transient, winding spiral arms occur in barred galaxy simulations (see also Baba *et al.*, 2009), but the pattern speed appears to be boosted slightly out of co-rotation by the bar feature. Furthermore, although

there are only three cases studied here and the differences are relatively small, comparison between this non-barred case and the two barred cases indicates that the pattern speed becomes faster with increasing bar strength, which deserves further investigation.

### 3.3.2 Radial Migration around the spiral arm

Radial migration at the co-rotation radius has been predicted to maintain the degree of random motion of orbits i.e. not to heat them kinematically (e.g. Lynden-Bell & Kalnajs, 1972; Sellwood & Binney, 2002; Roškar *et al.*, 2008a; Sánchez-Blázquez *et al.*, 2009a; Roškar *et al.*, 2012b; Minchev & Famaey, 2010; Minchev *et al.*, 2011; Brunetti *et al.*, 2011). In §2, we showed that the spiral arms co-rotate at all radii in a non-barred pure $N$-body disc. As a result, radial migration occurs over a wide range of radii. The spiral arms focused on in this chapter rotate slightly faster than the mean rotation velocity. We examine if radial migration still occurs at all radii.

Because the results of the early epoch are the same as the late epoch, we present the particle motion from the late epoch only. First, we select a sample of particles around a given radius of our chosen arm at the $t = 1.393$ Gyr snapshot in Fig. 3.2. In order to focus on star particles that are likely affected by the spiral arm, the particle sample is selected to be within the vertical height of $|z| < 200$ pc and azimuthal width of 4 kpc centred on highest density point of the arm i.e. a given radius of the peak line shown in Fig. 3.5. The radial thickness of the sample is chosen to be 0.25 kpc to ensure that a large sample of stars of approximately the same radius are chosen.

From the selected sample of particles, we compute the angular momentum change, $\Delta L$, over a period of 80 Myrs and choose those that exhibit the largest values of $|\Delta L|$, some of which are highlighted by symbols in Fig. 3.9. As a fraction of their initial angular momentum, $L$, this can be up to as much as $|\Delta L/L| \simeq 50\%$. Note that the angular momentum exchanges in this simulation are much stronger than those shown in §2, probably because the spiral arm structure is much more prominent in this barred spiral galaxy. The radii of the guiding centres of these high $|\Delta L|$ particles highlighted in Fig. 3.9 change significantly i.e. they migrate radially. We call these strongly migrating particles "extreme migrators", and further divide them into two subcategories: positive extreme

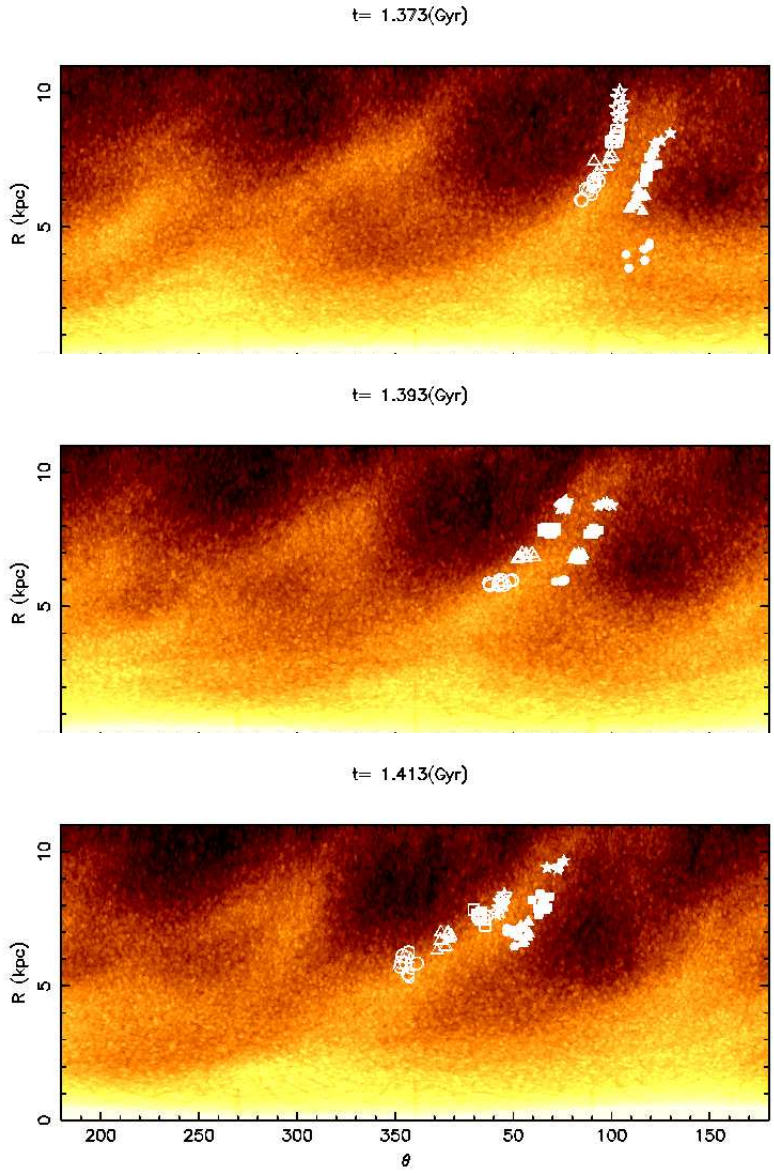


Figure 3.10: Stellar density distribution plotted in polar coordinates showing the time evolution of four sets of extreme migrators selected from particle samples around radii of 6, 7, 8 and 9 kpc at the $t = 1.393$ Gyr snapshot. The symbols correspond to those of Fig. 3.9. Azimuth ($\theta$) is expressed in degrees. The particles tend to migrate toward outer radii on the trailing edge of the spiral arm (filled symbols) and inwards on the leading edge (open symbols).

migrators and negative extreme migrators for particles that gain and lose their angular momentum in the sample respectively.

In Fig. 3.10 we show three successive snapshots during the migration period of the four extreme migrator samples highlighted in Fig. 3.9, each selected around radii of 6, 7, 8 and 9 kpc (positive and negative migrators are denoted by filled and open symbols respectively, where each type of symbol corresponds to a specific selection radius of a sample): 20 Myr before selection (top panel), at selection (middle panel) and 20 Myr after selection (bottom panel). The density snapshots for the stellar component are coordinate transformed from cartesian to polar in order to make the radial motion of the selected star particles with respect to the arm clearer. The positive migrators are always seen on the trailing side of the spiral arm and migrate towards the outer radii. They are trapped by the potential of the spiral arm, which accelerates them. During migration to outer radii, instead of passing through the spiral arm they remain in the vicinity of the arm on the trailing side. Therefore, they continue to be accelerated until the spiral arm is disrupted. The negative migrators are particles that migrate towards the inner radii on the leading side of the spiral arm. They are decelerated as they become caught in the potential of the spiral arm, and they continue to decelerate on the leading side, again until the spiral arm is disrupted. This illustrates the different systematic motion that occurs on each side of the spiral arm, which is reminiscent of the behaviour found in §2.

The same behaviour is observed at the early epoch as well. It is remarkable that although the spiral arm at the early epoch is systematically faster than the mean rotation velocity, we still observe these systematic migrations of star particles. This is probably because the pattern speed is not too different from the mean rotation velocity, and some star particles could be in a particular phase of their epicycle motion such that they are ripe for migration. Further studies of the orbits of these migrators are required, and will be studied in §5.

Fig. 3.6 shows that the spiral arm is not always a strong single peak structure, owing to the winding and breaking of the spiral arm as it begins to disappear. The evolving structure of the spiral arm may affect the degree of radial migration that occurs over the stages of evolution that span from formation to destruction. Therefore, we select a new sample of stars over the whole spiral arm ($5 - 10$ kpc radius) within 2 kpc in the azimuthal direction from the expected arm position

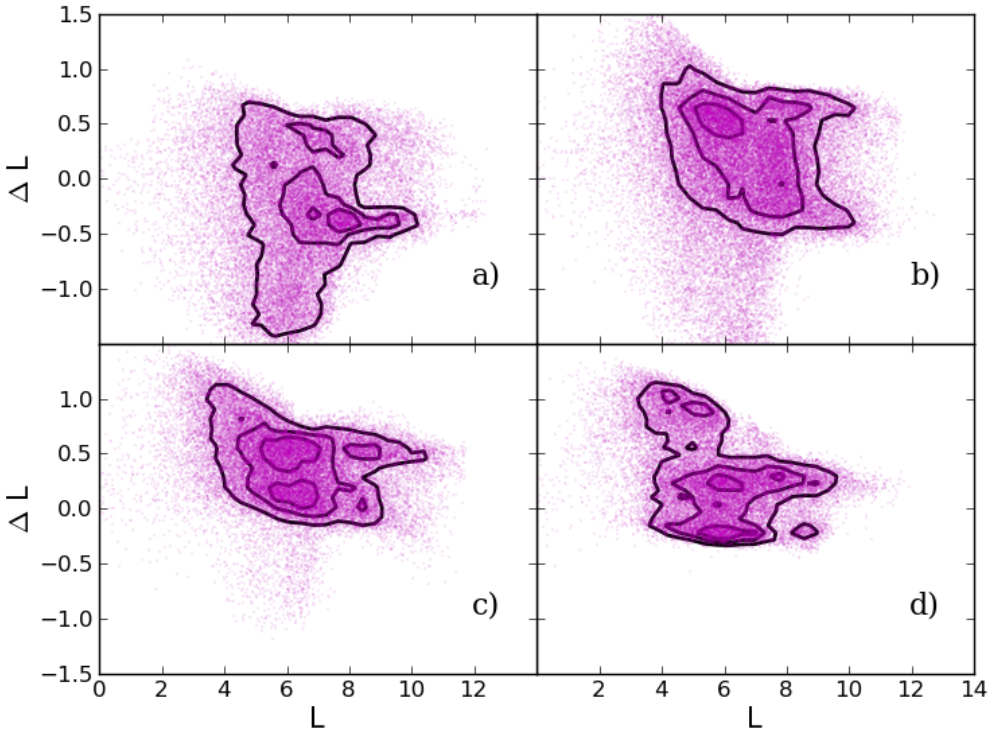


Figure 3.11: Initial angular momentum, $L$, as a function of the change in angular momentum, $\Delta L$, within a 40 Myr window for samples of star particles located around the spiral arm of the early epoch. Iso-contours indicate the 25%, 50% and 75% levels of number density. Each panel represents a stage of the spiral arm lifetime. From a) to d): formation (centred on $t = 0.994$ Gyr); fully formed single peak spiral arm ($t = 1.034$ Gyr); double peak spiral arm ($t = 1.074$ Gyr); breaking ($t = 1.114$ Gyr). The strongest migrations occurs at the stage when the arm is fully formed and single peaked (second panel). At later stages, the migration is less.

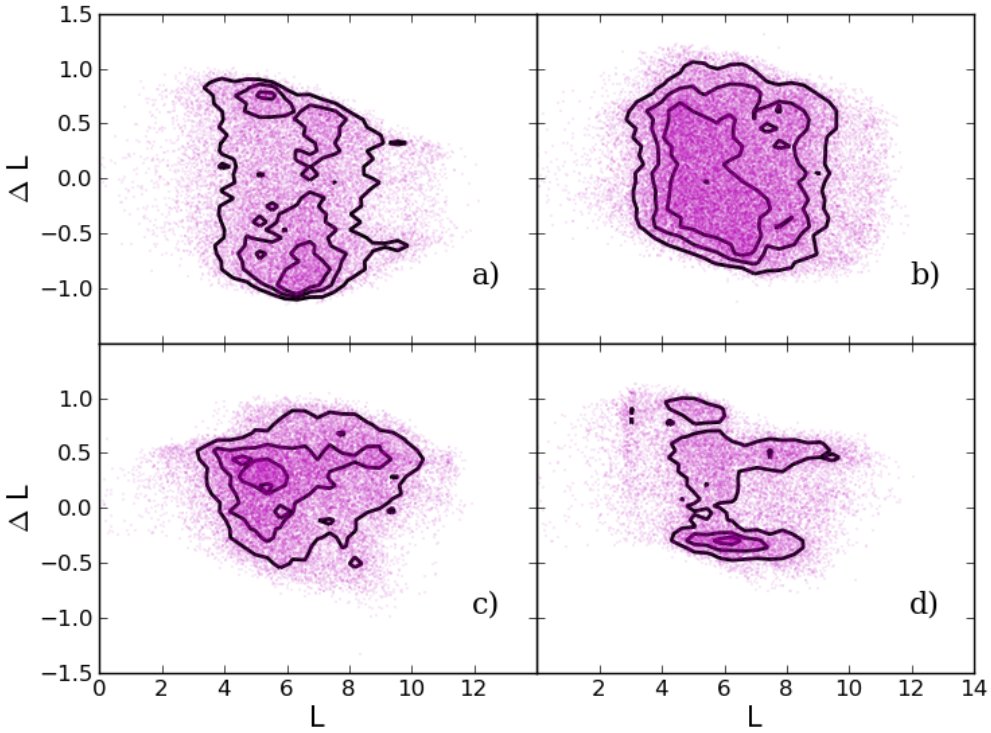


Figure 3.12: The same as Fig. 3.11, but at the late epoch of the weak bar. Each panel represents a stage of the spiral arm lifetime. From a) to d): formation ($t = 1.353$ Gyr); fully formed single peak spiral arm ($t = 1.393$ Gyr); double peak spiral arm ($t = 1.433$ Gyr); breaking ($t = 1.473$ Gyr). The trend is similar to that seen in the early epoch, but without the feature exhibiting large changes in angular momentum at lower initial angular momentum (seen in Fig. 3.11), which are induced by the strong bar.

if the arm co-rotates with star particles around $t = 1.034$ Gyr and $t = 1.393$ Gyr i.e. the positions of the anchors shown in Figs. 3.5 and 3.7. All selected particles are in the plane of the disc ($|z| < 200$ pc) as before. This is done at the four stages of the spiral arm's evolution: formation, single peak, double peak and finally destruction. In each case, the window of migration is 40 Myr, centred at each of these stages, which in total spans the lifetime of the spiral arm ($\sim$ 180 and 130 Myr for early and late epoch respectively).

The samples selected at the early epoch are plotted in the $L - \Delta L$ plane in Fig. 3.11. The largest migration occurs around the single peak stage when the arm is fully formed, and less migration occurs after this time when the double

peak at $R \sim 6.5$ kpc develops. However, there appears to be a lot of negative migration at the stage of formation. This may be due to the tightly wound arm seen in the $t = 0.978$ Gyr and $t = 0.994$ Gyr panels in Fig. 3.5. As seen from the anchor points, we sample the leading side of this arm and hence negative migrations are expected. There is also large migration present at low $L$, owing to the stronger bar at this early epoch. This procedure is repeated for the late epoch, and shown in Fig. 3.12. The same conclusions can be drawn for this weak bar case. As expected, the most migration occurs at the single peak stage when the arm is fully formed. At both epochs, significant migration occurs over a large range of radii. Furthermore, many panels show an obvious "two-pronged" structure in the $L-$direction, one at positive $\Delta L$ and the other at negative $\Delta L$. This is a clear indication that radial migration occurs at a wide range of radii. The horizontal features are likely to be caused by a maximum $|\Delta L|$ in this short time period for migrating star particles along spiral arms.

### 3.3.3 Angular momentum and energy evolution

In this section, we focus on the angular momentum-energy evolution at the late epoch only (that of the earlier epoch is the same). The orbital energy of a star particle can be affected by the gain and loss of angular momentum associated with radial migration. As in §2 and following Sellwood & Binney (2002), we calculate the energy, $E$, and angular momentum, $L$, of the extreme migrators in Fig. 3.10 at 20 Myr before and after the time-step at which they were selected (the top and bottom panels in Fig. 3.10). We call these two time-steps the "initial" and "final" time-steps respectively. In Fig. 3.13 we show the position of the extreme migrators at the initial (filled symbols) and final (open symbols) time-steps for all migrator samples in Fig. 3.9. The solid black line indicates the $L$ and $E$ expected for a pure circular orbit at each radius. This represents the minimum energy which a star particle can have at a given angular momentum. We see that the positive migrators (top panel) and negative migrators (bottom panel) move along the circular orbit curve in opposite directions to each other. Because they keep close to the circular orbit curve after migration, their orbits gain (or lose) little random energy and are not scattered into higher energy orbits (Sellwood & Binney, 2002). In other words, their kinematically cool orbits are largely preserved.

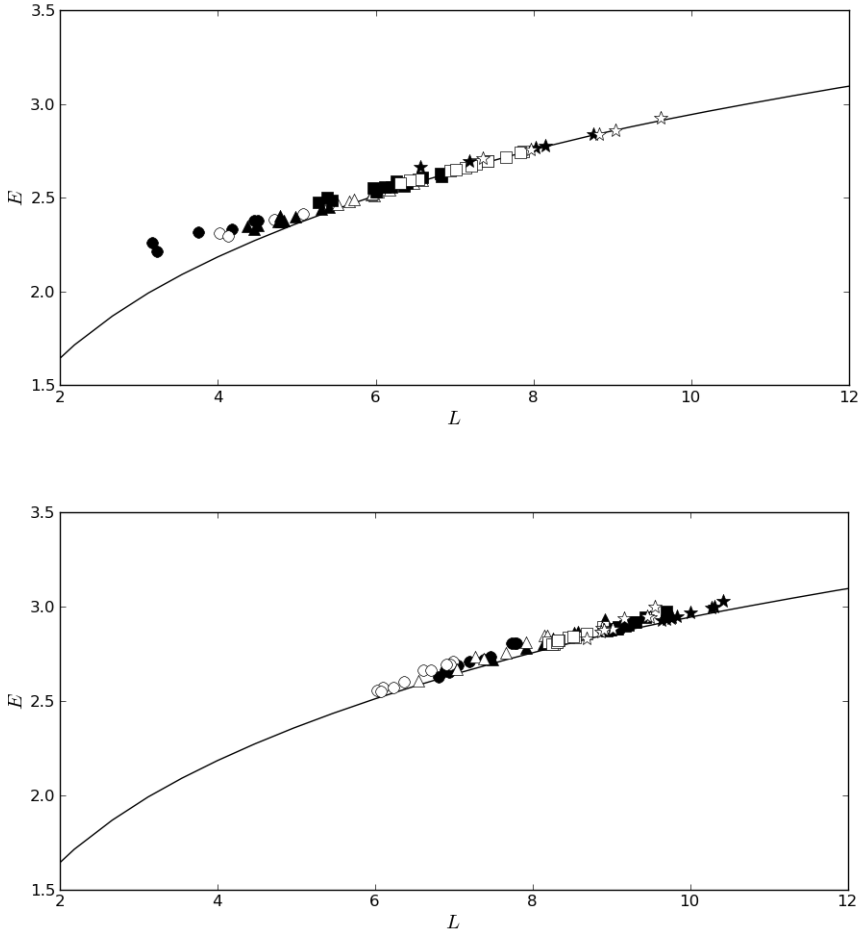


Figure 3.13: The energy, $E$, and angular momentum, $L$, distribution of the extreme migrators in Fig. 3.10 at 20 Myr before (filled symbols) and 20 Myr after (open symbols) the time-step at which they were selected. Each symbol represents a specific radius of selection corresponding to Fig. 3.10. The top (bottom) panel shows the results of the migrators that moved toward the outer (inner) radii. The solid black line indicates the circular orbit. Units are arbitrary.

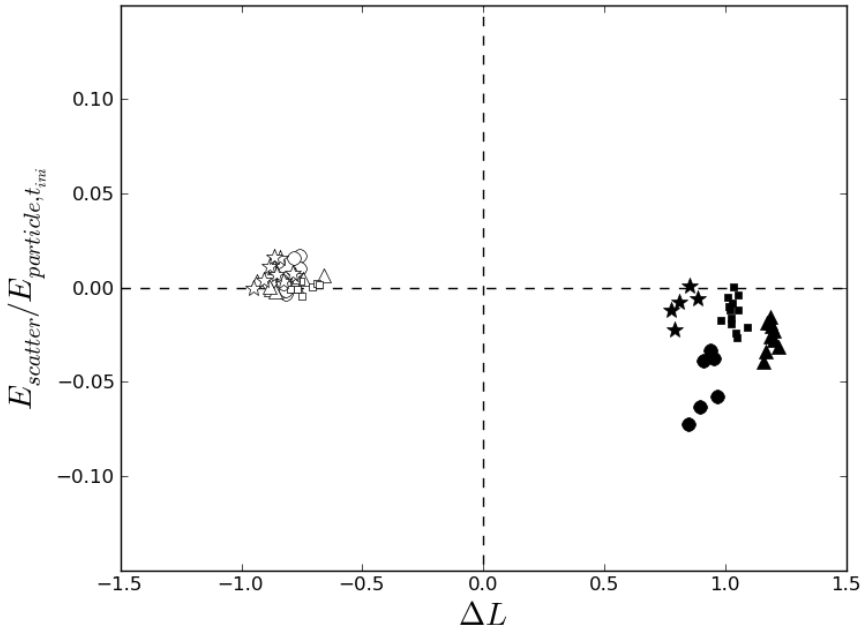


Figure 3.14: The groups of migrators shown in Fig. 3.13 are plotted here in the $\Delta L$ - $E_{scatter}/E_{particle,t_{ini}}$ plane, where $E_{scatter}$ is the change in the quantity defined by $E_{particle,t} - E_{circ}$ between the initial and final time. $E_{particle,t}$ is the total particle energy at a given time and $E_{circ}$ is the energy of a test particle of circular orbit for the given angular momentum (i.e. the minimum orbital energy allowed). $E_{scatter}/E_{particle,t_{ini}}$ tells us how much the star particle has gained or lost random energy as a fraction of the initial particle energy during the migration process. We can see the positive (filled symbols) and negative (open symbols) migrators lie in distinct groups, where the former are *cooled* and the latter *heated*, but only by a small amount.

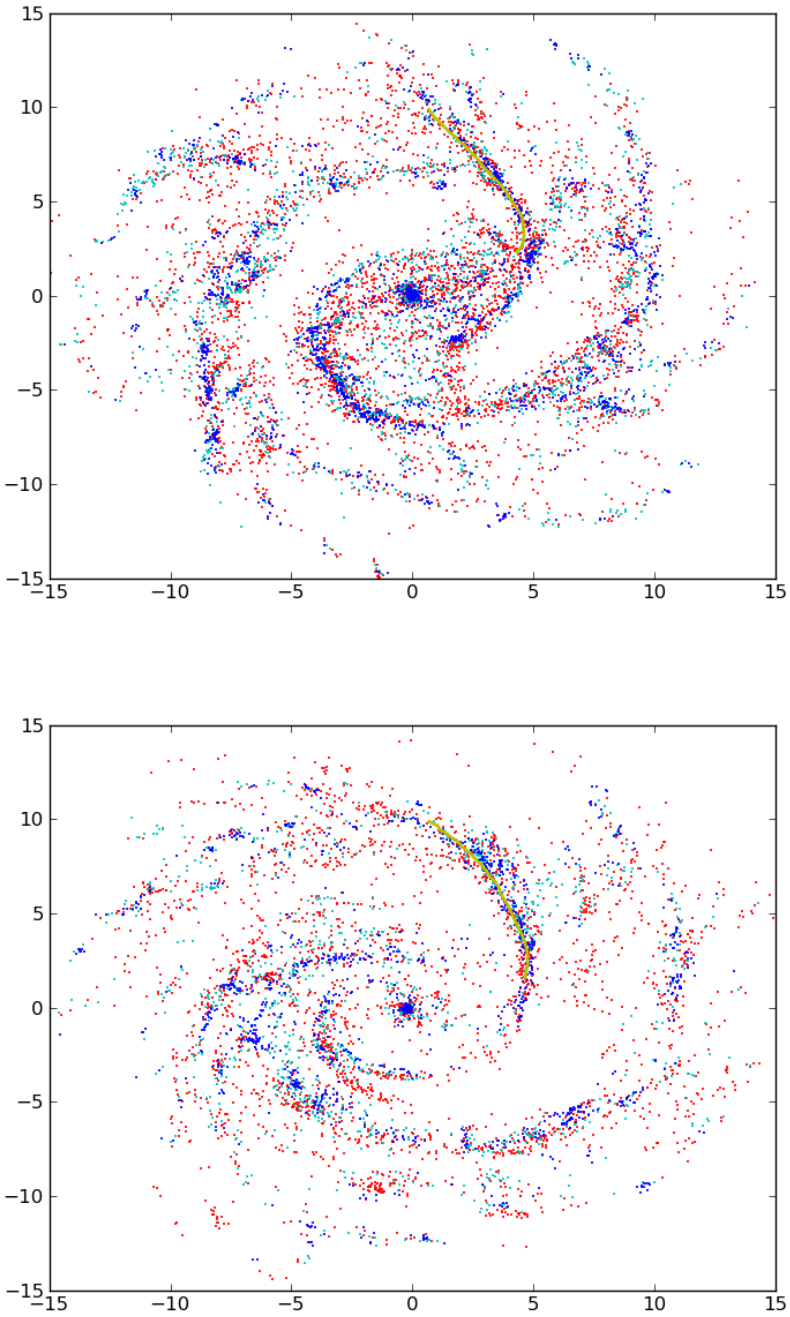


Figure 3.15: Snapshots of the disc at $t = 1.034$ Gyr (*top*) and $t = 1.393$ Gyr (*bottom*), showing only star particles of age: $t < 50$ Myr (blue); $50 < t < 100$ Myr (cyan); $100 < t < 200$ Myr (red). The yellow line indicates the stellar peak density of the spiral arm.

To quantify this, Fig. 3.14 shows the amount of non-circular kinetic energy change (normalised to total initial energy) over the migration period plotted as a function of the amount of angular momentum change that they have undergone. Each migrator shows very little scatter during migration. It appears that each type of migrator is grouped separately, such that the positive migrators become slightly cooler, and negative migrators become slightly hotter[1] (see also Roškar *et al.*, 2012b, and §2), although this is less than a few percent of the initial energy.

### 3.3.4 Stellar population distribution around spiral arms

Because we have a gas component forming stars, we can now make a further test of whether the spiral arms are long-lived density waves as in spiral density wave theory. The long-lived, stationary wave theory should predict clear azimuthal offsets between young star particles of different ages, and molecular clouds (MCs) that are the seeds of star formation. The single constant pattern speed predicted by this theory would mean that inside the co-rotation radius, gas and stars would be moving faster than the spiral arm feature. Then gas flows into the spiral arm from behind the arm, and is compressed into MCs. This leads to star formation. Newly born stars will then flow through and begin to overtake the arm feature as they age, which naturally leads to a temporal gradient over the spiral arm. Outside of co-rotation, where material moves slower than the spiral arm feature, the opposite temporal gradient is expected. Therefore, if we group star particles around the spiral arm into age bins, and examine their azimuthal distribution there should be apparent azimuthal offsets among star particles of different ages, which would become clearer further from co-rotation. Dobbs & Bonnell (2008) and Dobbs & Pringle (2010) performed a similar test by embedding a rigidly rotating spiral potential with a constant pattern speed.

We also analyse the azimuthal distribution of stellar ages found in our simulated galaxy. Note that although Dobbs & Pringle (2010) show similar analysis, they do not explicitly include radiative cooling or star formation, but assume an isothermal gas. They track the orbit of gas particles which have experienced the high density state, after which time the gas particles are tracked as very young stars ($2 - 100$ Myr), assuming the gas and stellar dynamics are similar in this

[1]This is different from the global heating caused by scattering from spiral arms (see Fujii *et al.*, 2011).

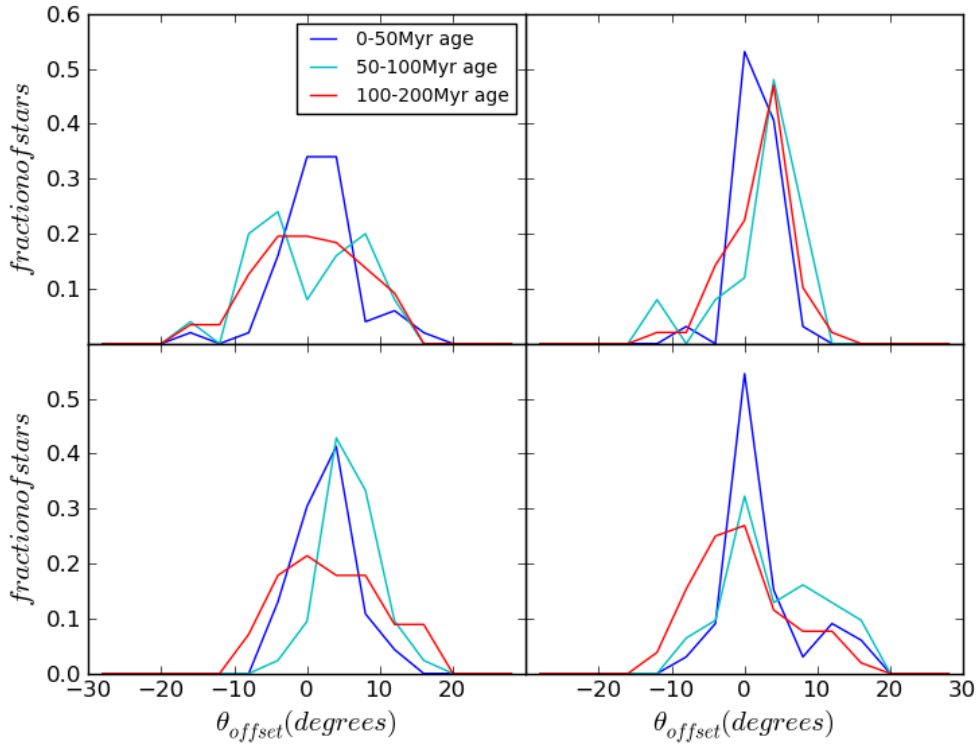


Figure 3.16: Histogram of star particles at both early (top row) and late (bottom row) epochs. Particle samples are selected in the 6 to 7 kpc (left column) and 7.5 to 8.5 kpc (right column) radial range. Particles are binned according to their azimuthal offset from the peak density line shown in Fig. 3.15. Negative offsets refer to the trailing side of the arm, and positive offsets refer to the leading side. No systematic offset of stellar ages is apparent.

short period. Therefore, our study is different and complementary. Fig. 3.15 shows the distribution of a young population, $t_{age} < 50$ Myr (blue); an intermediate population, $50 < t_{age} < 100$ Myr (cyan); and a relatively older population, $100 < t_{age} < 200$ Myr (red). The snapshots shown is at $t = 1.034$ Gyr (top) and $t = 1.393$ (bottom) Gyr.

Inspection by eye indicates that there is no obvious offset between the tracers. To quantify this, we select two samples of star particles: one between 6 and 7 kpc radius and the other between 7.5 and 8.5 kpc radius, each within $\pm$ 2 kpc from the peak density of the spiral arm in the azimuthal direction. The angular offset distribution from the peak density for selected star particles of different ages are shown in Fig. 3.16, where the abscissa is azimuth offset angle and the ordinate is the number fraction of star particles. A negative angular offset is taken to mean a position behind the spiral arm, and a positive one means a position in front of the spiral arm. In both cases, no significant offset is seen between star particles of different ages. Neither case finds any systematic spatial offset that would be present if the arm were a Lin-Shu type density wave. It is clear that the distribution broadens for older star particles, although the peak position remains about the same. Our results are qualitatively similar to the results of the flocculent and interacting galaxy cases in Dobbs & Pringle (2010)[1]. As we expect, it is completely different from their fixed pattern speed case.

## 3.4 Conclusions

In this chapter, we have presented three dimensional $N$-body/SPH simulations of an isolated barred spiral galaxy, and performed a dynamical analysis of the spiral arms and particles around the spiral arms, tracing their evolution and the azimuthal distribution of star particles as a function of age. We come to the following conclusions:

(i) We find in our simulation that spiral arms are transient recurring features: we observe the continuous disappearance of spiral arms and the reappearance of new ones. This transient nature has always been found in numerical simulations.

[1]Their barred galaxy case focuses on the stellar distribution around the bar not the spiral arm, and is therefore not relevant to our discussion in this section.

(ii) Our result shows that the pattern speed is decreasing with radius overall, and may be affected by the presence of a bar. The un-barred case shows convincing co-rotation with the mean rotational velocity. The weak bar case shows slight departure from mean rotational velocity at larger radii, and the stronger bar case shows a systematically faster pattern speed overall. Although we only studied three arms in this detail, this indicates that the bar may boost the pattern speed, and this deserves further study.

(iii) It is demonstrated that despite the differences in pattern speed, each case exhibits the same systematic motion found in §2, that leads to strong efficient migration.

(iv) The spiral arms analysed are shown to develop a double peak substructure as it winds and evolves. The break occurs at the same radius at which the pattern speed kinks. The amount of radial migration is weaker at this stage and subsequent stages of the spiral arm evolution, although it still occurs until the spiral arm disappears. This is valid for both the weak and strong bar cases. It is worth to note that the double peak structure occurring around the break radius may be interpreted as two overlapping wave modes moving away from one another. However, we cannot confirm nor reject this idea from the results of this study. Further detailed studies are required to test whether or not the spiral arm is a linear superposition of multiple wave modes.

(v) We quantify the amount of heating or cooling of each migrator in terms of random energy gained or lost over the process of migration. It is evident that each positive migrator loses some random energy (cools), while the negative migrators gain some random energy (heated). For each migrator, it is seen that the amount of heating/cooling is less than a percent of the total energy of a given particle. Hence this migration does not contribute significantly to disc heating. However the cause of this heating and cooling is not identified (see also Roškar *et al.*, 2012b), and is worthy of further study.

(vi) We find no offset between the distribution of young star particles ($< 200$ Myr) of different ages around the spiral arm at two different radii. This

is consistent with recent observations of extra-galaxies (Foyle *et al.*, 2011; Ferreras *et al.*, 2012).

This study is a follow-up study to our original work presented in §2, which focused on pure $N$-body simulations of a galaxy with no bar. As in that study, we have not addressed the mechanism of formation of the spiral arm features thoroughly nor their destruction, although we gain an insight into how the arm develops a double peak structure and then breaks. We note that the spiral arm features here are slightly longer-lived than our $N$-body galaxy, which could be because the bar is a powerful driver of spiral structure (e.g. Sparke & Sellwood, 1987; Salo *et al.*, 2010), and may help to maintain the feature for longer (e.g. Donner & Thomasson, 1994; Binney & Tremaine, 2008; Baba *et al.*, 2009; Quillen *et al.*, 2011). We also note that bars can be even stronger than the strong bar case presented here. It would be interesting to study the effects of spiral arm pattern speed on radial migration when the bar is much more prominent.

Again, we find that the spiral arms in this $N$-body/SPH barred galaxy are not consistent with the long-lived, rigidly rotating spiral arms of a classical spiral density wave theory. On the contrary, the spiral arm pattern speed decreases with radius and is similar to but slightly faster than the mean angular rotation velocity of the star particles. However, significant radial migration over a wide range of radii is repeatedly observed despite the differences in pattern speed. This suggests the existence of further criteria for radial migration, which will be studied in §5.

# Chapter 4

# Spiral arm pitch angle and galactic shear rate in N-body simulations of disc galaxies

*This chapter is based on Grand* et al. *(2013).*

## 4.1 Introduction

The morphology of spiral galaxies, as laid out in the Hubble classification (Hubble, 1926), can be broadly characterised by the tightness of spiral arm structure and the size of the central region or bulge. In this classification scheme, more tightly wound spiral arms are associated with large central mass concentrations (see §1.1). The strong correlation between central mass concentration and pitch angle predicted by modal density wave theory (e.g. Lin & Shu, 1964; Roberts *et al.*, 1975; Seiden & Gerola, 1979; Bertin *et al.*, 1989a) is in accordance with this. However, there are complications in the Hubble classification scheme insofar as that this relation was derived from optical information of galaxies only. The correlation is not observed in the near-infrared wavelengths (de Jong, 1996; Seigar & James, 1998a,b), and some observational studies in the infrared waveband highlight a difference in morphology from that seen in the optical (e.g. Block *et al.*, 1994; Thornley, 1996; Grosbol & Patsis, 1998). Moreover, the correlation between Hubble type and pitch angle has been shown to be weak (Kennicutt, 1981) and the

model predictions from density wave theory for spiral arm properties have been shown to have systematic offsets to observations (Kennicutt & Hodge, 1982).

Despite these uncertainties in the Hubble type-pitch angle relation, more recent observations have shown convincing evidence for a correlation between spiral arm pitch angle and the shear rate of differentially rotating discs of spiral galaxies. Seigar *et al.* (2005) derived shear rates from the rotation curves of a sample of several barred galaxies and used Fourier analysis to draw the spiral shape. They found evidence for the shear rate dependency of the spiral arm pitch angle. Because the rotation curve shape is determined by the mass distribution, this is essentially a correlation between the central mass concentration and spiral arm pitch angle. This survey was later extended and the conclusion strengthened by Seigar *et al.* (2006).

The shear rate-pitch angle correlation is also supported by the analytical work based on swing amplification theory (Goldreich & Lynden-Bell, 1965; Toomre, 1981) by Julian & Toomre (1966) (see also Fuchs, 2001), which calculated the spatial distribution of the response of the density of the differentially rotating stellar disc to a large perturbing mass. They showed that the density enhancement in this context is predicted to show smaller pitch angles[1] (hence a more tightly wound structure) with increasing amount of shear present.

While theoretical and observational studies provide evidence for the shear rate-pitch angle relation, it has yet to be explored in $N$-body simulations. In this chapter, we aim to study this relation by running a suite of $N$-body simulations of varying shear rates. For the first time we investigate the pitch angles of individual spiral wave mode patterns in $N$-body simulations by isolating the spiral wave mode patterns from the system using the conventional spectrogram analysis (e.g. Quillen *et al.*, 2011; Sellwood, 2012; Solway *et al.*, 2012; Minchev *et al.*, 2012b; Roškar *et al.*, 2012b) and calculating the spiral phase of the $m$-th mode. We find that the discs of higher shear rate exhibit systematically smaller pitch angles than their lower shear rate counterparts, as predicted from the theoretical studies mentioned above. We also trace the overall spiral arm feature and measure its pitch angle as a function of time. The motivation for exploring this pitch angle

[1]In this chapter, small pitch angle values correspond to tightly wound spiral arms, and large pitch angle values correspond to open spiral arms. This is different from the definition used in §1.2.2, and we use it in order to clearly compare with recent studies (e.g. Fuchs, 2001; Seigar *et al.*, 2006).

behaviour is that we and other authors have found that the pattern speed of the spiral arms in $N$-body simulations and observed galaxies decreases with radius in a similar manner to the angular rotation velocity of the disc particles (Merrifield *et al.*, 2005, 2006; Speights & Westpfahl, 2011; Wada *et al.*, 2011; Nelson *et al.*, 2012; Comparetta & Quillen, 2012; Baba *et al.*, 2013, and §2, 3). Because the pattern speed decreases in this way, the pitch angle decreases with time and leads to transient and recurrent spiral arm features that are seen in many simulations (e.g. Sellwood, 2010, 2011, and references therein). The evolving nature of the pitch angle of winding spiral arm features can be compared to the observational work of Seigar *et al.* (2006) which measures the pitch angle and shear rate of many spiral galaxies and reveals several different observed pitch angles for a given shear rate.

This chapter is organised as follows. The simulations are described in §4.2, the analysis techniques laid out in §4.3 and the results are described in §4.4 and §4.5 in which we also explore some of the other parameter space apart from shear rate. The discussion is presented in §4.6, followed by the conclusions in §4.7.

## 4.2 Simulations

The simulations in this chapter are performed with a hierarchical Tree N-body code GCD+ (Kawata & Gibson, 2003; Kawata *et al.*, 2013b). We run a suite of simulations, each of which consists of a spherical static dark matter halo (and a spherical static stellar bulge component in some cases) and a live stellar disc. The halo and bulge are static rather than live in order to facilitate greater control of the experimental scenarios. A live halo/bulge component will complicate the evolution of the stellar disc with effects such as scattering and heating, and may even act as large perturbing masses that greatly disturb the disc if the mass resolution for the dark matter is too small (D'Onghia *et al.*, 2013). These are unwanted effects, and because the focus of this study is on the stellar disc component only, we have elected to model the external components with static potentials. The dark matter halo is set up following the same density profile in §3.2 assuming the same cosmological parameters.

The spherical static stellar bulge component is modelled by the Hernquist profile (Hernquist, 1990), which is described by:

| Simulation | $M_d(\times 10^{10}\mathrm{M}_\odot)$ | $R_d$(kpc) | $M_{vir}(\times 10^{12}\mathrm{M}_\odot)$ | $c$ | $\zeta$ | N ($\times 10^6$) | $\epsilon$ (pc) | $M_b(\times 10^{10}\mathrm{M}_\odot)$ | $b$ |
|---|---|---|---|---|---|---|---|---|---|
| F | 5.0 | 3.5 | 1.5 | 15 | 0.30 | 1 | 340 | 4.0 | 0.5 |
| Fa | 5.0 | 3.5 | 1.5 | 15 | 0.30 | 5 | 340 | 4.0 | 0.5 |
| Fb | 5.0 | 3.5 | 1.5 | 15 | 0.30 | 5 | 200 | 4.0 | 0.5 |
| Fc | 5.0 | 3.5 | 1.5 | 15 | 0.30 | 5 | 90 | 4.0 | 0.5 |
| F2 | 2.5 | 3.5 | 1.5 | 15 | 0.17 | 1 | 270 | 4.0 | 0.5 |
| F3 | 5.0 | 3.5 | 0.75 | 15 | 0.37 | 1 | 340 | 2.5 | 0.5 |
| K | 5.0 | 3.5 | 0.1 | 15 | 0.5 | 1 | 340 | 10.0 | 0.01 |
| R | 1.0 | 3.5 | 2.5 | 5 | 0.28 | 1 | 200 | - | - |
| R2 | 5.0 | 3.5 | 1.5 | 20 | 0.35 | 1 | 340 | - | - |
| R3 | 5.0 | 3.5 | 2.0 | 20 | 0.30 | 1 | 340 | - | - |
| R4 | 5.0 | 3.5 | 3.0 | 10 | 0.46 | 1 | 340 | - | - |

Table 4.1: Table of simulation parameters. Column (1) simulation name (2) disc mass (3) scale length (4) virial mass (5) NFW concentration parameter (6) disc to halo mass ratio within two scale lengths (7) number of particles (8) softening length (9) bulge mass (10) bulge compacting factor.

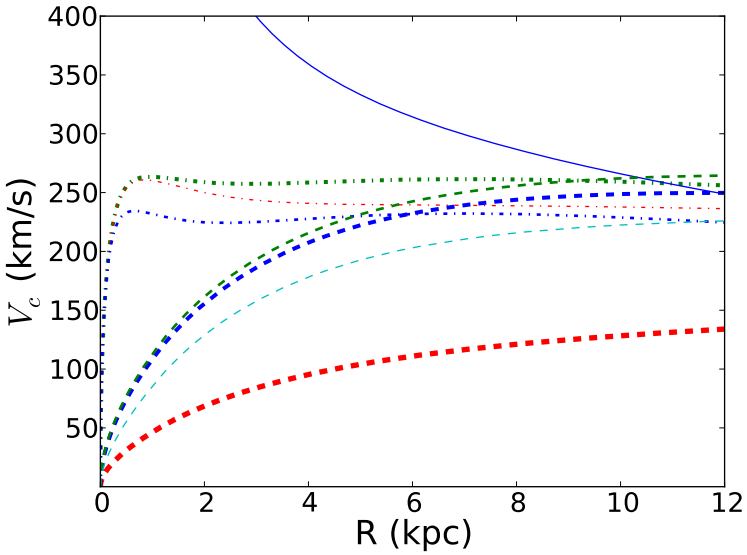


Figure 4.1: The circular velocity at $t = 0$ for simulation R (very thick dashed red), R2 (thick dashed blue), R3 (medium dashed green), R4 (thin dashed cyan), F (thick dot-dashed green), F2 (thin dot-dashed red), F3 (medium dot-dashed blue) and K (solid blue).

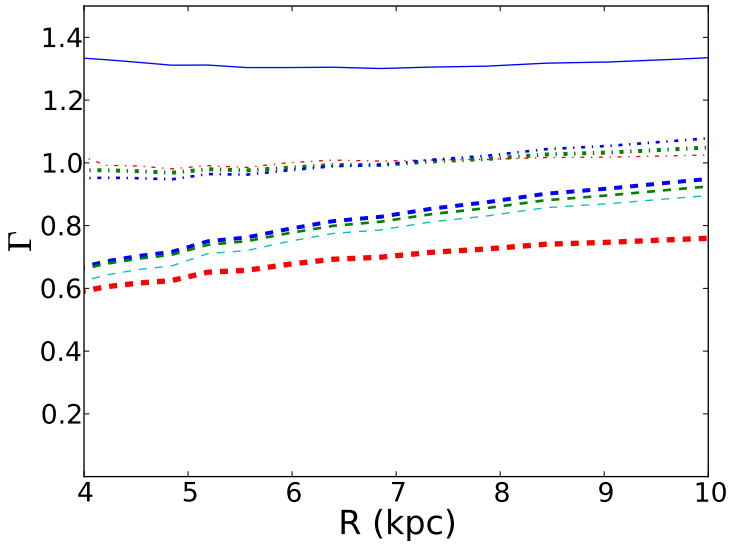


Figure 4.2: Galactic shear rate, Γ, for all simulations. Colours are the same as Fig. 4.1. Note the reduced radial range compared to Fig. 4.1.

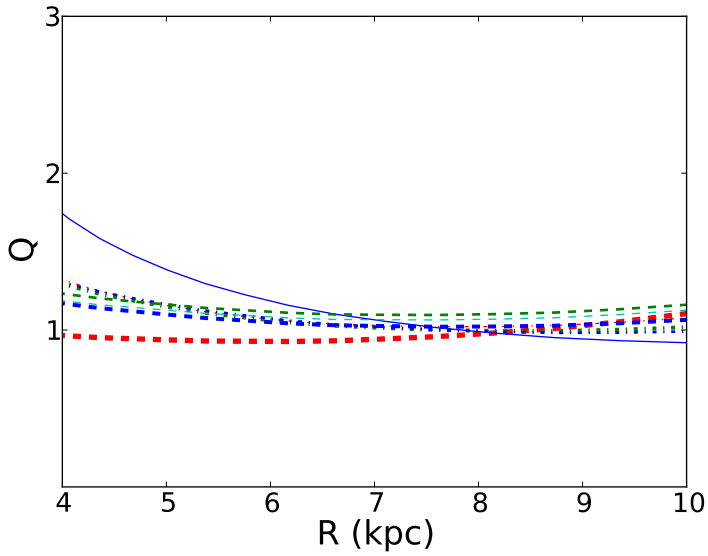


Figure 4.3: Toomre stability parameter, $Q$, at $t = 0$ for all simulations. Colours are the same as Fig. 4.1.

$$\rho_b(r) = \frac{M_b}{2\pi}\frac{a}{r}\frac{1}{(r+a)^3}, \tag{4.1}$$

where $M_b$ is the total bulge mass and $a$ is the scale length. The scale length is set to the effective radius, $R_e = 1.8153a$, which is given by the empirical relation (Shen *et al.*, 2003):

$$R_e = 4.16\left(\frac{M_b}{10^{11}\mathrm{M}_\odot}\right)\mathrm{kpc}. \tag{4.2}$$

The variation of bulge density is controlled by a compacting parameter, $b$, which modifies the scale-length through the relation $a = bR_e/1.8153$.

The stellar disc is assumed to follow the same exponential surface density profile outlined in §3.2. The fiducial number of disc particles used is $N = 1 \times 10^6$. Numbers of this order are reported to be sufficient to minimise numerical heating (Fujii *et al.*, 2011). Although larger particle numbers reduce numerical heating further, we note that the effect is always present (i.e. it does not disappear at a particular resolution), and that a compromise between parameter space and resolution must be made for suites of simulations such as the one presented in

this study.

We apply a fixed softening length, $\epsilon$, for star particles with the spline softening suggested by Price & Monaghan (2007). The softening length[1] is dependent on the particle mass, therefore the base value of $\epsilon = 340$ pc for the particle mass, $m_p = 5 \times 10^4 \mathrm{M}_\odot$ varies between simulations that have different particle masses. The model parameters for the simulations are summarised in Table. 4.1, and the rotation curves are shown in Fig. 4.1.

There are three groups of rotation curves. Simulation group R (R, R2, R3, R4) has a rising rotation curve. Simulation R is an extreme case, where we set a large halo mass with a low concentration parameter, $c$, in order to extend mass to the outer regions of the disc. Because of such a low concentration of dark matter mass in the central region, the disc mass must be lowered in order to prevent a bar from forming (Ostriker & Peebles, 1973). In this way, we avoid the added complication of the bar component and restrict the study to spiral galaxies only. Simulations R2, R3 and R4 are less extreme cases, which explore intermediate shear rates and different disc to halo mass ratios. To produce the flat (simulations F, Fa, Fb, Fc, F2 and F3) and Keplerian-like (simulation K) rotation curves, a bulge component is included. For simulation K, this is a very compact and massive bulge. Although this case is unrealistic, we include it in order to emphasise the effect of galactic shear on spiral morphology.

The radial profile of the galactic shear rate at $t = 0$, is given by:

$$\Gamma = 2A = 1 - (R/V_c)(dV_c/dR), \tag{4.3}$$

where $A$ is Oort's constant. The shear rate for each simulation is shown in Fig. 4.2. This suite of simulations represents a range of shear rates, which is the principal variable we want to investigate. However, there are other parameters that may affect the pitch angle, such as the disc-halo mass ratio, $\zeta$, softening length, $\epsilon$, and resolution. We also explore these parameters, mainly with simulation group F.

We set the initial Toomre stability parameter, $Q$, for all our simulations to

[1]It should be noted that we define the softening length at which the softening kernel function is truncated. Therefore, our softening length value is typically a factor $\sim 3$ larger than the traditional definition: to translate our softening lengths to the traditional values, our value should be divided by 3.

approximately 1 over the radial range $4 < R < 10$ kpc, which allows the spiral structure to grow[1,2] (Toomre, 1981; Sellwood, 2014). The radial dependence in shown in Fig. 4.3.

## 4.3 Method of Analysis

Here we present the analysis method of our two techniques for measuring pitch angles: mode pattern analysis and direct spiral arm peak trace method. An important difference between these techniques is that the mode pattern analysis assumes that the spiral arms are constructed by one or multiple density waves of mode, $m$, which describe patterns of $m$ spiral arms with a constant pitch angle. The direct spiral arm peak trace method does not assume any theory, but simply analyses the pitch angle of the overall spiral arm feature. The distinction between these two methods is that while both characterise the spiral arm as a logarithmic spiral of fixed pitch angle at all radii of interest, in the direct method the pitch angle and amplitude of the spiral arm changes with time. However, in the mode analysis, changes in the spiral arm (in particular the winding) may only occur through the changing *superposition* of the various mode patterns present.

Before we describe these two analysis techniques, we define the pitch angle which we will use with both. Given the positional information $(R, \theta)$ of a density enhancement, we can fit logarithmic spiral arms, described by:

$$\theta = B \ln R + C, \tag{4.4}$$

where $\theta$ is the azimuth coordinate, $R$ is the radial coordinate and $B$ and $C$ are constants. Logarithmic spirals have pitch angles, $\phi$, given by (Binney & Tremaine, 2008):

$$\tan \phi = \frac{\Delta R}{d_\theta}, \tag{4.5}$$

[1]If $Q < 1$, then violent axisymmetric instabilities of the kind described in §1.2.2 develop.

[2]Each simulation shows a rise in the radial $Q$ profile over time, owing to the heating by spiral arm structure (Fujii *et al.*, 2011).

where the distance, $d_\theta$, is the spatial distance of the density enhancement in the azimuthal direction defined as $d_\theta = R\Delta\theta$. The pitch angle of a logarithmic spiral is constant with radius. The next step is to recover the positional information $(R, \theta)$ required to apply the logarithmic chi-squared fitting using equation (4.4) and calculate the pitch angle of the fit using equation (4.5).

### 4.3.1 Mode pattern analysis method

By construction, a $m$-symmetric wave mode pattern has a constant pattern speed, $\Omega_p^m$. Therefore the shape of a wave mode pattern is time independent *i.e.* the pitch angle is constant over time. In this analysis, we focus on strong patterns because their behaviour is most evident. In order to find patterns of significant amplitude, we first search for dominant modes *i.e.* wave modes of $m$ spiral arms that exhibit large amplitudes. The amplitude of a given wave mode, $m$, is calculated from the quantities:

$$W_c^m(R,t) = \sum_i^N \cos(m\theta_i(R,t)),$$
$$W_s^m(R,t) = \sum_i^N \sin(m\theta_i(R,t)), \tag{4.6}$$

where $\theta_i$ is the azimuthal angle between the radial vector of the particle and a common reference vector. The amplitude is then calculated as:

$$A^m(R,t) = (W_c^m(R,t)^2 + W_s^m(R,t)^2)^{1/2}. \tag{4.7}$$

The mean amplitude in a radial range $4-10$ kpc is calculated using equation (4.7) for modes $m = 1-7$ over the entire 2 Gyr of the evolution for each simulation. This is shown in Fig. 4.4. In each simulation, prominent modes are identified for analysis. We aim to extract the positional information of the patterns. The adopted procedure is to compute their power spectra by taking the Fourier transform of the time sequence of each component in equation (4.6) (Quillen *et al.*, 2011):

$$\tilde{W}_c^m(R,\omega) = \int_{T_1}^{T_2} W_c^m(R,t) e^{i\omega t} h(t) dt,$$
$$\tilde{W}_s^m(R,\omega) = \int_{T_1}^{T_2} i W_s^m(R,t) e^{i\omega t} h(t) dt, \tag{4.8}$$

where $h(t)$ denotes the Hanning function used to reduce the aliasing. $T_1$ and $T_2$ denote the beginning and end of the time window of the Fourier transform. This is chosen to be at around a relatively late epoch of the simulation (when the system is more stable) and is centred around a peak of the most dominant mode present in each case. It spans $\Delta t = 256$ Myr, which is of similar order to a typical life time of a $m$-fold spiral pattern as shown in the next section.

The amplitude in each frequency as a function of radius is then calculated via:

$$A^m(R,\omega) = (\tilde{W}_c^m(R,\omega)^2 + \tilde{W}_s^m(R,\omega)^2)^{1/2}. \tag{4.9}$$

Because simulations generally possess several patterns for a given mode that can overlap in radius (e.g. see Fig. 4 of Roškar *et al.*, 2012b), care must be taken when computing the spiral phase of a pattern. In this technique each wave mode pattern is characterised by a pattern speed given by $\Omega_p^m = \omega/m$, which is *constant* over radius. Individual patterns should be selected by isolating a horizontal ridge (a single pattern speed) over a radial range where the signal significantly stands out from the noise. In each of the galaxies, we focus on the most dominant patterns and look at the three quantities, $\tilde{W}_c^m(R,\omega)$, $\tilde{W}_s^m(R,\omega)$ and $A^m(R,\omega)$ on the real and imaginary axis for each radial pixel in a ridge. We then calculate the real spiral arm phase position within the domain 0 to $2\pi$ as:

$$\theta_p(R,\omega) = \frac{\theta_{sp}^m(R,\omega)}{m} = \frac{1}{m} \arctan\left(\frac{\tilde{W}_s^m(R,\omega)}{\tilde{W}_c^m(R,\omega)}\right), \tag{4.10}$$

where $\theta_{sp}^m(R,\omega)$ is the spiral phase of the pattern at each radial bin, which is retrieved by considering only the Fourier coefficients of a single $\omega$. Because this quantity spans a domain of $2\pi m$, the spiral phase, $\theta_{sp}^m(R,\omega)$, is divided by $m$ in

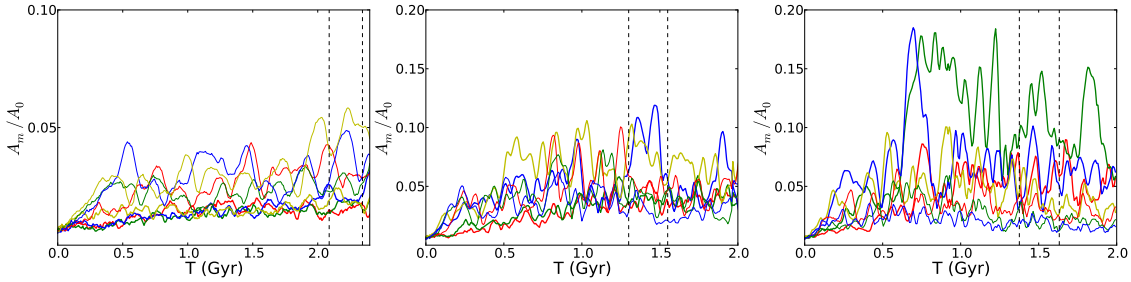


Figure 4.4: The amplitudes calculated from equation (4.7) and averaged over a radial range of 4 - 10 kpc of spiral modes $m = 1$ (thick red), 2 (thick green), 3(thick blue), 4(thick yellow), 5 (thin red) 6 (thin green), 7 (thin blue) and 8 (thin yellow) normalised to the axisymmetric $m = 0$ mode, as a function of time for simulations R (left), F (middle) and K (right). Vertical dashed lines represent the time window of a Fourier transform.

order to yield the real phase position of the wave mode pattern as a function of radius. This provides the azimuthal and radial values required for the calculation of the pitch angle using equations (4.4) and (4.5).

### 4.3.2 Direct spiral arm peak trace method

The method we use to trace the spiral arm peak position directly is a particle density weighting method, in which we select a point near the spiral arm of interest at some start radius ($\sim$ 5 kpc), define an azimuth range that encapsulates the width of the spiral arm and weight by particle density to find the peak position (see §3.3.1). This is iterated over a radial range until the spiral arm peak position is drawn out. Several spiral arms are traced over a range of snapshots between 1 and 2 Gyr of the simulation evolution. Spiral arms are only traced when they show a single density peak over azimuth for each radius in the radial range chosen for fitting. The pitch angles are then calculated using equations (4.4) and (4.5).

We remind the reader that this pitch angle is derived from the spiral arm line that traces out the overall density enhancement directly, which varies with time. This is different from the *time independent* pitch angle calculated from the positional information of the wave mode patterns derived from the power spectra in §4.3.1. The latter bears the assumption of a density wave of constant pattern speed and fixed pitch angle, whereas the former bears no assumptions at all.

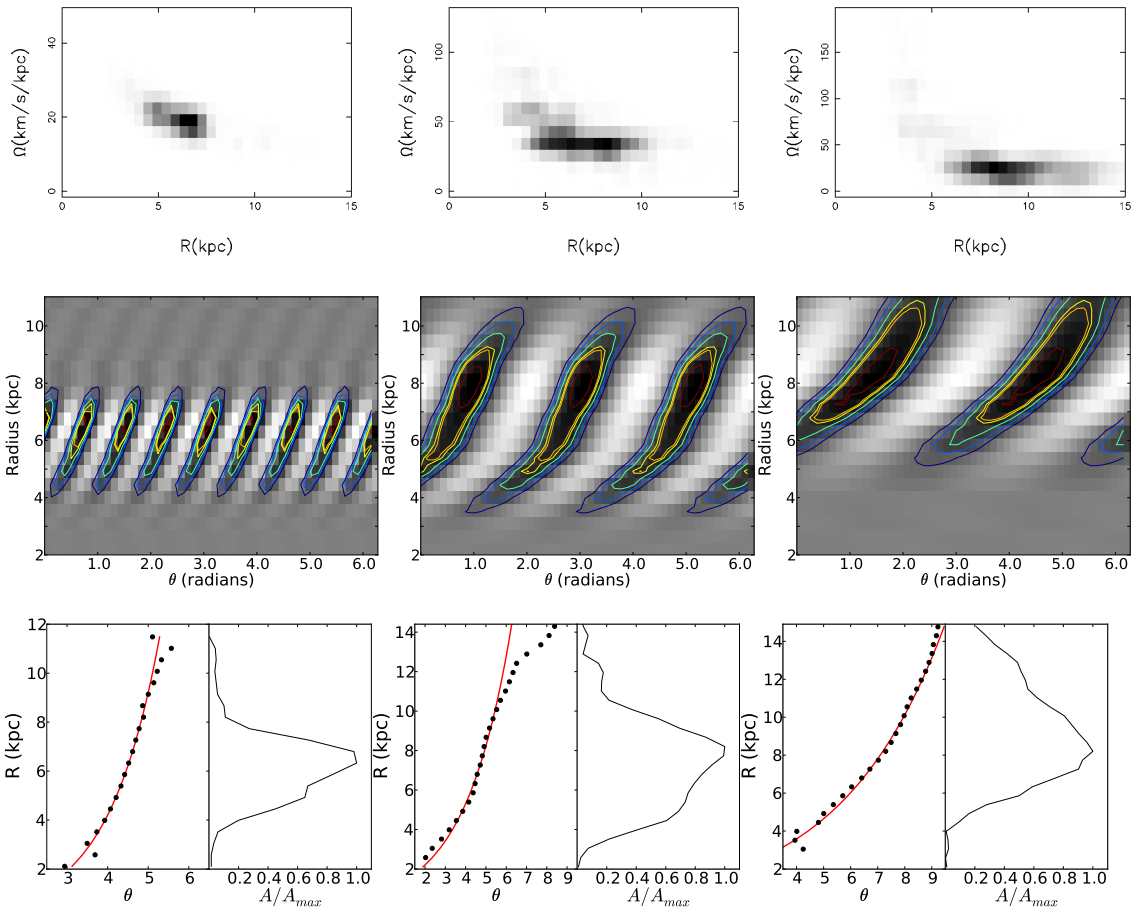


Figure 4.5: *Top row*: Power spectra calculated from equation (4.9) of simulation R for the $m = 8$ mode (left), F for the $m = 3$ mode (middle) and K for the $m = 2$ mode (right). Prominent ridges (dark pixels) span between 4 - 10 kpc in most cases. *Second row*: In polar coordinates, the density map of the dominant density wave mode pattern selected from rows of $\Omega_p^m = 18$, 30 and 24 km s$^{-1}$ kpc$^{-1}$ for simulations R, F and K respectively. White regions indicate areas of low density and black regions indicate areas of high density. Contours emphasize the highest density regions. *Bottom panels*: Dominant mode pattern positions (black points) calculated from equation (4.10) in the azimuth-radius plane for the corresponding patterns in the row above. The red lines show the lines of best fit for each pattern. The right side of each panel shows the radial amplitude profile, which is used to weight the fitting.

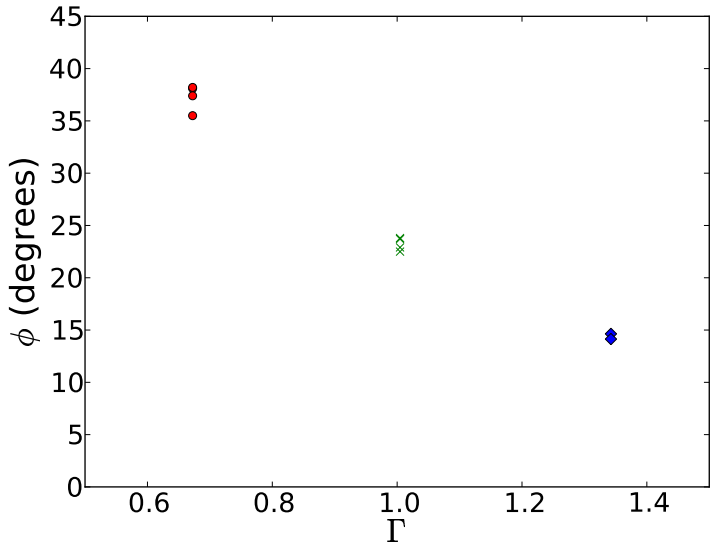


Figure 4.6: The mode pitch angles for the fiducial set of simulations, R (red circles), F (green crosses) and K (blue diamonds) as a function of shear rate.

## 4.4 Results of Fiducial Simulations

First, we show the results of three fiducial simulations, R, F and K in Table. 4.1, which represent rising, flat and decreasing rotation curves respectively. In the next section, we will show results of the other simulations in Table 4.1 to examine the robustness of the relation between pitch angle and the shear rate shown in this section.

### 4.4.1 Pitch angle of the mode patterns

The amplitude for several wave modes is shown for each of the fiducial simulations R, F and K as a function of time in Fig. 4.4. $A_m$ is normalised to the axisymmetric amplitude, $A_0$, and averaged over the radial range $4 - 10$ kpc, which defines the region of spiral structure. The strong mode patterns are isolated by the vertical dashed lines in Fig. 4.4, which define the time window for the Fourier transform. The time window used is $\Delta T = 256$ Myr. Because Fig. 4.4 shows that wave mode patterns appear to grow and fade on this time scale, this time window length enables the isolation of individual wave mode patterns. Although this results in limited frequency resolution, the positional information will be more reliable than that calculated from longer time windows, which may convolve multiple patterns

| Simulation | $\Omega_p^m$ ($\mathrm{kms^{-1}kpc^{-1}}$) | $m$ | $\phi$ (°) |
|---|---|---|---|
| F | 30 | 3 | 23.7 |
| | 42 | 3 | 22.9 |
| | 35 | 4 | 23.8 |
| | 40 | 4 | 22.5 |
| Fa | 35 | 4 | 21.2 |
| | 45 | 4 | 22.4 |
| | 28 | 4 | 23.2 |
| Fb | 37 | 4 | 21.5 |
| | 30 | 4 | 21.6 |
| | 45 | 4 | 22.2 |
| Fc | 42 | 4 | 24.1 |
| | 35 | 4 | 22.3 |
| | 35 | 5 | 24.0 |
| F2 | 40 | 7 | 24.6 |
| F3 | 25 | 3 | 26.0 |
| | 35 | 3 | 25.3 |
| K | 24 | 2 | 14.6 |
| | 12 | 2 | 14.1 |
| R | 18 | 8 | 38.2 |
| | 15 | 8 | 38.1 |
| | 20 | 7 | 37.4 |
| | 17 | 7 | 35.5 |
| R2 | 30 | 5 | 27.8 |
| | 25 | 5 | 28.7 |
| R3 | 37 | 4 | 32.5 |
| | 30 | 4 | 30.8 |
| | 45 | 4 | 35.1 |
| R4 | 35 | 3 | 36.2 |
| | 25 | 3 | 32.6 |

Table 4.2: Table of mode pitch angles calculated for each simulation from the modal analysis. Column (1) simulation name (2) pattern speed (3) wave harmonic (4) mode pattern pitch angle.

in the Fourier analysis. However, we have confirmed that the use of longer time windows has a negligible effect on the pitch angle values.

For each of our fiducial simulations, the power spectrum of the dominant mode highlighted in Fig. 4.4 is calculated from the square of the amplitude given in equation (4.9), and shown as a function of radius and the pattern speed, $\Omega_p^m = \omega/m$, in the top row of Fig. 4.5. A wave mode pattern is eligible to be analysed if its maximum power, $P_{max}^m$, is greater than 50% of the maximum power of the strongest pattern, $P_{max,strongest}^m$ (i.e. $P_{max}^m > 0.5 P_{max,strongest}^m$): all other patterns are considered subsidiary. There are typically several patterns in each simulation that fulfil this criterion.

To demonstrate the fitting process, we focus on the most dominant patterns in each of the simulations R, F and K. The density maps of these dominant wave mode patterns in real space polar coordinates are shown in the second row of Fig. 4.5. This is calculated from a sinusoidal wave of the form: $\rho = A^m(R)[\cos(m(\theta - \theta_p(R))) + \sin(m(\theta - \theta_p(R)))]$. The amplitudes and phases of each radial bin are calculated from the power spectrum in the top row of Fig. 4.5 using equations (4.9) and (4.10) respectively. Grey scale images highlight positive (black) and negative (white) normalised density, and contours emphasise the high density regions.

The bottom row of Fig. 4.5 shows the chi-squared fitting of a logarithmic function to the most dominant patterns in each simulation. The right side of each panel shows the normalised pattern amplitude as a function of radius, which reflects the relative strength of a pattern at a given radius. The logarithmic fitting is weighted by the amplitude shown in the right panel, and is represented by the red line (left panel). The fits are satisfactory for the radial ranges where the patterns are strong, and produce reliable pitch angles. The fitting of all other selected patterns for these simulations are very similar to those shown in the bottom row of Fig. 4.5. The derived pitch angles are given in Table 4.2.

Fig. 4.6 shows the pitch angle dependence with shear rate (equation 4.3). We take the shear rate value at the radius where the mode pattern in question attains maximum power. All the pitch angle values clearly show a dependence on shear rate. Simulations with higher shear rate show smaller pitch angles. This is in accordance with the qualitative trend expected of the pitch angle-shear relation from theoretical studies (e.g. Lin & Shu, 1964; Julian & Toomre, 1966). It is

interesting to note that modes of different $m$ and different pattern speeds in the same simulation (e.g. $m = 3$ and 4 in simulation F) show similar pitch angles.

### 4.4.2 Direct pitch angles of overall spiral arm features

As mentioned in §4.3.2, we trace the evolution of the overall spiral arm feature directly by use of the particle density weighting method described in §3.3.1. Fig. 4.7 demonstrates an example of the application of the arm tracing criteria to one of the spiral arms in simulation K. Because it is possible to reliably trace spiral arms which show only single peak structure for the radial range considered for fitting, we reject those snapshots that show the spiral arm with indistinct or double peak structure, which typically occurs during spiral arm formation ($t = 1.152$ Gyr in Fig. 4.7) and after the arm shows bifurcation or breaking ($t = 1.2$ Gyr in Fig. 4.7).

The results for several spiral arms in each fiducial simulation are shown in Fig. 4.8. In these plots, we take the shear rate value at the mid-point of the radial range of the traced spiral arm. It is clear that every spiral arm pitch angle decreases with time, which is consistent with winding, co-rotating spiral arms which have been reported in Wada *et al.* (2011); Baba *et al.* (2013, and §2, 3). Note that this winding is also seen in the previous formalism with mode analysis, but only through a superposition of the different mode patterns: the individual mode patterns of course are defined as being formed of fixed pattern speed, $\Omega_p^m$, at all radii of interest. The mean of the mode pattern pitch angles calculated in the previous section is highlighted by the horizontal lines in Fig. 4.8. The direct pitch angle values follow the same trend with shear rate as the mode pattern pitch angles presented in §4.4.1, but simulations of different shear rate can overlap in direct pitch angle owing to the spread in pitch angle values produced by the winding mechanism of the spiral arm features. A snapshot of a time when direct and mode pattern pitch angles are approximately the same is shown in Fig. 4.9 for simulation R, F and K. This shows the pitch angle - shear trend clearly[1].

The winding nature of the spiral arms means that each spiral arm can exhibit several pitch angles over the spiral arm lifetime. Fig. 4.10 shows these pitch

[1]Spiral arms of small pitch angle are seen also in a disc model with a massive bulge in Martig *et al.* (2012), who use an adaptive mesh refinement code, RAMSES (Teyssier, 2002).

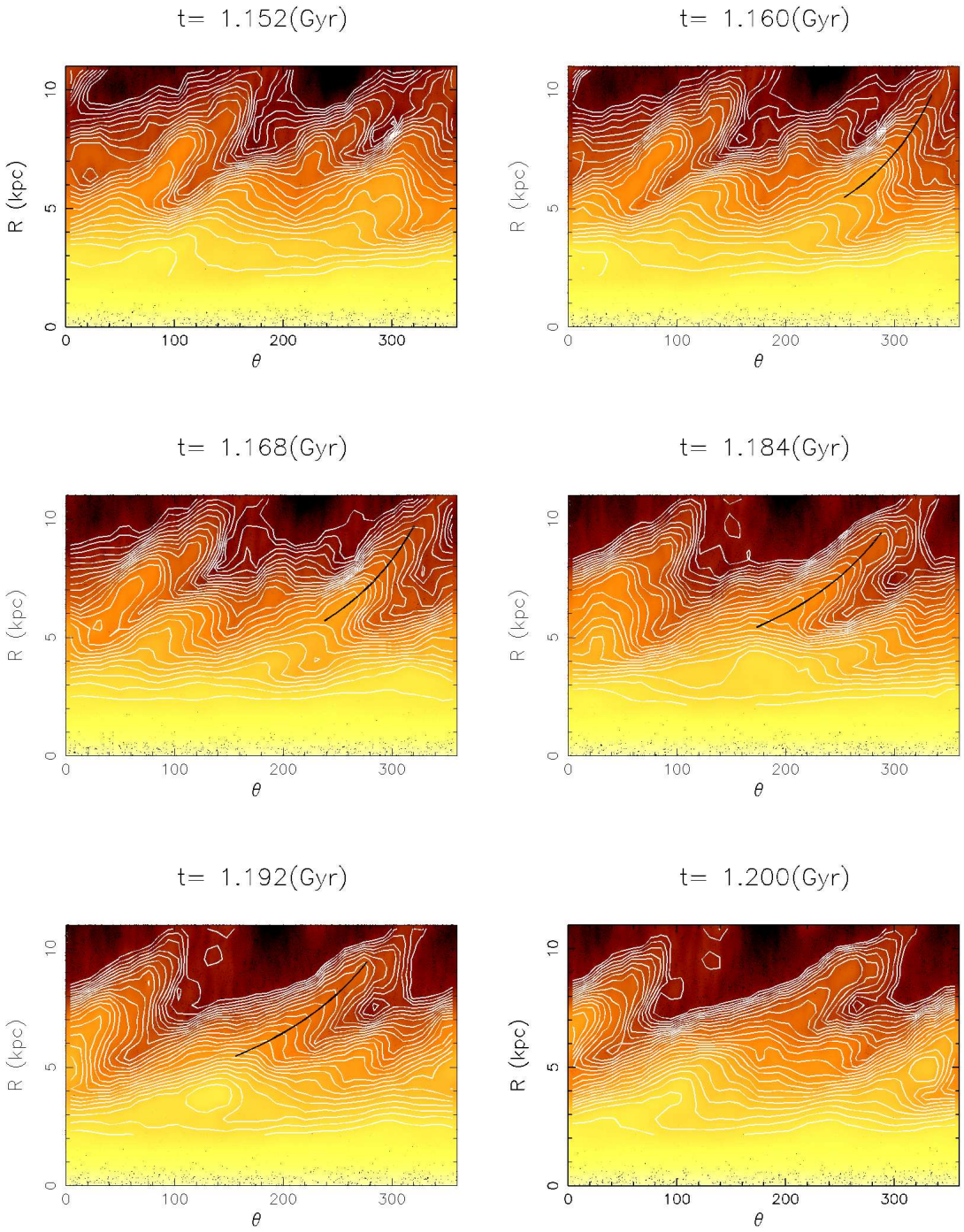


Figure 4.7: Snapshots of the disc density in polar coordinates. Density contours are overlaid in white. The traced spiral arm position is highlighted with a black line. The double peak structure at $R \sim 5.5$ and $\sim 9$ kpc at snapshots $t = 1.152$ and $t = 1.2$ Gyr prevents an unambiguous fitting to a single peak, and this defines the time range in which the spiral arm can be traced.

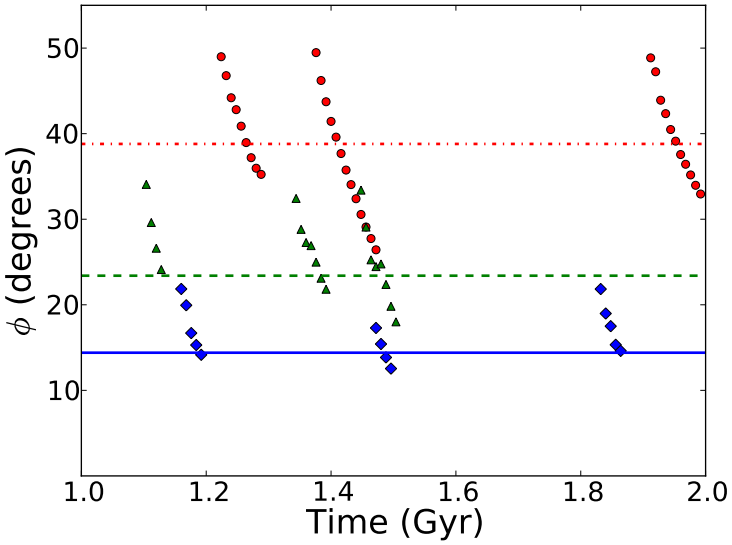


Figure 4.8: Pitch angle evolution of the overall spiral arm feature for simulations R (red circles), F (green triangles) and K (blue diamonds). In all cases the pitch angle decreases with time, which indicates the winding nature of the overall density peak. The horizontal lines represent the mean mode pattern pitch angle, determined from the patterns in Fig. 4.5 and shown in Table 4.2 for simulations R (dot-dashed red), F (dashed green) and K (solid blue). Note that the range of directly measured spiral arm pitch angles clearly map out separate domains about the mode pattern pitch angles of their respective galaxies.

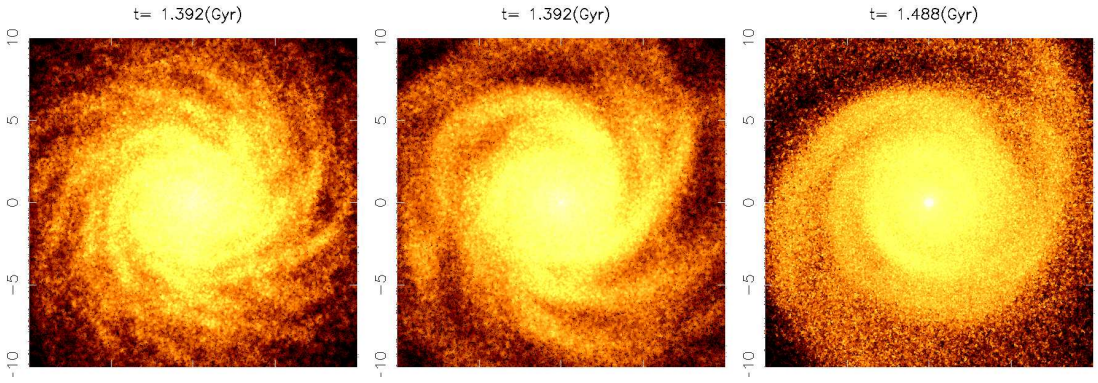


Figure 4.9: Face on view of each simulation (from left to right: simulations R, F and K) when the directly measured spiral arm pitch angle coincides with the calculated mode pattern pitch angle. The spirals become increasingly tight going from left to right.

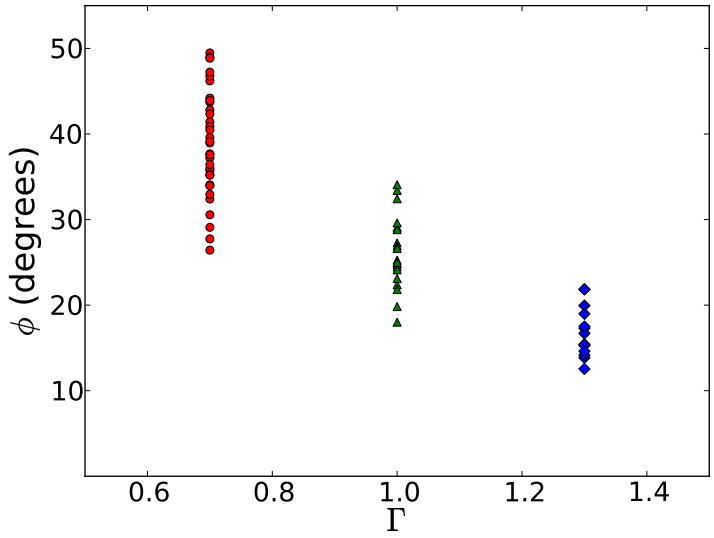


Figure 4.10: All directly calculated spiral arm feature pitch angles plotted as a function of galactic shear for simulations R (red circles), F (green triangles) and K (blue diamonds).

angles plotted against galactic shear, which clearly shows that the pitch angle decreases for increasing shear rate. The range of pitch angles becomes smaller with increasing shear rate as well. This trend and scatter shown in Fig. 4.10 are both consistent with the pitch angle-shear rate correlation and scatter seen in real observations (e.g. Fig. 3 of Seigar *et al.*, 2006). This may indicate that observers are seeing spiral arms at varying stages of their evolution, and therefore detect a range of pitch angles at a given rate of shear. To test the validity of these results, we explore the effect of other parameters on pitch angle in the next section.

## 4.5 Parameter Survey

Up to this point, we have presented results only from the fiducial simulations R, F and K, which clearly show the relationship between pitch angle and shear rate owing to their very different rates of shear. We now explore the effects on the pitch angle of the other parameters that vary between them.

### 4.5.1 Resolution and Softening length

We investigate the numerical robustness of the simulations by examining the effect of the number of particles and the choice of softening length. We start with simulations Fa, Fb and Fc, which use N=$5 \times 10^6$ particles with different softening lengths (see Table 4.1) together with the fiducial F. They are identical in every other parameter to the fiducial F simulation. The top panels of Fig. 4.11 shows their wave mode amplitudes and dominant mode pattern phase positions. There are some differences between the higher resolution simulations, Fa, Fb and Fc. For example, the $m = 5$ mode shows significant amplitude in Fc.

Because the softening length relates to the particle mass as $\epsilon \propto m_p^{1/3}$, a direct comparison to explore the effect of resolution is between simulation F and Fb. The spiral structure grows slightly more slowly in simulation Fb (as well as the other higher resolution simulations) than in simulation F, but modes of $m = 3$ and 4 remain strong in all of these simulations. The difference in level of spiral structure growth for the different particle number is as expected (Fujii *et al.*, 2011).

The chi-squared fitting of the most dominant patterns in each simulation is shown in the bottom row of Fig. 4.11. The mode pattern pitch angles for all three higher resolution simulations are given in Table 4.2, and are all very similar to the fiducial F mode pattern pitch angles.

Fig. 4.12 shows the pitch angles of several spiral arms that we analysed using the direct trace of the spiral arm features. Again, the arms are winding with time, and the range of pitch angles are consistent with simulation F in Fig. 4.8. In Fig. 4.12, at around $t = 1.6$ Gyr, simulation Fa shows a spiral arm that forms with an initial pitch angle of $\phi = 41$ degrees, and is quickly wound. Although this initial pitch angle is high compared to that of the other arms, the later pitch angle measurements for this spiral arm overlap the range of pitch angles of all the other arms in simulations F, Fa, Fb and Fc.

The general agreement between the mode pattern pitch angles and the range of direct pitch angles over the simulations F, Fa, Fb and Fc indicates that the fiducial resolution of $N = 1$ million particles is sufficient to capture robust pitch angles. Moreover, the variation of the softening length in the assumed range does not appear to be a significant factor either, owing to the very similar mode pattern pitch angles given in Table 4.2 and directly measured pitch angles shown

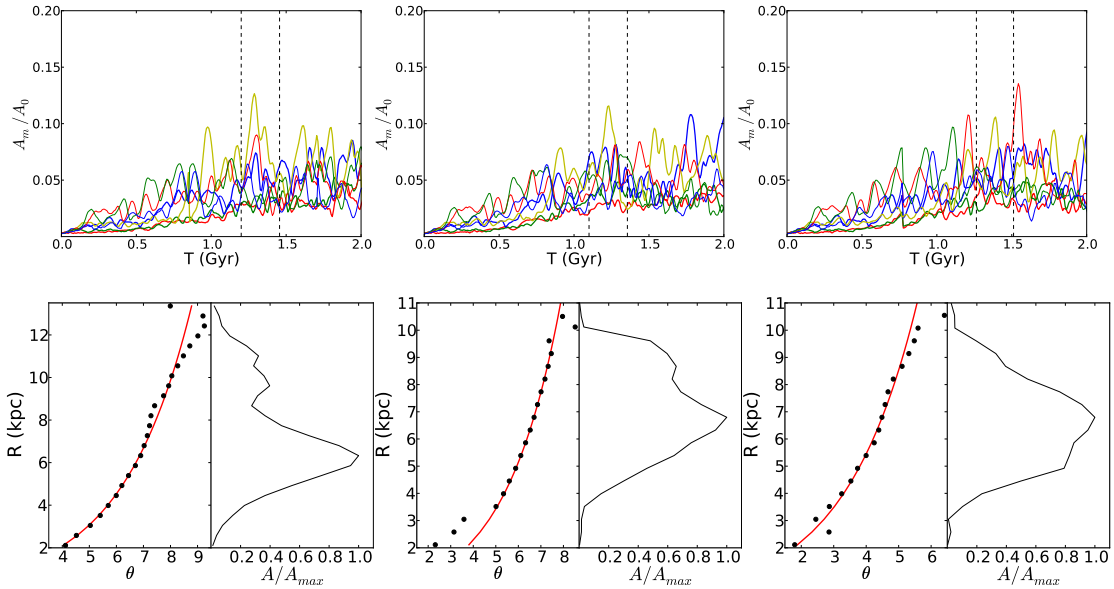


Figure 4.11: Top row: Amplitudes of the $m = 1 - 7$ wave mode numbers (colours as in Fig. 4.4). Bottom row: Phase positions of the strong mode patterns identified in top row. From left to right: simulations Fa ($m = 4$), Fb ($m = 4$) and Fc ($m = 4$) respectively.

in Fig. 4.12.

### 4.5.2 Disc-Halo mass ratio

Another variable in our simulations is the disc mass to halo mass ratio. To see whether or not this parameter affects the pitch angle, we perform the same analysis on simulations F2 and F3, which display shear rates within $\sim 2\%$ of the fiducial simulation F, with lower and higher disc-halo mass ratios respectively (see Table 4.1). The ratio, $\zeta$, is calculated as the ratio of the disc mass to the external mass within two radial scale lengths (as performed in D'Onghia *et al.*, 2013). The amplitudes and density mode pattern phase positions are shown in Fig. 4.13. The mode pattern pitch angles calculated from the fitting in the bottom rows in Fig. 4.13 is presented in Table 4.2. The pitch angle values of F2 and F3 are similar to that of F. The directly measured pitch angles from the spiral arm feature shown in Fig. 4.14 also show little difference between the simulations, with perhaps the exception of the F3 spiral arm beginning $t = 1$ Gyr at $\phi \sim 40°$. Overall, these results indicate that the disc to halo mass ratio does not affect the pitch angle

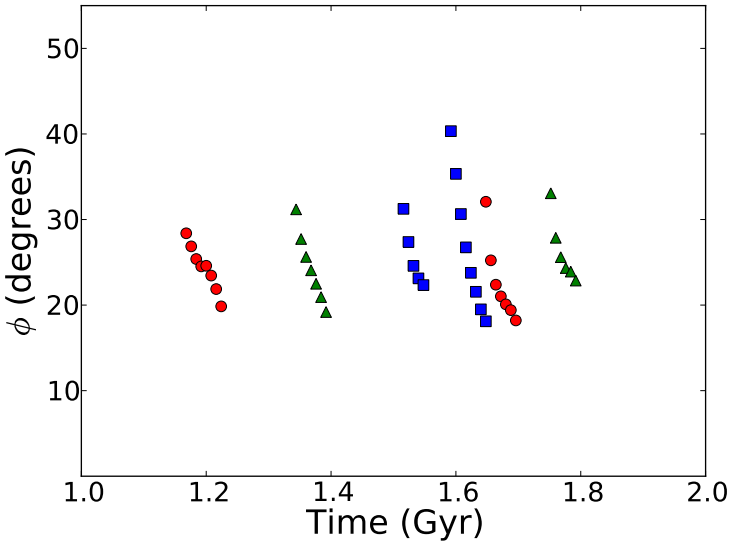


Figure 4.12: As for Fig. 4.8 but for simulations Fa (blue squares), Fb (red circles) and Fc (green triangles).

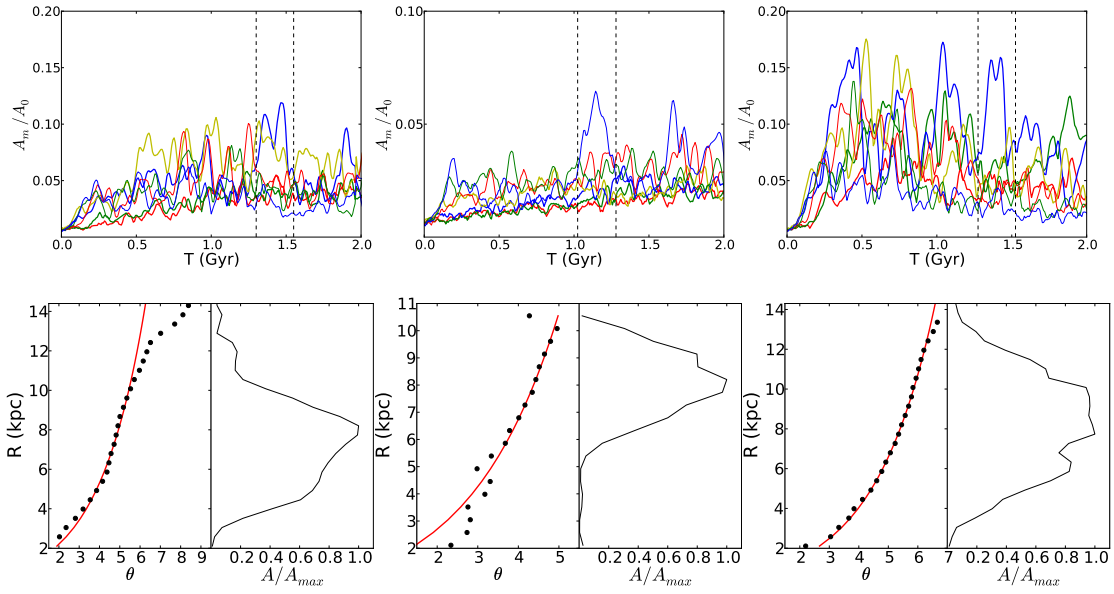


Figure 4.13: As in Fig. 4.11, but for simulations F ($m = 3$), F2 ($m = 7$) and F3 ($m = 3$).

of the spiral features, but instead the number of spiral arms, $m$. For example, in Fig. 4.13 the higher disc-mass ratio simulation, F3, displays more power in lower wave mode numbers ($m = 2, 3$) whereas the lowest disc-halo mass ratio simulation, F2, shows the $m = 7$ mode to be most prominent. This is consistent with previous studies (Julian & Toomre, 1966; Toomre, 1981; Efstathiou *et al.*, 1982; Carlberg & Freedman, 1985; D'Onghia *et al.*, 2013).

We also performed simulations of intermediate shear rate values between simulations R and F with a slight alteration of disc-halo mass ratio. These simulations, labelled R2, R3 and R4 (in order from higher to lower shear), have no bulge. Fig. 4.15 shows the direct pitch angle of several spiral arms in these simulations. While they are similar to each other, the range of pitch angles covers a slightly higher range than that of simulation F but slightly lower than that of simulation R. This agrees with the intermediate shear values shown in Fig. 4.2. Table 4.2 shows the measured pitch angle of the wave modes, which also indicates the intermediate mode pattern pitch angles between simulations R and F.

To examine the trends together, we plot the mode pattern pitch angles of simulations F, F2, F3, K, R, R2, R3 and R4 as a function of shear rate in Fig. 4.16. This figure shows a clear correlation between pitch angle and shear rate, which is the main finding of this study .

The lack of effect of disc-halo mass ratio on pitch angle in combination with the difference in pitch angle between simulations F and R2, which both have the same mass ratio, are convincing evidence that the shear rate is the dominant driver of pitch angle in $N$-body simulations of spiral galaxies.

## 4.6 Discussion

We have shown that in $N$-body simulations, the measured pitch angles (measured both through the wave mode patterns and directly tracing the spiral arm features) correlate with shear rate. The range of direct pitch angles produced is in agreement with observation. We explored other simulation parameters, and show that the pitch angle is not significantly affected by the disc-halo mass ratio, resolution or softening length. One other parameter whose effect we could not explore is the stability parameter, $Q$, owing to the fact that it cannot be directly specified and it evolves over time (Fujii *et al.*, 2011). Although we could not test

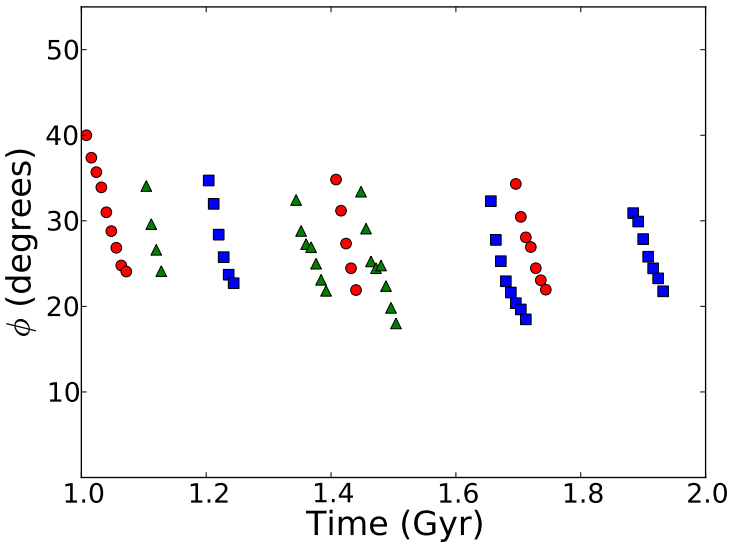


Figure 4.14: As for Fig. 4.8 but for simulations F (green triangles), F2 (blue squares) and F3 (red circles).

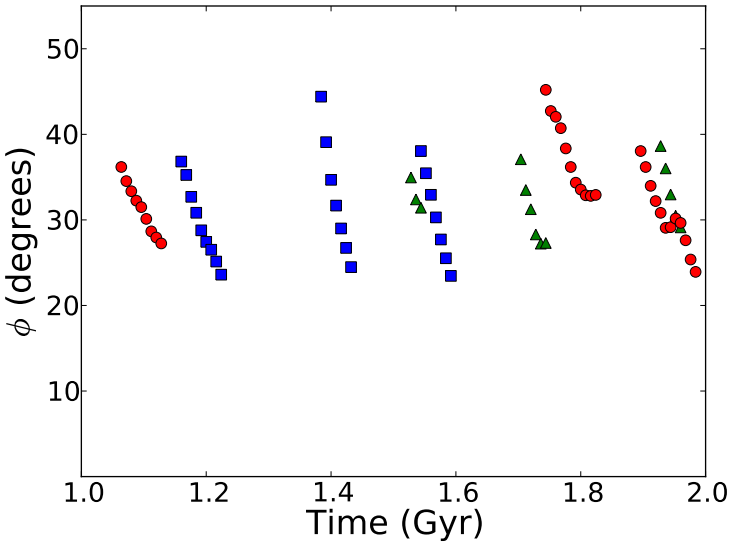


Figure 4.15: As for Fig. 4.8 but for simulations R2 (blue squares), R3 (green triangles) and R4 (red circles).

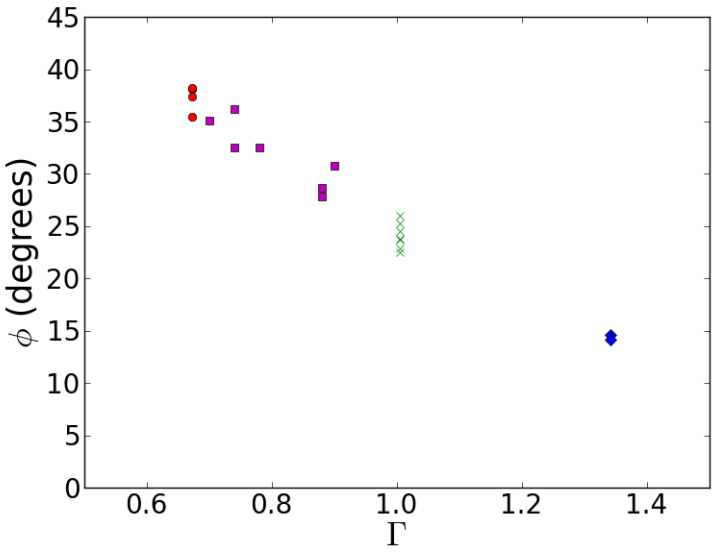


Figure 4.16: The mode pitch angles as a function of shear for simulations, R (red circles), R2, R3, R4 (magenta squares), F, F2, F5 (green crosses) and K (blue diamonds).

this parameter directly, we note that the $Q$ parameter is reported from analytical studies (e.g. Julian & Toomre, 1966; Athanassoula, 1984; Fuchs, 2001) to have negligible effect on the pitch angle of swing-amplified patches. Also, the density wave theory of Lin & Shu (1964) does not show an explicit correlation between the pitch angle and the $Q$ parameter. Therefore, we expect the major driver of the pitch angle value of spiral arms in $N$-body simulations to be the shear rate. However, this aspect still needs further study.

The observed correlation between the pitch angle of the density wave mode and galactic shear rate is qualitatively consistent with the prediction of the classic theories of both density wave theory (Lin & Shu, 1964) and swing amplification theory (Julian & Toomre, 1966; Toomre, 1981).

In the context of swing amplification theory, spiral structure grows from density perturbations as the stellar material swings from an open to a tightly wound structure, so as to exhibit a range of inclination angles. Therefore the pitch angle may correspond to the inclination angle when each density perturbation is most amplified, around a specific inclination angle, which is correlated to shear rate (Julian & Toomre, 1966).

In the context of the Lin-Shu density wave theory, each wave mode can be

interpreted as a standing wave mode of constant pitch angle and fixed pattern speed. Lin & Shu (1964) demonstrate that the pitch angle of such waves is lower for higher central mass concentrations, i.e. a higher shear rate. However, there must be more than one wave mode to manifest the winding of the spiral arm, which must then be interpreted in terms of a superposition of multiple mode patterns, which changes with time (e.g. Comparetta & Quillen, 2012). In this interpretation, the wave mode patterns in the inner disc region must have a faster pattern speed than that in the outer region, and must overlap at some intermediate radii. Therefore, the pitch angle begins larger than that measured for the wave mode, and then approaches the mode pitch angle while the density grows (constructive interfering). The waves then pass and move away from one another, which decreases the pitch angle further. This leads to a stretch in the azimuthal direction of the overall spiral arm density.

If multiple wave modes are the driving mechanism of spiral arms, the $N$-body simulations suggest that there are many patterns of various multiplicity, $m$, that are short-lived (as seen from the transient nature of the mode amplitudes in Fig. 4.4 for example) and recurrent. However, it is worth noting that such waves are some distance from the large scale, long timescale structures that classic spiral density wave theory was developed to produce. The formation and evolution of such wave modes should be non-linear and complicated (D'Onghia *et al.*, 2013; Baba *et al.*, 2013), which deserves further study, and is beyond the scope of this study.

## 4.7 Conclusions

For the first time, to our knowledge, we have analysed the pitch angle of the spiral arm features directly and the pitch angle of the wave mode pattern in $N$-body simulations of disc galaxies with different galactic shear rate. The former pitch angle is derived from tracing the physical movement of the actual surface density of the spiral arms, and the latter is calculated from Fourier analysis that aims to isolate density wave mode patterns from the system that may contribute to the overall movement of the spiral arms. We presented and compared the results of both techniques, and come to the following conclusions.

(i) We find that the pitch angle measured both through the wave mode anal-

ysis and direct analysis is correlated with the rate of galactic shear: the pitch angle is smaller for higher galactic shear rate and vice versa. This is consistent qualitatively with the analytical predictions based on density wave theory (Lin & Shu, 1964) and swing amplification theory in Julian & Toomre (1966), which we demonstrate in $N$-body simulations for the first time.

(ii) The direct pitch angles of the overall spiral arm density enhancement decrease with time, as the spiral arms grow from a relatively open arm morphology, then wind over time to become more tightly wound until they disrupt. This is consistent with previous simulations that reported winding and co-rotating spiral arms (Wada *et al.*, 2011; Baba *et al.*, 2013, and §2, 3).

(iii) The range of the direct pitch angles resulting from the winding spiral arm features is correlated with their shear rate: the direct pitch angle range tends to be smaller for the system with higher galactic shear and vice versa. The range of direct pitch angles at a given shear rate is similar to the scatter seen from the observed relation between the pitch angle and the shear rate in spiral galaxies reported in Seigar *et al.* (2006). This is consistent with the view that real galaxies exhibit transient and winding spiral arms.

Our $N$-body simulations demonstrate the relation between the pitch angle and the galactic shear rate. Although we explored several parameters, such as disc-total mass ratio and simulation resolution, this area of study is far from completion. We also used a fixed dark matter halo for simplicity, and left out the gas component. In real galaxies, there are also constant minor mergers and tidal interactions with satellite galaxies, which we have not explored. However, we suggest that this study highlights the relation between pitch angle and the galactic shear rate, and encourages further studies with more realistic and complicated models. If this relation is a dominant mechanism to determine the pitch angle of the spiral arms, because the late type spiral galaxies tend to have rising rotation curves, this relation will become key to explain the correlation between the pitch angle and the Hubble type (Hubble, 1926; Kennicutt, 1981).

# Chapter 5

# Orbits of radial migrators and non-migrators around a spiral arm in $N$-body simulations

*This chapter is based on Grand* et al. *(2014).*

## 5.1 Introduction

Radial migration produced from transient spiral arms has been highlighted in many recent numerical studies (Roškar *et al.*, 2008a; Minchev & Famaey, 2010; Fujii *et al.*, 2011; Minchev *et al.*, 2011, 2012b; Fujii & Baba, 2012; Roškar *et al.*, 2012b; Solway *et al.*, 2012, and §2, 3), although the precise mechanism of the radial migration process is still debated, which stems mainly from uncertainties in our understanding of the spiral arm nature. For example, Minchev & Quillen (2006); Minchev & Famaey (2010); Comparetta & Quillen (2012); Chamandy *et al.* (2014) explain the transient spiral arms as a superposition of multiple density wave mode patterns that span separate radial ranges that overlap. Because inner patterns rotate faster than outer patterns, they are said to constructively interfere periodically which causes the growth and decay of a spiral arm on the timescale of an interference. On the other hand, other studies (e.g. §2, 3, Wada *et al.*, 2011; Fujii *et al.*, 2011; Fujii & Baba, 2012) report the spiral arm to be an amplified over-density whose rotation speed matches that of the disc material

at all radii. Such spiral arms are naturally winding and transient as shown by Wada *et al.* (2011) who reports transient spiral arms that exhibit a very smoothly decreasing pattern speed as a function of radius. The co-rotating spiral arm is supported by the studies presented in §2 and §4, who performed $N$-body simulations of non-barred galaxies embedded in a static dark matter halo potential and traced the spiral arm peak density directly from the density distribution. This is further backed-up by Roca-Fàbrega *et al.* (2013), who performed high resolution $N$-body simulations with a live dark matter halo.

The orbital evolution of particles that radially migrate has to date been discussed in few studies. Roškar *et al.* (2012b) explain that in a spiral disc of multiple co-existing density wave patterns, radial migration occurs only at the co-rotation radius of each pattern. From a sample of star particles chosen from the top 10% of migrators, they interpret radial migration over a large radial range as two successive discrete particle-pattern interactions, where a particle may be transported from the co-rotation radius of one pattern close to the location of the other pattern. In our previous work described in §2 and §3, we showed that radial migration can occur continuously over a large radial range until the spiral arm disappears. We examined individual $N$-body star particles and found that the orbital eccentricity was largely conserved. Baba *et al.* (2013) study the orbit evolution of star particles in their high resolution $N$-body simulation. However, they focus on a random sample of star particles associated with the "non-steady" spiral arms in order to link the formation and disruption of spiral arms to the motions of its constituent stars, with less focus on radial migration.

In this chapter, we complement these studies and build upon our own work by running a high resolution simulation of a galactic disc to explore in detail the interaction of star particles with the spiral arm. In particular we focus on star particles that show significant radial migration (migrators), and star particles that show almost no migration (non-migrators) between the birth and death of a spiral arm. We present detailed step-by-step evolution of each group of particle, which reveals several types of migrators as well as non-migrators each with different orbital characteristics, none of which (to our knowledge) have been reported in literature (including our previous works described in §2 and §3). Individual orbits are tracked extensively to cover the time before, during and after a single spiral-particle interaction. Our spiral arm peak tracing method

(§3) enables us to follow the evolution of the particle position with respect to the spiral arm, which is a quantity currently unexplored in the literature. This is an important diagnostic that allows us to identify and explain the properties of the migrating/non-migrating star particles in our Milky Way sized simulation. Therefore, these types of orbits may be observable for the Galaxy in Galactic surveys such as RAVE (e.g. Steinmetz *et al.*, 2006; Pasetto *et al.*, 2012b,c; Siebert *et al.*, 2012; Williams *et al.*, 2013), *Gaia* (e.g. Lindegren *et al.*, 2008), Gaia-ESO (Gilmore *et al.*, 2012), APOGEE (e.g. Allende Prieto *et al.*, 2008; Bovy *et al.*, 2012), SEGUE (e.g. Yanny *et al.*, 2009; Lee *et al.*, 2011), LAMOST (e.g. Chen *et al.*, 2012) and 4MOST (de Jong, 2012).

The main results of this study come from the detailed analysis of many individual star particle orbits, hence for brevity we show the results from one high resolution simulation. However we briefly discuss the applicability of these results to other simulations of different spiral structure, and discuss the effects of radial migration on the global properties, such as the metallicity and angular momentum distribution.

This chapter is organised as follows. In §5.2, the simulation is described. In §5.3, the method of particle selection is described. In §5.4, we analyse the group evolution of the samples in various phase space projections and describe overall macroscopic behaviour. We then examine the orbits of individual particles and categorise several types of migrators and non-migrators in §5.5. The orbital characteristics of each type reveal determining factors, which when combined together distinguish the migrators from the non-migrators. In §5.6, we discuss the applicability of the results to other simulations, and briefly show the evolution of the global mass and metallicity distributions as a consequence of the radial migration. In §5.7, we summarise our conclusions.

## 5.2 Simulation

The simulation in this chapter is performed with a Tree $N$-body code (Kawata & Gibson, 2003; Kawata *et al.*, 2013b), and simulates a galaxy comprised of a spherical static dark matter halo and a live stellar disc only.

A live dark matter halo can respond to the self-gravitating stellar disc by exchanging angular momentum. This is prominent on long timescales for long-

lived non-axisymmetric structures such as a bar (Debattista & Sellwood, 2000; Athanassoula, 2002, 2012). However, the effect of the live dark matter halo is expected to be small for transient spiral arms, which justifies the use of a static dark matter halo for our investigation. Furthermore, for practical reasons a live dark matter halo is often modelled with particles more massive than disc particles, which may introduce some scattering and heating that depends on the scale of the mass difference between the particle species. Therefore, in the interest of computational speed and a more controlled experiment, we use a static dark matter halo.

The density profile of the dark matter halo and stellar disc are set up following the method outlined in §3.2 with the same cosmological parameters. The concentration parameter and virial mass of the dark matter halo are $c = r_{200}/r_{\rm s} = 20$ and $M_{200} = 1.5 \times 10^{12}$ M$_\odot$. The disc scale length, scale height and mass are $R_{\rm d,*} = 3.5$ kpc, $z_{\rm d,*} = 350$ pc and $M_{\rm d,*} = 5 \times 10^{10}$ M$_\odot$ respectively.

The simulation presented in this chapter has $N = 1{\times}10^7$ particles in the stellar disc, so that each star particle is 5000 M$_\odot$. This is sufficient to minimise numerical heating from Poisson noise (Fujii *et al.*, 2011; Sellwood, 2013). We apply a fixed softening length of 160 pc (Plummer equivalent softening length of 53 pc) for star particles with the spline softening suggested by Price & Monaghan (2007). We denote this simulated galaxy S2, to distinguish it from the other simulations presented in this thesis.

## 5.3 Particle selection of strong migrators and non-migrators

In this study, we focus on single spiral arm-star particle interactions on the timescale of the spiral arm lifetime, which we find to be $\sim 100$ Myr. We scrutinize the evolution of a sample of star particles in order to obtain detailed information on these interactions.

The first step is to identify coherent spiral arms for which we can reliably trace the spiral arm peak position. A reliable trace is defined as a radial range for which each radial point shows a smooth single density peak in azimuth. A snapshot in which the spiral arm exhibits a double peak structure anywhere within the defined radial range for tracing is rejected (see §3.3.1 and §4.3.2). Double peak features

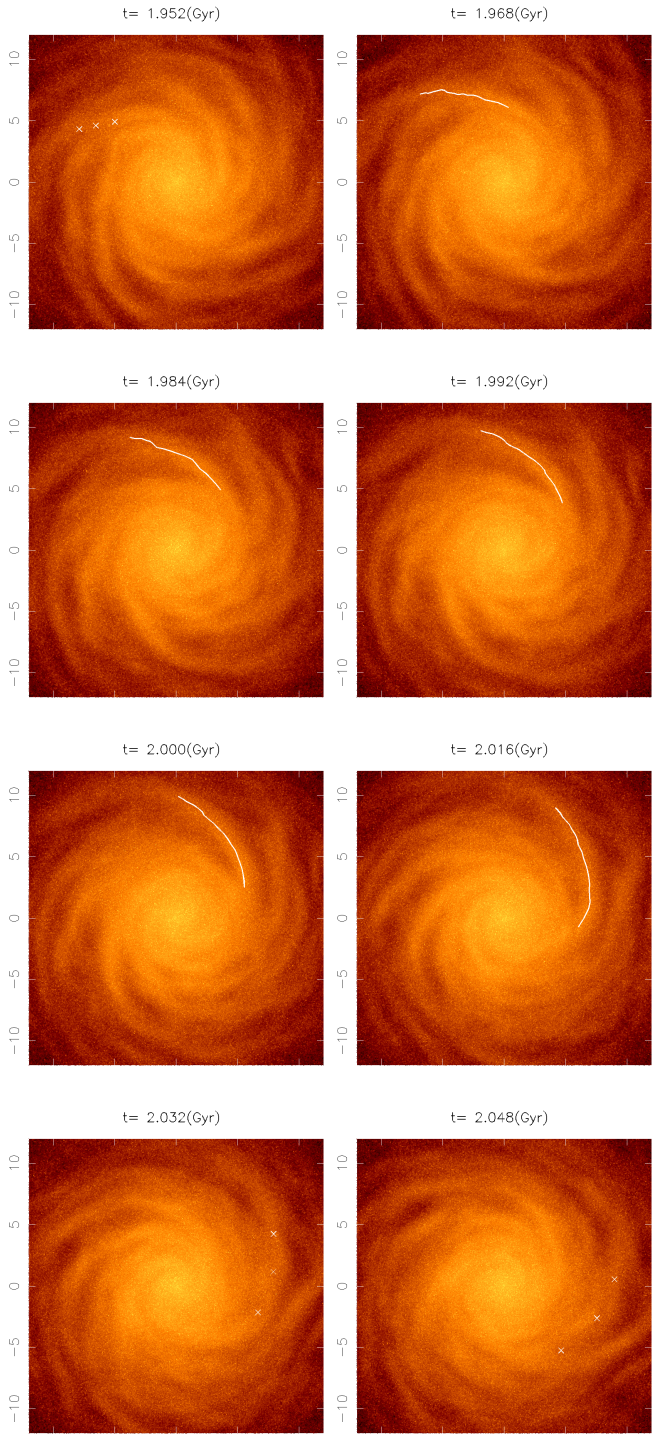


Figure 5.1: The face-on density snapshots showing the sequence of the traceable spiral arm. The white line indicates the traced spiral arm of interest. The spiral peak position for $R = 7, 8$ and 9 kpc radii at the $t = 2.0$ Gyr snapshot are rotated with the corresponding mean rotational velocity and marked as anchors (white crosses) on the $t = 1.952, 2.032$ and 2.048 Gyr snapshots, to guide the eye to the forming and disrupting stages of the spiral arm respectively.

are usually associated with the formation and destruction stages of spiral arm evolution, and are not suitable for an unambiguous trace. Fig. 5.1 shows the face-on density snapshots of our selected spiral arm. There is a time window over which the spiral arm can be reliably traced, and a wider time window which will be used to examine the prior and subsequent star particle behaviour. We could trace the spiral arm reliably at the radii between 6 and 10 kpc in the traceable time window spanning $t = 1.968$ to 2.024 Gyr (highlighted with the white line in Fig. 5.1). Outside of this time window, we extrapolate the spiral arm position by rotating the $R = 7, 8$ and 9 kpc peak positions of the $t = 2.0$ Gyr snapshot with the mean rotation velocity (anchors marked with white crosses) to guide the eye to the spiral arm when it forms and disrupts. The pattern speed is calculated by simple subtraction of the peak line between snapshots. Fig. 5.2 shows the radial profile of the time-averaged pattern speed (dashed red line) and the mean angular rotational velocity of the disc (solid black line). Fig. 5.2 confirms that the spiral arm is co-rotating with the rotational velocity of the disc (as shown in §2 and Roca-Fàbrega *et al.*, 2013). For the rest of the analysis, we focus on particle interactions with this spiral arm.

We choose a snapshot at a time when the spiral arm is fully formed and adopt $t = 2.0$ Gyr (Fig. 5.1) as the time of particle selection. From the traced spiral arm at this time, we define a region within a range of 4 kpc either side of the density peak of the spiral arm in the azimuthal direction. The region is bounded by a radial range of 6 - 10 kpc and a vertical height of $|z| < 0.1$ kpc. The sample is constituted of particles found inside this spatially defined region at $t = 2.0$ Gyr. This probes a wide range in radius and azimuthal position with respect to the spiral arm, and restricts the majority of particles to be in the plane of the disc because more migration takes place in the plane of the disc. Note that over time, the vertical oscillations cause some particles to move to heights that exceed the selection cut of $|z| < 0.1$ kpc. We found that about 15% of the star particles selected reach $z_{max} > 0.35$ kpc (one initial galactic scale height). However, we find that there is no significant difference between the trends discussed in this chapter for particles of different maximum heights.

The time at which the star particles are selected is defined as the central time-step, $T_c = 2$ Gyr, and a time window is then defined as $\Delta T = T_{fin} - T_{ini}$, where $T_{ini} = T_c - 48$ Myr and $T_{fin} = T_c + 48$ Myr. This time window spans the

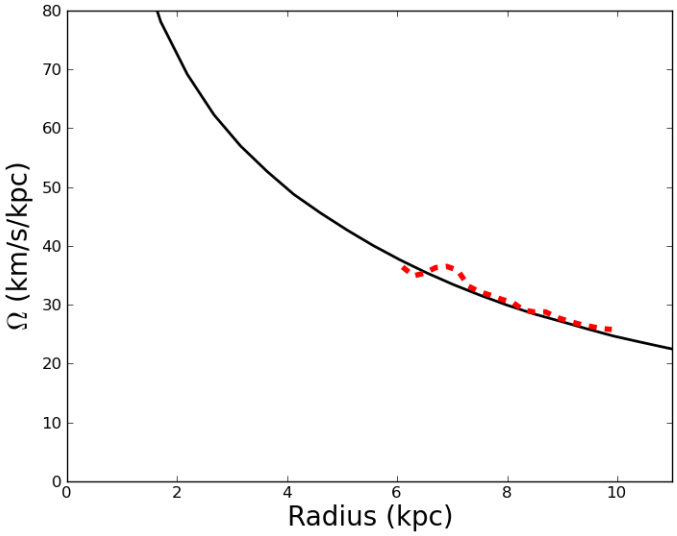


Figure 5.2: The pattern speed (red dashed line) of the traced spiral arm highlighted above. The mean angular rotation speed of the stellar disc is also plotted (solid black line). The pattern speed matches the angular speed of the disc material well.

$\sim 100$ Myr lifetime of the spiral arm. Note that this time window is longer than the time window for which we could trace the spiral arm. However, as seen in Fig. 5.1, the spiral arm begins to form at around $t = 1.952$ Gyr and disrupts at around $t = 2.048$ Gyr. The motion of nearby star particles can be affected at these times. In fact, we will demonstrate in §5.4 that the motion of some star particles can be affected as early as $t \sim 1.9$ Gyr and last until $t \sim 2.2$ Gyr. Hence this time window is set by convenience and not a strict definition of the formation and destruction time. The star particle sample is then plotted in the $L_{z,ini} - \Delta L_z$ plane, where $L_{z,ini}$ is the $z-$component of angular momentum of the star particles at the beginning of the time window, $T_{ini}$, and $\Delta L_z$ is the change in angular momentum from the initial time, $T_{ini}$, to the final time, $T_{fin}$. This is plotted in Fig. 5.3. From Fig. 5.3, we see that there is a wide range of initial angular momentum values over which the angular momentum i.e. the guiding centre, is changed, which is consistent with our previous studies described in §2 and §3.

From the star particle distribution in Fig. 5.3, we select a sample in the range $1.86 \times 10^3 < L_{z,ini} < 1.97 \times 10^3$ kpc km s$^{-1}$ (particle samples at other $L_{z,ini}$ exhibit similar behaviour, so we focus on one sample), which corresponds

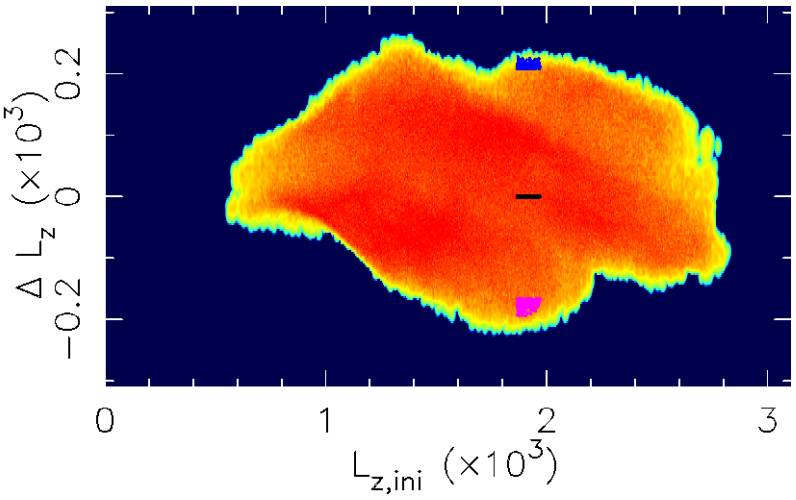


Figure 5.3: The change in angular momentum of the sample of particles over the time window $T_{fin} - T_{ini}$, as a function of their initial angular momentum. Over-plotted are the strong positive migrators (blue symbols), strong negative migrators (pink symbols) and non-migrator particles (black symbols) selected. The units are kpc km s$^{-1}$.

to a guiding centre radius of about 8 kpc. The sample is further cut into sub-groups: strong migrators (both negative and positive) and non-migrators. The strong positive (negative) migrators consist of those particles that have the largest positive (negative) $\Delta L_z$, and the non-migrators are those that have the lowest changes in angular momentum. These star particles are selected such that there are $\sim 200 - 300$ particles in each star particle group, and are highlighted in Fig. 5.3.

## 5.4 Evolution of sample in phase space

We plot each particle in the sample in various projections in phase space, and highlight the positive migrator (blue points), negative migrator (red points) and non-migrator (black points) groups in Fig. 5.4. Each column corresponds to a different time: the left column shows the sample at the earliest time that the spiral arm could be reliably traced (following criteria described in §3), the middle column is the time of selection, $T_c$, and the right column is the latest time that the spiral arm could be reliably traced.

The top row of Fig. 5.4 shows the sample plotted in the radial velocity, $v_R$ - azimuthal velocity, $v_\theta$, plane. Positive radial velocity, $v_R > 0$, is in the

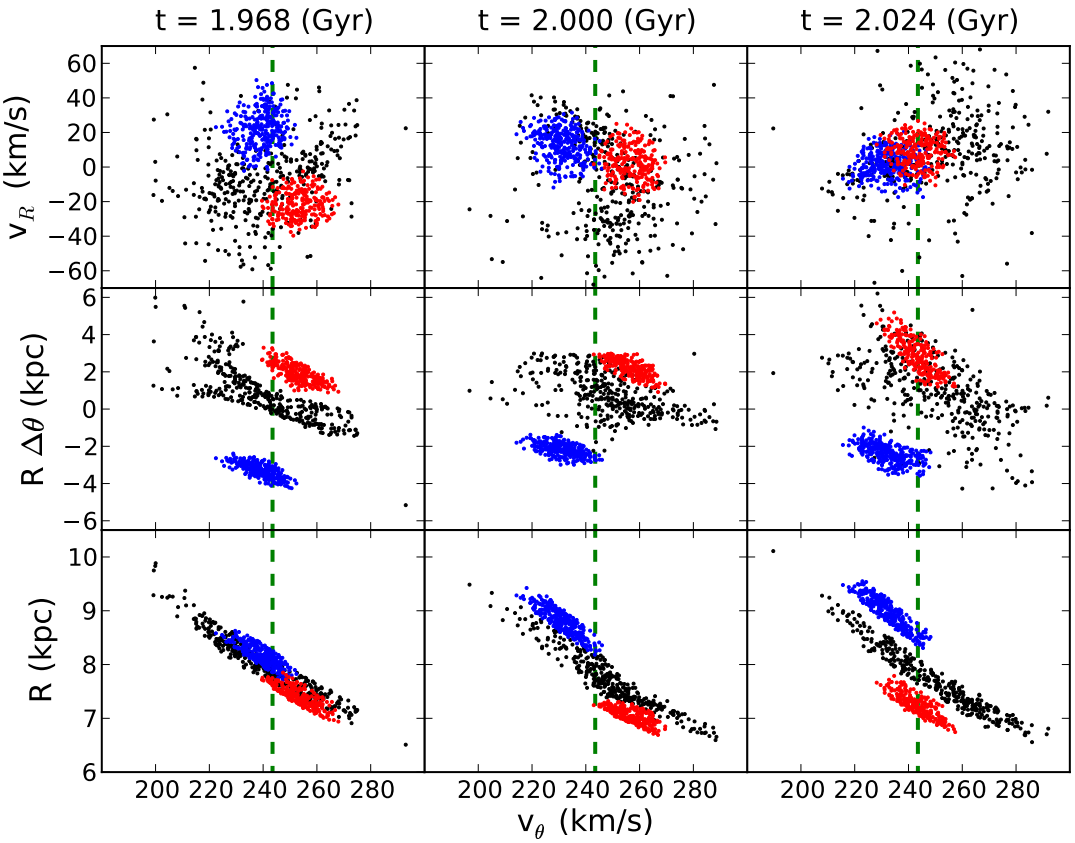


Figure 5.4: *Top row:* The negative migrators (red), positive migrators (blue) and non-migrators (black) of the sample in $v_\theta - v_R$ space. *Middle row:* Shows the azimuthal distance between the star particles and the spiral arm peak position, $R\Delta\theta$, as a function of azimuthal velocity, $v_\theta$. *Bottom row:* Plots the radius of the same star particles with $v_\theta$. Each column shows these projections at three time epochs, increasing from left to right. The circular velocity at the 8 kpc radius, $v_c = 243.5$ km s$^{-1}$, is marked in each panel by the vertical dashed green line.

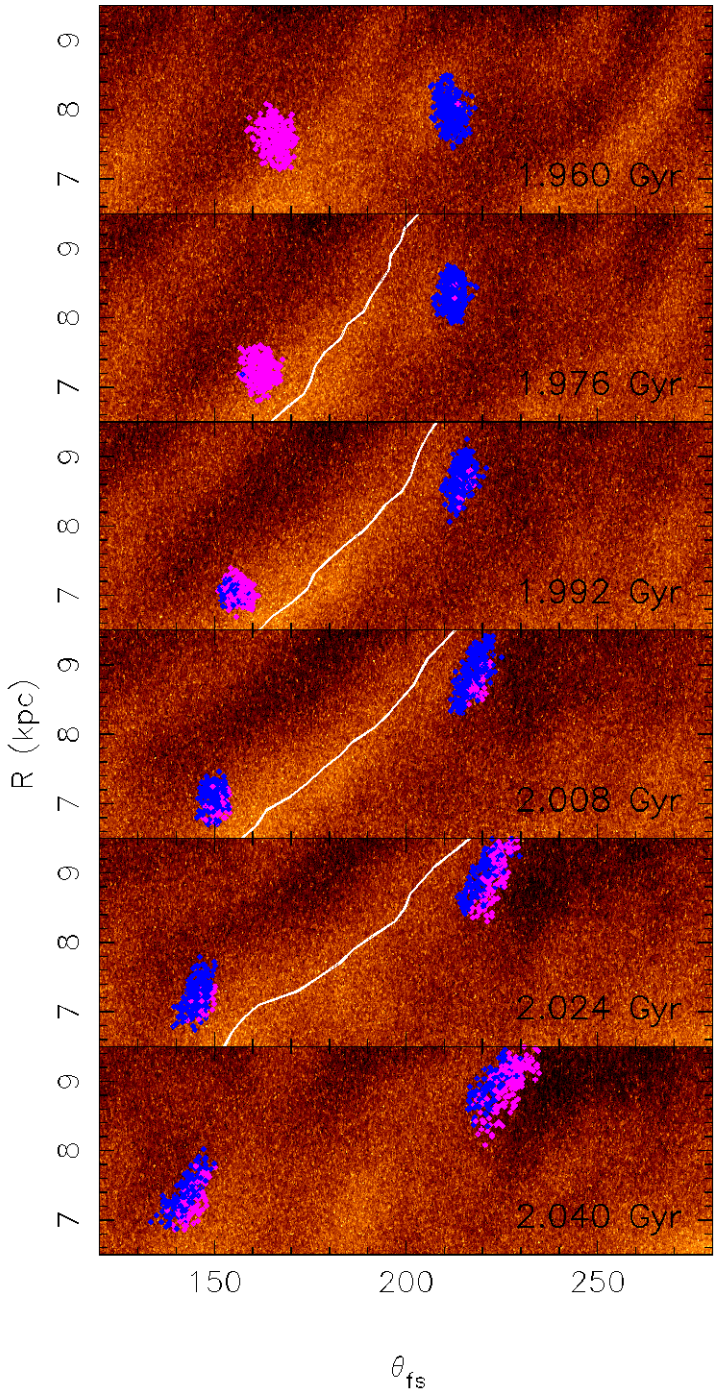


Figure 5.5: Time sequence of a close up of the density map in the $R - \theta_{fs}$ plane. The rotation is from right to left in a rotating frame that co-rotates with the circular velocity at $R = 8$ kpc. Positive migrators are always to the right of the spiral arm, and negative migrators are to the left. The radial velocity direction is indicated by the blue and pink coloured symbols, which represent outward and inward moving radial velocities respectively. The white line (present in some panels) highlights the peak position of spiral arm at each radius.

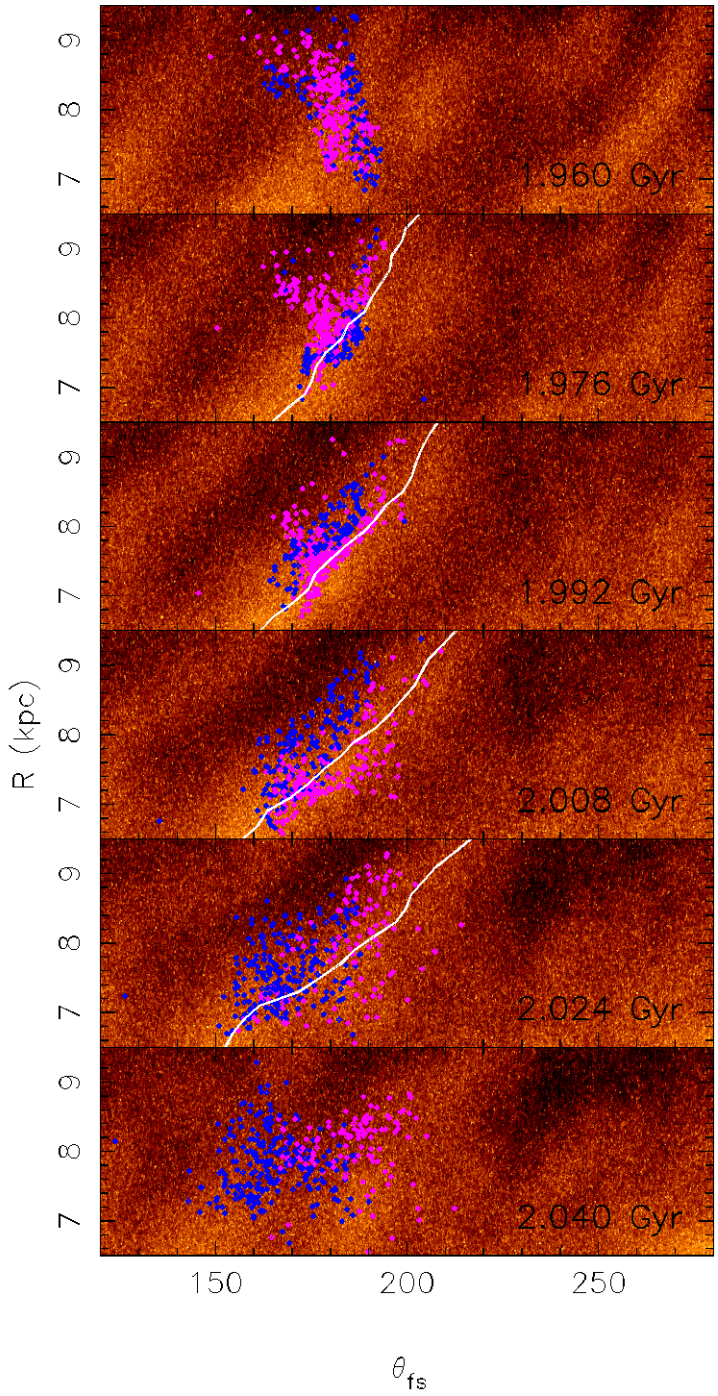


Figure 5.6: The same as Fig. 5.5 but showing non-migrator particles. The white line indicates the spiral arm peak position.

direction away from the galactic centre. The circular velocity at $R = 8$ kpc is $v_c(R = 8) = 243.5$ km s$^{-1}$, which is marked by the dashed green lines in Fig. 5.4. The positive and negative migrators appear to occupy separate regions of velocity space, whereas the non-migrators (black diamonds) are more evenly distributed and overlap the migrator groups. The positive migrators have outward facing velocities ($v_R > 0$) during their outward migration. It is interesting to see that their azimuthal velocity tends to be slower than the circular velocity at $R = 8$ kpc. The opposite is applied to the negative migrators, which move inward ($v_R < 0$) and rotate faster than the circular velocity at $R = 8$ kpc.

The azimuthal distance of a star particle with respect to the spiral arm, $R\Delta\theta$, is defined as the length of an arc that joins the star particle azimuth position to the spiral arm peak azimuth position at that radius. The second row of Fig. 5.4 shows this quantity as a function of azimuthal velocity for the sample. In this plane, each group of particles (including non-migrators) is very clearly separated. The positive migrators always stay behind the spiral arm ($R\Delta\theta < 0$), and the negative migrators always stay in front of the spiral arm ($R\Delta\theta > 0$), throughout the traceable spiral arm lifetime. The non-migrators are clustered around the spiral arm. At the $t = 1.968$ Gyr (left panel), the arrangement of each particle group is highly ordered. The non-migrator group in particular is spread over a large range of azimuthal velocity, which appears tightly correlated with the azimuthal distance between star particle and spiral arm. For example, at $t = 1.968$ Gyr, at $v_\theta = 220$ km s$^{-1}$ the positive migrators have a negative $R\Delta\theta$, i.e. they are behind the spiral arm, while the non-migrators have a positive $R\Delta\theta$, i.e. they are in the front of the spiral arm. Conversely, at $v_\theta \sim 265$ km s$^{-1}$, the negative migrators have a positive $R\Delta\theta$, i.e. they are in the front of the spiral arm, while the non-migrators have a negative $R\Delta\theta$, i.e. they are behind the spiral arm. In §5.5.3, we demonstrate that non-migrators must pass or be passed by the spiral arm at some point during the spiral arm lifetime. Roughly speaking, the star particle will cross the spiral arm if: $|R\Delta\theta| < |\int_{t_0}^{t_1} v_{\theta,sub} dt|$, where $t_1 - t_0 < \Delta T$, and $v_{\theta,sub} = v_\theta - v_c$, where $v_\theta$ is the azimuthal velocity of the star particle and $v_c$ is the circular velocity at the particle radius. Although these star particles were selected at $t = 2.0$ Gyr, their distribution in phase space is more ordered at $t = 1.968$ Gyr. This indicates that the $R\Delta\theta - v_\theta$ phase space can be diagnostic at the early stages of spiral arm formation (middle-left panel of Fig. 5.4) in pre-

determining whether a star particle will be a migrator or a non-migrator. At later times, the groups become less clearly separated, but still maintain the trend.

The bottom row of Fig. 5.4 shows the sample in the $R-v_\theta$ plane. At $t = 1.968$ Gyr (left panel), migrator and non-migrator particle groups occupy the same region of this space, and become more separated at the later times (middle and right panels of Fig. 5.4) owing to the migration taking place. The distribution of non-migrators in this plane highlights the epicyclic motion of the star particles. Star particles that are at a radius greater than the guiding centre of the sample, $R > R_g \sim 8$ kpc, possess azimuthal velocities lower than the circular velocity at the guiding centre, $v_\theta < v_c(R_g)$, whereas star particles at a radius smaller than the guiding centre possess azimuthal velocities larger than the circular velocity at the guiding centre. Positive migrators obviously move toward larger radii, and are outside of their guiding centre owing to their relatively low rotation velocity with respect to the circular velocity at that radius. In other words, the positive migrators are always close to the apocentre phase during their migration, and the negative migrators are always close to the pericentre phase.

Fig. 5.5 shows the evolution of both positive migrators and negative migrators plotted on the face-on density maps of the disc in the $R-\theta_{fs}$ plane. The evolution is shown in a rotating frame that co-rotates with the circular velocity at $R = 8$ kpc. The $\theta$ coordinate of all star particles has been subtracted by an amount corresponding to the rotating frame such that the spiral arm and sample particles remain within the 120-280 degree azimuth window i.e. $\theta_{fs} = \theta_{true} - \Omega_{fr}\Delta t$, where $\Delta t = T_{ini} - t$. Here $\Omega_{fr}$ is the angular rotation speed of the frame. The direction of motion is from right to left. Each migrator particle is coloured blue (pink) to indicate the outward, $v_R > 0$ (inward, $v_R < 0$) direction of the radial velocity vector, in order to indicate the epicycle phase i.e. $v_R > 0$ means that the star particle is moving from pericentre to apocentre, while $v_R < 0$ indicates that the star particle is moving from apocentre to pericentre. Both groups exhibit a range of radial velocities at each snapshot, which indicates there is some spread in the epicycle phase within the groups. For the positive migrators, particles closer to the spiral arm at $t = 1.992$ - $2.024$ Gyr have positive radial velocities (approaching apocentre) and particles further from the spiral arm have negative radial velocities (moving away from apocentre). The opposite trend is seen in the negative migrator group. Despite the different epicycle phases of these migrator

groups, all star particles in the positive and negative migrator groups radially migrate eventually, as we show below.

Fig. 5.6 shows the evolution of the non-migrators in the $R-\theta_{fs}$ density plane in the rotating frame described above for Fig. 5.5. The symbols are coloured blue and pink corresponding to inward and outward radial velocity unit vectors respectively. Most of the non-migrators are clustered close around the spiral arm (peak position marked in white), and appear spatially separated according to the direction of radial motion. For example, at $t = 1.992$ and 2.008 Gyr, most star particles behind (in front of) the spiral arm are moving towards pericentre (apocentre). This is a clear contrast from the migrators. At $t = 1.976$ Gyr, the positive migrators behind the spiral arm are moving toward apocentre, i.e. outward, while the negative migrators in the front of the spiral arm are moving toward pericentre, i.e. inward.

## 5.5 Individual particle orbits

In this section, we analyse the orbits of the positive, negative and non-migrator particles of the sample individually. We took $\sim$ 100 random samples of each star particle group, and followed the evolution of each orbit individually. We scrutinised the orbits over the course of the particle-spiral arm interaction, and categorise several types of migrators and non-migrators. Below we show an example of each type and outline their defining features. We refer to positive migrators with a suffix 'g' because they gain angular momentum, negative migrators with a suffix 'l' because they lose angular momentum and non-migrators with a suffix 'n'. In Table. 5.1, we list the orbital properties of each orbital type mentioned below.

### 5.5.1 Orbits of positive migrators

Fig. 5.7 shows an example of three different types of positive migrator. In the left panels, we show a selection of snapshots from the time sequence evolution of these particles in the same rotating frame adopted in Fig. 5.5. The symbol in each snapshot indicates the position of the particle at the time given in the bottom-right corner of the panel, and the lines show the history of the orbit in the co-rotating frame. Because the spiral arm rotates with the mean rotational

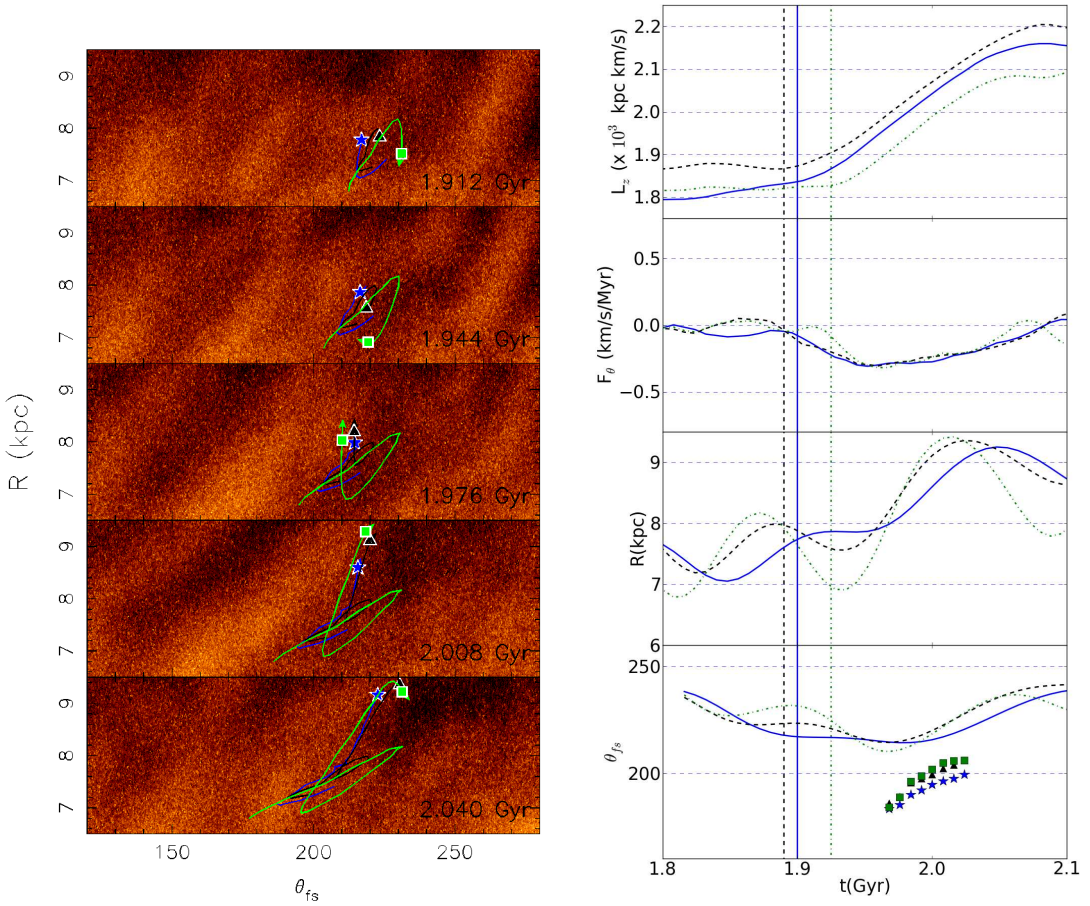


Figure 5.7: The evolution of three types of positive migrator. *Left panels*: The time evolution of the particles in the close up $R-\theta_{fs}$ density map in a rotating frame equal to the circular velocity at $R = 8$ kpc. Rotation is from right to left. The symbols depict the current position of each star particle, and the lines show the history of each star particle orbit relative to the spiral arm (see text for more details). *Top-right panel:* The evolution of the angular momentum of the star particles. *Second-right panel*: The evolution of the tangential force per unit mass, $F_\theta$, acting upon the star particles. *Third-right panel*: The radial evolution of the star particles. *Bottom-right panel*: The azimuthal angle of the star particles in the rotating frame of the left panels, $\theta_{fs}$, (lines) and spiral arm azimuthal angle at the particle radius (symbols). The latter can only be calculated in the traceable spiral arm time window defined in §5.3. In all right-hand panels, the time at which each particle first feels the tangential force is indicated by a vertical line of corresponding line style.

velocity (Fig. 5.2), the spiral arm in the left panels of Fig. 5.7 moves relative to the rotating frame in time: for $R < 8$ kpc, the spiral arm moves to lower $\theta_{fs}$, whereas for $R > 8$ kpc the spiral arm moves to higher $\theta_{fs}$. We remove the relative motion between the spiral arm and star particle orbit histories by making a further adjustment to the orbit history. We calculate the difference between the velocity of the rotating frame and the circular velocity at the radius of the line point. At each subsequent time-step after the line point appears the position of the line point is shifted by the amount corresponding to this velocity difference. The purpose of this adjustment is to give an idea of where the past particle positions were *relative to the spiral arm* at previous times, although it is not exact because it is impossible to place the past orbit around the dynamically changing spiral arm.

The 1st- and 2nd-right panels of Fig. 5.7 shows the evolution of particle angular momentum, $L_z$, and the tangential force per unit mass, $F_\theta$, where the positive direction is opposite to the direction of rotation, i.e. from left to right in the left panels of Fig. 5.7. Blue solid, black dashed and green dot-dashed lines correspond to the blue, black and green lines in the left panels of Fig. 5.7.

We define radial migration to be a change in angular momentum over time, such as the change seen in the top-right panel of Fig. 5.7, e.g. the black dashed line from $t \sim 1.89$ to 2.08 Gyr when $L_z$ increases. Note that the tangential force is always negative during the increase in $L_z$. The magnitude of the tangential force indicates the rate of change of angular momentum, which allows us to see more clearly when and where the star particles migrate in the left panels of Fig. 5.7. The third-right and bottom-right panels of Fig. 5.7 show the evolution of the particle radius, $R$, and azimuth angle in the rotating frame, $\theta_{fs}$, respectively. In the bottom panel, the blue star, black triangle and green square indicate the azimuth angle of the spiral arm that we identified in Fig. 5.1 at the star particle radius at the corresponding time. Note that we could trace the spiral arm for only part of the period when the spiral arm is clearly seen. However, this demonstrates that the spiral arm affects the orbit of the star particles well before the arm is clearly seen and even after it begins to disrupt. At least in this short period when we can clearly trace the spiral arm, we can show the particle position with respect to the spiral arm as seen in the bottom panel of Fig. 5.7. The evolution of each quantity shown in the right panels of Fig. 5.7 will determine the type of

each positive migrator.

#### 5.5.1.1 Type 1g positive migrator

The first type (Type 1g) of positive migrator (blue star and solid blue line in the left panels and blue solid line in the right panels of Fig. 5.7) is quite close to the spiral arm when it begins to feel a negative tangential force at around $t \sim 1.9$ Gyr (2nd-right panel of Fig. 5.7). The top left panel of Fig. 5.7 shows that the spiral arm begins to build up at $t \sim 1.9$ Gyr. It appears that the density enhancements around $\theta_{fs} = 180$ and $\theta_{fs} = 220$ at $R \sim 8$ kpc at $t = 1.912$ Gyr merge and form the single spiral arm around $t \sim 1.976$ Gyr. At $t = 1.912$ Gyr the blue star is located behind the density enhancement at $\theta_{fs} = 220$, and therefore the direction of tangential force is negative ($F_\theta < 0$) and the star particle is accelerated.

At $t \sim 1.9$ Gyr, the particle is approaching the apocentre phase of orbit (3rd-right panel of Fig. 5.7). However, as a result of strong negative tangential force at this phase (2nd-right panel of Fig. 5.7), the radius of the star particle does not decrease again according to normal epicycle motion. This is because of the competition between mainly the radial gravitational force and the increase in centrifugal force caused by the gain in angular momentum. In this case, the radial force is balanced by the increased centrifugal force. As a result, the star particle pauses at a radius of $R \sim 7.9$ kpc for $\sim 20 - 30$ Myr at around $t \sim 1.94$ Gyr, then increases again once the angular momentum has increased such that the centrifugal force is large enough to overcome the radial gravitational force.

Note that irrespective of the evolution of radius, the increase in angular momentum is sustained as the particle continues to be accelerated by the negative tangential force, because the particle is always behind the spiral arm. The bottom-right panel of Fig. 5.7 shows that the azimuth angle of the particle is always larger than that of the spiral arm (star particle is behind the spiral arm) during the epoch at which the spiral arm is clearly traced. The strong migrators are able to stay on one side of the spiral arm, because the spiral arm co-rotates with the disc material (§2). As a result, positive migrators maintain their position behind the spiral arm and continue to be accelerated and migrate along the spiral arm. At around $t \sim 2.08$ Gyr when the spiral arm is disrupted, the particle stops gaining angular momentum and the star particle resumes epicycle motion.

#### 5.5.1.2 Type 2g positive migrator

The second type (Type 2g) of positive migrator (black triangle and solid black line in the left panels and black dashed line in the right panels of Fig. 5.7) begins to feel a negative tangential force at about the same time as the Type 1g positive migrator mentioned above ($t \sim 1.89$ Gyr), and is accelerated. Again, there is a competition between the radial gravitational force and the increase in angular momentum. However, at this time the particle has just passed the apocentre phase of the epicycle motion (3rd-right panel of Fig. 5.7) when the angular momentum begins to increase. Therefore, the star particle begins to move inward for a while, until the angular momentum increases sufficiently to overcome the gravitational force. As a result, the amplitude of the epicycle motion is shortened. This shortening in amplitude is shown by the changed pericentre radii between $t \sim 1.83$ and 1.93 Gyr in the 3rd-right panel of Fig. 5.7. The pericentre radius is larger at the later time owing to the increase in guiding centre. Note that although the radial evolution of the orbit looks different to that of the Type 1g positive migrator shown above, the angular momentum steadily increases irrespective of their radial evolution because the star particle is always located behind the spiral arm and accelerated (bottom-right panel of Fig. 5.7).

This is the most common type of positive migrator in this sample. The shortened epicycle motion present in the radial evolution of the Type 2g positive migrator is also reported in Roškar *et al.* (2012b). The strongest migrators in their simulation are shown to exhibit several shortened epicycle motions, which they interpret as effects of co-rotation resonances of two spiral waves: one inner, faster rotating spiral pattern and one outer, slower rotating spiral pattern. For example, in the top panels of Fig. 11 of Roškar *et al.* (2012b), the orbit of the migrator shows $\sim 6$ epicycle motions from $t \sim 5.4$ to 5.9 Gyr. In our study, we focus on 1-2 epicycle periods which corresponds to the lifetime of the spiral arm in our simulation. The Type 2g migrator demonstrates that during the shortened epicycle motion the guiding centre of the star particle continuously increases owing to the angular momentum increase at every radius. Therefore, we think that it is difficult to attribute 6 shortened epicycle motions seen in Roškar *et al.* (2012b) to only two co-rotation resonances. Instead, we think that the spiral arm feature co-rotates with the disc material at every radius (§2), and induces a continuous gain in angular momentum of migrators as long as the feature persists. We sus-

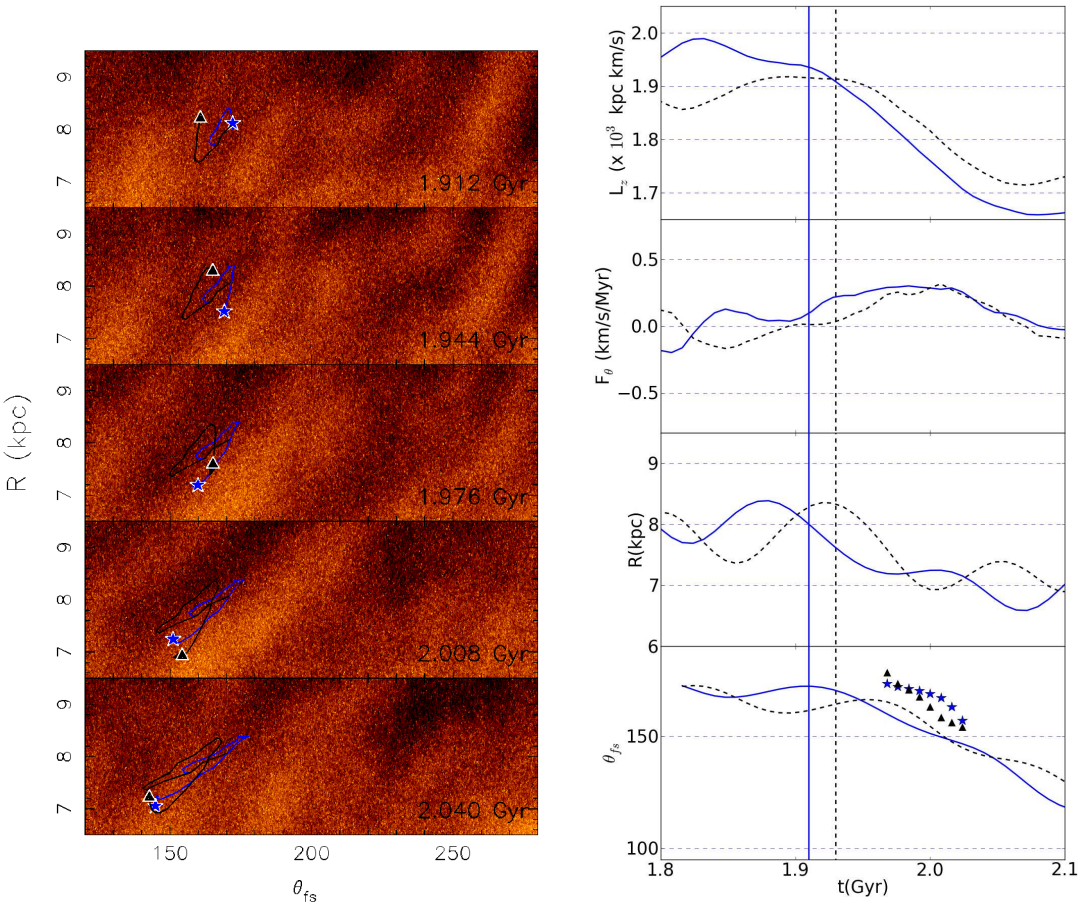


Figure 5.8: The same as Fig. 5.7 but for types of negative migrator.

pect that their spiral arm is short-lived, and that the 6 epicycle motions seen over $\sim 0.5$ Gyr are affected by several transient spiral arm features that co-rotate and accelerate star particles behind the spiral arm at all radii.

#### 5.5.1.3 Type 3g positive migrators

The third type (Type 3g) of positive migrator (green square and green solid line in the left panels and green dot-dashed line in the right panels of Fig. 5.7) originates much farther from the spiral arm as it begins to build up at around $t \sim 1.9$ Gyr (top-left panel of Fig. 5.7), and consequently begins to feel a negative tangential force at the later time of $t \sim 1.93$ Gyr with respect to Types 1g and 2g. At this time, the star particle approaches the pericentre phase of the epicycle (3rd-right panel of Fig. 5.7), and therefore it moves closer to the spiral arm at $t \sim 1.976$

Gyr in the left panels and bottom-right panel of Fig. 5.7. In this case, both the outward epicycle motion and the angular momentum increase facilitate the outward motion of the star particle. As a result, the particle radius increases very rapidly (third-right panel of Fig. 5.7).

Note that the star particle reaches the apocentre at $t \sim 2.02$ Gyr, well before the angular momentum gain ends at $t \sim 2.06$ Gyr. This means that around $t \sim 2.02$ Gyr, the radial gravitational force becomes greater than the enhanced centrifugal force provided by the boost in angular momentum. The radial evolution of the star particle then proceeds inwards while the particle continues to gain angular momentum until epicycle motion resumes at $t \sim 2.06$ Gyr.

### 5.5.2 Orbits of negative migrators

Fig. 5.8 shows the evolution of an example of each type of negative migrator found in the particle sample. Each panel is the same as in Fig. 5.7.

#### 5.5.2.1 Type 1l negative migrator

The first type (Type 1l) of negative migrator (blue star and solid blue line in the left panels and blue solid line in the right panels of Fig. 5.8) is the counterpart of the Type 1g positive migrator shown in Fig. 5.7. The 2nd-right panel of Fig. 5.8 shows that the star particle begins to feel a positive tangential force at a time of around $t \sim 1.91$ Gyr, when the particle is moving towards the pericentre phase of orbit (3rd-right and 1st-left panel of Fig. 5.8). As the spiral arm grows in density, e.g. $t = 1.944$ and 1.976 Gyr (2nd- and 3rd-left panels of Fig. 5.8), the star particle continues to feel a strong positive tangential force accompanied by a steep negative slope in the angular momentum evolution (1st-right panel of Fig. 5.8). At $t \sim 1.98$ Gyr, the radial gravitational force and centrifugal force are temporarily balanced and the star particle stays at $R \sim 7.2$ kpc for $\sim 30 - 40$ Myr - a similar radial pause to that of the Type 1g migrator described in the previous section. At $t \sim 2.02$ Gyr, the radial gravitational force plus the loss in angular momentum overcome the centrifugal force, hence the star particle moves radially inward again. As the spiral arm begins to fade at around $t \sim 2.06$ Gyr, the tangential force diminishes, and the star particle resumes normal epicycle motion. Again, the star particle has remained in front of the spiral arm and continually migrated along the spiral arm.

#### 5.5.2.2 Type 3l negative migrator

The other example star particle shown in Fig. 5.8 is the negative migrator counterpart of the Type 3g positive migrator, and therefore we designate it as Type 3l (black triangle and black solid line in the left panels and black dashed line in the right panels of Fig. 5.8). This star particle originates farther from the spiral arm than Type 1l as the spiral arm begins to build up at $t = 1.912$ Gyr (top-left panel of Fig. 5.8). Therefore, the star particle begins to feel the positive tangential force (deceleration) at a time of $t \sim 1.93$ Gyr, which is later than the time at which the Type 1l negative migrator begins to lose angular momentum (2nd-left and 2nd-right panels of Fig. 5.8). At this time, the star particle is close to the apocentre phase of orbit (3rd-right panel of Fig. 5.8), and consequently moves closer to the spiral arm at $t \sim 1.976$ Gyr (3rd-left panel of Fig. 5.8). Similar to the Type 3g positive migrator, the inward direction of the angular momentum change and epicycle motion means that the star particle moves rapidly towards the centre of the galaxy (left panels of Fig. 5.8). Again, the star particle reaches the pericentre at $t \sim 2.01$ Gyr, before the angular momentum loss has ceased. This means that the centrifugal force becomes greater than the radial gravitational potential even though the star particle continues to lose angular momentum. The tangential force diminishes at $t \sim 2.07$ Gyr, when the particle resumes epicycle motion.

#### 5.5.2.3 No Type 2l negative migrator

We could not find a negative migrator counterpart to the Type 2g positive migrator. This may be attributed to the presence of another spiral arm e.g. the one seen on the front side of the main spiral arm at around ($R$ kpc, $\theta_{fs}$) = $(8, 130)$ at 1.976 Gyr (3rd-left panel of Fig. 5.8) relative to the main spiral arm on which we focus $(R, \theta_{fs}) = (8, 185)$. This is closer than the spiral arm behind the main spiral arm at $(R, \theta_{fs}) = (8, 265)$. The closer proximity to the main spiral of the density enhancement on the front-side of the spiral arm in comparison to the density enhancement on the back-side of the spiral may cause the motions of star particles in front of the spiral to be more influenced by neighbouring density enhancements than those behind the main spiral arm.

To mirror the Type 2g positive migrator, the Type 2l negative migrators would have begun to lose angular momentum just after they passed pericentre. In this

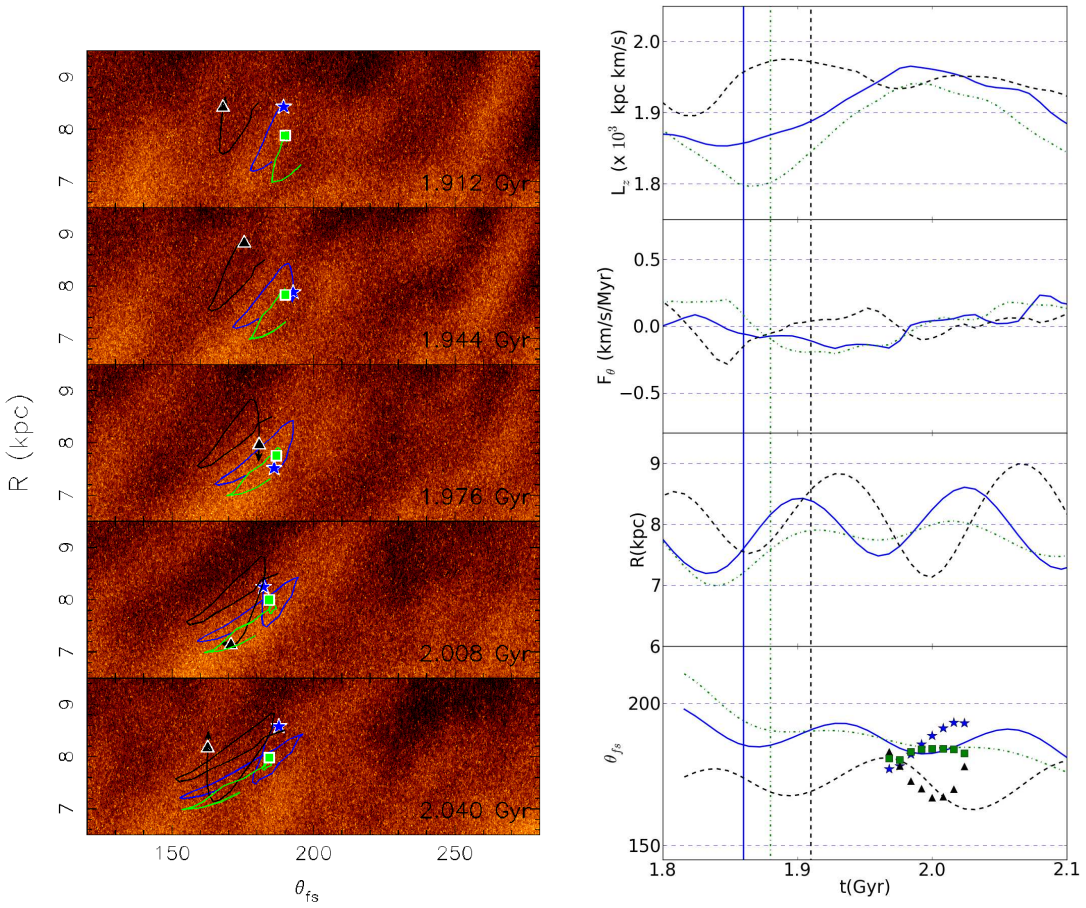


Figure 5.9: The same as Fig. 5.7 but for types of non-migrator.

epicycle phase, the Type 2l star particle would temporarily move away from the spiral arm (because it has a higher rotation velocity in this phase than the spiral arm), and it is possible that the over-density in front of the spiral arm "mopped up" these star particles, which would either reduce or change sign of the positive tangential force acting upon the star particle. This would mean that these star particles gained some angular momentum from this over-density during the time window examined. Therefore, these star particles would not be strong migrators, because they would populate a region of lower $|\Delta L_z|$ in Fig. 5.3. In this case, they will not be selected in our strong migrator sample.

### 5.5.3 Orbits of non-migrators

In this section, we analyse the orbital evolution of those star particles that experience very little or no net change in angular momentum over the time window (non-migrators). Fig. 5.9 shows an example of each of the three types of non-migrator in the sample.

#### 5.5.3.1 Type 1n non-migrator

The first type of non-migrator (Type 1n, represented by the blue star and solid blue line in the left panels and the solid blue line in the right panels of Fig. 5.9), is very close to where the spiral arm begins to build up at $t \sim 1.912$ Gyr (1st-left panel of Fig. 5.9), and it begins to feel a negative tangential force early at $t \sim 1.86$ Gyr (2nd-right panel of Fig. 5.9). At $t = 1.944$ Gyr (2nd-left panel Fig. 5.9), the star particle is located in between the main spiral arm at $(R, \theta_{fs})$ $= (8, 185)$ and the weaker spiral arm behind it at $(R, \theta_{fs}) = (8, 205)$ - in contrast to the positive migrators which were behind both density enhancements at this time. The star particle moves towards pericentre (3rd-right panel of Fig. 5.9), while it gains angular momentum (top-right panel of Fig. 5.9). Because the star particle is around pericentre and located close behind the arm (3rd-left panel of Fig. 5.9), the star particle moves towards the spiral arm until $t \sim 1.99$ Gyr when it passes the spiral arm, as seen in the bottom-right panel and the 3rd- and 4th-left panels of Fig. 5.9. The particle is now located on the front side of the spiral and as a result the tangential force acting upon the star particle has become positive, which causes the star particle to begin to lose angular momentum. The star particle then resumes epicycle motion as the spiral arm fades at $t \sim 2.05$ Gyr.

The general properties of these non-migrators is that they originate very close to the spiral arm, and orbit the spiral arm until it disappears, continually gaining and losing angular momentum such that the net angular momentum gain is $\Delta L_z \sim 0$, at the end of the time window. It is worth noting that when the star particle is circling around the spiral arm, the amplitude of the epicycle motion is smaller. This is because the tangential force from the spiral arm acts always to change the guiding centre in the direction opposite to that of epicycle motion. Therefore, as the star particle moves towards pericentre, it is accelerated $(F_\theta < 0)$, which increases the guiding centre and in turn increases the pericentre

radius. For example, the pericentre radius is larger at $t \sim 1.96$ Gyr than at $t = 1.84$ Gyr, and at $t \sim 2.09$ Gyr the pericentre is returned to that at $t \sim 1.84$ Gyr. This indicates the amplitude of the epicycle motion is shortened, because the tangential force from the spiral arm acts against the epicycle motion. The Type 1n orbit is found to originate also in front of the spiral arm when it first feels the tangential force.

#### 5.5.3.2 Type 2n non-migrator

The second type (Type 2n) of non-migrator (black triangle and solid black line in left panels and dashed black line in right panels of Fig. 5.9) is located in front of the spiral arm as it forms at $t \sim 1.944$ Gyr (1st- and 2nd-left panels of Fig. 5.9). It begins to feel a positive tangential force and migrates inward at $t \sim 1.91$ Gyr. This occurs just before the star particle reaches the apocentre of the orbit, and at $t \sim 1.95 - 1.97$ Gyr the loss of angular momentum and the inward epicycle motion (1st- and 3rd-right panels of Fig. 5.9) cause the radius of the star particle to decrease rapidly in a manner similar to Type 3l negative migrator. This causes a decrease in pericentre radius (see the radius at $t \sim 1.87$ and $t \sim 2.0$ Gyr in 3rd-right panel of Fig. 5.9). However, unlike the Type 3l negative migrator, this non-migrator is too close to the spiral arm when it reaches apocentre at $t = 1.94$ Gyr and as a result is passed by the spiral arm at $t \sim 1.98$ Gyr (bottom-right panel of Fig. 5.9). This causes the change of tangential force from positive to negative, and the star particle then gains back the angular momentum lost previously (top-right panel of Fig. 5.9). This once again ensures that this non-migrator has a net angular momentum change of $\Delta L_z \sim 0$ at the end of the time window.

The difference in radial evolution between this Type 2n and the Type 1n non-migrators is that the Type 2n non-migrator shows an increase in epicycle amplitude because the pericentre at $t \sim 2.0$ Gyr is lower with respect to the earlier time, $t \sim 1.86$ Gyr, i.e. the amplitude of epicycle motion is increased instead of decreased as in the case of the Type 1n non-migrator.

It is interesting to note that this type of non-migrator is not found to originate from behind the spiral arm. This may be related to the differences between the front- and back-side of the spiral arm as discussed in §5.5.2.3. In addition, as discussed in §5.5.1.1 and §5.5.3.1, there is a small density enhancement that

| Name | $t_{capture}$ (Gyr) | Initial position | Initial phase | epicycle amplitude | Remain on same side |
|---|---|---|---|---|---|
| 1g | 1.90 | behind arm | before apocentre | none | yes |
| 2g | 1.89 | behind arm | apocentre | shortened | yes |
| 3g | 1.93 | behind arm | pericentre | lengthened | yes |
| 1l | 1.91 | in front of arm | before pericentre | none | yes |
| 3l | 1.93 | in front of arm | apocentre | lengthened | yes |
| 1n | 1.86 | close behind (in front of) arm | pericentre (apocentre) | shortened | no |
| 2n | 1.91 | in front of arm | apocentre | lengthened | no |
| 3n | 1.88 | very close behind (in front of) arm | apocentre (pericentre) | shortened | no |

Table 5.1: Summary of orbital characteristics for each orbital type. Columns show 1) orbital type name 2) the time at which the particle first feels the tangential force, $t_{capture}$ (measured by eye to provide an indication) 3) initial particle position with respect to the spiral arm at $t_{capture}$ 4) the epicycle phase of the particle at $t_{capture}$ 5) the effect on their epicycle amplitude 6) whether or not they remain on the same side of the spiral throughout the spiral lifetime.

merges with the back-side of the spiral arm at $t \sim 1.976$ Gyr. Therefore the back-side of the spiral arm seems to build up later than the front-side, and this likely causes the difference in the variety in the orbits of star particles that originate from the front- and back-side of the spiral arm.

#### 5.5.3.3 Type 3n non-migrator

The third type (Type 3n) of non-migrator particle found in this sample (the green square and solid green line in left panels and green dot-dashed line in the right panels of Fig. 5.9) begins to feel a negative tangential force at $t \sim 1.88$ Gyr (2nd-right panel of Fig. 5.9) just as it reaches the apocentre of the orbit at $t \sim 1.912$ Gyr (top-left and third-right panels of Fig. 5.9). This is accompanied by an increase in angular momentum (top-right panel of Fig. 5.9) from about $t \sim 1.88 - 1.99$ Gyr. During this time, the radius of the star particle proceeds to apocentre and exhibits a small dip in radius at $t \sim 1.96$ Gyr (3rd-right panel of Fig. 5.9). This is obviously the feature of an increased pericentre radius owing to the imbalance between the radial gravitational force and centrifugal force boosted

by a gain in angular momentum. The pericentre-like feature is also seen in the bottom-right panel of Fig. 5.9, which shows a decreasing $\theta_{fs}$ of the star particle (line) that brings the star particle closer to the spiral arm in azimuth angle (square symbols) at $t \sim 1.96$ Gyr.

At $t \sim 1.99$ Gyr, the star particle passes the spiral arm and begins to lose angular momentum (right panels in Fig. 5.9). Up to $t \sim 1.99$ Gyr, this non-migrator exhibited similar evolution to Type 1g positive migrators, but it differed after this time by crossing the spiral arm instead of remaining behind it. This is entirely because this non-migrator is too close to the spiral arm, such that even a $v_\theta$ that is slightly faster than the spiral arm rotation velocity will take the particle past the spiral arm. Again this highlights the importance of azimuth angle of the star particle with respect to the spiral arm. This type of non-migrator exhibits shortened epicycle amplitude during the period before it crosses the spiral arm. This is different from Type 2n, which shows extended epicycle amplitude, and it is also different from Type 1n, which shows shortened epicycle amplitude as it circles the spiral arm. This Type 3n non-migrator is found both in front of and behind the spiral arm, unlike Type 2n.

### 5.5.4 The tangential force

We have shown above that time periods of sustained tangential force, which cause strong radial migration, depend on the star particle position with respect to the spiral arm. For example, the negative migrators that feel strong positive tangential forces lose angular momentum while they feel that force, which is possible because the particle always remains in front of the spiral arm. However, there exist some non-migrators that spend time in similar regions around the spiral as migrators, but upon which almost no tangential force acts.

To explore this, we compute a map of the tangential force. Fig. 5.10 shows the density map of the spiral arm with contours of tangential force over-plotted in white at $t = 1.976$ Gyr (solid for positive values and dashed for negative values). As expected, the tangential force is zero at the density peak of the spiral arm. The tangential force becomes stronger with increasing azimuthal distance from the spiral arm, until it reaches a maximum, $\sim$ 10-20 degrees away from the density peak on either side. At distances farther from the peak of the spiral arm, the tangential force decreases and eventually changes the sign, owing to the force

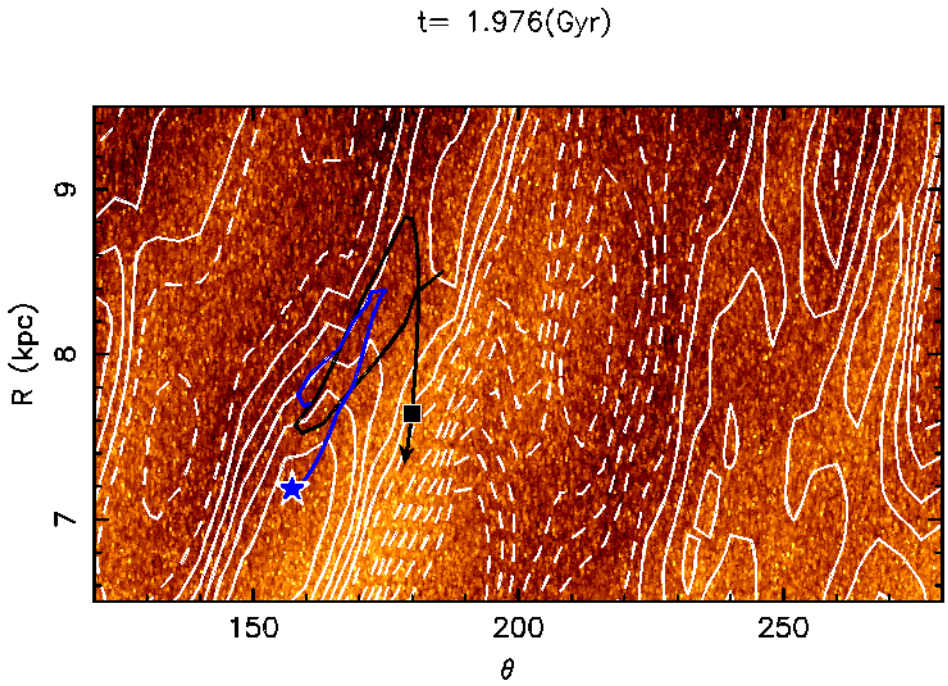


Figure 5.10: Close up of the density map in the $R - \theta_{fs}$ plane at $t = 1.976$ Gyr, with contours of the tangential force over-plotted in white. Solid lines indicate positive tangential force (acting in the direction of positive $\theta_{fs}$) and dashed lines indicate negative tangential force (acting in the direction of negative $\theta_{fs}$). The position of the Type 1l negative migrator and Type 2n non-migrator are represented by a blue star and black square respectively, and their orbit histories shown by the solid lines of the same colour.

contributions from neighbouring spiral arms. It is interesting to see the difference between the front- and back-sides of the spiral arm. On the front-side of the arm the point of the maximum tangential force is closer to the density peak of the spiral arm than that on the back-side of the spiral arm. This is because the neighbouring spiral arm on the front-side is closer than the one on the back-side. On the back-side, the small density enhancement merges to the main spiral arm around $R = 8.5$ kpc, which pushes the point of the maximum tangential force farther from the density peak of the main spiral arm.

We show the orbit history of the Type 1l negative migrator (blue star and solid blue line in Fig. 5.10) shown in §5.5.2.1 and the Type 2n non-migrator (black square and solid black line in Fig. 5.10) shown in §5.5.3.2. The figure shows that the negative migrator is captured in a region of strong tangential force in front of the spiral arm, which continues over the spiral arm lifetime (see 2nd-right panel of Fig. 5.8). However, the non-migrator, despite being located in front of the spiral arm and having a very similar orbit to the negative migrator, feels almost no tangential force over this time period (see 2nd-right panel of Fig. 5.9) because the star particle is too close to the peak of the spiral arm. This implies that it is not enough that the star particle is located on one side of the spiral arm in order to become a migrator: the migrator must be far enough away from the spiral arm peak line - yet not too far! - in order to be captured by regions of strong tangential force such as those shown in Fig. 5.10. We therefore refine the condition for a strong positive (negative) migrator to be a star particle able to remain at a *suitable* distance behind (in front of) the spiral arm. This re-emphasizes the importance of the $R\Delta\theta$ parameter in distinguishing strong migrators from non-migrators.

## 5.6 Broader Implications of Radial migration

The main results of this study focus on the complicated interactions between the spiral arm and a variety of orbital types, on timescales roughly equal to the spiral arm lifetime. Each type of migrator particle experiences a change in angular momentum on these timescales (Fig. 5.3). On longer timescales, i.e. 1 Gyr, a star particle may interact with a spiral several times. The cumulative effect of consecutive spiral arm-star particles interactions is reflected in the evolution of

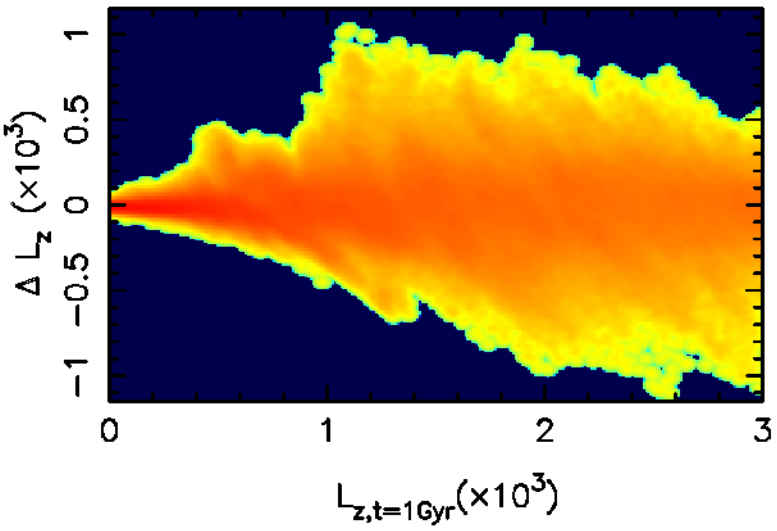


Figure 5.11: The change in angular momentum, $\Delta L_z$, between $t = 1.0$ and 2.0 Gyr of the disc particles as a function of their angular momentum at $t = 1.0$ Gyr. Red colours indicate regions of high number density.

global properties of the disc, such as the mass and metal distribution. In this section, we briefly discuss the effects of radial migration in this simulation on longer timescales.

Co-rotating spiral arms have been shown to cause radial migration at many radii, and this work confirms that migration will continue as long as the star particle remains on the same side of the spiral arm in a region of strong tangential force. This means that radial migration in this simulation is efficient at transporting star particles to different guiding radii. This is shown in Fig. 5.11, which shows the change in angular momentum of disc particles between the times of 1.0 and 2.0 Gyr as a function of their angular momenum at $t = 1.0$ Gyr. This shows much more radial migration than for the shorter timescale shown in Fig. 5.3 ($\sim 5$ times as much). Although this radial migration redistributes the individual angular momenta of star particles (see also Figs. 5.7, 5.8 and 5.9), the overall angular momentum distribution of the disc and the cumulative mass profile remain almost unchanged (see Fig. 5.12).

The movement of star particles from one guiding radius to another affects

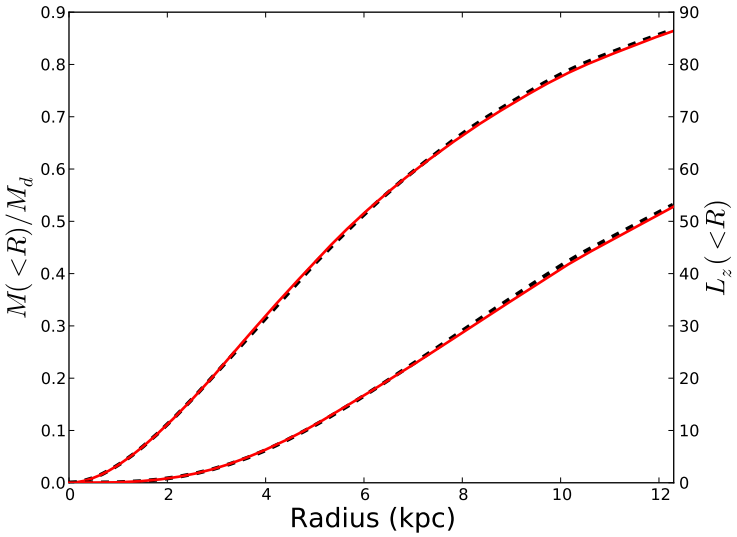


Figure 5.12: The cumulative profiles of total disc mass fraction (upper curve) and angular momentum (lower curve). The solid red and dashed black curves show the profiles at $t = 1.0$ and $t = 2.0$ Gyr, respectively.

the distribution of metals in the disc. To give an indication of the effect on the metal distribution of the radial migration in this simulation, we artificially assign metallicity values to each star particle in the simulation at a time of $t = 1.0$ Gyr. We randomly assign each star particle a metal value by drawing from the gaussian metallicity distribution function at each radius with a dispersion of 0.05 dex. The mean on which a gaussian is centred at a given radius is defined by a metallicity gradient of $-0.05$ dex/kpc, and $[\mathrm{Fe/H}](R = 0) = 0.25$ dex. The top row of Fig. 5.13 shows the smoothed distribution of stars in metallicity as a function of radius at $t = 1.0$ Gyr (left panel) and $t = 2.0$ Gyr (right panel). The metallicity gradient does not change much at all between 1.0 and 2.0 Gyr. This is because the radial migration is not strong enough to mix stars at such a rate as to affect the slope. However, the metallicity distribution at any given radius broadens with time. The bottom row of Fig. 5.13 shows the same as the top row but for an initial radial metallicity gradient of $-0.1$ dex/kpc. At $t = 2.0$ Gyr, although the radial metallicity gradient remains unchanged, the metallicity distribution shows a much larger broadening owing to the the steeper gradient, as expected. Despite our crude metallicity analysis, a similar effect is seen in Fig. 16 of Casagrande *et al.* (2011), who show that in the solar neighbourhood, the metallicity distribution of stars aged between $1 - 5$ Gyr is comparatively broad

in comparison with that of stars younger than 1 Gyr, and both populations have the same peak metallicity value (see also Haywood, 2008). We stress that these results are from this simulation only, and should not be taken as the general case for simulated spiral galaxies. For example, parameters such as spiral arm strength and pitch angle likely play a role in the amount of radial migration and therefore the degree of mixing that occurs in a spiral disc. Moreover, this result is derived from a $N$-body simulation in which metallicities have been assigned artificially at an arbitrary time. For a robust analysis on the effect of spiral morphology on metal distributions, many simulations that include the gas component and recipes for star formation and chemical evolution need to be analysed and compared with each other and observation. This topic deserves a thorough numerical study (see §6).

All of the analysis presented in this chapter has been with regard to one simulation, which has a flocculent spiral structure with no bulge or bar at the centre. However, we have seen some evidence that the group characteristics of the positive, negative and non- migrators are present also in simulated galaxies of different spiral structure, and show similar separations in the phase space planes shown in Fig. 5.4. These simulations include a 3-4 armed galaxy with a static bulge in the centre (simulation F in §4), and the barred-spiral galaxy of two arms presented in §3.

## 5.7 Conclusions

We have performed high resolution N-body simulations of a spiral disc embedded in a static dark matter halo potential. We focus on a sample of star particles taken from around the spiral arm and divide this sample into three groups according to the amount of change in angular momentum, i.e. radial migration, of the star particles over a given time period when the spiral arm is strong. These groups are: star particles that gain the most angular momentum (positive migrators), star particles that lose the most angular momentum (negative migrators) and star particles that show almost no change in angular momentum (non-migrators).

We follow the evolution of these groups in $v_\theta - v_R$, $v_\theta - R\Delta\theta$ and $v_\theta - R$ planes, and come to the following conclusions:

- Positive migrators tend to cluster around the region of velocity space that is

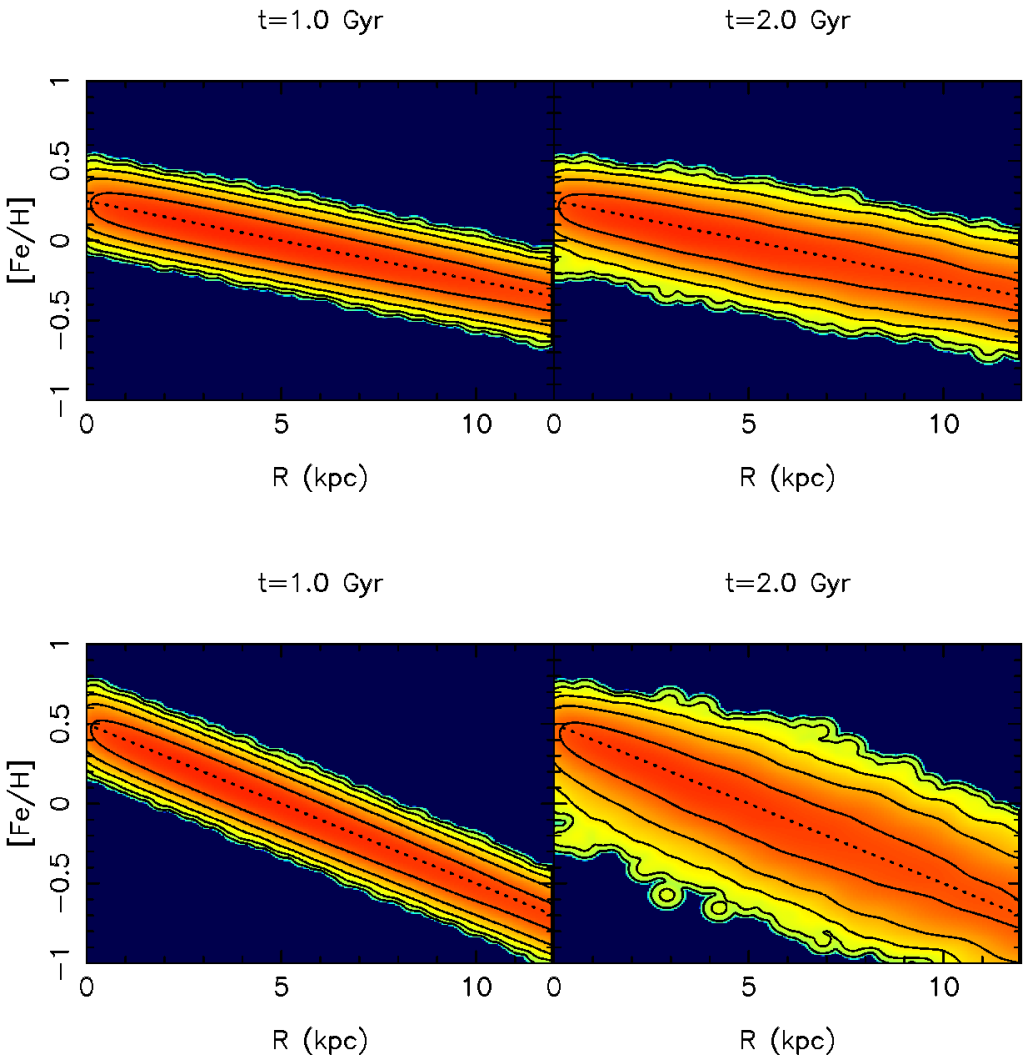


Figure 5.13: Metallicity distribution of all disc stars as a function of radius at $t = 1.0$ Gyr (left panel) and $t = 2.0$ Gyr (right panel). *Top:* The initial assigned metallicity gradient is $-0.05$ dex/kpc, and the dispersion of the gaussian metallicity distribution function is 0.05 dex. *Bottom:* The initial assigned metallicity gradient is $-0.1$ dex/kpc, and the dispersion of the gaussian metallicity distribution function is 0.05 dex. In all panels the initial metallicity gradient is shown by the dashed black line. Contours and red colours indicate regions of high number density.

slower than the mean rotation velocity (apocentre), whereas negative migrators tend to cluster around the region of velocity space that is faster than the mean rotation velocity (pericentre). Non-migrators are more evenly distributed in $v_\theta - v_R$ space.

- Positive migrators always stay behind the spiral arm ($R\Delta\theta < 0$) and negative migrators always stay in front of the spiral arm ($R\Delta\theta > 0$). Non-migrators are found on both sides of the spiral arm; those with azimuthal velocities faster than the circular velocity tend to be located behind the spiral arm, whereas those with azimuthal velocities slower than the circular velocity tend to be located in front of the spiral arm.

- The slope in the $v_\theta - R\Delta\theta$ space of the distribution of non-migrators indicates that non-migrators located behind the arm have higher azimuthal velocities the farther behind the arm they are. Similarly, the non-migrators in front of the spiral arm have lower azimuthal velocities the farther in front of the spiral arm they are when the spiral is forming.

We then examined the orbital evolution of individual star particles in each particle group in detail. We categorised and contrasted several orbital types of each group, each of which is a new type of orbit shown for the first time in this study.

There are three types of positive migrators, each characterised by the time they feel the tangential force, their phase of epicycle motion when this force is introduced and their azimuthal distance from the spiral arm:

- Type 1g originates relatively close to the spiral arm and begins to migrate just before apocentre. It exhibits a radial pause owing to the temporary balance between radial gravitational force and centrifugal force, before continuing to move outward.

- Type 2g originates from a similar position to Type 1g, and begins to migrate at a similar time but after it reaches apocentre. This causes the star particle to exhibit a shortened epicycle amplitude because angular momentum increases the radius of the pericentre.

- Type 3g originates farther from the arm than Types 1g and 2g, and begins to migrate at later times than Types 1g and 2g, around the pericentre phase, and as a result exhibits rapid changes in radius.

This variety of orbits shows that positive migrators can be in any epicycle phase at the time the tangential force is introduced. However, migrators that originate far from the spiral arm must be in the pericentre phase of orbit in order to catch the spiral arm and undergo large angular momentum changes. Migrators that are located closer to the spiral arm begin to migrate around apocentre because if they are in pericentre, they will pass the spiral arm and any increase in angular momentum will be arrested, as we show in §5.5.3. Hence, the key for strong positive migrators is to stay behind the spiral arm, which is verified in the bottom-right panel of Fig. 5.7 for each positive migrator example. In this way, irrespective of the phase of epicycle motion, the star particles continue to gain angular momentum from the spiral arm. We find similar types of orbits for the negative migrators. However, we did not find any Type 2 negative migrator analogue to Type 2g positive migrator. We think that this is because the spiral arm on which we focus has different properties and formation processes on the front- and back-side of the spiral arm.

We found three types of non-migrators:

- Type 1n originates very close to where the spiral arm forms, and always moves in the radial direction opposite to that of the change of guiding centre. They generally move toward pericentre when they are behind the spiral arm, and toward apocentre when they are in front of the spiral arm. This causes them to orbit the spiral arm for $\sim$ 1 epicycle period with a shortened epicycle amplitude. This type is found on both sides of the spiral arm.

- Type 2n originates farther from the spiral arm than Type 1n. It crosses the spiral arm from the front side as it moves towards pericentre, and therefore exhibits an elongated epicycle amplitude. This type is found on the front-side of the spiral arm only.

- Type 3n originates close behind the spiral arm, and gains angular momentum such that it exhibits shortened epicycle motion while remaining on the

same side of (behind) the spiral arm. It is so close to the spiral arm that it passes the spiral arm as it moves through pericentre. This type is found on both sides of the spiral arm.

Each type of non-migrator shows that position relative to the spiral arm is very important, and has consequences for the star particle evolution. It is again important to note that although these particles were selected as showing $\Delta L_z \sim 0$ within the selected migration time window, they may go on to migrate around other spiral arms at later times, and may have undergone migration around past spiral arms at earlier times.

The importance of the proximity of the star particle to the spiral arm and the epicycle phase of motion of the particle found in the orbital anaylsis is consistent with the trend seen in the sample distribution in the $R\Delta\theta - v_\theta$ plane shown in the middle row of Fig. 5.4. It shows that strong migrators are always located on the same side of the spiral arm throughout the lifetime of the spiral arm, while non-migrators tend to pass/be passed by the spiral arm owing to the faster/slower rotation velocities of the non-migrators relative to that of the spiral arm, given close enough proximity. This underscores the criterion for star particles to become strong positive (negative) migrators as the ability of a star particle to remain behind (in front of) and stay close to the spiral arm as long as it is present.

We have found that there are certain distances from the spiral arm at which exist regions of strong tangential force. Migrators tend to be captured by these regions, whereas non-migrators may miss the strong force regions by moving too close to the spiral arm. In that case, the star particle does not feel much tangential force and does not change angular momentum. This emphasizes the importance of azimuthal distance from the spiral arm. Indeed we find that strong migrators remain at a suitable distance from the spiral arm.

The detailed information of particle orbit histories of large star samples may provide clues to how the spiral arm is formed and destroyed. This information is likely to be found in not just strong migrators and non-migrators, but from much larger star particle samples that exhibit many different degrees of radial migration. From these kind of data, it may be possible to see how the spiral arm is constructed as the influx of star particles from regions around the disc into the forming spiral arm increases the density and eventually leads to the fully formed spiral features. In the same spirit, the future trajectories of many star

particles that make up the spiral features may give us an insight into how these features are disrupted. The non-linear nature of the particle motion that we have glimpsed makes this method of analysis a promising direction to pursue, and we leave this complicated investigation to future studies.

# Chapter 6

# Conclusions and Future work

This thesis describes our studies of high resolution $N$-body/SPH simulations of disc galaxies that develop spiral structure. We examine the evolution of spiral structure and the influence of spiral structure on the dynamics of disc stars, and compare our findings with predictions of spiral density wave theory and swing amplification theory. The results obtained are highly relevant to disc galaxy evolution, and probe the nature of the spiral arm. They are summarised below.

## 6.1 Co-rotating spiral arms

From pure $N$-body simulations, we show in §2 that the spiral arms are transient features, and traced the position of the spiral arm density at several moments in time. From this information, we show that spiral arms rotate with a pattern speed that decreases with radius and closely matches the circular velocity profile of the disc stars (see also Wada *et al.*, 2011; Sellwood, 2011; Comparetta & Quillen, 2012; Roca-Fàbrega *et al.*, 2013), contrary to the constant pattern speed of density wave theory. This naturally leads to the winding up of the spiral arms because stars in the inner regions rotate faster than those in the outer regions. As a result, spiral arms disrupt and new spiral arms appear, such that the galaxy always displays spiral morphology, but individual arms have lifetimes of order $\sim 100$ Myr.

In §3, we confirmed that the same conclusions hold in a barred disc with a gas component. We further test the spiral arm nature by examining the distribution of different age star particles across the spiral arm at different radii. For a rigidly

rotating spiral arm that has a constant pattern speed, there is only one radius of co-rotation where the spiral arm rotates at the same speed as the stars. Inside this radius, stars rotate faster than the spiral arm, therefore one would expect young stars born in the spiral arm to move in front of the spiral as they age. The opposite would be the case outside the co-rotation radius. Observationally, this predicts a spatial offset between different star forming tracers and young stars near the spiral arm (Roberts, 1969). From our analysis we found no evidence for an offset between ongoing and recent star formation sites at any radius (see also Dobbs & Pringle, 2010), which indicates that the majority of stars born in the spiral arms travel with the spiral arms owing to their co-rotating nature. This result is at odds with density wave theory, but consistent with recent observational studies (e.g. Foyle *et al.*, 2011; Ferreras *et al.*, 2012).

## 6.2 Extended radial migration

Radial migration is the process by which the orbital guiding centre of a star changes owing to angular momentum changes caused by non-axisymmetric structure. The change in angular momentum of a star is accompanied by a near zero change in non-circular kinetic energy, therefore the orbit of the migrated star remains kinematically cool (see §1.3). In §2 and §3, we showed that because stars rotate at the same speed as the spiral arm at all radii, radial migration occurs at every radius where spiral structure exists. Star particles migrating radially outward always stay behind the spiral arm. Similarly, stars that migrate radially inward stay in front of the spiral arm (later confirmed by Roškar *et al.*, 2012b; Baba *et al.*, 2013). This means that radial migration continues until the spiral arm disrupts and that radial mixing is stronger than previously thought, which is a direct consequence of the co-rotating spiral arm. In addition, we show that the orbital eccentricity of migrated stars is almost conserved, as expected at co-rotation (Lynden-Bell & Kalnajs, 1972), with a slight decrease in eccentricity for outward moving migrators and increase for inward migrators (in agreement with Minchev *et al.*, 2012a).

In §5, we traced individual star particle motion in detail and showed that migrating star particles have particular velocities and orbits that create systematic streaming motions along the spiral arm. We uncovered several new previously

unreported types of orbits. For example, one such orbit is a star particle that does not migrate but instead stays within the spiral arm, continuously passing through the spiral arm until it disappears. The orbital analysis reveals that the position of the star particles in phase space at the early stages of spiral arm formation is an important factor in the subsequent orbital evolution. In particular, migrating particles close behind the spiral arm are typically at their apocentre phase of their epicycle motion, while if a star particle behind the spiral arm is in the pericentre phase of epicycle motion, it passes the spiral arm and is classified as a non-migrator particle. The same trend holds on the leading side of the spiral arm.

Our studies in §5 have shown that while the radial migration of individual particles is an effect of the co-rotating spiral arm, the overall angular momentum distribution is hardly affected. In addition, the radial metallicity gradient of stars does not appear to change over 1 Gyr periods of galaxy evolution, although the scatter in the metallicity distribution at all radii increases by an amount that scales with the steepness of the assumed initial metallicity gradient (for a given spiral structure).

## 6.3 A Hubble sequence of pitch angles

The extensive numerical study presented in §4 showed for the first time that the pitch angle of spiral arms is strongly correlated with the galactic shear rate in $N$-body simulations, with rising rotation curves associated with open spirals (high pitch angle). We showed that the results are robust against particle mass resolution, softening length and variations of disc-halo mass ratio. The correlation found in §4 is consistent with the analytically derived relation of Fuchs *et al.* (2005) based on swing amplification theory (Julian & Toomre, 1966; Toomre, 1981), and recent observations of a sample of spiral and barred-spiral galaxies (Seigar *et al.*, 2005, 2006). In addition, the result offers an explanation of the scatter in the observed correlation because the winding spiral arm naturally leads to a range of pitch angles over the lifetime of each spiral arm.

## 6.4 Implications

As discussed above, our studies clearly highlight that the evolution of spiral structure and nearby stars is inconsistent with the classic density wave theory proposed by Lin & Shu (1964), implicating that, at least in numerical simulations of isolated spiral discs, the spiral density wave description does not hold. We speculate that the orbital behaviour of stars (particles) found in our studies applies to any co-rotating spiral arm, and as such, all isolated galaxies including those with a bar. However, it is possible that galaxies with companion satellites are experiencing different evolution (Dobbs *et al.*, 2010; Purcell *et al.*, 2011). Therefore, for the moment we restrict our findings to be important for isolated galaxies.

Our studies suggest that the formation of transient spiral arms in numerical simulations is different from swing amplification theory (Julian & Toomre, 1966; Toomre, 1981). In $N$-body simulations, the lifetime of a spiral arm, defined as the time between the initial growth and disruption of an over-dense region, is of order $\sim$ 100 Myr ($\sim$ half a galactic rotation). However, the swing amplified, over-dense patch described in Toomre (1981) rotates slower than the disc material, and as a result takes $\sim$ few galactic rotations to wind up and fade away (see their Fig. 8). Furthermore, the orbital analysis presented in §5 reveals that although migrator particles undergo a motion similar to what is predicted by swing amplification (star particles on the trailing (leading) side join the arm at the apocentre (pericentre) phase of their epicycle motion while the spiral arm grows), their orbits proceed to be strongly influenced by the spiral arm through radial migration because the migrating stars continue to co-rotate with the spiral arms. Therefore, particles continue to migrate along the spiral arm, instead of retreat away as expected from swing amplification. This produces hitherto unexpected systematic streaming motions caused by continuous radial migration along the spiral arm.

The discrepancy between swing amplification theory and $N$-body simulations probably arises because the former is a linear theory, whereas $N$-body simulations are able to capture non-linear effects. Indeed, the simulations seem to show that the growth and decay of spiral arms is a non-linear phenomenon; rapid growth from small perturbations in the disc density and subsequent rapid decay cannot be linear. Further evidence of the non-linearity of $N$-body simulations is presented in D'Onghia *et al.* (2013), who showed that the growth of spiral arms is perpetuated

by non-linear effects, in contrast with the predicted decay of such structures in the swing amplification formalism.

In recent years, alternative mechanisms of spiral evolution have arisen in attempt to explain winding, transient spiral arms. One such mechanism is the multiple mode theory, in which there are present in the disc more than one spiral density wave pattern. In these descriptions, two (or more) waves, a fast rotating pattern in the inner region of the disc and a slow rotating pattern in the outer region of the disc, may periodically interfere with each other at a range of radii over which the wave patterns overlap (e.g. Roškar *et al.*, 2012b; Comparetta & Quillen, 2012; Sellwood & Carlberg, 2014). The winding of spiral arms is reproduced in these theories, but the spiral arm density is assumed to follow a linear superposition of the densities of two or more individual wave modes, which may be inconsistent with the non-linear behaviour of spiral arms implied by numerical simulations. Furthermore, they obtain the conclusion of co-existing multiple wave modes from wave mode analysis techniques such as computing power spectra of Fourier transforms, the application of which we showed in §2 to be dubious for the rapidly evolving spiral discs seen in simulations. Even in studies that support the multiple mode theory, the wave modes are found to be short-lived (Roškar *et al.*, 2012b), which indicates that even in this picture there are no such thing as stationary waves.

Based on current numerical results, we speculate that the formation, evolution and disruption of spiral arms is related to the galactic shear rate and the radial migration of stars and gas along the co-rotating spiral arm. The simulations have highlighted the prominence of radial migration as a response to the formation of spiral structure, and that the same particles that radially migrate also take part in the growth of spiral arm strength. We believe that the governing process holds a central mechanism akin to the concept of swing amplification - although non-linear in nature, that may propagate radially and stimulate growth at all radii. The growth attains a maximum amplitude at a pitch angle determined by the shear rate, and proceeds to disrupt as it winds further. It is possible that the disruption of the spiral arm may be caused by a combination of radial migration and epicycle motion which may act to move stars away from the spiral feature. Indeed, the lifetime of the spiral arm is comparable to an epicycle period. The high degree of complexity of the formation and evolution of spiral arms

shown in simulations highlights the need for increasingly detailed analyses of ever improving numerical simulations, and many comparisons with observations. Below, we outline some ideas for progressing our understanding of the nature of spiral arm structure.

## 6.5 Future work

The conclusions of this thesis highlight the need for a re-examination of how spiral arms form. To address this issue, we plan to develop a clear set of predictions from high resolution simulations taking into account self-gravity, hydrodynamics, radiative cooling, star formation and metal enrichment. The simulations will be tuned to a sample of galaxies (including the Milky Way) distributed among the Hubble types. This will allow us to scrutinise important mechanisms in galaxy formation and evolution, and make detailed comparisons with astrometric and spectroscopic data from current and next generation Galaxy surveys such as *Gaia* (e.g. Lindegren *et al.*, 2008), Gaia-ESO (Gilmore *et al.*, 2012), SEGUE (e.g. Yanny *et al.*, 2009; Lee *et al.*, 2011), APOGEE (e.g. Allende Prieto *et al.*, 2008; Bovy *et al.*, 2012) and HERMES-GALAH (Zucker *et al.*, 2012). For extra-galaxies, we can compare the simulation results with multi-wavelength images from Spitzer (Kennicutt *et al.*, 2003), Swift/UVOT (Roming *et al.*, 2005), high resolution molecular gas images and kinematics from instruments such as ALMA and spectroscopy from integral field unit spectroscopy (IFU) instruments such as CALIFA (Sánchez *et al.*, 2012) and SAMI (Croom *et al.*, 2012).

### 6.5.1 Spiral galaxy catalogue

The aim of the main future project we plan to undertake is to build on our current understanding of co-rotating spiral arms and develop a theory of spiral arm formation and evolution consistent with observation. In order to change the paradigm of our understanding of the spiral arm, many simulations of different types of spiral galaxies are required. To this end, we will examine the nature of the spiral structure by combining current and future observational data with output predictions from simulations. This study will include a range of galaxy types, because the spiral arm nature is linked to their morphology as shown in

§4.

A suite of $N$-body/SPH simulations will be tailored to a sample of spiral and barred-spiral galaxies that span a broad range of Hubble types. Each simulation will match observable parameters such as the rotation curve, gas fraction, structural parameters, number of spiral arms, spiral arm pitch angle and amplitude. Each simulation will be run twice: once with the transient, co-rotating spiral arms that arise naturally in $N$-body simulations, and once with an imposed spiral arm potential to mimic density waves. Density wave theory can then be tested critically by comparing the distribution and kinematics of star forming tracers in the simulations (dense gas and different age star particles), with those of the observed star forming tracers such as HI, CO, $H_\alpha$, and UV data. In the future, ALMA will observe star forming tracers with up to 10 milliarcsecond resolution and further refine this test observationally.

At the same time, this suite of realistic simulations will be used to scrutinise the formation of spiral arms across the Hubble sequence (Hubble, 1926). Insight into the growth and development of spiral arms will be obtained by examining individual particle motions (as shown in §5) and how they contribute to the macroscopic growth and decay of spiral arms.

### 6.5.2 Metallicity gradients and star formation

Radial migration has significant effects on the galactic radial stellar age profile and metallicity distribution (Sellwood & Binney, 2002; Roškar *et al.*, 2008b; Sánchez-Blázquez *et al.*, 2009b). Such effects may include a flattening of the radial metallicity gradient of stars, broadening of the metallicity distribution at many radii and the production of inhomogeneities in the metal distribution in the azimuthal direction (Di Matteo *et al.*, 2013). Because radial migration occurs at all radii around the co-rotating spiral arm, the evolution of the metallicity distribution may be different from those expected in other spiral arm theories, for example density wave theory in which radial migration occurs at a single radius (Lépine *et al.*, 2003). However, this has not been well studied to date. We aim to make observable predictions of these effects from the spiral galaxy catalogue, and use them to look for signatures of co-rotating spiral arms in IFU data of external galaxies. In addition, these data can be used to infer the impact of radial

migration on galactic evolution as a function of morphology.

A further extension of this work will be to examine the distribution of star formation sites in discs. In numerical simulations, high density gas is always found to trace the stellar spiral arms (Wada *et al.*, 2011). However, some observations, for example M74, reveal dust lanes on the trailing side of the spiral arms. In order to find the reason for this apparent discrepancy, the distribution of dust lanes and stars can be compared to the gas and stars in simulations with varying star formation and feedback strengths.

### 6.5.3 Application to the Milky Way

*Gaia* will observe parallaxes, radial velocities, proper motions, metallicities and photometry of around 1 billion stars in 6-20 magnitude range in the disc, bulge and halo. In addition, ground based spectroscopic surveys such as the Gaia-ESO survey will supplement this information with radial velocity and metallicity measurements.

The study presented in §5 shows that co-rotating spiral arms predict that radially migrating stars make up moving groups around the spiral arm, which may be detectable in the observed kinematics (see Kawata *et al.*, 2014, for a preliminary study). We may be able to use this prediction as a test of the nature and origin of spiral arms in the Milky Way by developing a mock data set from a Milky Way-like simulation including a bar and spiral arms via the use of tools such as population synthesis and line of sight extinction (Pasetto *et al.*, 2012a). The position of spiral arms can be located from *Gaia* data, which would make it possible to search suitable observed star samples for the predicted moving group features as seen in the mock data. This will add to the variety of tests of co-rotating spiral arms that we will make.

# Appendix A: Density Wave theory

In their linear analysis, Lin & Shu (1964) expand the perturbed time-independent surface density and potential in equations (1.2) as a series of individual harmonic components

$$\Sigma_m(r)\cos m\theta \tag{A.1a}$$
$$F_m(r,z)\cos m\theta, \tag{A.1b}$$

where

$$\Sigma_m(r) = Re\{\Sigma^{(1)}(r)\exp^{i\lambda f(r)}\} \tag{A.2a}$$
$$F_m(r,z) = Re\{A(r,z,\lambda)\exp^{i\lambda\Phi(r)}\}, \tag{A.2b}$$

and $\lambda$ is a positive large quantity used in the asymptotic expansion of the amplitude function, $A(r,z,\lambda)$, in inverse powers of $\lambda$, i.e.,

$$A(r,z,\lambda) = A^{(0)}(r,z) + \lambda^{-1}A^{(1)}(r,z) + \lambda^{-2}A^{(2)}(r,z). \tag{A.3}$$

Inserting equations (A.1) and (A.2) into equation (1.3) gives the pair of conditions:

$$\left[\frac{\partial A}{\partial z}\right] + i\lambda A(r,0)\left[\frac{\partial \Phi}{\partial z}\right] = -4\pi G\Sigma^{(1)}(r), \qquad \Phi(r,0) = f(r). \tag{A.4}$$

The second of equations (A.4) means that the phase factors of both the density and potential are the same, i.e. they are in phase with each other, owing to the WKB approximation. The form of the phase factor is found by substituting equations (A.2) into the Poisson equation (1.1d) to give

$$\begin{aligned}
&\frac{\partial^2 A}{\partial r^2} + \frac{\partial^2 A}{\partial z^2} + \frac{1}{r}\frac{\partial A}{\partial r} - \frac{m^2 A}{r^2} \\
&+ i\lambda\left[A\left(\frac{\partial^2 \Phi}{\partial r^2} + \frac{\partial^2 \Phi}{\partial z^2} + \frac{1}{r}\frac{\partial \Phi}{\partial r}\right) + 2\left(\frac{\partial A}{\partial r}\frac{\partial \Phi}{\partial r} + \frac{\partial A}{\partial z}\frac{\partial \Phi}{\partial z}\right)\right] \\
&- \lambda^2 A\left[\left(\frac{\partial \Phi}{\partial r}\right)^2 + \left(\frac{\partial \Phi}{\partial z}\right)^2\right] = 0.
\end{aligned} \tag{A.5}$$

To first order in this linear expansion, the term proportional to $\lambda^2$ is required to be equal to zero, which is satisfied by solutions

$$\Phi(r,z) = \begin{cases} f(r + i\epsilon z) & \text{if } z > 0, \\ f(r - i\epsilon z) & \text{if } z < 0. \end{cases} \tag{A.6}$$

where $\epsilon = \mathrm{sgn}(f'(r))$. It follows that the derivative of the phase factor with respect to $z$ is written as

$$\frac{\partial \Phi(r,z)}{\partial z} = \frac{\partial f(r \pm i\epsilon z)}{\partial (r \pm i\epsilon z)}\frac{\partial (r \pm i\epsilon z)}{\partial z} = \pm i\epsilon f'(r \pm i\epsilon z), \tag{A.7}$$

and because the $[\partial\phi/\partial z]$ is evaluated either side of $z = 0$ in the original boundary condition in equation (1.3), the condition in equation (A.4) becomes

$$\left[\frac{\partial A}{\partial z}\right] + i\lambda A(r,0)(2i)|f'(r)| = -4\pi G\Sigma^{(1)}(r). \tag{A.8}$$

Substituting equation (A.3) into equation (A.8) gives

$$\left[\frac{\partial A^{(0)}}{\partial z}\right] + \lambda^{-1}\left[\frac{\partial A^{(1)}}{\partial z}\right] + \lambda^{-2}\left[\frac{\partial A^{(2)}}{\partial z}\right] = -4\pi G\Sigma^{(1)}(r) + 2\lambda|f'(r)|(A^{(0)} + \lambda^{-1}A^{(1)} + \lambda^{-2}A^{(2)}). \tag{A.9}$$

Equating coefficients of $\lambda$ gives

$$2\lambda|f'(r)|A^{(0)} = 0, \tag{A.10}$$

which yields $A^{(0)} = 0$ because $\lambda, |f'(r)| \neq 0$. Therefore the solution for $A$ is

$$A(r, z, \lambda) = \lambda^{-1}(A^{(1)}(r, z) + \lambda^{-1}A^{(2)}(r, z) + \mathcal{O}(\lambda^{-2})) \tag{A.11}$$

Equating coefficients of $\lambda^0$ gives the boundary condition at the disc plane,

$$-4\pi G\Sigma^{(1)}(r) + 2|f'(r)|A^{(1)}(r, 0) = \left[\frac{\partial A^{(0)}}{\partial z}\right] = 0. \tag{A.12}$$

The form of $\Phi(r, z)$ in equation (A.6), together with the expressions for the harmonic components of surface density and potential in equations (1.2), are combined with Poisson's equation to yield

$$\left(\frac{\partial^2 A}{\partial r^2} + \frac{\partial^2 A}{\partial z^2} + \frac{1}{r}\frac{\partial A}{\partial r} - \frac{m^2 A}{r^2}\right) + i\lambda f'(r \pm iz)\left[\frac{A}{r} + 2\left(\frac{\partial A}{\partial r} \pm i\frac{\partial A}{\partial z}\right)\right] = 0. \tag{A.13}$$

If we substitute only the first order term in the expansion of $A$ in equation (A.11), the first term in equation (A.13) is proportional to $\lambda^{-1}$, and is assumed negligible compared to the second term. This leads to the requirement,

$$\frac{\partial}{\partial r}[r^{1/2}A^{(1)}] \pm i\frac{\partial}{\partial z}[r^{1/2}A^{(1)}] = 0, \tag{A.14}$$

which has the solution

$$r^{1/2}A^{(1)} = g(r \pm iz). \tag{A.15}$$

In the disc plane, the solution of the amplitude function is found from the boundary condition in equation (A.12) to be

$$A^{(1)} = r^{-1/2}g(r) = \frac{2\pi G\Sigma^{(1)}(r)}{\lambda|f'(r)|}. \tag{A.16}$$

By inserting equation (A.16) and (A.6) into equations (A.2), it is found that the first order perturbed surface density

$$\Sigma' = \Sigma^{(1)}e^{i(\lambda f(r)+\omega t-m\theta)}, \tag{A.17}$$

produces the potential

$$\phi'(r,z) = \frac{2\pi G\Sigma^{(1)}(r)}{\lambda|f'(r+iz)|}e^{i(\lambda f(r+iz)+\omega t-m\theta)}. \tag{A.18}$$

Therefore, the force per unit mass in the disc plane is, in the WKB approximation, given by

$$\frac{\partial\phi'(r,0)}{\partial r} = 2\pi i G\Sigma'. \tag{A.19}$$

The form of the variables $v'$ and $u'$ in equations (1.1) follow that of the perturbed surface density given in equation (A.17), and therefore solving equations (1.1b-1.1c) for the radial and azimuthal velocity components respectively gives (Binney & Tremaine, 2008)

$$u' = -\frac{i}{\Delta}\left[(m\Omega-\omega)\frac{d\phi'}{dr} + \cancel{\frac{2m\Omega}{r}\phi'}\right], \tag{A.20a}$$

$$v' = \frac{1}{\Delta}\left[-\frac{\kappa^2}{\Omega}\frac{d\phi'}{dr} + \cancel{\frac{m(m\Omega-\omega)}{r}\phi'}\right], \tag{A.20b}$$

where $\Omega$ is the angular rotation of stars and $\Delta = \kappa^2-(m\Omega-\omega)^2$. The second term in equations (A.20) is assumed to be negligible compared to the term proportional

to $d\phi'/dr$ because of the rapid variation of the perturbed potential in the WKB approximation. By use of equation (A.19), equations (A.20) become

$$u' = \frac{1}{\Delta}(m\Omega - \omega)2\pi G\Sigma', \tag{A.21a}$$

$$v' = -\frac{i}{\Delta}\frac{\kappa^2}{\Omega}2\pi G\Sigma'. \tag{A.21b}$$

Similarly, the continuity equation (1.1a) becomes

$$i(m\Omega - \omega)\Sigma' + k\Sigma_0 u' + \cancel{\frac{im\Sigma_0}{r}}v' = 0\ , \tag{A.22}$$

where the last term is dropped because it is smaller than the second term by $\mathcal{O}(kr)$ (see Binney & Tremaine, 2008, p. 491). Finally, substituting the perturbed radial velocity term from equation (A.21a) into equation (A.22) yields the dispersion relation equation (1.4).

# Appendix B: Numerical method and GCD+

In this chapter we describe the method used to simulate galaxy evolution throughout this thesis. The dynamics of stars are calculated by an $N$-body technique, and the gas component is modelled with a smoothed particle hydrodynamics (SPH) code, GCD+. This code is based on earlier Tree SPH methods (Hernquist & Katz, 1989; Katz *et al.*, 1996), and is a fully parallelised code that can be run on large supercomputers. In this thesis, the latest version of the code presented in Kawata *et al.* (2013b) is used, which improves upon the original code developed by Kawata & Gibson (2003). Note that the studies presented in this thesis did not involve any new development or improvement of GCD+. GCD+ was used as an already developed tool. Although we mainly make use of the $N$-body code in this thesis, a full description of the SPH code used for the simulation in §3 is given in this Appendix for completeness.

## B.1 The N-body method

The goal of $N$-body simulations is to model the dynamics of a gravitational system of $N$ particles of given masses under their mutual gravitational attraction. $N$-body simulations fall into two broad categories: collisional and collisionless. In either category, the gravitationally bound system can be treated as a Hamiltonian

system:

$$H = \sum_{i}^{N} \frac{\mathbf{p}_i^2}{2m_i} - G \sum_{i}^{N} \sum_{j \neq i}^{N} \frac{m_i m_j}{|\mathbf{x}_i - \mathbf{x}_j|}, \tag{B.1.1}$$

where $\mathbf{p}_i$, $\mathbf{x}_i$ and $m_i$ are the momentum, position and mass of the $i$-th particle. Therefore the equations of motion can be derived via Hamilton's equations:

$$\frac{d\mathbf{p}_i}{dt} = -\frac{\partial H}{\partial \mathbf{x}_i}; \qquad \frac{d\mathbf{x}_i}{dt} = \frac{\partial H}{\partial \mathbf{p}_i}, \tag{B.1.2}$$

which give the acceleration and velocity of the $i$-th particle respectively:

$$\mathbf{a_i} = \frac{1}{m_i}\frac{d\mathbf{p}_i}{dt} = -G \sum_{j \neq i}^{N} m_j \frac{\mathbf{x}_i - \mathbf{x}_j}{|\mathbf{x}_i - \mathbf{x}_j|^3}; \qquad \frac{d\mathbf{x}_i}{dt} = \frac{\mathbf{p}_i}{m_i}. \tag{B.1.3}$$

For collisional systems such as globular clusters, the acceleration is calculated directly from equation (B.1.3). A system is described as collisional if close-range two-body encounters occur frequently over a time period of evolution, or in other words, if the *relaxation* timescale is short compared to the period of evolution. For disc galaxies, the relaxation time is longer than a Hubble time, therefore disc galaxies are well-approximated as collisionless systems (see Dehnen & Read, 2011, for a recent review).

In $N$-body simulations, however, two body interactions must be numerically suppressed, owing to the denominator of equation (B.1.3) that can lead to large forces between particles in close proximity to each other, i.e. $|\mathbf{x}_i - \mathbf{x}_j| \to 0$. To prevent such large forces, a softening length, $\epsilon$, is used, which modifies the total gravitational potential per unit mass acting on the $i$-th particle to be:

$$\Phi_i = -G \sum_{j \neq i}^{N} m_j \phi(|\mathbf{x}_i - \mathbf{x}_j|, \epsilon), \tag{B.1.4}$$

where $\phi$ denotes the gravitational potential kernel of the $j$-th particle, a commonly used form of which is the Plummer sphere, given by:

$$\phi(r_{ij}, \epsilon) = \frac{1}{\epsilon}\left(1 + \xi^2\right)^{-1/2}, \tag{B.1.5}$$

where $r_{ij} = |\mathbf{x}_i - \mathbf{x}_j|$ and $\xi = r_{ij}/\epsilon$. In the case of a fixed softening length, the

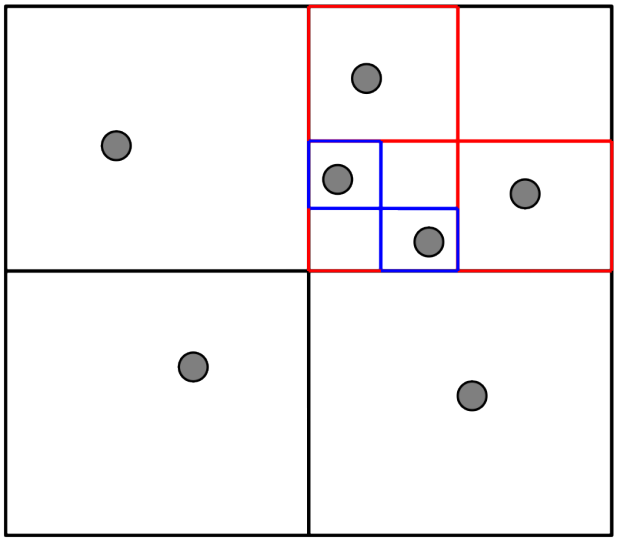

Figure B.1: A schematic illustration of the Barnes & Hut (1986) algorithm in 2-D for simplicity. The root cell encompasses all the particles in the simulation, which is further divided into smaller daughter cells. Cells that contain more than one particle are called "node" cells, and are further subdivided until each cell contains only one particle. These cells are called "leaf" cells. Empty cells are ignored in the tree.

acceleration due to the *softened* gravitational potential is expressed as:

$$\tilde{\mathbf{a}}_\mathbf{i} = -G\sum_{j=1}^{N} m_j \nabla\phi(r_{ij},\epsilon) = -G\sum_{j=1}^{N} m_j \frac{\mathbf{x}_i - \mathbf{x}_j}{(|\mathbf{x}_i - \mathbf{x}_j|^2 + \epsilon^2)^{\frac{3}{2}}}. \tag{B.1.6}$$

The acceleration from this modified equation of motion does not diverge as particles become very close; any particle that comes within one softening length, $\epsilon$, the force on those particles stays constant. However, the softening length does introduce bias into the force calculation, which underestimates the force on small scales (Dehnen & Read, 2011).

### B.1.1 The Tree Force

A direct particle-by-particle calculation of equation (B.1.6) requires $N^2$ calculations, which is computationally very demanding. This number can be halved by use of the symmetry in Newtons third law as derived from the Hamiltonian in equation (B.1.1), which is still too large, especially for modern simulations that typically employ $\log N \sim 6 - 8$ particles.

There are some modern techniques that reduce this high number of calculations in order to make high resolution simulations possible, one of which is the Tree algorithm (Barnes & Hut, 1986). This algorithm defines cubic *cells* which comprise groups of localised particles. Each cubic cell containing more than one particle is a "node" cell and is further subdivided into eight daughter cells, for which the process is repeated until a sub-cell contains one particle (see Fig. B.1 for two dimensional case). These cells are the last in the tree hierarchy and are termed "leaf" cells. The advantage of grouping particles that are localised to each other is that one can obtain a good approximation to the force contribution to a particle far from the cell from all particles inside the cell. This approximation is obtained by Taylor expansion of the force per unit mass from the cell around the centre of mass of the particle group (e.g. Dehnen & Read, 2011):

$$\tilde{\mathbf{a}}(\mathbf{x_i} - \mathbf{x_j}) = \sum_{k}^{n} \frac{1}{k!}(\mathbf{x}_j - \mathbf{z}_A)^k \nabla^k \tilde{\mathbf{a}}(\mathbf{x}_i - \mathbf{z}_A). \tag{B.1.7}$$

Here, $n$ is the order of the expansion, $\mathbf{x}_j$ is the position of a single particle belonging to the group cell $A$, which has centre of mass $\mathbf{z}_A$, and $\mathbf{x}_i$ is the position of a particle at a large distance from both $\mathbf{z}_A$ and $\mathbf{x}_j$. Equation (B.1.7) gives an expression for the force per unit mass felt by particle $i$ from particle $j$, therefore to calculate the force per unit mass on particle $i$ from all the particles in cell $A$ requires a summation of equation (B.1.7) over $N$ particles in cell $A$:

$$\tilde{\mathbf{a}}_{\mathbf{A}}(\mathbf{x_i}) = \sum_{k}^{n} \mu_{jA}^{k} \cdot \nabla^k \tilde{\mathbf{a}}(\mathbf{x}_i - \mathbf{z}_A), \tag{B.1.8}$$

where

$$\mu_{jA}^{k} = \sum_{j}^{N} m_j \frac{(-1)^k}{k!}(\mathbf{x}_j - \mathbf{z}_A)^k \tag{B.1.9}$$

denotes the multipoles of cell A with respect to its expansion centre, $\mathbf{z}_A$. In practise, the multipole moments (equation B.1.9) of all the nodes are calculated first. This leaves only the single calculation of equation (B.1.6) between the $i$-th particle and the centre of mass of the cell to get the force contribution from the cell. The cell can be re-used for other particles that satisfy equation (B.1.11).

To determine which of equations (B.1.6) or (B.1.8) is used to evaluate the

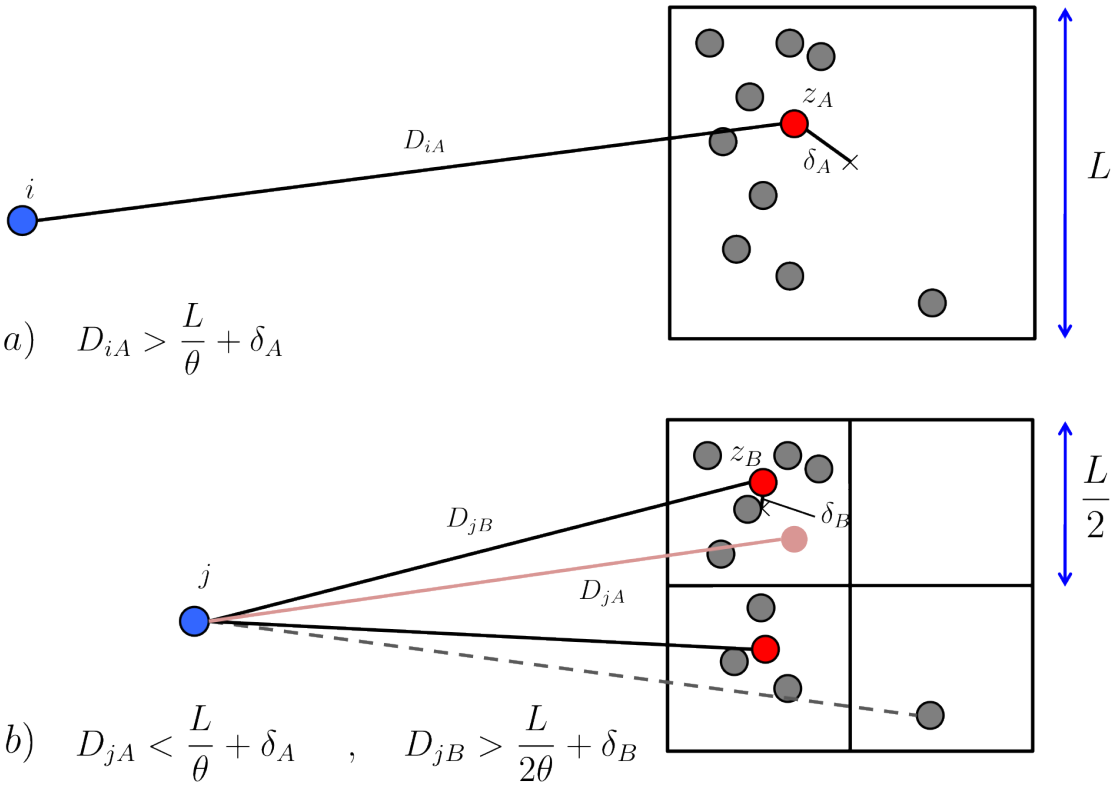


Figure B.2: Schematic illustration of the tree force algorithm in 2D for simplicity. a) The centre of mass of a group of particles (grey circles) in a cell of length, $L$, is calculated and denoted as $\mathbf{z}_A$ (red circle). The distance between the centre of mass of the cell and particle $i$ (blue circle) is denoted $D_{iA}$, and the distance between the centre of mass and the geometric centre of cell A is denoted $\delta_A$. The condition of equation (B.1.10) is satisfied and the force from all particles in cell $A$ on the particle $i$ is calculated using the approximation given in equation (B.1.8). b) A different particle, $j$, is closer to the cell, and equation (B.1.10) is not satisfied for $D_{jA}$, the distance between particle $j$ and the centre of mass, $\mathbf{z}_A$ (pink circle). The "node" cell $A$ is then subdivided into 4 (8 for 3D case) daughter cells each of length $L/2$. Equation (B.1.10) is now satisfied for the distance, $D_{jB}$, to the centre of mass of the upper-left daughter cell, $\mathbf{z}_B$ (and similarly for the lower-left daughter cell), therefore the force from cell $B$ is calculated using equation (B.1.8). The lower-right daughter cell contains only one particle (leaf cell), and the force contribution on particle $j$ is calculated directly from equation (B.1.6).

force between particles, we apply cell opening conditions. At the initial time-step, the cell opening condition is controlled by a tolerance parameter, $\theta$, defined as the ratio between the size of the cell, $L$, and the distance, $D$, between the $i$-th particle and the centre of mass of the cell plus the distance, $\delta$, between the centre of mass and geometric centre of the cell (Dubinski, 1996). The condition to be satisfied is:

$$D > \frac{L}{\theta} + \delta. \tag{B.1.10}$$

If the inequality holds, then the force per unit mass is calculated from the approximation of equation (B.1.8), otherwise cell $A$ is further split into 8 daughter cells and the inequality is checked again (see Fig. B.2 for two dimensional case). If the cells continue to split until there is only one particle left in a cell, then the force is calculated via the direct method of equation (B.1.6).

From the second step onwards, in place of equation (B.1.10), the cell opening criterion is given by (Springel, 2005):

$$\frac{GM}{D^2}\left(\frac{L}{D}\right)^4 \leq \alpha|\mathbf{a}_i|, \tag{B.1.11}$$

where $\mathbf{a_i}$ is the acceleration of the $i$-th particle in the previous time-step, and $\alpha$ is the tolerance parameter. When equation (B.1.11) satisfied, a cell of mass $M$ is eligible for usage in the Tree force calculation. This ensures that the force per unit mass contribution from a node cell is always a small fraction of the total acceleration, which improves the accuracy of the total force calculation (Springel, 2005).

Both the criteria described in equations (B.1.10) and (B.1.11), and the order of the Taylor expansion in equation (B.1.8) control the balance between computational speed and accuracy of the calculation. For the initial opening angle criterion, lower values of $\theta$ restrict the size of node cells, $L$, to be smaller compared to the distance, $D$, than the size required for higher values of $\theta$, thereby restricting node cells to only the most distant particles. Therefore, lower values of $\theta$ lead to more accurate force calculations (because fewer node cells are used) and longer computation times. A similar argument is valid for equation (B.1.11). In the simulations presented in this thesis, the opening angle is $\theta = 0.8$, and $\alpha = 0.0025$. The Taylor expansion in equation (B.1.8) is calculated to the

quadrupole moment ($n = 4$).

### B.1.2 Time integration

Once the gravitational force on a particle is calculated, the position and velocity of the particle is updated by numerically integrating the equations of motion. There are several integration schemes from which to choose (see Dehnen & Read, 2011, for a detailed description), which include the Euler, leapfrog and Hermite integrators, in increasing order of accuracy.

#### The Euler Integrator

The Euler method is the most basic integrator. It updates first the particle velocity, which is then used to update position. Both quantities are calculated at each time-step:

$$\mathbf{x}_{k+1} = \mathbf{x}_k + \mathbf{v}_{k+1}\Delta t; \quad \mathbf{v}_{k+1} = \mathbf{v}_k + \mathbf{a}_k\Delta t, \tag{B.1.12}$$

which yields:

$$\mathbf{x}_{k+1} = \mathbf{x}_k + \mathbf{v}_k\Delta t + \mathbf{a}_k\Delta t^2. \tag{B.1.13}$$

However, a quick comparison to the Taylor expansion:

$$\mathbf{x}_{k+1} = \mathbf{x}_k + \frac{\dot{\mathbf{x}}_k}{1!}\Delta t + \frac{\ddot{\mathbf{x}}_k}{2!}\Delta t^2 \quad ... \tag{B.1.14}$$

shows that equations (B.1.12) are only first order accurate. The error introduced from this method is much larger than the second order Leapfrog integrator described below.

#### The Leapfrog Integrator

Unlike the Euler integration, the Leapfrog integrator evaluates the velocity halfway between each time-step ($k \pm 1/2$) and the acceleration and position at each time-

step $(k)$:

$$\mathbf{v}_{k+\frac{1}{2}} = \mathbf{v}_{k-\frac{1}{2}} + \mathbf{a}_k \Delta t; \qquad \mathbf{x}_{k+1} = \mathbf{x}_k + \mathbf{v}_{k+\frac{1}{2}} \Delta t. \tag{B.1.15}$$

Because $\mathbf{v}_k = \mathbf{v}_{k+\frac{1}{2}} - \mathbf{a}_k \Delta t/2$, equations (B.1.15) can be combined to show:

$$\mathbf{x}_{k+1} = \mathbf{x}_k + \mathbf{v}_k \Delta t + \frac{\mathbf{a}_k \Delta t^2}{2}, \tag{B.1.16}$$

which is the same as the Taylor expansion up to second order (equation B.1.14). This second order accuracy method of integration is used in GCD+.

### The Hermite integrator

Hermite integration schemes are higher order schemes that make use of higher time derivatives of the position. For example, the time derivative of the acceleration, termed the *jounce*, enters into the equation for the velocity, and the acceleration enters into the equation for the position:

$$\begin{aligned} \mathbf{v}_{k+1} &= \mathbf{v}_k + \frac{1}{2}(\mathbf{a}_k + \mathbf{a}_{k+1})\Delta t + \frac{1}{12}(\mathbf{j}_k - \mathbf{j}_{k+1})(\Delta t)^2, \\ \mathbf{x}_{k+1} &= \mathbf{x}_k + \frac{1}{2}(\mathbf{v}_k + \mathbf{v}_{k+1})\Delta t + \frac{1}{12}(\mathbf{a}_k - \mathbf{a}_{k+1})(\Delta t)^2. \end{aligned} \tag{B.1.17}$$

where $\mathbf{j}$ is the jounce. The Hermite integration scheme can be thought of as a higher order generalisation of the leapfrog, because if the terms quadratic in $\Delta t$ are neglected in equation (B.1.17), and the terms linear in $\Delta t$ are written in terms of half-steps, equations (B.1.15) in the leapfrog integration scheme are recovered.

### Individual Time-step scheme

The accuracy of the time integration of particle motion depends on the size of the time-step employed in the integrator. Small time-steps yield a smoother evolution of the orbital motion. However, such small time-steps are impractical to use for every particle because the computational demand is much too high. In addition, while short time-steps are important for particles in dense regions of the galaxy where the force can change rapidly owing to the close proximity of neighbouring particles, they are unnecessary in the outer regions of the galaxy where the change is relatively slow. Therefore, particles in low dense regions can

be integrated over larger time-steps than particles in high dense regions, with negligible damage to the accuracy of their integrated motion. Therefore, it is in the interest of the simulation speed and accuracy to use individual time-steps, whereby $\Delta t_i$ is calculated individually for each particle. The choice of $\Delta t_i$ for particles that follow collisionless dynamics is given by

$$\Delta t_i = 0.2(0.5\epsilon/|d\mathbf{v}_i/dt|)^{1/2}, \tag{B.1.18}$$

where $\epsilon$ is the gravitational softening. This ensures that the velocities and positions of particles with large accelerations are updated after short time-steps in order to accurately integrate the orbit. For particles whose next time-step is longer than that of the short time-step particles, the position and velocity are evaluated by Euler integration, i.e.,

$$\begin{aligned} \mathbf{v}_{k+1} &= \mathbf{v}_l + (t_{k+1} - t_l) \cdot \mathbf{a}_l, \\ \mathbf{v}_{k+1/2} &= \mathbf{v}_l + 0.5(t_{k+1} - t_l) \cdot \mathbf{a}_l, \\ \mathbf{x}_{k+1} &= \mathbf{x}_l + (t_{k+1} - t_l) \cdot \mathbf{v}_{k+1/2}, \end{aligned} \tag{B.1.19}$$

where $k$ and $l$ represent the short and long time-step respectively, $t_{k+1}$ is the next time-step and $t_l$ is the time when the acceleration, $\mathbf{a}_l$, of the long time-step particle was last calculated. The acceleration of long time-step particles (and therefore their new time-step sizes) is updated only after their individual time-steps. The Euler integration at smaller time-step sizes described here increases the accuracy of the force contribution from long time-step particles to short time-step particles. This integration scheme ensures the accurate global integration of the entire system of particles forward in time.

## B.2 Smoothed Particle Hydrodynamics

There are two principal methods that are used to model hydrodynamics: Eulerian and Lagrangian. The Eulerian method evaluates the properties of a flow field, e.g. velocity, at each fixed point in space and time. Conversely, the Lagrangian scheme follows the hydrodynamics of individual fluid elements or particles as they are advected by the flow. Smoothed particle hydrodynamics (first introduced by Lucy, 1977; Gingold & Monaghan, 1977) is a method that adopts the Lagrangian

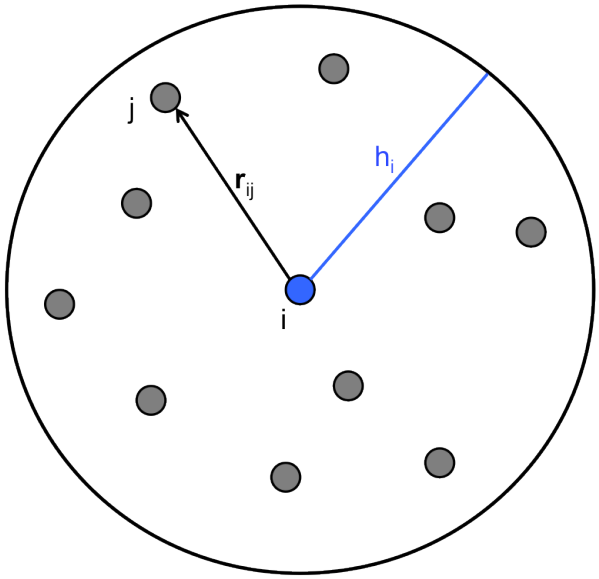


Figure B.3: A group of neighbour particles found within a sphere (drawn as a 2-D circle for simplicity) of radius equal to one smoothing length, $h_i$.

concept of solving the hydrodynamical equations by following the motion of individual particles. The hydrodynamical quantities are "smoothed" by estimating their values at each particle position from a summation of weighted contributions from neighbouring particles.

For any physical value, $f$, a smoothed interpolated version can be defined by its convolution with a smooth, differentiable kernel, $W(\mathbf{x}, h)$:

$$f(\mathbf{x}) = \int_V f(\mathbf{x}')W(|\mathbf{x} - \mathbf{x}'|, h)d\mathbf{x}', \tag{B.2.1}$$

given that $\int_V W(\mathbf{x}, h)d\mathbf{x}' = 1$, where $h$ is the smoothing length. Equation (B.2.1) is equivalent to

$$f(\mathbf{x}) = \int_V \frac{f(\mathbf{x}')}{\rho(\mathbf{x}')}W(|\mathbf{x} - \mathbf{x}'|, h)\rho(\mathbf{x}')d\mathbf{x}', \tag{B.2.2}$$

where $\rho(\mathbf{x})$ is the density at position $\mathbf{x}$. In a system of particles, the value of the quantity is known at a sample of discrete points, $\mathbf{x}_i$. Provided the points sufficiently sample the kernel volume, equation (B.2.2) can be discretised on to a set of particles of $m = \rho(\mathbf{x}')d\mathbf{x}'$, and becomes an expression for the smoothed

field at the $i$-th particle position:

$$f(\mathbf{x}_i) \approx \sum_j \frac{m_j}{\rho_j} f(\mathbf{x}_j) W(|\mathbf{x}_i - \mathbf{x}_j|, h), \tag{B.2.3}$$

where $m_j$, $\rho_j$ and $\mathbf{x}_j$ are the mass, density and position of the $j$-th particle respectively. Equation (B.2.3) represents the backbone of SPH formalisms, in which the quantity, $f$, is continuous and differentiable because operators act on the kernel which is itself a smooth function. The density of the $i$-th particle is expressed as

$$\rho_i = \sum_j m_j W(|\mathbf{x}_i - \mathbf{x}_j|, h_i), \tag{B.2.4}$$

where $\rho_i = \rho(\mathbf{x}_i)$, and $h_i$ is the smoothing length of the $i$-th particle which is schematically described in Fig. B.3. The velocity field can be smoothed and its derivative taken to estimate the local velocity divergence (Monaghan, 1992; Price, 2012):

$$\langle \nabla \cdot \mathbf{v} \rangle_i = -\frac{1}{\rho_i} \sum_j m_j \mathbf{v}_{ij} \cdot \nabla_i W_{ij}(h_i), \tag{B.2.5}$$

where $\mathbf{v}_{ij} = \mathbf{v}_i - \mathbf{v}_j$ and $W_{ij}(h_i) = W(|\mathbf{x}_i - \mathbf{x}_j|, h_i)$. The $x$-component of curl is

$$\langle \nabla \times \mathbf{v} \rangle_{i,x} = -\frac{1}{\rho_i} \sum_j m_j [v_{ij,z} \nabla_{i,y} W_{ij}(h_i) - v_{ij,y} \nabla_{i,z} W_{ij}(h_i)], \tag{B.2.6}$$

where $v_{ij,z}$ is the magnitude of the $z$-component velocity difference between the $i$-th and $j$-th particle. The smoothing kernel follows a piece-wise polynomial form:

$$W_{ij}(h_i) = \frac{8}{\pi h_i^3} \begin{cases} 1 - 6(r_{ij}/h_i)^2 + 6(r_{ij}/h_i)^3 & \text{if } 0 \le r_{ij}/h_i \le 1/2, \\ 2[1 - (r_{ij}/h_i)]^3 & \text{if } 1/2 \le r_{ij}/h_i \le 1, \\ 0 & \text{if } r_{ij}/h_i > 1, \end{cases} \tag{B.2.7}$$

where $r_{ij} = |\mathbf{x}_i - \mathbf{x}_j|$. This is the spherically symmetric spline (as used by Monaghan & Lattanzio, 1985; Steinmetz, 1996) kernel that vanishes outside of a sphere of radius $h_i$, designated as the smoothing length (see Fig. B.3). We adopt the spline kernel of equation (B.2.7) because it has been shown to be more stable with a low number of neighbour particles than more sophisticated kernels recently suggested by several authors (e.g. Read *et al.*, 2010; Dehnen & Aly, 2012). The smoothing length of the $i$-th particle is defined to depend on the smoothed density of the particle following

$$h_i = \eta \left( \frac{m_i}{\rho_i} \right)^{1/3}. \tag{B.2.8}$$

The final value of the smoothing length is found by solving equation (B.2.8) iteratively until the relative change between two values is less than $10^{-3}$ (see Price & Monaghan, 2007; Kawata *et al.*, 2013b). The relationship between smoothing length and density in equation (B.2.8) means that particles in relatively dense regions of the simulated galaxy have shorter smoothing lengths and higher spatial resolution, whereas those in lower dense regions have longer smoothing lengths. This ensures that each particle has the same number of neighbour particles (i.e. particles within the smoothing length) if the particles are distributed homogeneously. The number of neighbour particles can be scaled by parameter $\eta$, which we take to be $\eta = 3.0$, which corresponds to 113 neighbour particles.

### B.2.1 SPH Equations of Motion

The equations that govern the fluid dynamics in SPH are derived using a Lagrangian formalism. The Lagrangian of a self-gravitating inviscid ideal gas can be split into two parts: a hydrodynamical and a gravitational part

$$\mathcal{L} = \mathcal{L}_{hyd} + \mathcal{L}_{grav} = \int \rho \left( \frac{\mathbf{v}^2}{2} - u \right) dV - \int \rho \Phi dV, \tag{B.2.9}$$

where $\rho$ is the density and $u$ is the internal energy per unit mass of the gas. Following Gingold & Monaghan (1982); Springel & Hernquist (2002), the Lagrangian

is discretised into the case for a system of point mass particles:

$$\mathcal{L} = \mathcal{L}_{hyd} + \mathcal{L}_{grav} = \sum_j m_j \left( \frac{\mathbf{v}_j^2}{2} - u_j \right) - \sum_j m_j \Phi_j. \tag{B.2.10}$$

The Euler-Lagrange equations for a system of particles are

$$\frac{d}{dt}\frac{\partial \mathcal{L}}{\partial \mathbf{v}_i} = \frac{\partial \mathcal{L}}{\partial \mathbf{x}_i}, \tag{B.2.11}$$

for $i = 1, ....N$. This formalism yields equations of motion containing hydrodynamical and gravitational terms that contribute to the acceleration of a gas particle, and conserves mass, momentum and energy exactly (if integrated perfectly).

### Hydrodynamical forces

For the hydrodynamical part of the Lagrangian, $\mathcal{L}_{hyd}$, we have

$$m_i \frac{d\mathbf{v}_i}{dt} = \frac{\partial \mathcal{L}_{hyd}}{\partial \mathbf{x}_i} = -\sum_j m_j \frac{\partial u_j}{\partial \mathbf{x}_i} = -\sum_j m_j \frac{\partial u_j}{\partial \rho_j} \cdot \frac{\partial \rho_j}{\partial \mathbf{x}_i}. \tag{B.2.12}$$

The last term in equation (B.2.12) is found by considering the properties of an inviscid gas. In the absence of shocks and thermal conduction, the entropy, $A$, of the gas is constant i.e. $\partial A/\partial t = 0$. In this case, the internal energy is expressed as

$$du = TdA - PdV = \frac{P}{\rho^2} d\rho, \tag{B.2.13}$$

where $T$, $P$ and $V$ are the temperature, pressure and volume of an element of gas respectively. Therefore equation (B.2.12) can be written as:

$$m_i \frac{d\mathbf{v}_i}{dt} = -\sum_j m_j \frac{P_j}{\rho_j^2} \frac{\partial \rho_j}{\partial \mathbf{x}_i}. \tag{B.2.14}$$

The remaining partial differentiation in equation (B.2.14) represents the total variation of the density with respect to the $\mathbf{x}_i$ coordinate and the smoothing length, $h$, which is allowed to adapt according to the local density (equation

B.2.8). It is given as (see Appendix for derivation)

$$\frac{d\rho_j}{d\mathbf{x}_i} = \Omega_j^{-1} \nabla_i \rho_j, \tag{B.2.15}$$

where the $\nabla_i$ denotes the differentiation with respect to $\mathbf{x}_i$ with the smoothing lengths held constant, and

$$\Omega_i = \left( 1 + \frac{h_j}{3\rho_j} \cdot \sum_j m_j \frac{\partial W_{ij}}{\partial h_j} \right). \tag{B.2.16}$$

The above is a correction term that takes into account the variable smoothing. In the fixed smoothing length regime, $\Omega_i = 1$, and the correction vanishes. Note that the inclusion of this term drastically reduces the force integration error in the case of variable smoothing (Springel & Hernquist, 2002; Price & Monaghan, 2007).

The hydrodynamic component of the equation of motion is written as

$$\frac{d\mathbf{v}_i}{dt} = -\sum_j m_j \left( \frac{P_i}{\Omega_i \rho_i^2} \nabla_i W_{ij}(h_i) + \frac{P_j}{\Omega_j \rho_j^2} \nabla_i W_{ij}(h_j) \right), \tag{B.2.17}$$

where $W_{ij}(h_i) = W(r_{ij}, h_i)$, and the gradient of the scalar smoothing kernel is

$$\nabla_i W_{ij}(h_i) = \frac{\partial W_{ij}(h_i)}{\partial \mathbf{x}_i} = \frac{\partial W_{ij}(h_i)}{\partial r_{ij}} \cdot \frac{\mathbf{x}_i - \mathbf{x}_j}{|\mathbf{x}_i - \mathbf{x}_j|}. \tag{B.2.18}$$

**Gravitational forces**

The gravitational part of the momentum equation is derived from the gravitational part of the Lagrangian, $\mathcal{L}_{grav}$, in the same way:

$$\mathcal{L}_{grav} = -\frac{G}{2} \sum_j \sum_k m_j m_k \phi_{jk}(h_j), \tag{B.2.19}$$

where $\phi_{jk}$ is the gravitational potential kernel between particle $j$ and particle $k$ [1]. The spatial derivative of this is:

$$\frac{\partial \mathcal{L}_{grav}}{\partial \mathbf{x}_i} = -\frac{G}{2}\sum_j \sum_k m_j m_k \left( \frac{\partial \phi_{jk}(h_j)}{\partial |\mathbf{x}_{jk}|} \frac{\partial |\mathbf{x}_{jk}|}{\partial \mathbf{x}_i} + \frac{\partial \phi_{jk}(h_j)}{\partial h_j} \frac{\partial h_j}{\partial \rho_\mathbf{j}} \frac{\partial \rho_j}{\partial \mathbf{x}_i} \right) \tag{B.2.20}$$

where

$$\frac{\partial |\mathbf{x}_{jk}|}{\partial \mathbf{x}_i} = \frac{\mathbf{x}_j - \mathbf{x}_k}{|\mathbf{x}_j - \mathbf{x}_k|}(\delta_{ji} - \delta_{ki}). \tag{B.2.21}$$

Substituting this and equation (B.2.15) into equation (B.2.20) yields the final form of the momentum equation is given as

$$\begin{aligned} \frac{d\mathbf{v}_i}{dt} = &-G\sum_j \frac{m_j}{2}\left( \frac{\partial \phi_{ij}(h_i)}{\partial |\mathbf{x}_{ij}|} + \frac{\partial \phi_{ij}(h_j)}{\partial |\mathbf{x}_{ij}|} \right) \frac{\mathbf{x}_i - \mathbf{x}_j}{|\mathbf{x}_i - \mathbf{x}_j|} \\ &-\frac{G}{2}\sum_j m_j \left( \frac{\zeta_i}{\Omega_i} \frac{\partial W_{ij}(h_i)}{\partial \mathbf{x}_i} + \frac{\zeta_j}{\Omega_j} \frac{\partial W_{ij}(h_j)}{\partial \mathbf{x}_i} \right) \\ &-\sum_j m_j \left( \frac{P_i}{\Omega_i \rho_i^2} \nabla_i W_{ij}(h_i) + \frac{P_j}{\Omega_j \rho_j^2} \nabla_i W_{ij}(h_j) \right), \end{aligned} \tag{B.2.22}$$

where the last line is the hydrodynamical term added from equation (B.2.17), and

$$\zeta_i = \frac{\partial h_i}{\partial \rho_i} \sum_j m_j \frac{\phi_{ij}(h_i)}{\partial h_i}. \tag{B.2.23}$$

The only derivatives to be calculated from equation (B.2.22) are spatial derivatives of the gravitational kernel functions. We use the cubic spline (Price &

[1] Note that for gas particles the softening length is always equal to the smoothing length, and therefore the softening length is variable.

Monaghan, 2007), of which the derivatives are:

$$\phi'(r_{ij}, h_i) = \begin{cases} \frac{4}{h_i^2}(\frac{8}{3}q - \frac{48}{5}q^3 + 8q^4) & \text{if } 0 \leq q < 1/2; \\ \frac{4}{h_i^2}(\frac{16}{3}q - 12q^2 + \frac{48}{5}q^3 - \frac{8}{3}q^4 - \frac{1}{60q^2}) & \text{if } 1/2 \leq q < 1; \\ 1/r_{ij}^2 & \text{if } q \geq 1, \end{cases} \tag{B.2.24}$$

and

$$\frac{\partial \phi}{\partial h_i} = \begin{cases} \frac{2}{h_i^2}(-8q^2 + 24q^4 - \frac{96}{5}q^5 + \frac{7}{5}) & \text{if } 0 \leq q < 1/2; \\ \frac{2}{h_i^2}(-16q^2 + 32q^3 - 24q^4 + \frac{32}{5}q^5 + \frac{8}{5}) & \text{if } 1/2 \leq q < 1; \\ 0 & \text{if } q \geq 1, \end{cases} \tag{B.2.25}$$

where $q = r_{ij}/h_i$, and $r_{ij} = |\mathbf{x}_i - \mathbf{x}_j|$.

### B.2.2 Entropy Equation

The equations of motion described in equation (B.2.22) follow the evolution of an inviscid gas, for which the equation of state is

$$P_i = A_i \rho_i^\gamma, \tag{B.2.26}$$

where $\gamma$ is the adiabatic index. The function, $A_i$, is an entropy term, whose evolution follows (Springel & Hernquist, 2002)

$$\frac{dA_i}{dt} = 0, \tag{B.2.27}$$

for an isentropic flow (the full entropy equation for the galaxy simulation is given in equation (B.3.1)). The entropy may be related to the thermal energy by substituting equation (B.2.26) into equation (B.2.13), which gives

$$u_i = \int \frac{A\rho^\gamma}{\rho^2} d\rho = A_i \frac{\rho_i^{\gamma-1}}{\gamma - 1}. \tag{B.2.28}$$

### B.2.3 Artificial Viscosity

Euler's equation of motion (B.2.22) is based on an inviscid, isentropic gas. To treat shocks, the hydrodynamics are required to be modified by artificial viscosity. Artificial viscosity provides an additional force term to the Euler equation (B.2.22) analogous to a drag force, and has the form (Morris & Monaghan, 1997; Kawata *et al.*, 2013b):

$$\left(\frac{d\mathbf{v}}{dt}\right)_{diss,i} = \sum_j Q_{ij} \tag{B.2.29}$$

where

$$Q_{ij} = \begin{cases} -m_j \frac{\alpha_{ij}^{AV}(t) v_{sig} \mathbf{v}_{ij} \cdot \mathbf{e}_{ij}}{\rho_{ij}} \cdot \overline{\nabla_i W_{ij}}, & \text{if } \mathbf{x}_{ij} \cdot \mathbf{v}_{ij} < 0, \\ 0, & \text{otherwise,} \end{cases} \tag{B.2.30}$$

where $\mathbf{e}_{ij} = (\mathbf{x}_i - \mathbf{x}_j)/|\mathbf{x}_i - \mathbf{x}_j|$, $\rho_{ij} = (\rho_i + \rho_j)/2$ and

$$\overline{\nabla_i W_{ij}} = \frac{1}{2}\left\{\frac{1}{\Omega_i}\nabla_i W_{ij}(h_i) + \frac{1}{\Omega_j}\nabla_i W_{ij}(h_j)\right\}, \tag{B.2.31}$$

is the symmetrised kernel gradient. The mean signal speed at which information can propagate between two particles is given by

$$v_{sig} = \frac{c_{s,i} + c_{s,j} - \beta^{AV}\mathbf{v}_{ij} \cdot \mathbf{e}_{ij}}{2}, \tag{B.2.32}$$

where $c_{s,i}$ is the sound speed of the $i$-th particle and $\beta^{AV} = 3$.

Equation (B.2.30) is non-zero for two particles that move towards one another. This criterion is designed to model bulk viscosity caused by shocks. However, this criterion can also be satisfied in pure shear flows. In the case of a differentially rotating gas disc, particles at different radii may possess at least one velocity component that satisfies $\mathbf{x}_{ij} \cdot \mathbf{v}_{ij} < 0$, which would lead to an unwanted non-zero artificial viscosity between them. In order to minimise this effect, the amount of artificial viscosity introduced is controlled according to the parameter,

$$\alpha_{ij}^{AV}(t) = \frac{1}{4}(\alpha_i^{AV}(t) + \alpha_j^{AV}(t))(f_i + f_j), \tag{B.2.33}$$

where (Balsara, 1995):

$$f_i = \frac{|\langle \nabla \cdot \mathbf{v} \rangle_i|}{|\langle \nabla \cdot \mathbf{v} \rangle_i| + |\langle \nabla \times \mathbf{v} \rangle_i| + 0.0002 c_{s,i}/h_i}, \tag{B.2.34}$$

which acts to suppress artificial viscosity in pure shear flows. The viscosity coefficient of the $i$-th particle, $\alpha_i^{AV}(t)$, evolves according to:

$$\frac{d\alpha_i^{AV}(t)}{dt} = -\frac{\alpha_i^{AV}(t) - \alpha_{min}^{AV}}{\tau_i} + S_i, \tag{B.2.35}$$

as suggested by Morris & Monaghan (1997). The minimum value for the artificial viscosity coefficient of any particle is set as $\alpha_{min}^{AV} = 0.5$, and

$$\tau_i = \frac{h_i}{0.2 c_{s,i}}, \tag{B.2.36}$$

is a decay timescale. The source term for the artificial viscosity coefficients is

$$S_i = \max(-\nabla_{\mathrm{i}} \cdot \mathbf{v}_{\mathrm{i}}, 0)(\alpha_{\mathrm{max}}^{\mathrm{AV}} - \alpha_{\mathrm{i}}^{\mathrm{AV}}(\mathrm{t})), \tag{B.2.37}$$

where $\alpha_{max}^{AV} = 2.0$. For the case of no compression i.e. $\nabla \cdot \mathbf{v} > 0$, the source term is equal to zero, and $\alpha_i^{AV}$ decays to $\alpha_{min}^{AV}$. For the case of strong compression, e.g. strong shocks, the source term increases $\alpha_i^{AV}$ up to values of $\alpha_{max}^{AV}$. The scheme ensures that the artificial viscosity in equation (B.2.33) is regulated as required[1].

### Entropy Equation

Hydrodynamical shocks cause dissipation of thermal energy as a consequence of viscosity. In this case, the hydrodynamical flow ceases to be isentropic, and the evolution the entropy parameter, $A_i$, is modelled by

$$\frac{dA_i}{dt} = \frac{\gamma - 1}{\rho_i^{\gamma - 1}} \left( \frac{du}{dt} \right)_{diss}. \tag{B.2.38}$$

Following Price (2008), the dissipation of thermal energy can be derived from the viscosity term in equation (B.2.30) and the conservation of energy, $e = \frac{1}{2}v^2 + u$,

[1]Note that there are other artificial viscosity switches available (e.g. Cullen & Dehnen, 2010).

which are related by

$$\frac{du}{dt} = \frac{de}{dt} - \mathbf{v} \cdot \frac{d\mathbf{v}}{dt}. \tag{B.2.39}$$

The thermal dissipation becomes

$$\left(\frac{du}{dt}\right)_{diss} = \sum_j Q_{u,ij} + \sum_j Q_{AC,ij}, \tag{B.2.40}$$

where the artificial viscosity term is given as

$$Q_{u,ij} = \begin{cases} \frac{m_j v_{sig}}{\rho_{ij}} \frac{\alpha_{ij}^{AV}}{2} (\mathbf{v}_{ij} \cdot \mathbf{e}_{ij})^2 \cdot \mathbf{e}_{ij} \cdot \overline{\nabla_i W_{ij}}, & \text{if } \mathbf{x}_{ij} \cdot \mathbf{v}_{ij} < 0, \\ 0 & \text{otherwise.} \end{cases} \tag{B.2.41}$$

### B.2.4 Artificial thermal conductivity

Thermal energy dissipation in the form of heat flows from hot to cold particles is modelled by artificial thermal conductivity (Rosswog & Price, 2007; Price, 2008), which appears in equation (B.2.40) as

$$Q_{AC,ij} = \frac{m_j v_{sig}}{\rho_{ij}} \alpha_{ij}^C (u_i - u_j) \cdot \mathbf{e}_{ij} \cdot \overline{\nabla_i W_{ij}}, \tag{B.2.42}$$

where $\alpha_{ij}^C(t) = (\alpha_i^C(t) + \alpha_j^C(t))/2$.

The amount of thermal conductivity is controlled by the parameter, $\alpha_i^C(t)$, that evolves as

$$\frac{d\alpha_i^C(t)}{dt} = -\frac{\alpha_i^C(t)}{\tau_i} + S_i^C, \tag{B.2.43}$$

where the source term is

$$S_i^C = 0.05 h_i |\nabla^2 u_i| / \sqrt{u_i}, \tag{B.2.44}$$

and

$$\nabla^2 u_i = 2 \sum_j m_j \frac{u_i - u_j}{\rho_j} \frac{\mathbf{e}_{ij} \cdot \overline{\nabla_i W_{ij}}}{r_{ij}}. \tag{B.2.45}$$

It is clear that in this scheme, thermal conductivity is applied whereever a temperature difference is significant: the magnitude of the term in equation (B.2.42) is proportional to the thermal energy difference between the $i$-th particle and its neighbours, whose temperatures evolve according to the same principle. The thermal conductivity scheme is able to resolve Kelvin-Helmholtz instabilities that occur at contact discontinuities between shearing flows of different densities and temperatures (Price, 2008; Kawata *et al.*, 2013b). Thus, the scheme rectifies a long-standing fundamental problem in the SPH method[1] (Agertz *et al.*, 2007).

### B.2.5 Time integration scheme

To evolve the system, the equations of motion (B.2.22) and the entropy equation (B.2.38) must be integrated forward over time. The leapfrog integration method described in equation (B.1.15) is used to integrate equations (B.2.22). To integrate the entropy equation (B.2.38), the trapezoidal rule (Hernquist & Katz, 1989) is employed:

$$A_i^{k+1} = A_i^k + 0.5 \left[ \left( \frac{dA_i}{dt} \right)^k + \left( \frac{dA_i}{dt} \right)^{k+1} \right] \Delta t_i. \tag{B.2.46}$$

The complete entropy equation (see equation (B.3.1) in §B.3 below) includes terms for a heating rate from UV-background, $H$, and a radiative cooling rate, $\Lambda$, that is very sensitive to temperature, which itself is related to entropy through equation (B.2.28). Therefore, equation (B.2.46) must be solved iteratively. The first step is to assume that the adiabatic part of the entropy equation (eq. B.2.38) is equal at time-steps $k$ and $k+1$: $(dA_i/dt)_{ad}^k = (dA_i/dt)_{ad}^{k+1}$. This approximation modifies equation (B.2.46) to give an estimate for the entropy, $\tilde{A}_i^{k+1}$, given by (here we ignore the stellar energy feedback terms in §B.3)

$$\begin{aligned} \tilde{A}_i^{k+1} = A_i^k + \left( \frac{dA_i}{dt} \right)_{ad}^k \Delta t_i + 0.5 \left[ \frac{(\gamma-1)}{(\rho_i^k)^{\gamma-1}} \frac{-\Lambda(\rho_i^k, T_i^k) + H(\rho_i^k, T_i^k)}{\rho_i^k} \right. \\ \left. + \frac{(\gamma-1)}{(\rho_i^{k+1})^{\gamma-1}} \frac{-\Lambda(\rho_i^{k+1}, \tilde{T}_i^{k+1}) + H(\rho_i^{k+1}, \tilde{T}_i^{k+1})}{\rho_i^{k+1}} \right] \Delta t_i. \end{aligned} \tag{B.2.47}$$

[1]There are other solutions to this problem besides the artificial conductivity of Price (2008), such as those described by Read *et al.* (2010); Saitoh & Makino (2013); Hopkins (2013).

Equation (B.2.47) is iterated by re-calculating the entropy from the new cooling and heating rate - holding the adiabatic term constant, until the cooling and heating rates from equation (B.2.47) converge. Once the cooling and heating rates are consistent, $(dA_i/dt)_{ad}^{k+1}$ is estimated from equation (B.2.38) using the values for $\rho_i^{k+1}$, $\tilde{A}_i^{k+1}$ and the estimation of the velocity at the $k+1$ time-step from the leapfrog method:

$$\tilde{\mathbf{v}_i}^{k+1} = \mathbf{v}_i^{k+1/2} + 0.5\ \mathbf{a}_i^k \Delta t_i. \tag{B.2.48}$$

The value for $(dA_i/dt)_{ad}^{k+1}$ is then inserted into equation (B.2.46) to give the equation for the corrected entropy,

$$\begin{aligned} A_i^{k+1} = A_i^k + 0.5 & \left[ \left( \frac{dA_i}{dt} \right)_{ad}^{k} + \left( \frac{dA_i}{dt} \right)_{ad}^{k+1} \right] \Delta t_i \\ & + 0.5 \left[ \frac{(\gamma-1)}{(\rho_i^k)^{\gamma-1}} \frac{-\Lambda(\rho_i^k, T_i^k) + H(\rho_i^k, T_i^k)}{\rho_i^k} \right. \\ & \left. + \frac{(\gamma-1)}{(\rho_i^{k+1})^{\gamma-1}} \frac{-\Lambda(\rho_i^{k+1}, T_i^{k+1}) + H(\rho_i^{k+1}, T_i^{k+1})}{\rho_i^{k+1}} \right] \Delta t_i. \end{aligned} \tag{B.2.49}$$

Equation (B.2.49) is then iterated until the values for $A_i^{k+1}$, $\Lambda(\rho_i^{k+1}, T_i^{k+1})$ and $H(\rho_i^{k+1}, T_i^{k+1})$ converge. Thus two sets of iterations of equation (B.2.46) are required to integrate the entropy and thermodynamic variables.

### Individual time-steps

The time-step over which the $i$-th SPH particle is integrated is given by

$$\Delta t_{hyd,i} = \min(\Delta t_{CFL,i}, \Delta t_{DYN,i}), \tag{B.2.50}$$

where $\Delta t_{CFL,i}$ is the Courant-Friedrich-Levy condition

$$\Delta t_{CFL,i} = C_{CFL} \frac{0.5 h_i}{v_{dt,ij}}, \tag{B.2.51}$$

where $C_{CFL} = 0.2$, and $v_{dt,ij} = v_{sig,ij}$ (equation B.2.32), if $\mathbf{x}_{ij} \cdot \mathbf{v}_{ij} < 0$, otherwise $v_{dt,ij} = 0.5(c_{s,i} + c_{s,j} - \mathbf{v}_{ij} \cdot \mathbf{e}_{ij})$. The requirement that the force should not change

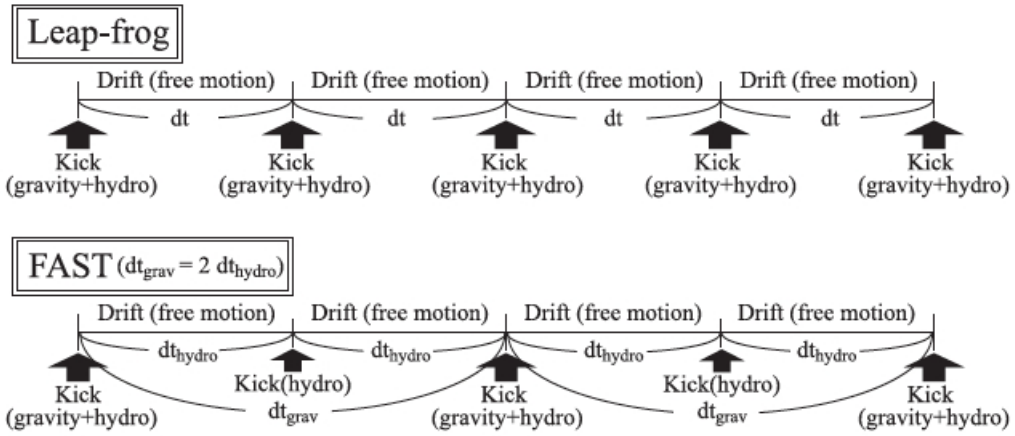


Figure B.4: The schematic picture of the leapfrog and FAST methods for the integration of a self-gravitating fluid. "Kick" refers to momentum exchanges between particles, and "Drift" refers to the free motions of the particles given their velocity vectors. The "kick" from hydrodynamical forces is updated twice as frequently as the gravitational forces. From Saitoh & Makino (2010)

significantly in one time-step is satisfied by

$$\Delta t_{DYN,i} = C_{DYN} \left( \frac{0.5 h_i}{|d\mathbf{v}_i/dt|} \right)^{1/2}, \tag{B.2.52}$$

where $C_{DYN} = 0.2$. The values of $C_{CFL}$ and $C_{DYN}$ are determined from testing in one-dimensional Riemann problems (Kawata *et al.*, 2013b).

### FAST scheme

The code implements the Fully Asynchronous Split Time-Integrator (FAST) scheme (Saitoh & Makino, 2010), which splits the hydrodynamical contributions from the pure gravitational contributions to the force (termed "kicks" ) on a SPH particle, and integrates each at different rates (the scheme is outlined in Fig. B.4). First, the time-step for the gravitational "kick" is assigned a preliminary value through the calculation of

$$\Delta \tilde{t}_{grav,i} = C_{DYN} \frac{0.5 h_i}{|(d\mathbf{v}_i/dt)_{grav}|}, \tag{B.2.53}$$

where $(d\mathbf{v}_i/dt)_{grav}$ is the acceleration from gravity only. Then, $\Delta\tilde{t}_{grav,i}$ is passed into the inequality

$$2^{l+1} \times \Delta t_{hyd,i} \geq \Delta\tilde{t}_{grav,i} \geq 2^l \times \Delta t_{hyd,i}, \tag{B.2.54}$$

where $\Delta t_{hyd,i}$ is calculated in equation (B.2.50) and $l \geq 0$ and is a natural number. The value of $l$ that satisfies this inequality is used to set the time-step for the gravitational part as

$$\Delta t_{grav,i} = 2^l \Delta t_{hyd,i}. \tag{B.2.55}$$

Because $l$ is a positive integer, the "kicks" associated with gravity and hydrodynamics are asynchronous as demonstrated in Fig. B.4. The benefit of this scheme is to reduce the computational cost of the gravitational force calculations without damaging the accuracy of the time integration.

### Time-step limiter

The above scheme works well when the particles in low dense regions either remain in low dense regions or move to a higher dense region on a timescale slower than their time-step. However, this is not always the case. For example, a supernova explosion generates a fast moving shock front, which propagates a dense shell of gas often into relatively low dense ambient gas. The time-step of the low dense gas can be larger than the arrival time of the supernova shell, in which case the low dense gas particle would not feel the shell until after it passes the gas particle. To remedy this caveat, a time-step limiter (suggested by Saitoh & Makino, 2009) is implemented, which sets an upper limit on the time-step size:

$$\Delta t_{lim,i} \leq 4 \times \min(\Delta t_{hyd,j}), \tag{B.2.56}$$

where $\Delta t_{lim,i}$ is the time-step limit of the $i$-th particle, and $\Delta t_{hyd,j}$ is the time-step of the $j$-th neighbour particle. At every time-step, $\Delta t_{hyd,i}$ is compared with the time-step of each of its neighbour particles, $\Delta t_{hyd,j}$. If $\Delta t_{hyd,i}$ is greater than four times the smallest of these, $\Delta t_{hyd,i} > 4 \times \min(\Delta \mathrm{t_{hyd,j}})$, then the time-step of the $i$-th particle is lowered to $\Delta t_{hyd,i} = 4 \times \min(\Delta \mathrm{t_{hyd,j}})$. Durier & Dalla Vecchia (2012) performed test simulations of a point-like explosion to mimic a super-

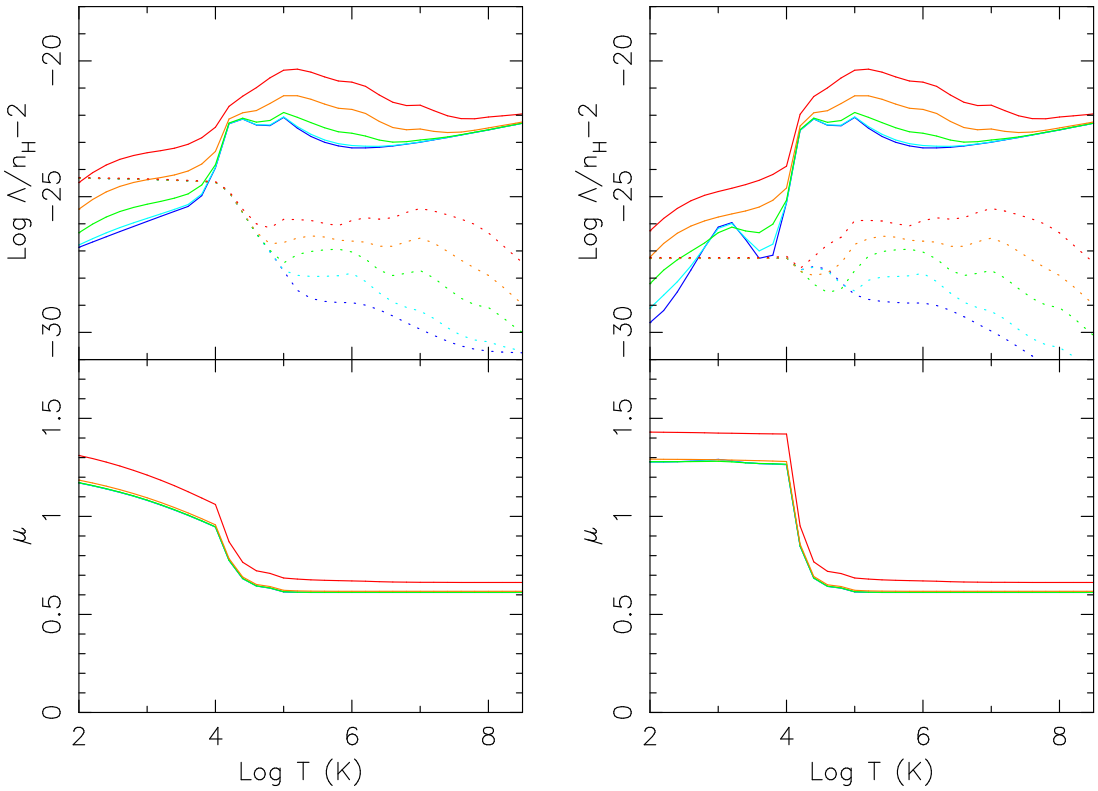


Figure B.5: *Left panel*: The top indicates the cooling rate (solid lines) and heating rate (dotted lines) for $n_H = 1$ cm$^{-3}$ density gas as a function of temperature. Colour indicates [Fe/H] $= -3, -2, -1, 0, +1$ from blue to red. The bottom indicates the mean molecular weight as a function of temperature. *Right*: The same as the left panel but for a $n_H = 1000$ cm$^{-3}$ density gas.

nova explosion, and demonstrated that the expansion of the supernova bubble is resolved only when the time-step limiter is implemented.

## B.3 Radiative Cooling and Star formation

### B.3.1 Gas Heating and Radiative Cooling

In the interstellar medium of galaxy systems, gas can be heated by stellar radiation through the processes such as photoionisation, supernovae and stellar winds. Gas is also subject to cooling through processes such as radiative cooling, which provides an effective way to radiate thermal energy away by the de-excitation

of ions from high to low energy states (see Katz *et al.*, 1996, for example of implementing these processes in galaxy formation simulations). In general, these processes are not resolved in simulations, but are included with sub-grid modelling. In this section, I outline how heating and cooling rates of gas particles are calculated, and how they are implemented in the simulation code.

The heating and cooling of gas gives rise to additional terms in the entropy equation (B.2.38), which now reads

$$\frac{dA_i}{dt} = \frac{(\gamma-1)}{\rho_i^{\gamma-1}}\left[\left(\frac{du}{dt}\right)_{diss} + \frac{-\Lambda_i + H_i}{\rho_i} + \Delta E_{SN} + L_{SW}\right], \tag{B.3.1}$$

where $\Lambda_i/\rho_i$, $H_i/\rho_i$, $\Delta E_{SN}$ and $L_{SW}$ are the cooling rate per unit mass, UV-background heating rate per unit mass, energy feedback per unit mass from supernova and stellar winds[1] within each time-step of the $i$-th particle, respectively. Radiative cooling can occur through the de-excitation of metal lines, and so $\Lambda_i$ and $H_i$ depend on the metallicity of the gas as well as the temperature and density. The top and bottom panels of Fig. B.5 show how $\Lambda_i/n_H^2$, $H_i/n_H^2$ and the mean molecular weight, $\mu$, depend on temperature and metallicity. The calculation is made by CLOUDY v08.00 (Ferland *et al.*, 1998), (similar method to Robertson & Kravtsov, 2008), for gas with a density of $n_H = 1$ cm$^{-3}$ (left) and $n_H = 1000$ cm$^{-3}$ (right). Heating is modelled from the UV background produced by quasars, which is the dominant source at low redshifts (see for example Fig. 8 of Haardt & Madau, 2012). We adopt the Haardt & Madau (1996) UV background radiative transfer model, and CLOUDY provides the heating rate of gaseous media according to the background UV flux and cross-sectional density of a given species (see for example Katz *et al.*, 1996, for a simplified version). In order to avoid overcooling and catastrophic fragmentation, a thermal energy floor following Robertson & Kravtsov (2008) is employed. This ensures that the Jeans mass is kept above $2N_{nb}m_p$, where $N_{nb}$ is the number of neighbour particles and $m_p$ is the particle mass.

[1]The energy input from supernovae and stellar winds are non-zero only for "feedback particles", which make up a fraction of particles that specifically model feedback from massive stars during the transition from star to gas particle (see §B.3.4).

### B.3.2 Star formation

Star formation is modelled by changing gas particles into a star particles. A gas particle is eligible for star formation if the following criteria are met:

- The gas density must be greater than a pre-determined number density threshold, $n_{H,th}$.
- The velocity field must be convergent: $\nabla \cdot \mathbf{v}_i < 0$.

The star formation rate (SFR) is given by the Schmidt law (see Kawata & Gibson, 2003)

$$\frac{d\rho_*}{dt} = -\frac{d\rho_g}{dt} = \frac{C_*\rho_g}{t_g}, \tag{B.3.2}$$

where $C_*$ is a dimensionless parameter, $\rho_*$ and $\rho_g$ are the mass density of stellar and gas material respectively, and

$$t_g = \sqrt{3\pi/16G\rho_g}, \tag{B.3.3}$$

is the dynamical time, which is longer than the cooling time-scale in the region eligible to form stars. In reality, the form of the star formation rate in equation (B.3.2) means that the gas mass depletes exponentially over time as gas becomes locked up into stars during star formation. Therefore the amount of gas converted to stars after a time interval, $\Delta t$, is

$$\Delta m_* = m_{g,0} - m_{g,0}e^{-C_*\Delta t/t_g}, \tag{B.3.4}$$

where $m_{g,0}$ is the initial gas mass at the beginning of the time interval. However, the discrete particle nature of SPH means that it is not practical to change $\Delta m$ worth of material into stars every $\Delta t$ (although see Springel & Hernquist, 2003). In GCD+, a particle is either completely star or completely gas, therefore the *fractional* amount of gas turned into stars in equation (B.3.4) serves as a probability that a gas particle changes into a star particle. This is expressed as

$$p_* \equiv \frac{\Delta m_*}{m_{g,0}} = 1 - e^{-C_*\Delta t/t_g}. \tag{B.3.5}$$

This probability increases with gas particle density, because equation (B.3.3) shows that as $\rho_g$ increases, the dynamical time, $t_g$, decreases, which in turn ensures a larger negative exponent in equation (B.3.5).

In this scheme, the global star formation rate follows the Schmidt law because the probability corresponds to a fraction of newly formed star particles in a sample of gas particles that ensures that the total amount of star formation is consistent with the Schmidt law. In addition, the conversion of whole star particles into whole gas particles is spread over time which avoids extreme numbers of new stars being born at once (as long as $\Delta t$ is reasonably small), and guarantees mass conservation because all gas and star particles in the simulation are kept at the same mass. This suppresses numerical fluctuations in the gravitational potential.

Once a gas particle is converted into a star particle, the particle follows collisionless dynamics, and ceases to be influenced by hydrodynamical forces.

### B.3.3 Initial Mass Function

Owing to computational restrictions, galactic discs are simulated with approximately $N = 10^{6-7}$ number of particles, which means that for a simulation of Milky Way size, each star/gas particle holds masses of $m_p \sim 10^{4-5}$ $\mathrm{M}_\odot$. Masses of this order represent a group of stars rather than a single star, and therefore a star particle is regarded as a group of stars of individual masses distributed among the initial mass function (IMF). In the studies presented in this thesis, the IMF is assumed to be universal and of the Salpeter (1955) form. The Salpeter IMF describes the relative fraction of stars in a population, $\Phi(m)$, born in a given initial mass range:

$$\Phi(m)dm = Am^{-(1+x)}dm, \tag{B.3.6}$$

where $x = 1.35$ is the Salpeter index. The coefficient $A$ is determined by the normalisation over the entire initial mass range, whose lower and upper limits are set to $M_l = 0.1$ $\mathrm{M}_\odot$ and $M_u = 100$ $\mathrm{M}_\odot$ respectively.

### B.3.4 Feedback

GCD+ incorporates mass, energy and metal feedback from supernovae types Ia (SNe Ia) and II (SNe II) and stellar winds based on the assumed IMF (as described in Kawata *et al.*, 2013a). In this section, I describe how each source of feedback is modelled.

First, every star particle in the simulation is assigned a mass group ID number, which ranges from 1 to 61 (61 is chosen as a compromise between sampling the stellar mass range of the IMF and the resolution i.e. number of neighbour particles). In this feedback scheme, 61 particles describe a whole mass range of stars in a star cluster, although in practice, all particles are kept at the same mass and maintain a constant mass resolution. A star cluster with a range of stellar masses corresponding to the assumed Salpeter IMF will undergo a mass loss, in the form of SNe Ia and SNe II, equal to about 30% of the original cluster mass in a Hubble time. Therefore, star particles with an ID between 1 and 19 are used to describe the mass loss, energy feedback and metal enrichment from SNe Ia and SNe II. These are called feedback particles. Particles with smaller IDs are responsible for feedback from higher mass stars.

Depending on their ID and age, a star particle becomes a feedback particle for a period of time as described below during which the feedback effects take place. Afterwards, the feedback particle becomes a normal gas particle. The transition of a star to a gas particle models the mass loss from the cluster and ensures that the particle mass of a gas and star particle is always equal.

The increased pressure of the feedback particle affects neighbouring gas particles through the Euler equation (B.2.22). For simplicity, feedback particles do not feel any reaction from the neighbour particles and follow the collisionless $N$-body equation (see Pelupessy *et al.*, 2004). The thermal energy of the feedback particles is calculated in the SPH scheme with radiative cooling and additional heating from stellar winds and SNe Ia and SNe II.

The metals produced by SNe II, SNe Ia and intermediate-mass stars are distributed from the feedback particles to neighbouring gas particles through the metal diffusion scheme of Greif *et al.* (2009), i.e. the metal diffusion applied to the feedback particles and normal gas particles is the same. Once the feedback particles are old enough, they become normal gas particles. The new gas particles inherit the gas density, temperature and metal abundance from the feedback

particles.

### SNe II particles

SNe II eject approximately 13% of the mass of a star cluster following the assumed IMF and the remnant masses calculated in Woosley & Weaver (1995). Therefore, each star particle whose ID is in the range 1-8 becomes a feedback particle, or "SNeII particle", which are responsible for the energy and metals produced by stellar winds and SNe II. All SNe II particles are identical.

A star particle in the ID range 1-8 becomes a SNeII particle as soon as it is born, which means that they are effective immediately. For example, SNe II particles of solar metallicity are responsible for mass loss and feedback from 100 to 7 $M_\odot$ stars from the time they are born until they reach the age of a 7 $M_\odot$ star, after which time they become a normal gas particle.

Each supernova produces thermal energy $E_{SN}$ ergs. Stellar winds from each massive star (defined as $M_* > 15$ $M_\odot$) produces thermal energy of $L_{SW}$ ergs $s^{-1}$, which is added to the SNe II particles at a rate consistent with their metallicity and age. To find the number of supernova, $N_{SN}$, per cluster, the initial mass function must be integrated over the mass range in which supernovae can occur. Each stellar mass corresponds to a lifetime, therefore the number of supernovae that occur in a time interval, $\Delta t = \tau_2 - \tau_1$, where $\tau_1$ and $\tau_2$ are time-steps since the star particle was born (i.e. stellar lifetimes), is equal to the number of supernovae that occur in the corresponding stellar mass range. The number is calculated as

$$\begin{aligned} N_{SN} = m_{cl} \times \frac{\int_{m_1}^{m_2} \Phi(m) dm}{\int_{M_l}^{M_u} \Phi(m) m dm} &= m_{cl} \times \frac{\int_{m_1}^{m_2} m^{-(1+x)} dm}{\int_{M_l}^{M_u} m^{-x} dm} \\ &= m_{cl} \times \frac{x-1}{x} \frac{(1-(m_1/m_2)^{-x}) m_2^{-x}}{(1-(M_l/M_u)^{-x+1}) M_u^{-x+1}} \end{aligned} \tag{B.3.7}$$

where $m_2$ and $m_1$ are the masses of stars that have lifetimes $\tau_2$ and $\tau_1$ respectively, $M_l = 8$ $M_\odot$ and $M_u = 100$ $M_\odot$ are the lower and upper masses for SNe II, and $m_{cl}$ is the mass of the cluster (61$\times$ the mass of a star particle). The total energy released in the form of SNe II per cluster between time interval, $\Delta t$, is $N_{SN} \times E_{SN}$. Because there are 8 SNeII particles per 61 star particle cluster, each SNeII particle

receives 1/8th of the energy and metals[1] produced by a star cluster of 61 star particles, depending on the age and metallicity. This energy is received by only the SNeII particle that produced it at a rate governed by the above equation, which raises the pressure and temperature of the SNeII particle.

Radiative cooling is turned off until either the age of the SNeII particle exceeds the lifetime of a 8 $M_\odot$ star or the cooling time becomes longer than the dynamical time. Feedback energy is not distributed to neighbouring particles, which guarantees that the SNeII particles are hot enough to avoid rapid cooling that is expected in dense regions associated with star formation (e.g. Kay *et al.*, 2002; Booth *et al.*, 2007; Dalla Vecchia & Schaye, 2012). The sustained high pressure of the SNe II particles means that the expansion of individual bubbles driven by the pressure force in the Euler equation must be resolved. Kawata *et al.* (2013b) demonstrates that the new version of GCD+ is able to resolve the expansion of a feedback bubble thanks to the small time-steps employed by the time-step limiter (Saitoh *et al.*, 2008).

### Other feedback particles

A similar algorithm is applied to star particles of IDs in the range 9-19. These star particles turn into normal gas particles as a function of their age, which models the rest of the 30% mass loss of the cluster and metal enrichment from SN Ia feedback.

Unlike the SNe II particles, each ID number in this range corresponds to a different stellar mass range. For example, the star particle for which ID = 9 with solar metallicity represents stars with masses from 7 to 5.6 $M_\odot$. When the age of the particle exceeds the lifetime of a 7 $M_\odot$, it becomes a feedback particle. The particle inherits the original metal abundance of the star and receives additional metals that the stars in this mass range produce (van den Hoek & Groenewegen, 1997), which are then diffused to neighbouring particles. The thermal energy is calculated with the SPH scheme, and the additional pressure from these feedback particles is applied to their neighbour particles. Radiative cooling is turned on during the mass loss. Once the particle becomes older than the lifetime of a 5.6

[1]To calculate the metal yield per cluster as a function of time, the integrands on the top and bottom of equation (B.3.7) are multiplied by the metal production for stars of given mass, as calculated in Woosley & Weaver (1995).

$M_\odot$ star, the particle becomes a normal gas particle.

The same algorithm is applied to particles in the ID range 10-19, which are each responsible for a different stellar mass range. The particle whose ID is high enough to cover the mass range of SNe Ia progenitors receive the energy and metals from SNe Ia as a function of their age. For these feedback particles, radiative cooling is turned on.

The main free parameters in GCD+ include the energy per supernova, $E_{SN}$ and the stellar wind energy per massive star, $L_{SW}$, which together control the strength of feedback and the effect of feedback on star formation.

# References


Aarseth, S.J. (1963). Dynamical evolution of clusters of galaxies, I. MNRAS, **126**, 223. 26

Agertz, O., Moore, B., Stadel, J., Potter, D., Miniati, F., Read, J., Mayer, L., Gawryszczak, A., Kravtsov, A., Nordlund, Å., Pearce, F., Quilis, V., Rudd, D., Springel, V., Stone, J., Tasker, E., Teyssier, R., Wadsley, J. & Walder, R. (2007). Fundamental differences between SPH and grid methods. MNRAS, **380**, 963–978. 173

Aguerri, J.A.L., Debattista, V.P. & Corsini, E.M. (2003). Measurement of fast bars in a sample of early-type barred galaxies. MNRAS, **338**, 465–480. 25

Allende Prieto, C., Majewski, S.R., Schiavon, R., Cunha, K., Frinchaboy, P., Holtzman, J., Johnston, K., Shetrone, M., Skrutskie, M., Smith, V. & Wilson, J. (2008). APOGEE: The Apache Point Observatory Galactic Evolution Experiment. *Astronomische Nachrichten*, **329**, 1018. 107, 146

Athanassoula, E. (1984). The spiral structure of galaxies. Phys. Rep., **114**, 319–403. 102

Athanassoula, E. (2002). Bar-Halo Interaction and Bar Growth. ApJ, **569**, L83–L86. 108

Athanassoula, E. (2012). Bars and secular evolution in disk galaxies: Theoretical input. *ArXiv e-prints*. 108

Athanassoula, E., Romero-Gómez, M. & Masdemont, J.J. (2009). Rings and spirals in barred galaxies - I. Building blocks. MNRAS, **394**, 67–81. 14

Baba, J., Asaki, Y., Makino, J., Miyoshi, M., Saitoh, T.R. & Wada, K. (2009). The Origin of Large Peculiar Motions of Star-Forming Regions and Spiral Structures of Our Galaxy. ApJ, **706**, 471–481. 27, 63, 77

Baba, J., Saitoh, T.R. & Wada, K. (2013). Dynamics of Non-steady Spiral Arms in Disk Galaxies. ApJ, **763**, 46. 25, 27, 80, 93, 103, 104, 106, 142

Balsara, D.S. (1995). von Neumann stability analysis of smooth particle hydrodynamics–suggestions for optimal algorithms. *Journal of Computational Physics*, **121**, 357–372. 171

Banerjee, A., Patra, N.N., Chengalur, J.N. & Begum, A. (2013). A slow bar in the dwarf irregular galaxy NGC 3741. MNRAS, **434**, 1257–1263. 25

Barnes, J. & Hut, P. (1986). A hierarchical O(N log N) force-calculation algorithm. Nature, **324**, 446–449. xi, 50, 156, 157

Bertin, G. & Lin, C.C. (1996). *Spiral structure in galaxies a density wave theory*. 14

Bertin, G., Lin, C.C., Lowe, S.A. & Thurstans, R.P. (1989a). Modal approach to the morphology of spiral galaxies. I - Basic structure and astrophysical viability. ApJ, **338**, 78–120. 4, 78

Bertin, G., Lin, C.C., Lowe, S.A. & Thurstans, R.P. (1989b). Modal Approach to the Morphology of Spiral Galaxies. II. Dynamical Mechanisms. ApJ, **338**, 104. 4

Binney, J. (2010). Distribution functions for the Milky Way. MNRAS, **401**, 2318–2330. 33

Binney, J. & Tremaine, S. (2008). *Galactic Dynamics: Second Edition*. Princeton University Press. 11, 16, 77, 85, 152, 153

Bird, J.C., Kazantzidis, S., Weinberg, D.H., Guedes, J., Callegari, S., Mayer, L. & Madau, P. (2013). Inside Out and Upside Down: Tracing

the Assembly of a Simulated Disk Galaxy Using Mono-Age Stellar Populations. *ArXiv e-prints*. 27

Block, D.L., Bertin, G., Stockton, A., Grosbol, P., Moorwood, A.F.M. & Peletier, R.F. (1994). 2.1 $\mu$m images of the evolved stellar disk and the morphological classification of spiral galaxies. A&A, **288**, 365–382. 78

Booth, C.M., Theuns, T. & Okamoto, T. (2007). Molecular cloud regulated star formation in galaxies. MNRAS, **376**, 1588–1610. 183

Bottema, R. (2003). Simulations of normal spiral galaxies. MNRAS, **344**, 358–384. 27

Bovy, J. *et al.* (2012). The Milky Way's Circular-velocity Curve between 4 and 14 kpc from APOGEE data. ApJ, **759**, 131. 107, 146

Brook, C.B., Stinson, G.S., Gibson, B.K., Kawata, D., House, E.L., Miranda, M.S., Macciò, A.V., Pilkington, K., Roškar, R., Wadsley, J. & Quinn, T.R. (2012). Thin disc, thick disc and halo in a simulated galaxy. MNRAS, **426**, 690–700. 18

Brunetti, M., Chiappini, C. & Pfenniger, D. (2011). Stellar diffusion in barred spiral galaxies. A&A, **534**, A75. 64

Buta, R. & Block, D.L. (2001). A Dust-penetrated Classification Scheme for Bars as Inferred from Their Gravitational Force Fields. ApJ, **550**, 243–252. 56, 57

Buta, R., Vasylyev, S., Salo, H. & Laurikainen, E. (2005). The Distribution of Bar and Spiral Arm Strengths in Disk Galaxies. AJ, **130**, 506–523. 56

Carignan, C. & Freeman, K.C. (1985). Basic parameters of dark halos in late-type spirals. ApJ, **294**, 494–501. 2

Carlberg, R.G. & Freedman, W.L. (1985). Dissipative models of spiral galaxies. ApJ, **298**, 486–492. 27, 100

Carlberg, R.G. & Sellwood, J.A. (1985). Dynamical evolution in galactic disks. ApJ, **292**, 79–89. 15

Casagrande, L., Schönrich, R., Asplund, M., Cassisi, S., Ramírez, I., Meléndez, J., Bensby, T. & Feltzing, S. (2011). New constraints on the chemical evolution of the solar neighbourhood and Galactic disc(s). Improved astrophysical parameters for the Geneva-Copenhagen Survey. A&A, **530**, A138. 19, 134

Chamandy, L., Subramanian, K. & Quillen, A. (2014). Magnetic arms generated by multiple interfering galactic spiral patterns. MNRAS, **437**, 562–574. 105

Chen, L., Hou, J.L., Yu, J.C., Liu, C., Deng, L.C., Newberg, H.J., Carlin, J.L., Yang, F., Zhang, Y.Y., Shen, S.Y., Zhang, H.T., Chen, J.J., Chen, Y.Q., Christlieb, N., Han, Z.W., Lee, H.T., Liu, X.W., Pan, K.K., Shi, J.R., Wang, H.C. & Zhu, Z. (2012). The LEGUE disk targets for LAMOST's pilot survey. *Research in Astronomy and Astrophysics*, **12**, 805–812. 107

Combes, F. & Sanders, R.H. (1981). Formation and properties of persisting stellar bars. A&A, **96**, 164–173. 57

Comparetta, J. & Quillen, A.C. (2012). Stellar Migration by Short Lived Density Peaks Arising from Interference of Spiral Density Waves in an N-body Simulation. *ArXiv e-prints*. 80, 103, 105, 141, 145

Cox, D.P. (2005). The Three-Phase Interstellar Medium Revisited. ARA&A, **43**, 337–385. 2

Croom, S.M., Lawrence, J.S., Bland-Hawthorn, J., Bryant, J.J., Fogarty, L., Richards, S., Goodwin, M., Farrell, T., Miziarski, S., Heald, R., Jones, D.H., Lee, S., Colless, M., Brough, S., Hopkins, A.M., Bauer, A.E., Birchall, M.N., Ellis, S., Horton, A., Leon-Saval, S., Lewis, G., López-Sánchez, Á.R., Min, S.S., Trinh, C. & Trowland, H. (2012). The Sydney-AAO Multi-object Integral field spectrograph. MNRAS, **421**, 872–893. 146

Cullen, L. & Dehnen, W. (2010). Inviscid smoothed particle hydrodynamics. MNRAS, **408**, 669–683. 171

Dalla Vecchia, C. & Schaye, J. (2012). Simulating galactic outflows with thermal supernova feedback. MNRAS, **426**, 140–158. 183

de Jong, R. (2012). 4MOST: 4-metre Multi-Object Spectroscopic Telescope. In *Science from the Next Generation Imaging and Spectroscopic Surveys*. 107

de Jong, R.S. (1996). Near-infrared and optical broadband surface photometry of 86 face-on disk dominated galaxies. III. The statistics of the disk and bulge parameters. A&A, **313**, 45–64. 78

de Jong, R.S., Simard, L., Davies, R.L., Saglia, R.P., Burstein, D., Colless, M., McMahan, R. & Wegner, G. (2004). Structural properties of discs and bulges of early-type galaxies. MNRAS, **355**, 1155–1170. 2

Debattista, V.P. & Sellwood, J.A. (2000). Constraints from Dynamical Friction on the Dark Matter Content of Barred Galaxies. ApJ, **543**, 704–721. 108

Debattista, V.P., Corsini, E.M. & Aguerri, J.A.L. (2002). A fast bar in the post-interaction galaxy NGC 1023. MNRAS, **332**, 65–77. 25

Dehnen, W. & Aly, H. (2012). Improving convergence in smoothed particle hydrodynamics simulations without pairing instability. MNRAS, **425**, 1068–1082. 165

Dehnen, W. & Read, J.I. (2011). N-body simulations of gravitational dynamics. *European Physical Journal Plus*, **126**, 55–+. 26, 155, 156, 157, 160

Di Matteo, P., Haywood, M., Combes, F., Semelin, B. & Snaith, O.N. (2013). Signatures of radial migration in barred galaxies: Azimuthal variations in the metallicity distribution of old stars. A&A, **553**, A102. 18, 147

Dobbs, C.L. & Bonnell, I.A. (2008). Simulations of spiral galaxies with an active potential: molecular cloud formation and gas dynamics. MNRAS, **385**, 1893–1902. 72

Dobbs, C.L. & Pringle, J.E. (2010). Age distributions of star clusters in spiral and barred galaxies as a test for theories of spiral structure. MNRAS, **409**, 396–404. 72, 75, 142

Dobbs, C.L., Theis, C., Pringle, J.E. & Bate, M.R. (2010). Simulations of the grand design galaxy M51: a case study for analysing tidally induced spiral structure. MNRAS, **403**, 625–645. 15, 144

Dobbs, C.L., Krumholz, M.R., Ballesteros-Paredes, J., Bolatto, A.D., Fukui, Y., Heyer, M., Mac Low, M.M., Ostriker, E.C. & Vázquez-Semadeni, E. (2013). Formation of Molecular Clouds and Global Conditions for Star Formation. *ArXiv e-prints*. 20

D'Onghia, E., Vogelsberger, M. & Hernquist, L. (2013). Self-perpetuating Spiral Arms in Disk Galaxies. ApJ, **766**, 34. 27, 80, 98, 100, 103, 144

Donner, K.J. & Thomasson, M. (1994). Structure and evolution of long-lived spiral patterns in galaxies. A&A, **290**, 785–795. 26, 77

Dubinski, J. (1996). A parallel tree code. New Astron., **1**, 133–147. 159

Durier, F. & Dalla Vecchia, C. (2012). Implementation of feedback in smoothed particle hydrodynamics: towards concordance of methods. MNRAS, **419**, 465–478. 177

Efstathiou, G. & Eastwood, J.W. (1981). On the clustering of particles in an expanding universe. MNRAS, **194**, 503–525. 26

Efstathiou, G., Lake, G. & Negroponte, J. (1982). The stability and masses of disc galaxies. MNRAS, **199**, 1069–1088. 100

Egusa, F., Kohno, K., Sofue, Y., Nakanishi, H. & Komugi, S. (2009). Determining Star Formation Timescale and Pattern Speed in Nearby Spiral Galaxies. ApJ, **697**, 1870–1891. 21, 22, 57

Elmegreen, D.M. & Elmegreen, B.G. (2014). The Onset of Spiral Structure in the Universe. ApJ, **781**, 11. 4

Elmegreen, D.M., Elmegreen, B.G. & Bellin, A.D. (1990). Statistical evidence that galaxy companions trigger bars and change the spiral Hubble type. ApJ, **364**, 415–419. 4

Emsellem, E., Fathi, K., Wozniak, H., Ferruit, P., Mundell, C.G. & Schinnerer, E. (2006). Gas and stellar dynamics in NGC 1068: probing the galactic gravitational potential. MNRAS, **365**, 367–384. 25

Ferland, G.J., Korista, K.T., Verner, D.A., Ferguson, J.W., Kingdon, J.B. & Verner, E.M. (1998). CLOUDY 90: Numerical Simulation of Plasmas and Their Spectra. PASP, **110**, 761–778. 179

Ferreras, I., Cropper, M., Kawata, D., Page, M. & Hoversten, E.A. (2012). The Swift/UVOT catalogue of NGC 4321 star-forming sources: a case against density wave theory. MNRAS, **424**, 1636–1646. 21, 22, 50, 57, 77, 142

Flynn, C., Holmberg, J., Portinari, L., Fuchs, B. & Jahreiss, H. (2006). On the mass-to-light ratio of the local Galactic disc and the optical luminosity of the Galaxy. MNRAS, **372**, 1149–1160. 32

Foyle, K., Rix, H.W., Walter, F. & Leroy, A.K. (2010). Arm and Interarm Star Formation in Spiral Galaxies. ApJ, **725**, 534–541. 20

Foyle, K., Rix, H.W., Dobbs, C.L., Leroy, A.K. & Walter, F. (2011). Observational Evidence Against Long-lived Spiral Arms in Galaxies. ApJ, **735**, 101. 21, 22, 50, 57, 77, 142

Freeman, K.C. (1970). On the Disks of Spiral and so Galaxies. ApJ, **160**, 811. 2

Fuchs, B. (2001). Density waves in the shearing sheet. I. Swing amplification. A&A, **368**, 107–121. 79, 102

Fuchs, B., Dettbarn, C. & Tsuchiya, T. (2005). Density waves in the shearing sheet. V. Feedback cycle for swing amplification by non-linear effects. A&A, **444**, 1–13. 143

Fujii, M.S. & Baba, J. (2012). Destruction of star clusters due to the radial migration in spiral galaxies. MNRAS, **427**, L16–L20. 105

Fujii, M.S., Baba, J., Saitoh, T.R., Makino, J., Kokubo, E. & Wada, K. (2011). The Dynamics of Spiral Arms in Pure Stellar Disks. ApJ, **730**, 109–+. 26, 27, 34, 54, 72, 83, 85, 97, 100, 105, 108

Fujimoto, M. (1968). Modeling of gas flow through a spiral sleeve. In *Non-stable Phenomena in Galaxies*, vol. 29 of *IAU Symposium*, 453. 1, 20

Gabbasov, R.F., Repetto, P. & Rosado, M. (2009). On the Bar Pattern Speed Determination of NGC 3367. ApJ, **702**, 392–402. 25

Garcia-Burillo, S., Guelin, M. & Cernicharo, J. (1993). CO in M51 - Part One - Molecular Spiral Structure. A&A, **274**, 123. 21

Gerssen, J., Kuijken, K. & Merrifield, M.R. (1999). The pattern speed of the bar in NGC 4596. MNRAS, **306**, 926–930. 25

Gilmore, G. & Reid, N. (1983). New light on faint stars. III - Galactic structure towards the South Pole and the Galactic thick disc. MNRAS, **202**, 1025–1047. 2

Gilmore, G. *et al.* (2012). The Gaia-ESO Public Spectroscopic Survey. *The Messenger*, **147**, 25–31. 107, 146

Gingold, R.A. & Monaghan, J.J. (1977). Smoothed particle hydrodynamics - Theory and application to non-spherical stars. MNRAS, **181**, 375–389. 50, 163

Gingold, R.A. & Monaghan, J.J. (1982). Kernel estimates as a basis for general particle methods in hydrodynamics. *Journal of Computational Physics*, **46**, 429–453. 166

Goldreich, P. & Lynden-Bell, D. (1965). II. Spiral arms as sheared gravitational instabilities. MNRAS, **130**, 125–+. 11, 41, 79

Grand, R.J.J., Kawata, D. & Cropper, M. (2012a). The dynamics of stars around spiral arms. MNRAS, **421**, 1529–1538. 25, 27, 30

Grand, R.J.J., Kawata, D. & Cropper, M. (2012b). zDynamics of stars around spiral arms in an N-body/SPH simulated barred spiral galaxy. MNRAS, **426**, 167–180. 25, 27, 49

Grand, R.J.J., Kawata, D. & Cropper, M. (2013). aSpiral arm pitch angle and galactic shear rate in N-body simulations of disc galaxies. A&A, **553**, A77. 78

Grand, R.J.J., Kawata, D. & Cropper, M. (2014). Orbits of radial migrators and non-migrators around a spiral arm in N-body simulations. MNRAS, **439**, 623–638. 105

Greif, T.H., Glover, S.C.O., Bromm, V. & Klessen, R.S. (2009). Chemical mixing in smoothed particle hydrodynamics simulations. MNRAS, **392**, 1381–1387. 51, 182

Grosbøl, P., Patsis, P.A. & Pompei, E. (2004). Spiral galaxies observed in the near-infrared K band. I. Data analysis and structural parameters. A&A, **423**, 849–859. 15

Grosbol, P.J. & Patsis, P.A. (1998). Stellar disks of optically flocculent and grand design spirals. Decoupling of stellar and gaseous disks. A&A, **336**, 840–854. 78

Haardt, F. & Madau, P. (1996). Radiative Transfer in a Clumpy Universe. II. The Ultraviolet Extragalactic Background. ApJ, **461**, 20. 179

Haardt, F. & Madau, P. (2012). Radiative Transfer in a Clumpy Universe. IV. New Synthesis Models of the Cosmic UV/X-Ray Background. ApJ, **746**, 125. 179

Haywood, M. (2008). Radial mixing and the transition between the thick and thin Galactic discs. MNRAS, **388**, 1175–1184. 18, 19, 135

Haywood, M., Di Matteo, P., Lehnert, M.D., Katz, D. & Gómez, A. (2013). The age structure of stellar populations in the solar vicinity. Clues of a two-phase formation history of the Milky Way disk. A&A, **560**, A109. 18

Hernquist, L. (1990). An analytical model for spherical galaxies and bulges. ApJ, **356**, 359–364. 80

Hernquist, L. & Katz, N. (1989). TREESPH - A unification of SPH with the hierarchical tree method. ApJS, **70**, 419–446. 50, 154, 173

Hirota, A., Kuno, N., Baba, J., Egusa, F., Habe, A., Muraoka, K., Tanaka, A., Nakanishi, H. & Kawabe, R. (2014). Wide-field $^{12}$CO (J = 1-0) imaging of the nearby barred galaxy M 83 with NMA and Nobeyema 45 m

telescope: Mole cular gas kinematics and star formation along the bar. PASJ, **66**, 46. 22

Hohl, F. (1971). Numerical Experiments with a Disk of Stars. ApJ, **168**, 343. 8

Holmberg, E. (1941). On the Clustering Tendencies among the Nebulae. II. a Study of Encounters Between Laboratory Models of Stellar Systems by a New Integration Procedure. ApJ, **94**, 385. 26

Holmberg, J., Nordström, B. & Andersen, J. (2009). The Geneva-Copenhagen survey of the solar neighbourhood. III. Improved distances, ages, and kinematics. A&A, **501**, 941–947. 18, 33

Hopkins, P.F. (2013). Pressure-Entropy SPH: Pressure-entropy smooth-particle hydrodynamics. Astrophysics Source Code Library. 27, 173

Hopkins, P.F., Quataert, E. & Murray, N. (2012). The structure of the interstellar medium of star-forming galaxies. MNRAS, **421**, 3488–3521. 27

Hubble, E.P. (1926). Extragalactic nebulae. ApJ, **64**, 321–369. 2, 78, 104, 147

Julian, W.H. & Toomre, A. (1966). Non-Axisymmetric Responses of Differentially Rotating Disks of Stars. ApJ, **146**, 810–+. 11, 41, 79, 92, 100, 102, 104, 143, 144

Kalnajs, A.J. (1972). The Equilibria and Oscillations of a Family of Uniformly Rotating Stellar Disks. ApJ, **175**, 63. 6

Katz, N., Weinberg, D.H. & Hernquist, L. (1996). Cosmological Simulations with TreeSPH. ApJS, **105**, 19. 50, 154, 177, 179

Kawata, D. & Gibson, B.K. (2003). GCD+: a new chemodynamical approach to modelling supernovae and chemical enrichment in elliptical galaxies. MNRAS, **340**, 908–922. 50, 80, 107, 154, 179

Kawata, D., Grand, R.J.J. & Cropper, M. (2012). Stellar dynamics around transient co-rotating spiral arms. *Assembling the Puzzle of the Milky Way, Le Grand-Bornand, France, Edited by C. Reylé; A. Robin; M. Schultheis; EPJ Web of Conferences, Volume 19, id.07006*, **19**, 7006. 57

Kawata, D., Gibson, B.K., Barnes, D.J., Grand, R.J.J. & Rahimi, A. (2013a). Numerical simulations of bubble-induced star formation in dwarf irregular galaxies with a novel stellar feedback scheme. MNRAS. 181

Kawata, D., Okamoto, T., Gibson, B.K., Barnes, D.J. & Cen, R. (2013b). Calibrating an updated smoothed particle hydrodynamics scheme within gcd+. MNRAS, **428**, 1968–1979. 50, 80, 107, 154, 165, 170, 173, 175, 183

Kawata, D., Hunt, J.A.S., Grand, R.J.J., Pasetto, S. & Cropper, M. (2014). Gas and Stellar Motions and Observational Signatures of Co-Rotating Spiral Arms. *ArXiv e-prints*. 148

Kay, S.T., Pearce, F.R., Frenk, C.S. & Jenkins, A. (2002). Including star formation and supernova feedback within cosmological simulations of galaxy formation. MNRAS, **330**, 113–128. 183

Kendall, S., Kennicutt, R.C. & Clarke, C. (2011). Spiral structure in nearby galaxies - I. Sample, data analysis and overview of results. MNRAS, **414**, 538–564. 15

Kennicutt, R., Jr. & Hodge, P. (1982). A comparison of measured spiral arm properties with model predictions. ApJ, **253**, 101–107. 79

Kennicutt, R.C. & Evans, N.J. (2012). Star Formation in the Milky Way and Nearby Galaxies. ARA&A, **50**, 531–608. 2

Kennicutt, R.C., Jr. (1981). The shapes of spiral arms along the Hubble sequence. AJ, **86**, 1847–1858. 78, 104

Kennicutt, R.C., Jr. *et al.* (2003). SINGS: The SIRTF Nearby Galaxies Survey. PASP, **115**, 928–952. 146

Kormendy, J. & Kennicutt, R.C., Jr. (2004). Secular Evolution and the Formation of Pseudobulges in Disk Galaxies. ARA&A, **42**, 603–683. 2, 56

Kormendy, J. & Norman, C.A. (1979). Observational constraints on driving mechanisms for spiral density waves. ApJ, **233**, 539–552. 4, 15

Lee, Y.S., Beers, T.C., An, D., Ivezić, Ž., Just, A., Rockosi, C.M., Morrison, H.L., Johnson, J.A., Schönrich, R., Bird, J., Yanny, B., Harding, P. & Rocha-Pinto, H.J. (2011). Formation and Evolution of the Disk System of the Milky Way: [$\alpha$/Fe] Ratios and Kinematics of the SEGUE G-dwarf Sample. ApJ, **738**, 187. 107, 146

Lépine, J.R.D., Acharova, I.A. & Mishurov, Y.N. (2003). Corotation, Stellar Wandering, and Fine Structure of the Galactic Abundance Pattern. ApJ, **589**, 210–216. 18, 147

Lin, C.C. & Shu, F.H. (1964). On the Spiral Structure of Disk Galaxies. ApJ, **140**, 646–+. 4, 5, 6, 7, 13, 14, 30, 39, 78, 92, 102, 103, 104, 144, 149

Lin, C.C., Yuan, C. & Shu, F.H. (1969). On the Spiral Structure of Disk Galaxies. III. Comparison with Observations. ApJ, **155**, 721. 4

Lindblad, P.O. (1960). The development of spiral structure in a galaxy approached by numerical computations. *Stockholms Observatoriums Annaler*, **21**, 4–+. 4

Lindegren, L., Babusiaux, C., Bailer-Jones, C., Bastian, U., Brown, A.G.A., Cropper, M., Høg, E., Jordi, C., Katz, D., van Leeuwen, F., Luri, X., Mignard, F., de Bruijne, J.H.J. & Prusti, T. (2008). The Gaia mission: science, organization and present status. In W.J. Jin, I. Platais & M.A.C. Perryman, eds., *IAU Symposium*, vol. 248 of *IAU Symposium*, 217–223. 107, 146

Loebman, S.R., Roškar, R., Debattista, V.P., Ivezić, Ž., Quinn, T.R. & Wadsley, J. (2011). The Genesis of the Milky Way's Thick Disk Via Stellar Migration. ApJ, **737**, 8. 18

Lucy, L.B. (1977). A numerical approach to the testing of the fission hypothesis. AJ, **82**, 1013–1024. 50, 163

Lynden-Bell, D. & Kalnajs, A.J. (1972). On the generating mechanism of spiral structure. MNRAS, **157**, 1–+. 15, 16, 18, 30, 49, 64, 142

Maciejewski, W. (2006). Response of the integrals in the Tremaine-Weinberg method to multiple pattern speeds: a counter-rotating inner bar in NGC 2950? MNRAS, **371**, 451–458. 25

Mark, J.W.K. (1974). On density waves in galaxies. I - Source terms and action conservation. ApJ, **193**, 539–559. 11

Martig, M., Crocker, A.F., Bournaud, F., Emsellem, E., Gabor, J.M., Alatalo, K., Blitz, L., Bois, M., Bureau, M., Cappellari, M., Davies, R.L., Davis, T.A., Dekel, A., de Zeeuw, P.T., Duc, P.A., Falcon-Barroso, J., Khochfar, S., Krajnovic, D., Kuntschner, H., Morganti, R., McDermid, R.M., Naab, T., Oosterloo, T., Sarzi, M., Scott, N., Serra, P., Shapiro Griffin, K., Teyssier, R., Weijmans, A.M. & Young, L.M. (2012). The ATLAS3D project - XXII. Low-efficiency star formation in early-type galaxies: hydrodynamic models and observations. *ArXiv e-prints*. 93

Masset, F. & Tagger, M. (1997). Non-linear coupling of spiral waves in disk galaxies: a numerical study. A&A, **322**, 442–454. 39

Mathewson, D.S., van der Kruit, P.C. & Brouw, W.N. (1972). A High Resolution Radio Continuum Survey of M51 and NGC 5195 at 1415 MHz. A&A, **17**, 468. 21

McKee, C.F. & Ostriker, J.P. (1977). A theory of the interstellar medium - Three components regulated by supernova explosions in an inhomogeneous substrate. ApJ, **218**, 148–169. 2

McMillan, P.J. (2011). Mass models of the Milky Way. MNRAS, **414**, 2446–2457. 2, 32, 54

Meidt, S.E., Rand, R.J., Merrifield, M.R., Debattista, V.P. & Shen, J. (2008a). Tests of the Radial Tremaine-Weinberg Method. ApJ, **676**, 899–919. 25

Meidt, S.E., Rand, R.J., Merrifield, M.R., Shetty, R. & Vogel, S.N. (2008b). Radial Dependence of the Pattern Speed of M51. ApJ, **688**, 224–236. 25

Meidt, S.E., Rand, R.J. & Merrifield, M.R. (2009). Uncovering the Origins of Spiral Structure by Measuring Radial Variation in Pattern Speeds. ApJ, **702**, 277–290. 25

Merrifield, M.R. & Kuijken, K. (1995). The pattern speed of the bar in NGC 936. MNRAS, **274**, 933–938. 25

Merrifield, M.R., Rand, R.J. & Meidt, S.E. (2005). Measuring Pattern Evolution: Winding Spiral Structure and Counter-Rotating Double Bars. In *American Astronomical Society Meeting Abstracts*, vol. 37 of *Bulletin of the American Astronomical Society*, 1313. 80

Merrifield, M.R., Rand, R.J. & Meidt, S.E. (2006). The lifetime of grand design. MNRAS, **366**, L17–L21. 23, 24, 25, 80

Minchev, I. & Famaey, B. (2010). A New Mechanism for Radial Migration in Galactic Disks: Spiral-Bar Resonance Overlap. ApJ, **722**, 112–121. 18, 64, 105

Minchev, I. & Quillen, A.C. (2006). Radial heating of a galactic disc by multiple spiral density waves. MNRAS, **368**, 623–636. 18, 105

Minchev, I., Famaey, B., Combes, F., Di Matteo, P., Mouhcine, M. & Wozniak, H. (2011). Radial migration in galactic disks caused by resonance overlap of multiple patterns: Self-consistent simulations. A&A, **527**, A147. 18, 64, 105

Minchev, I., Famaey, B., Quillen, A.C., Dehnen, W., Martig, M. & Siebert, A. (2012a). Radial migration does little for Galactic disc thickening. A&A, **548**, A127. 19, 142

Minchev, I., Famaey, B., Quillen, A.C., Di Matteo, P., Combes, F., Vlajić, M., Erwin, P. & Bland-Hawthorn, J. (2012b). Evolution of galactic discs: multiple patterns, radial migration, and disc outskirts. A&A, **548**, A126. 18, 79, 105

Minchev, I., Chiappini, C. & Martig, M. (2013). Chemodynamical evolution of the Milky Way disk. I. The solar vicinity. A&A, **558**, A9. 18

Monaghan, J.J. (1992). Smoothed particle hydrodynamics. ARA&A, **30**, 543–574. 164

Monaghan, J.J. & Lattanzio, J.C. (1985). A refined particle method for astrophysical problems. A&A, **149**, 135–143. 165

Morris, J.P. & Monaghan, J.J. (1997). A Switch to Reduce SPH Viscosity. *Journal of Computational Physics*, **136**, 41–50. 170, 171

Navarro, J.F., Frenk, C.S. & White, S.D.M. (1997). A Universal Density Profile from Hierarchical Clustering. ApJ, **490**, 493–+. 2, 31, 51

Nelson, D., D'Onghia, E. & Hernquist, L. (2012). The Morphology and Pattern Speed of Spiral Structure. In R. Capuzzo-Dolcetta, M. Limongi & A. Tornambè, eds., *Advances in Computational Astrophysics: Methods, Tools, and Outcome*, vol. 453 of *Astronomical Society of the Pacific Conference Series*, 369. 25, 80

Nordström, B., Mayor, M., Andersen, J., Holmberg, J., Pont, F., Jørgensen, B.R., Olsen, E.H., Udry, S. & Mowlavi, N. (2004). The Geneva-Copenhagen survey of the Solar neighbourhood. Ages, metallicities, and kinematic properties of
14 000 F and G dwarfs. A&A, **418**, 989–1019. 18

Oort, J.H. (1962). Spiral Structure. In L. Woltjer, ed., *The Distribution and Motion of Interstellar Matter in Galaxies*, 234. 15

Ostriker, J.P. & Peebles, P.J.E. (1973). A Numerical Study of the Stability of Flattened Galaxies: or, can Cold Galaxies Survive? ApJ, **186**, 467–480. 33, 54, 84

Pasetto, S., Chiosi, C. & Kawata, D. (2012a). Theory of stellar population synthesis with an application to N-body simulations. A&A, **545**, A14. 148

Pasetto, S., Grebel, E.K., Zwitter, T., Chiosi, C., Bertelli, G., Bienayme, O., Seabroke, G., Bland-Hawthorn, J., Boeche, C., Gibson, B.K., Gilmore, G., Munari, U., Navarro, J.F., Parker, Q., Reid, W., Silviero, A. & Steinmetz, M. (2012b). Thin disk kinematics from RAVE and the solar motion. A&A, **547**, A71. 107

Pasetto, S., Grebel, E.K., Zwitter, T., Chiosi, C., Bertelli, G., Bienayme, O., Seabroke, G., Bland-Hawthorn, J., Boeche, C., Gibson, B.K., Gilmore, G., Munari, U., Navarro, J.F., Parker, Q., Reid, W., Silviero, A. & Steinmetz, M. (2012c). Thick disk kinematics from RAVE and the solar motion. A&A, **547**, A70. 107

Pelupessy, F.I., van der Werf, P.P. & Icke, V. (2004). Periodic bursts of star formation in irregular galaxies. A&A, **422**, 55–64. 182

Pfenniger, D. & Norman, C. (1990). Dissipation in barred galaxies - The growth of bulges and central mass concentrations. ApJ, **363**, 391–410. 56

Pohlen, M. & Trujillo, I. (2006). The structure of galactic disks. Studying late-type spiral galaxies using SDSS. A&A, **454**, 759–772. 19

Press, W.H., Teukolsky, S.A., Vetterling, W.T. & Flannery, B.P. (1992). *Numerical recipes in FORTRAN. The art of scientific computing*. 37

Price, D.J. (2008). Modelling discontinuities and Kelvin Helmholtz instabilities in SPH. *Journal of Computational Physics*, **227**, 10040–10057. 172, 173

Price, D.J. (2012). Smoothed particle hydrodynamics and magnetohydrodynamics. *Journal of Computational Physics*, **231**, 759–794. 164

Price, D.J. & Monaghan, J.J. (2007). An energy-conserving formalism for adaptive gravitational force softening in smoothed particle hydrodynamics and N-body codes. MNRAS, **374**, 1347–1358. 33, 54, 84, 108, 165, 167, 169

Purcell, C.W., Bullock, J.S., Tollerud, E.J., Rocha, M. & Chakrabarti, S. (2011). The Sagittarius impact as an architect of spirality and outer rings in the Milky Way. Nature, **477**, 301–303. 15, 144

Quillen, A.C., Dougherty, J., Bagley, M.B., Minchev, I. & Comparetta, J. (2011). Structure in phase space associated with spiral and bar density waves in an N-body hybrid galactic disc. MNRAS, **417**, 762–784. 18, 27, 36, 39, 57, 77, 79, 86

Rand, R.J. (1995). Berkeley-Illinois-Maryland Array Observations of Molecular Spiral Structure in M100 (NGC 4321). AJ, **109**, 2444. 21

Rand, R.J. & Wallin, J.F. (2004). Pattern Speeds of BIMA SONG Galaxies with Molecule-dominated Interstellar Mediums Using the Tremaine-Weinberg Method. ApJ, **614**, 142–157. 25

Read, J.I., Hayfield, T. & Agertz, O. (2010). Resolving mixing in smoothed particle hydrodynamics. MNRAS, **405**, 1513–1530. 165, 173

Renaud, F., Bournaud, F., Emsellem, E., Elmegreen, B., Teyssier, R., Alves, J., Chapon, D., Combes, F., Dekel, A., Gabor, J., Hennebelle, P. & Kraljic, K. (2013). A sub-parsec resolution simulation of the Milky Way: global structure of the interstellar medium and properties of molecular clouds. MNRAS, **436**, 1836–1851. 27

Rix, H.W. & Zaritsky, D. (1995). Nonaxisymmetric Structures in the Stellar Disks of Galaxies. ApJ, **447**, 82. 1, 15

Roberts, W.W. (1969). Large-Scale Shock Formation in Spiral Galaxies and its Implications on Star Formation. ApJ, **158**, 123. 1, 20, 142

Roberts, W.W., Jr., Roberts, M.S. & Shu, F.H. (1975). Density wave theory and the classification of spiral galaxies. ApJ, **196**, 381–387. 78

Robertson, B.E. & Kravtsov, A.V. (2008). Molecular Hydrogen and Global Star Formation Relations in Galaxies. ApJ, **680**, 1083–1111. 179

Roca-Fàbrega, S., Valenzuela, O., Figueras, F., Romero-Gómez, M., Velázquez, H., Antoja, T. & Pichardo, B. (2013). On galaxy spiral arms' nature as revealed by rotation frequencies. MNRAS, **432**, 2878–2885. 106, 110, 141

Rodionov, S.A. & Athanassoula, E. (2011). Extensions and applications of the iterative method. A&A, **529**, A98. 51

Roming, P.W.A. *et al.* (2005). The Swift Ultra-Violet/Optical Telescope. Space Sci. Rev., **120**, 95–142. 146

Rosswog, S. & Price, D. (2007). MAGMA: a three-dimensional, Lagrangian magnetohydrodynamics code for merger applications. MNRAS, **379**, 915–931. 172

Rots, A.H. (1975). Distribution and kinematics of neutral hydrogen in the spiral galaxy M 81. II - Analysis. A&A, **45**, 43–55. 21

Roškar, R., Debattista, V.P., Quinn, T.R., Stinson, G.S. & Wadsley, J. (2008a). Riding the Spiral Waves: Implications of Stellar Migration for the Properties of Galactic Disks. ApJ, **684**, L79–L82. 18, 64, 105

Roškar, R., Debattista, V.P., Stinson, G.S., Quinn, T.R., Kaufmann, T. & Wadsley, J. (2008b). Beyond Inside-Out Growth: Formation and Evolution of Disk Outskirts. ApJ, **675**, L65–L68. 18, 19, 27, 147

Roškar, R., Debattista, V.P. & Loebman, S.R. (2012a). The Effects of Radial Migration on the Vertical Structure of Galactic Discs. *ArXiv e-prints*. 19

Roškar, R., Debattista, V.P., Quinn, T.R. & Wadsley, J. (2012b). Radial migration in disc galaxies - I. Transient spiral structure and dynamics. MNRAS, **426**, 2089–2106. 18, 64, 72, 76, 79, 87, 105, 106, 122, 142, 145

Saitoh, T.R. & Makino, J. (2009). A Necessary Condition for Individual Time Steps in SPH Simulations. ApJ, **697**, L99–L102. 177

Saitoh, T.R. & Makino, J. (2010). FAST: A Fully Asynchronous Split Time-Integrator for a Self-Gravitating Fluid. PASJ, **62**, 301–. 175, 176

Saitoh, T.R. & Makino, J. (2013). A Density-independent Formulation of Smoothed Particle Hydrodynamics. ApJ, **768**, 44. 173

Saitoh, T.R., Daisaka, H., Kokubo, E., Makino, J., Okamoto, T., Tomisaka, K., Wada, K. & Yoshida, N. (2008). Toward First-Principle Simulations of Galaxy Formation: I. How Should We Choose Star-Formation Criteria in High-Resolution Simulations of Disk Galaxies? PASJ, **60**, 667–. 184

Salo, H., Laurikainen, E., Buta, R. & Knapen, J.H. (2010). Bars do Drive Spiral Density Waves. ApJ, **715**, L56–L61. 15, 77

Salpeter, E.E. (1955). The Luminosity Function and Stellar Evolution. ApJ, **121**, 161. 181

Sánchez, S.F. *et al.* (2012). CALIFA, the Calar Alto Legacy Integral Field Area survey. I. Survey presentation. A&A, **538**, A8. 146

Sánchez-Blázquez, P., Courty, S., Gibson, B.K. & Brook, C.B. (2009a). The origin of the light distribution in spiral galaxies. MNRAS, **398**, 591–606. 18, 19, 64

Sánchez-Blázquez, P., Courty, S., Gibson, B.K. & Brook, C.B. (2009b). The origin of the light distribution in spiral galaxies. MNRAS, **398**, 591–606. 147

Schönrich, R. & Binney, J. (2009). Chemical evolution with radial mixing. MNRAS, **396**, 203–222. 18, 19

Seiden, P.E. & Gerola, H. (1979). Properties of spiral galaxies from a stochastic star formation model. ApJ, **233**, 56–66. 78

Seigar, M.S. & James, P.A. (1998a). The structure of spiral galaxies - I. Near-infrared properties of bulges, discs and bars. MNRAS, **299**, 672–684. 78

Seigar, M.S. & James, P.A. (1998b). The structure of spiral galaxies - II. Near-infrared properties of spiral arms. MNRAS, **299**, 685–698. 78

Seigar, M.S., Block, D.L., Puerari, I., Chorney, N.E. & James, P.A. (2005). Dust-penetrated arm classes: insights from rising and falling rotation curves. MNRAS, **359**, 1065–1076. 79, 143

Seigar, M.S., Bullock, J.S., Barth, A.J. & Ho, L.C. (2006). Constraining Dark Matter Halo Profiles and Galaxy Formation Models Using Spiral Arm Morphology. I. Method Outline. ApJ, **645**, 1012–1023. 79, 80, 96, 104, 143

Sellwood, J.A. (2010). New Developments in Spiral Structure Theory. *ArXiv e-prints*. 27, 80

Sellwood, J.A. (2011). The lifetimes of spiral patterns in disc galaxies. MNRAS, **410**, 1637–1646. 14, 27, 39, 80, 141

Sellwood, J.A. (2012). Spiral Instabilities in N-body Simulations. I. Emergence from Noise. ApJ, **751**, 44. 14, 79

Sellwood, J.A. (2013). Relaxation in N-body Simulations of Disk Galaxies. ApJ, **769**, L24. 108

Sellwood, J.A. (2014). Secular evolution in disk galaxies. *Reviews of Modern Physics*, **86**, 1–46. 7, 48, 85

Sellwood, J.A. & Binney, J.J. (2002). Radial mixing in galactic discs. MNRAS, **336**, 785–796. 17, 18, 19, 30, 40, 45, 48, 49, 64, 69, 147

Sellwood, J.A. & Carlberg, R.G. (1984). Spiral instabilities provoked by accretion and star formation. ApJ, **282**, 61–74. 15, 26, 27

Sellwood, J.A. & Carlberg, R.G. (2014). Transient spirals as superposed instabilities. *ArXiv e-prints*. 13, 27, 145

Sellwood, J.A. & Kahn, F.D. (1991). Spiral modes driven by narrow features in angular-momentum density. MNRAS, **250**, 278–299. 14, 27

Sellwood, J.A. & Lin, D.N.C. (1989). A recurrent spiral instability cycle in self-gravitating particle discs. MNRAS, **240**, 991–1007. 14, 39

Shen, S., Mo, H.J., White, S.D.M., Blanton, M.R., Kauffmann, G., Voges, W., Brinkmann, J. & Csabai, I. (2003). The size distribution of galaxies in the Sloan Digital Sky Survey. MNRAS, **343**, 978–994. 83

Siebert, A. *et al.* (2012). The properties of the local spiral arms from RAVE data: two-dimensional density wave approach. MNRAS, **425**, 2335–2342. 107

Solway, M., Sellwood, J.A. & Schönrich, R. (2012). Radial migration in galactic thick discs. MNRAS, **422**, 1363–1383. 18, 19, 79, 105

Sparke, L.S. & Gallagher, J.S., III (2007). *Galaxies in the Universe*. Cambridge University Press. 1

Sparke, L.S. & Sellwood, J.A. (1987). Dissection of an N-body bar. MNRAS, **225**, 653–675. 77

Speights, J.C. & Westpfahl, D.J. (2011). The Shearing H I Spiral Pattern of NGC 1365. ApJ, **736**, 70. 25, 80

Speights, J.C. & Westpfahl, D.J. (2012). The Pattern Speeds of NGC 3031, NGC 2366, and DDO 154 as Functions of Radius. ApJ, **752**, 52. 25

Springel, V. (2005). The cosmological simulation code GADGET-2. MNRAS, **364**, 1105–1134. 159

Springel, V. & Hernquist, L. (2002). Cosmological smoothed particle hydrodynamics simulations: the entropy equation. MNRAS, **333**, 649–664. 166, 167, 169

Springel, V. & Hernquist, L. (2003). Cosmological smoothed particle hydrodynamics simulations: a hybrid multiphase model for star formation. MNRAS, **339**, 289–311. 180

Springel, V., Di Matteo, T. & Hernquist, L. (2005). Modelling feedback from stars and black holes in galaxy mergers. MNRAS, **361**, 776–794. 33, 52

Steinmetz, M. (1996). GRAPESPH: cosmological smoothed particle hydrodynamics simulations with the special-purpose hardware GRAPE. MNRAS, **278**, 1005–1017. 165

Steinmetz, M. *et al.* (2006). The Radial Velocity Experiment (RAVE): First Data Release. AJ, **132**, 1645–1668. 107

Tamburro, D., Rix, H.W., Walter, F., Brinks, E., de Blok, W.J.G., Kennicutt, R.C. & Mac Low, M.M. (2008). Geometrically Derived Timescales for Star Formation in Spiral Galaxies. AJ, **136**, 2872–2885. 21, 22, 57

Tasker, E.J. & Tan, J.C. (2009). Star Formation in Disk Galaxies. I. Formation and Evolution of Giant Molecular Clouds via Gravitational Instability and Cloud Collisions. ApJ, **700**, 358–375. 27

Teyssier, R. (2002). Cosmological hydrodynamics with adaptive mesh refinement. A new high resolution code called RAMSES. A&A, **385**, 337–364. 93

Thomasson, M., Elmegreen, B.G., Donner, K.J. & Sundelius, B. (1990). A computer-generated galaxy model with long-lived two-armed spiral structure. ApJ, **356**, L9–L13. 27

Thornley, M.D. (1996). Uncovering Spiral Structure in Flocculent Galaxies. ApJ, **469**, L45. 78

Toomre, A. (1964). On the gravitational stability of a disk of stars. ApJ, **139**, 1217–1238. 8

Toomre, A. (1969). Group Velocity of Spiral Waves in Galactic Disks. ApJ, **158**, 899. viii, 9

Toomre, A. (1981). What amplifies the spirals. In S. M. Fall & D. Lynden-Bell, ed., *Structure and Evolution of Normal Galaxies*, 111–136. 10, 11, 12, 13, 41, 79, 85, 100, 102, 143, 144

Tremaine, S. & Weinberg, M.D. (1984). A kinematic method for measuring the pattern speed of barred galaxies. ApJ, **282**, L5–L7. 23, 25

Treuthardt, P., Salo, H. & Buta, R. (2009). Dynamical Simulations of NGC 2523 and NGC 4245. AJ, **137**, 19–33. 25

van Albada, T.S., Bahcall, J.N., Begeman, K. & Sancisi, R. (1985). Distribution of dark matter in the spiral galaxy NGC 3198. ApJ, **295**, 305–313. 2

van den Hoek, L.B. & Groenewegen, M.A.T. (1997). New theoretical yields of intermediate mass stars. A&AS, **123**, 305–328. 184

Vogel, S.N., Kulkarni, S.R. & Scoville, N.Z. (1988). Star formation in giant molecular associations synchronized by a spiral density wave. Nature, **334**, 402–406. 21

von Hoerner, S. (1960). Die numerische Integration des n-Körper-Problemes für Sternhaufen. I. ZAp, **50**, 184–214. 26

Wada, K., Baba, J. & Saitoh, T.R. (2011). Interplay between Stellar Spirals and the Interstellar Medium in Galactic Disks. ApJ, **735**, 1–+. 25, 27, 30, 31, 36, 47, 80, 93, 104, 105, 106, 141, 148

Williams, M.E.K. *et al.* (2013). The wobbly Galaxy: kinematics north and south with RAVE red-clump giants. MNRAS, **436**, 101–121. 107

Woosley, S.E. & Weaver, T.A. (1995). The Evolution and Explosion of Massive Stars. II. Explosive Hydrodynamics and Nucleosynthesis. ApJS, **101**, 181. 182, 183

Yanny, B. *et al.* (2009). SEGUE: A Spectroscopic Survey of 240,000 Stars with g = 14-20. AJ, **137**, 4377–4399. 107, 146

Yoachim, P., Roškar, R. & Debattista, V.P. (2010). Integral Field Unit Spectroscopy of the Stellar Disk Truncation Region of NGC 6155. ApJ, **716**, L4–L8. 19

Yoachim, P., Roškar, R. & Debattista, V.P. (2012). Spatially Resolved Spectroscopic Star Formation Histories of nearby Disks: Hints of Stellar Migration. ApJ, **752**, 97. 19

Zimmer, P., Rand, R.J. & McGraw, J.T. (2004). The Pattern Speeds of M51, M83, and NGC 6946 Using CO and the Tremaine-Weinberg Method. ApJ, **607**, 285–293. 25

Zucker, D.B., de Silva, G., Freeman, K., Bland-Hawthorn, J. & Hermes Team (2012). The Galactic Archaeology with HERMES Survey. In W. Aoki, M. Ishigaki, T. Suda, T. Tsujimoto & N. Arimoto, eds., *Galactic Archaeology: Near-Field Cosmology and the Formation of the Milky Way*, vol. 458 of *Astronomical Society of the Pacific Conference Series*, 421. 146

# Peer-reviewed Publications

Updated on 15/04/2014: 7 papers (4 first author)

1. Kawata, D., Hunt, J. A. S., Grand, R. J. J., Pasetto, S., & Cropper, M. 2014, "Gas and Stellar Motions and Observational Signatures of Co-Rotating Spiral Arms", *ArXiv e-prints*, arXiv:1404.2620.

2. Grand, R. J. J., Kawata, D., & Cropper, M. 2014, "Orbits of radial migrators and non-migrators around a spiral arm in N-body simulations", *Monthly Notices of the Royal Astronomical Society*, 439, 623.

3. Kawata, D., Gibson, B. K., Barnes, D. J., Grand, R. J. J., & Rahimi, A. 2014, "Numerical simulations of bubble-induced star formation in dwarf irregular galaxies with a novel stellar feedback scheme", *Monthly Notices of the Royal Astronomical Society*, 438, 1208.

4. Grand, R. J. J., Kawata, D., & Cropper, M. 2013, "Spiral arm pitch angle and galactic shear rate in N-body simulations of disc galaxies", *Astronomy and Astrophysics*, 553, A77.

5. Grand, R. J. J., Kawata, D., & Cropper, M. 2012, "Dynamics of stars around spiral arms in an N-body/SPH simulated barred spiral galaxy", *Monthly Notices of the Royal Astronomical Society*, 426, 167.

6. Grand, R. J. J., Kawata, D., & Cropper, M. 2012, "The dynamics of stars around spiral arms", *Monthly Notices of the Royal Astronomical Society*, 421, 1529.

7. Saito, R. K., ... Grand, R. J. J., ... (110 authors) 2012, "VVV DR1: The first data release of the Milky Way bulge and southern plane from the near-infrared ESO public survey VISTA variables in the Vía Láctea", *Astronomy and Astrophysics*, 537, A107.

# Proceedings

1. Kawata, D., Grand, R. J. J., & Cropper, M. 2012, "Stellar dynamics around transient co-rotating spiral arms", *European Physical Journal Web of Conferences*, 19, 7006.